Cranfield University

Oyedele Oluwaseun Oyekoya

Structural Integrity of Engineering Components made of Functionally Graded Materials

School of Engineering

PhD

Cranfield University

School of Engineering

PhD THESIS

2008

Oyedele Oluwaseun Oyekoya

Structural Integrity of Engineering Components made of Functionally Graded Materials

Supervisor: Dr. D Mba and Dr. A El-Zafrany

Academic Year 2004 to 2008

Acknowledgement

Abstract

Functionally graded materials (FGM) are composite materials with microstructure gradation optimized for the functioning of engineering components. For the case of fibrous composites, the fibre density is varied spatially, leading to variable material properties tailored to specific optimization requirements. There is an increasing demand for the use of such *intelligent* materials in space and aircraft industries. The current preferred methods to study engineering components made of FGM are mainly modelling particularly those that are finite element (FE) based as experimental methods have not yet sufficiently matured. Hence this thesis reports the development of a new Mindlin-type element and new Reissner-type element for the FE modelling of functionally graded composite (FGC) structures subjected to various loadings such as tensile loading, in-plane bending and out-of-plane bending, buckling and free vibration.

The Mindlin-type element formulation is based on averaging of transverse shear distribution over plate thickness using Lagrangian interpolation. Two types of Mindlin-type element were developed in this report. The properties of the first Mindlin-type element (i.e. Average Mindlin-type element) are computed by using an average fibre distribution technique which averages the macro-mechanical properties over each element. The properties of the second Mindlin-type element (i.e. Smooth Mindlin-type element) are computed by using a smooth fibre distribution technique, which directly uses the macro-mechanical properties at Gaussian quadrature points of each element.

The Reissner-type element formulation is based on parabolic transverse shear distribution over plate thickness using Lagrangian and Hermitian interpolation. Two types of Reissner-type element were developed in this report, which include the Average and Smooth Reissner-type elements.

There were two types of non-linearity considered in the modelling of the composite structures, which include finite strain and material degradation. The composite structures considered in this paper are functionally graded in a single direction only, but the FE code developed is capable of analysing composite structures with multi-directional functional gradation. This study was able to show that the structural integrity enhancement and strength maximisation of composite structures are achievable through functional gradation of material properties over the composite structures.

Dedication

To the memory of

my supervisor, Dr. Ali El-Zafrany

LIST OF CONTENTS

LIST OF FIGURES

LIST OF TABLES

LIST OF NOTATIONS

<u>List of Symbols</u>

B	Matrix of shape function derivatives
F	Nodal load vector
K	Element stiffness matrix
q	Interpolated displacement component
R	Residual vector
δ	Displacement component
γ	Transverse shear strain vector
σ	x-y stress vector
τ	Transverse shear stress vector
ε	x-y strain vector
$\bar{a}$	Acceleration vector
F_i, G_i, H_i, P_i	Hermitian shape functions
N_i	Lagrangian shape functions
U	Strain energy
u, v, w	Displacement components along the x, y and z directions respectively
V	Volume fraction
W	Work done by actual load
X	Longitudinal strength
Y	Transverse strength
ξ, η	Non-dimensional x and y location
ρ	Density
μ	Shear modulus
ψ	Transverse shear deformation
ν	Poisson's ratio
Av.	Average
Conf.	Conforming
F.I.	Failure Index

FE	Finite Element
FGC	Functionally Graded Composite
FGM	Functionally Graded Material
NonC.	Non-conforming
Sm.	Smooth

List of Subscripts

1	Longitudinal direction of the material axis
2	Transverse direction of the material axis
c	Compressive strength
f	Fibre
m	Matrix
t	Tensile strength
x	Longitudinal direction of the local axis
y	Transverse direction of the local axis
comp	Traditional composite
fgm	Functionally graded material
b	Out of plane displacement component
uv	u and v displacement components
w	w displacement component
o	Midplane displacement component
ψ	Transverse shear component
θ	Bending component

List of Superscripts

L	L^{th} layer of composite
0	Midplane of composite
σ	Non-linear terms

1 Introduction

Composite materials have fully established themselves as workable engineering materials and are now relatively commonplace around the world, particularly for structural purposes. Early military applications of polymer matrix composites during World War II led to large-scale commercial exploitation, especially in the marine industry, during the late 1940s and early 1950s. Today, the aircraft, automobile, leisure, electronic and medical industries are quite dependent on fibre-reinforced plastics, and these composites, namely particulate or mineral filled plastics, are also widely used in industry because of the associated cost reduction.

In the continuing quest for improved performance, which may be specified by various criteria including less weight, more strength and lower cost, traditional materials frequently reach the limit of their usefulness. Hence, material scientists, engineers and scientists are always striving to produce either improved traditional composite materials or new materials such as functionally graded materials (FGMs).

FGMs are composite materials with microstructure gradation optimized for the functioning of the engineering component. For the case of fibrous composites, the fibre density is varied spatially, leading to variable material properties tailored to specific optimization requirements. There is an increasing demand for the use of such *intelligent* materials in space and aircraft industries.

The objective of this research is to study the structural integrity of engineering components made of FGMs. This research objective can be broken down into subtopics which include micromechanics analysis, finite element static and dynamic analysis, buckling analysis and progressive damage analysis.

The technique employed in this thesis for the determination of the structural integrity of engineering components is to carry out a computational damage assessment of the component. In order to determine failure, the maximum stress in the component needs to be compared with the maximum permissible stress obtained from a selected failure criterion. Hence maximum stress was determined by employing a numerical method called Finite Element Method. Also in order to analyse the functionally graded composite, the micromechanical equations were employed.

This thesis does not only determine the structural integrity of engineering components but it also determines the optimum design of engineering components. The FE code developed in this thesis carries out the structural integrity of engineering components and the analysis of the results obtained from running the code for different fibre distributions enables the code user to determine the optimum fibre distribution. The flow chart that explains the FE code structure with the implementation of the optimisation technique is as shown in Figure 1-1.
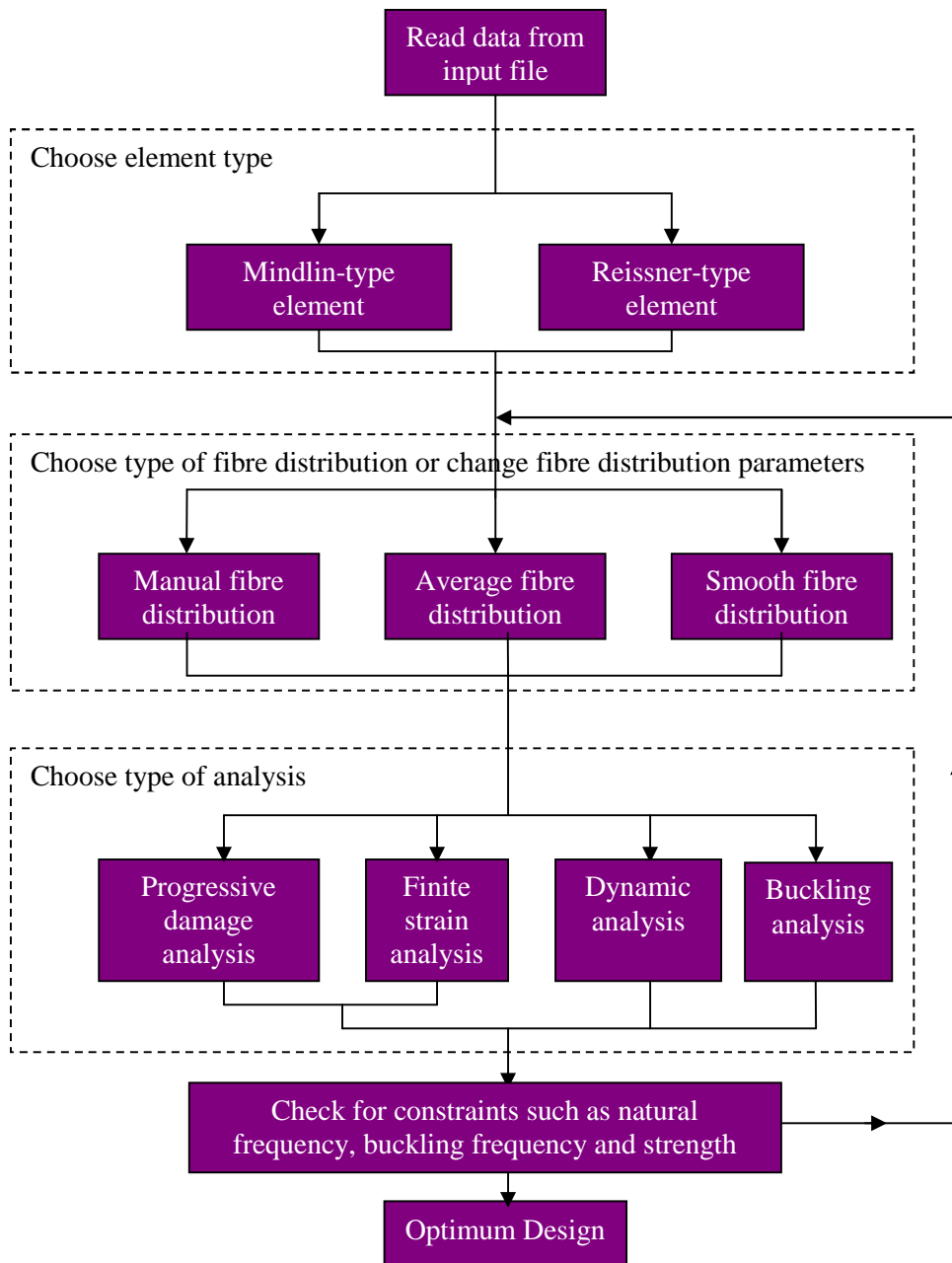
Figure 1-1: FE analysis and optimisation flowchart

1.1 Background

Composite materials are often used in different engineering fields, especially in the aerospace field. The main advantage of composite materials is the high stiffness-to-weight and strength-to-weight ratios. The limitations of composite materials are the following: the weakness of interfaces between layers may lead to delamination, extreme thermal loads may lead to debonding between matrix and fibre due to mismatch of mechanical properties, and residual stresses may be present due to difference in coefficients of thermal expansion of the fibre and the matrix. To overcome the limitations, functionally graded materials (FGMs) have recently been proposed.

The FGMs are made in such a way that the volume fractions of two or more materials are varied continuously along a certain dimension. The FGMs can be made as required for application, for example, thermal barrier plate structures can be made from a mixture of ceramic and metal for high temperature application. The advantage of the FGM plate is that its material properties vary continuously from one surface to the other, thus it avoids the interface problem that exists in homogeneous composites.

The FGM concept was originated in Japan in 1984 during the space-plane project, in the form of a proposed thermal barrier material capable of withstanding a surface temperature of 2000 K and a temperature gradient of 1000 K across a cross section <10 mm. Since 1984, FGM thin films have been comprehensively researched, and are almost a commercial reality. The FGMs were first developed by Japanese scientists in the 1980s. Since that time, the FGMs have been used in several branches and are still being broadened. The main research works on functionally graded materials cover topics such as thermo-elasticity, fracture mechanics, buckling vibration and control. The main applications of functionally graded materials include fibre optics, space rockets, engines, armour tanks etc.

1.2 Objectives

This research aims at developing the theory and software for finite element stress and vibration analysis of engineering components made of functionally graded fibrous layered composite materials. The basic aspects of the research are as follows:

- A full study of the micromechanics of fibrous composites, so as to be able to

predict accurately all required material properties from those of the constituents.

- A full study of failure criteria and damage mechanisms as appropriate to FGM.

- Derivation of special finite elements capable of efficiently dealing with FGM, including centrifugal loading and different non-linear aspects.

- The development of computer software based on the derived theories, for stress and vibration analysis of engineering components made of functionally graded fibrous layered composite materials, and capable of assessing the structural integrity of the components.

- Applications on optimum design of engineering components such as rotating turbine discs, and any other useful industrial application

1.3 FGM Applications

FGMs offer great promise in applications where the operating conditions are severe. For example, wear-resistant linings for handling large heavy abrasive ore particles, rocket heat shields, heat exchanger tubes, thermoelectric generators, heat-engine components, plasma facings for fusion reactors, and electrically insulating metal/ceramic joints. They are also ideal for minimising thermomechanical mismatch in metal-ceramic bonding.

Koch and Gunter (2003) carried out a research on a new generation of cutting tools based on functionally graded sialons for solving the machining problems of the 21st century. It was proposed that new ceramic tool materials on the basis of Silicon Nitride/Oxide ("Sialons") with a tough core would be developed, to allow a significantly higher performance in machining, in particular for "heavy-to-machine-parts". It was also proposed that the output would enable the European machining industry to increase and speed up the production combined with saving of resources and should benefit for health and environment.

The Swedish Defence Research Agency (2002) presented an article in their annual report on armour for future combat vehicle. In order to meet the conflicting demands of lower vehicle weight and much improved protection, future generations of fighting vehicles will need new types of armour. A promising passive armour concept, studied

at Swedish Defence Research Agency, is designed to cause interface defeat of the projectile. Interface defeat of tungsten kinetic energy long-rod projectiles has been demonstrated at velocities close to 2000m/s using today's ceramics and armour technologies. Spark Plasma Sintering is an interesting technology to produce FGMs. FGM have the potential to be very efficient armour materials. Swedish Defence Research Agency has been conducting initial experiments to produce an FGM with a hard outer surface of TiB2 and a strong, ductile inner surface of titanium. There are still some difficulties to overcome but the results so far are encouraging. Swedish Defence Research Agency also conducts research into active protection systems against KE-projectiles and electromagnetic armour.

Siegmund (2005) describes a program to develop low-cost, functionally graded (FG) carbon-carbon composites for use in a wide range of new applications including automotive structural and heat transfer components, orthopaedic implants, friction materials for the specialty automotive, truck and aerospace industries. C-C composites have been the material of choice for high-end high temperature applications for commercial and military aircraft. However, their high cost has limited their application to other significant markets. The research team (Purdue University, University of Notre Dame, Indiana University, Honeywell Aircraft Landing Systems, and National Composite Centre) proposes to change this by introducing a new class of C-C composites with significantly lower cost. The program merges the related expertise of the team members and proposes the development of new technologies to make FG-C-C composites with $10/lb a reality. The program uniquely integrates a robotic manufacturing process, a novel process chemistry approach, materials design and structural analysis with an industrial-scale operation.

Bey (2002) investigated functionally graded metallic foams as an alternative thermal protection system for space transportation vehicles. An integrated thermal-structural concept in which the load bearing structure has insulating capability and has potential for significant weight savings over current thermal protection systems (TPS). Current TPS do not have a structural function so they are parasitic from a structural viewpoint. Current TPS include coated ceramic tiles or blankets of fibrous insulation affixed to the vehicle surface and metallic panels in which fibrous insulation is encapsulated in foil and placed between an outer metal surface and the vehicle structure. A multifunctional

TPS concept is based on metallic panels that are continuously graded in composition and porosity.

U.S. DoD (2002) researched on F135 engine and PW J52 engine and they applied functional graded thermal barrier coatings on turbine components, which will increase component life under severe environment and reduce the down-time for the repair of components and enhance readiness of the fleet. These were run in two engine tests for qualification: (i) F402 engine (AV-8B) test as test engine for insertion in F135 engine (JSF) and (ii) PW J52 (EA-6B) engine test.

1.4 Thesis Layout

Chapter 1 describes the advent of FGMs, and presents the research objectives. It also reviews the application of FGMs which helps to justify the research objectives.

Chapter 2 reviews publications on composites and FGMs. Then it reviews publications on the application of FEM to composite plates and shells which also reflects the developments of non-linear Mindlin and Reissner-type elements. It also reviews publications on the application of FEM on FGMs.

Chapter 3 describes how to compute the elastic and strength properties of FGMs using micromechanics techniques. It also describes the fibre distribution techniques employed in this work, such as manual fibre distribution, average fibre distribution and smooth fibre distribution technique. Finally the chapter describes the failure criteria and the damage mechanism used in the progressive damage modelling of FGMs.

Chapter 4 explains the Mindlin-type plate bending element theory and derives the equation used in the finite element programming. The finite element formulation of displacement equation, strain equation, stress equation, strain energy variation and generalised equation of equilibrium were summarised in the chapter. The generalised equation of equilibrium is then linearised in-order to obtain the Mindin-type element equation. Material non-linearity and geometrical non-linearity have been considered.

Chapter 5 explains the Reissner-type plate bending element theory and derives the equation used in the finite element programming. The non-linear Reissner-type element theory defines the displacement equation, strain equation, stress equation, strain energy

variation and generalised equation of equilibrium. The generalised equation of equilibrium is then linearised in-order to obtain the Reissner-type element equation.

Chapter 6 describes how the micromechanical equations and the FE equations derived in previous chapters were used in developing the FE codes which were used in the analysis of functionally graded composites. The use of flowcharts was employed to give an in-depth explanation of the FE codes.

Chapter 7 explains the validation of the FE codes. The validation exercise was carried out in three stages. The first stage involves the validation of the infinitesimal strain part of the Average Mindlin programs against analytical solutions using traditional composite plate cases. The second stage involves the validation of the infinitesimal strain part of the Average, Smooth and Ordinary Mindlin programs against Abaqus results using the functionally graded composite (FGC) cases. The third stage involves the validation of infinitesimal and finite strain part of the Average and Smooth programs against the Ordinary programs using the FGC cases.

Chapter 8 describes the optimisation technique and presents the optimum design. This optimisation technique involves changing the fibre distribution parameters and running the FE codes for the given fibre distribution, checking to see if all constraints have been satisfied. The constraints that have been considered include stress constraints, buckling load constraints and natural frequency constraints.

Chapter 9 summarises the conclusion of the research and gave some recommendation of future works.

Appendix A presents the constitutive equations for laminates in order to explain all equations used in this thesis.

Appendix B explains why certain integrated **D** matrices become zero in the analysis of symmetric composite laminates of the Reissner-type elements.

2 Literature Review

In order to demonstrate a significant contribution in the FGM technology, an awareness of the history and current development in FGM technology was required. Hence, an extensive literature review was undertaken. The scope of this literature review focussed on the various components that constitute this research work. Hence this chapter reviews publications on composites and FGMs. It reviews publications on the FE analysis of composite plates and shells which also reflect the developments of non-linear Mindlin and Reissner-type elements. It also reviews publications on the FE analysis of FGMs.

2.1 Composites and FGMs

This section reviews the publications on the developments in research of composites and FGMs. It is well recognized that shear deformation can be more significant in laminated, anisotropic plates than in isotropic, homogeneous plates. Shear deformation theories based on Mindlin's assumptions have been developed for laminated, anisotropic plates as described by Yang et al (1966) and Whitney and Pagano (1970). A theory has also been developed by Whitney (1990) for the bending of laminated, anisotropic plates which includes the effects of transverse shear deformation in a manner similar to the theory of Reissner (1950) for homogeneous, isotropic plates. This theory has been modified by Whitney and Rose (1991) to include the effect of transverse normal stress without increasing the number of bending equations above those generated in classical shear deformation theory. Whitney (1992) investigated the effect of transverse shear and normal stresses on the bending of symmetrically laminated, anisotropic plates subjected to cylindrical bending under uniform lateral load.

There were no publications found on progressive damage analysis of functionally graded composite. Hence the literature review in this section only focuses on progressive damage analysis of traditional composite. A comprehensive literature review on progressive damage analysis of composites was undertaken by Zahari (2005). Padhi et al (1998) presented a method, which study the non-linear behaviour, first ply failure and ultimate collapse of laminated composite plates with clamped edges,

subjected to transverse pressure. Several failure criteria, including Hashin and Tsai-Wu, are used to predict the failure mechanisms. The effect of aspect ratio on the strength and stiffness of laminated composite plates is studied. Non-linear strain-displacement relations that contain large strain and large rotation are used in the analysis. The general purpose finite element program Abaqus is used for analysis. The predictions of the model correlate well with experimental data for different aspect ratios.

Prusty et al (2001) developed a first ply failure analysis method for predicting the failure load on the laminated composite stiffened panels under various loading conditions. Various failure theories such as maximum stress, maximum strain, Hoffman, Tsai-Wu and Yeh-Stratton theories have been implemented for prediction of first ply failure loads using iterative procedure. A few laminated composite bare stiffened panels with various loading cases are solved for first-ply failure analysis. The results of un-stiffened and stiffened plates with various loading cases are compared with the published ones. New results for different stiffened shell panels having various radius-to-span ratios are presented and convergence study is made for the validation.

A key publication on the developments in research of FGMs was published by Koizumi (1997) which reviews FGM activities in Japan. Japanese scientists STA (1987) proposed the unique FGM concept to prepare new composite by using heat-resistant ceramics on the high temperature side and tough metals with high thermal conductivity on the low-temperature side, with a gradual compositional variation from ceramic to metal. In order to extend the applications of FGMs to different fields of industry such as optics and/or electronic materials, in 1990 the needs of FGM were surveyed. Through this survey, about 200 possibilities for utilising the FGM concept to improve conventional materials and to create new materials were proposed and these proposals were published by the Society of Non-Traditional Technology (1991). Japanese scientists STA (1993) focussed on the possibility of improving the efficiency of energy conversion materials by FGM technology. The results revealed that FG technology would remarkably increase efficiency for photoelectric, thermoelectric, thermionic and nuclear energy conversions.

2.2 FE Analysis of Composite Plates and Shells

This section discusses the development of the FE method and reviews the publications on FE analysis of composite plates and shells. The concept of the FE method stems from work done in the 1940s, in which Courant (1943), Prager and Synge (1947) made variational assumptions in solving differential equations. Many of the early attempts for the solution of continuum elasticity problems were based on representing the continuum by an equivalent assemblage of bars and beams as described by Hrennikoff (1941) and McHenry (1943).

The next step in the utilisation of FEM was taken by Boeing in the 1950s when Boeing, followed by others, used triangular stress elements to model airplane wings. Levy (1953) proposed an analysis for aircraft wings using a collection of elementary beam and torque boxes. The first engineering applications of the FE method were described by Argyris (1954). Turner et al (1956) refined Levy's work by reducing the torque boxes to assemblies of triangular and rectangular slices. Yet it was not until the 1960 that Clough (1960) made the term "finite element" popular. Melosh (1963) established the basic conditions for accurate finite element derivations. Zienkiewicz and Cheung (1967) wrote the first book entirely devoted to the FE method in 1967. Engineers have managed to develop finite elements for the analysis of many linear and nonlinear problems as described by Zienkiewicz (1977).

The developments of non-linear Mindlin and Reissner-type elements will now be discussed. A good literature review on plate theory was published by Apetre and Sankar (2008). Reissner (1945) was the first to propose a plate theory that included the effect of shear deformation and that assumed linear longitudinal displacements and constant transverse displacements. Mindlin (1951) introduced the correction factor into the shear stress to account for the fact that the model predicts a uniform shear stress through the thickness of the plate. Yang et al (1966) extended Mindlin's theory for homogeneous plates to laminates consisting of arbitrary number of bonded layers. Whitney and Pagano (1970) developed a Mindlin-type theory for anisotropic laminated plates consisting of an arbitrary number of bonded anisotropic layers that includes shear deformation and rotary inertia. Displacement field is assumed to be linear in thickness coordinate. Since 1970, the plate theory was improved by including higher-order terms

11

in displacement assumptions. Essenburg (1975) assumed second-order transverse displacements and linear longitudinal displacements. Also Reissner (1975) included third-order terms in the in-plane displacements' z-expansion. Lo et al (1977) included third-order in-plane and second-order out-of-plane terms. Reddy (1984) developed a third order shear deformation theory (TSDT) for composite laminates based on assumed displacement fields (third-order in-plane, and constant out-of-plane displacements).

Finite elements based upon Kirchoff's theory were the first plate-bending elements to be published. The first element to employ Mindlin's theory, was introduced by Hinton et al (1975). It was recognized that the finite element solutions which employed Mindlin elements become less accurate than those based upon Kirchoff elements, when the plate thickness was reduced. This reduction in accuracy associated with Mindlin elements has been referred to as the "locking" phenomenon. In 1978, many researchers such as Pugh (1978) and Hughes et al (1978a) investigated this phenomenon, and the reduced and selective integration schemes have been proposed as a means to avoid locking. Also a nine-node quadrilateral element known as the "heterosis" element which exhibits improved characteristics in comparison with both the eight-node serendipity and the nine-node Lagrangian elements was derived by Hughes et al (1978b). An analysis of a sufficient and necessary criterion of selective reduced integration which must be satisfied in order that locking is avoided; was introduced by Tsach (1981). Shape functions are considered the most important part in the derivation of a new finite element. In 1986, El-Zafrany and Cookson (1986a, b) introduced a general theory for the derivation of shape functions for triangular and quadrilateral family of finite elements. Attia (1996) introduced a new conforming and non-conforming finite elements for the static and dynamic analysis of rotating composite layered plates and shells. The elements consider parabolic distribution of transverse shear stresses and were based on Lagrangian and Hermitian shape functions. In 1999, a family of high-order facetted shell elements of linear and non-linear stress and vibration analysis of composite layered plates and shell structures was introduced by Attia and El-Zafrany (1999). Engineering slope angles were employed in element equations and transverse stresses were expanded over the thickness.

Tang et al (1983, 1984) introduced the quasi-conforming element technique. However all of the examples were limited to linear formulations. The quasi-conforming non-

linear formulation is based on the updated Lagrangian method with the assumption of small strains and large displacements. Guan et al (1992, 1995) presented a nine-node quasi-conforming degenerated shell element for linear and non-linear analysis. Many articles have been published by Shi and Voyiadjis (1991 - 1993) using the quasi-conforming formulation. Park et al (2006) studied the linear static and dynamic response of laminated composite plates and shells using a quasi-conforming shell element. The quasi-conforming shell element has been fully extended for the large displacement of elasto-plastic analysis by Kim and Lomboy (2006).

2.3 FE Analysis of FGMs

Pervaiz (1999) investigated the structural integrity of a functionally graded disk. Two cases were considered which includes the disk under a bending load and the disk under a centrifugal loading. Generally it was observed that stress distribution improvement was achieved with different fibre distribution, hence suggesting that it is possible to find a fibre distribution capable of minimising stress in the component and this formulated the optimisation objective in this report. Also, Martinez (2001) developed the work of Pervaiz (1999) further.

Reddy (2000) presented a theoretical formulation and finite element models based on third order shear deformation theory for the analysis of through-thickness functionally graded plates. The Navier solution for simply supported plates based on the linear third-order theory, also the non-linear static and dynamic finite element results based on the first-order theory were presented by Reddy (2000) to show effects of volume fractions and modulus ratio of the constituents on deflections and transverse shear stresses.

Javaheri and Eslami (2002) derived equilibrium and stability equations for rectangular simply supported functionally graded plates. The derivation was based on the classical plate theory and with the assumption of power law composition for the material. And the buckling analysis of functionally graded plates under in-plane compression was investigated.

Bobaru and Jian (2004) undertook a study of optimisation of FGMs with temperature dependent properties using a mesh-free solution. In this study, mass is minimised, whilst a constraint is defined in terms of violating the critical tensile and compressive

stresses. This study started with a configuration that has thin coatings of pure metal and pure ceramic at the exterior with a thick FGM layer in-between. Nine designs were used. They converge to a profile that has a thin FGM layer. The metal (ZrO_2) is lighter than the ceramic (Ti-6Al-4V) and the resulting FGM is metal rich. This work highlights the significance of the objective of this report.

Silvia and Paulino (2004) developed a design solution for FGM structures by using the concept of continuum topology optimisation. It was concluded that novel structural types are obtained by exploring the functionally graded materials idea. Hence, it was recommended that the design of composite unit cells made of FGMs be considered using continuum topology optimisation concepts. This recommendation justifies the optimisation objective of this report.

Chen and Liew (2004) investigated the buckling behaviour of FGM rectangular plates subjected to non-linearly distributed in-plane edge loads. They stated that a mesh-free method which approximates displacements based on scattered nodes (i.e. radial basis function and polynomial basis) was employed, in-order to avoid complicated numerical procedures that arises in the FEM from the use of elements. This FEM complication was dealt with in this thesis.

Kim et al (2008) extended the non-linear quasi-conforming formulation to the case of FGM structures and the associated FE model that accounts for the mechanical behaviour. The quasi-conforming non-linear formulation is based on the updated Lagrangian method with the assumption of small strains and large displacements. The geometrically non-linear formulation is derived using the full definition of the Green strain tensor that includes bending and transverse shear stresses in the geometric stiffness. The explicit definition of stiffness matrix was used hence no Gauss integration was employed. Thus the computational time is significantly reduced in the incremental non-linear analysis. The material properties of the FGM plates and shells are assumed to change continuously throughout the thickness of the plate and shell, according to the volume fraction of the constituent materials based on sigmoid functions.

2.4 Summary

This section summarizes the lessons learnt from the literature review carried out in this report. The lessons learnt include:

- Weight minimization without strength reduction is achievable in FGM components.

- Strength maximization without increase in weight is achievable in FGM components.

- FGM components with complex geometry require FE method.

- FE method for FGMs requires complicated mathematical procedures.

- Very little research works have been carried out on non-linear FEA and progressive damage analysis of FGM components.

- FGM technology can be beneficial in vast application such as aerospace, mechanical application, medical application etc.

In comparison to existing publications, this thesis has been able to give unique contributions to the subject matter. These contributions include Mindlin-type element formulation based on averaging of transverse shear distribution over plate thickness using Lagrangian interpolation, Reissner-type element formulation based on parabolic transverse shear distribution over plate thickness using Lagrangian and Hermitian interpolation, finite strain modelling based on Green's strain-displacement equation and smooth fibre distribution technique based on numerical computation of macro-mechanical properties at Gaussian quadrature points.

3 Micromechanics and Failure Criteria of Fibrous Composites

In the traditional method, the equations that describe the stress-strain behaviour of a lamina and the load-deformation behaviour of a laminate are based on the elastic properties of the lamina, and as such, ignore the microscopic nature of the material. In other words, no direct account of the fact that fibre reinforced materials is being considered.

Since the starting point of a significant proportion of composites' manufacture is the combination of fibres and matrix, it would be appropriate to predict the behaviour of the composite (laminate) from the knowledge of the properties of the constituents alone. It is important to note that micromechanics models have proven to be successful in predicting the longitudinal modulus in tension and compression, and reasonably successful in predicting the corresponding strengths. Whilst models exist for predicting transverse and shear stiffness, they do not compare well with experimental data. There are no satisfactory methods for predicting transverse and shear strengths. A good literature which gives a detailed explanation of micromechanics can be found in the book written by Matthews and Rawlings (1999)

The deficiencies in micromechanics models mean that the prediction of laminate performance from only the knowledge of fibre and matrix properties is not possible at the moment. However, successful use of macro-mechanics to predict laminate behaviour is possible; provided the values of stiffness and strength obtained from experiments on representative unidirectional samples are used as input values.

This chapter defines the elastic and strength properties of FGMs. It describes the micromechanics algorithm and the fibre distribution techniques such as manual fibre distribution, average fibre distribution and smooth fibre distribution technique developed in this work. The basic failure criteria of composites are also summarised.

3.1 Elastic and Mass Properties of FGMs

In order to compute the elastic and mass properties of FGMs, micromechanical analysis is required. The micromechanical properties of unidirectional composite such as longitudinal stiffness, transverse stiffness, shear modulus, Poisson's ratio and density are presented. The following derivations in this chapter assume that composites considered are perfect mixtures of fibres and matrix (i.e. negligible air space in composite). More information on Micromechanics can be found in the book written by Matthews and Rawlings (1999); Datoo (1991); Argarwal et. al. (2006) and Kaw (1997).

Longitudinal stiffness

Consider a unidirectional composite loaded by a force F_c parallel to the fibres as shown in the Figure 3-1. In order to establish equilibrium, it can be shown that:

$$F_c = F_f + F_m \tag{3.1}$$

where subscript c, f and m stands for composite, fibre and matrix respectively.
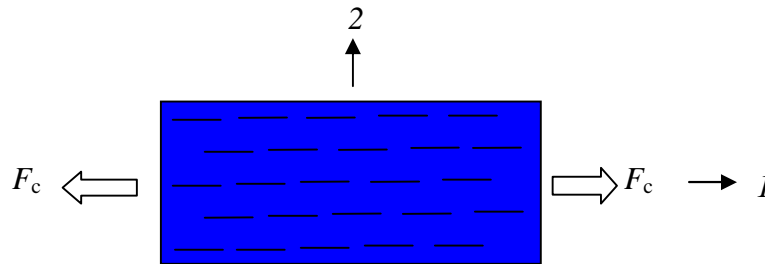
Figure 3-1: Unidirectional composite loaded in the fibre direction

Equation 3.1 can be re-written as:

$$\sigma_c A_c = \sigma_f A_f + \sigma_m A_m \tag{3.2}$$

where A_c, A_f and A_m represents the cross-sectional area of the composite, fibre and matrix respectively.

Using the definition of fibre volume fraction (V_f) and matrix volume fraction (V_m) given below

$$V_F = \frac{A_f}{A_c}; \qquad V_m = \frac{A_m}{A_c} \tag{3.3}$$

Equation 3.2 becomes:

$$\sigma_c = \sigma_f V_f + \sigma_m V_m \tag{3.4}$$

Equation 3.4 can be rewritten as:

$$E_c \varepsilon_c = E_f \varepsilon_f V_f + E_m \varepsilon_m V_m \tag{3.5}$$

where E is the Young's modulus. Also ε_c, ε_f and ε_m represent the transverse strain of the composite, fibre and matrix respectively.

In this case, perfect bonding is assumed (i.e. $\varepsilon_c = \varepsilon_f = \varepsilon_m$ which implies there is no slippage at the fibre/matrix interface), also $E_c = E_{11}$ it can be shown that Equation 3.5 simplifies to:

$$E_{11} = E_f V_f + E_m V_m \tag{3.6}$$

Transverse stiffness

Consider a unidirectional composite loaded by a stress σ_c perpendicular to the fibre as shown in the Figure 3-2. The transverse extension of the composite (δ_c) is the sum of the matrix extension (δ_m) and fibre extension (δ_f):

$$\delta_c = \delta_f + \delta_m \tag{3.7}$$
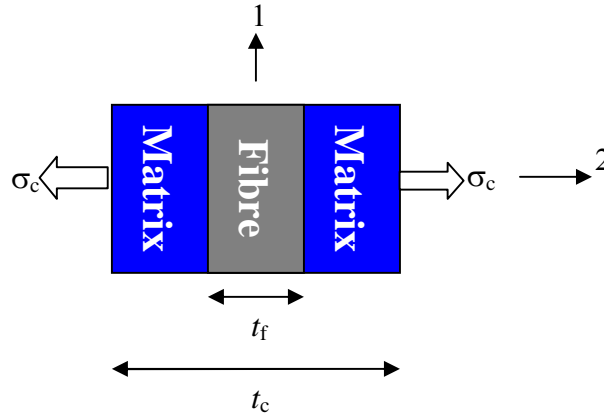
Figure 3-2: Unidirectional composite loaded perpendicular to the fibre direction

Equation 3.7 can be re-written as:

$$\varepsilon_c t_c = \varepsilon_f t_f + \varepsilon_m t_m \tag{3.8}$$

where t_c, t_f and t_m represents the thickness of the composite, fibre and matrix respectively. Also ε_c, ε_f and ε_m represent the transverse strain of the composite, fibre and matrix respectively.

Using the definition of fibre volume fraction (V_f) and matrix volume fraction (V_m) given below

$$V_F = \frac{t_f}{t_c}; \qquad V_m = \frac{t_m}{t_c}$$

(3.9)

Equation 3.8 becomes:

$$\varepsilon_c = \varepsilon_f V_f + \varepsilon_m V_m$$

(3.10)

Equation 3.10 can be rewritten as:

$$\frac{\sigma_c}{E_c} = \frac{\sigma_f}{E_f} V_f + \frac{\sigma_m}{E_m} V_m$$

(3.11)

where E is the Young's modulus.

In this case, the transverse stress on the fibres and the matrix are equal i.e. $\sigma_c = \sigma_f = \sigma_m$, also $E_c = E_{22}$ hence Equation 3.11 simplifies to:

$$\frac{1}{E_{22}} = \frac{V_f}{E_f} + \frac{V_m}{E_m}$$

(3.12)

Shear modulus

Consider a unidirectional composite loaded by a shear stress τ_c as shown in the Figure 3-3. The shear deformation of the composite (Δ_c) is the sum of the matrix extension (Δ_m) and fibre extension (Δ_f):

$$\Delta_c = \Delta_f + \Delta_m$$

(3.13)
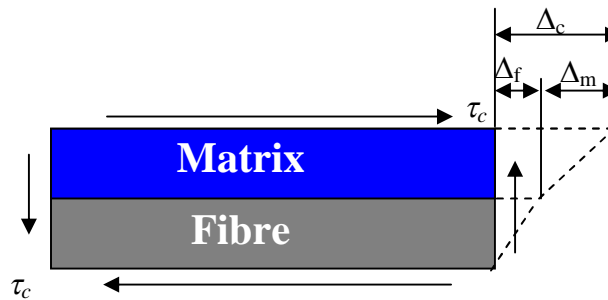
Figure 3-3: Shear deformation model

Equation 3.13 can be re-written as:

$$\gamma_c t_c = \gamma_f t_f + \gamma_m t_m$$

(3.14)

where l_c, l_f and l_m represents the length of the composite, fibre and matrix respectively. Also γ_c, γ_f and γ_m represent the in-plane shear strain of the composite, fibre and matrix respectively.

Using the definition of fibre volume fraction (V_f) and matrix volume fraction (V_m) given in Equation 3.9, Equation 3.14 becomes:

$$\gamma_c = \gamma_f V_f + \gamma_m V_m \qquad (3.15)$$

Equation 3.15 can be rewritten as:

$$\frac{\tau_c}{\mu_c} = \frac{\tau_f}{\mu_f} V_f + \frac{\tau_m}{\mu_m} V_m \qquad (3.16)$$

where μ is the in-plane shear modulus.

In this case, the shear stress on the fibre and matrix are equal i.e. $\tau_c = \tau_f = \tau_m$, also $\mu_c = \mu_{12}$ hence Equation 3.16 simplifies to:

$$\frac{1}{\mu_{12}} = \frac{V_f}{\mu_f} + \frac{V_m}{\mu_m} \qquad (3.17)$$

where $\qquad \mu_f = \dfrac{E_f}{2(1+\nu_f)} \quad$ and $\quad \mu_m = \dfrac{E_m}{2(1+\nu_m)}$

Also ν_f and ν_m represent the Poisson's ratio of the fibre and matrix respectively.

Poisson's ratio

Consider a unidirectional composite loaded by a stress σ_c parallel to the fibre as shown in the Figure 3-4. The transverse contraction of the composite (δ_c) is the sum of the matrix transverse contraction (δ_m) and fibre transverse contraction (δ_f):

$$\delta_c = \delta_f + \delta_m \qquad (3.18)$$
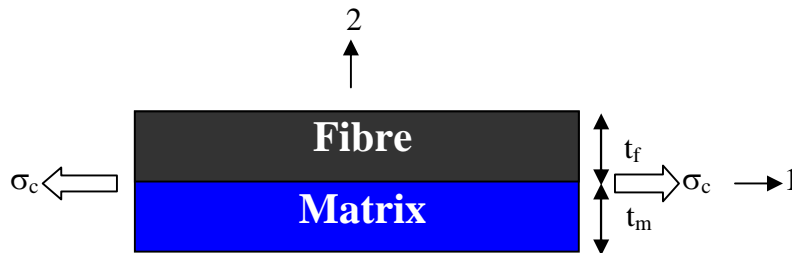
Figure 3-4: Unidirectional composite loaded in the fibre direction

Equation 3.18 can be re-written as:

$$-t_c \nu_c \varepsilon_c = -t_f \nu_f \varepsilon_f - t_m \nu_m \varepsilon_m \qquad (3.19)$$

where ν_c, ν_f and ν_m represent the Poisson's ratio of the composite, fibre and matrix respectively. Also ε_c, ε_f and ε_m represent the transverse strain of the composite, fibre and matrix respectively.

Using the definition of fibre volume fraction (V_f) and matrix volume fraction (V_m) given in Equation 3.9, Equation 3.19 becomes:

$$\nu_c \varepsilon_c = \nu_f \varepsilon_f V_f + \nu_m \varepsilon_m V_m \qquad (3.20)$$

In this case, perfect bonding is assumed (i.e. $\varepsilon_c = \varepsilon_f = \varepsilon_m$ which implies there is no slippage at the fibre/matrix interface), also $\nu_c = \nu_{12}$ it can be shown that Equation 3.20 simplifies to:

$$\nu_{12} = \nu_f V_f + \nu_m V_m \qquad (3.21)$$

Density

The density of a composite can be computed by taking into account the conservation of mass which is given below.

$$M_c = M_f + M_m \qquad (3.22)$$

where M_c, M_f, and M_m represent the mass of the composite, fibre and matrix respectively.

Equation 3.22 can be re-written as:

$$\rho_c v_c = \rho_f v_f + \rho_m v_m \qquad (3.23)$$

where v_c, v_f, and v_m represent the volume of the composite, fibre and matrix respectively.

Using the definition of fibre volume fraction (V_f) and matrix volume fraction (V_m) given below

$$V_F = \frac{v_f}{v_c}; \qquad V_m = \frac{v_m}{v_c} \qquad (3.24)$$

Equation 3.23 becomes:

$$\rho_c = \rho_f V_f + \rho_m V_m \qquad (3.25)$$

3.2 Strength Properties of FGMs

The strength properties of FGMs can be computed in terms of the strength properties of their constituents by using the rules of mixture as described in this section. More information on the strength properties can be found in the book written by Daniel and Ishai (2006).

Longitudinal Tensile Strength

Consider a composite under longitudinal tensile force, the phase with lower ultimate strain will fail first. For perfectly bonded fibres, two cases are distinguished depending on the relative magnitudes for the ultimate tensile strains of the constituents.

In the case in which the ultimate tensile strain of the fibre ($\varepsilon_{ft}{}^u$) is lower than that of the matrix i.e. $\varepsilon_{ft}{}^u < \varepsilon_{mt}{}^u$, the composite will fail when its longitudinal strain reaches the ultimate tensile strain of the fibre. Hence, the longitudinal composite tensile strength of the composite can be approximated by Equation 3.26 [Daniel and Ishai (2006)].

$$X_t = X_{ft}\left[V_f + V_m \frac{E_m}{E_{1f}}\right]$$

(3.26)

where X_{ft} represents the longitudinal fibre tensile strength, V_f and V_m represent the fibre and matrix volume fraction respectively, E_{1f} and E_m and Longitudinal Young's modulus of fibre and matrix respectively.

In the case in which the ultimate tensile strain of the matrix ($\varepsilon_{mt}{}^u$) is lower than that of the fibre i.e. $\varepsilon_{mt}{}^u < \varepsilon_{ft}{}^u$, the composite will fail when its longitudinal strain reaches the ultimate tensile strain of the matrix. Hence, the longitudinal tensile strength of the composite can be approximated by Equation 3.27 [Daniel and Ishai (2006)].

$$X_t = X_{mt}\left[V_m + V_f \frac{E_{1f}}{E_m}\right]$$

(3.27)

where X_{mt} represents the longitudinal matrix tensile strength.

The above equations do not take into consideration the random distribution of fibre and matrix strength. In the case of fibre-dominated strength, for example, fibre strength varies from point to point and from fibre to fibre.

Longitudinal Compressive Strength

Consider a composite under a longitudinal compressive force, failure is assumed to be associated with microbuckling or kinking of the fibres within the matrix. In the case of low fibre volume ratio values, the extensional or out-of-phase mode of microbuckling is predicted with a longitudinal composite compressive strength given by Equation 3.28 [Daniel and Ishai (2006)].

$$X_c = 2\,V_f \left[\frac{E_m E_{1f}\,V_f}{3(1 - V_f)} \right]^{1/2}$$

$$X_c = 2\,V_f \left[\frac{E_m E_{1f}\,V_f}{3\,V_m} \right]^{1/2} \tag{3.28}$$

where V_f and V_m represent the fibre and matrix volume fraction respectively, E_{1f} and E_m and Longitudinal Young's modulus of fibre and matrix respectively.

In the case of high fibre volume ratios i.e. $V_f \geq 0.5$, the most likely failure mode is the shear mode which is governed by the shear strength of the fibre. The predicted strength based on this mode is given by Equation 3.29 [Daniel and Ishai (2006)].

$$X_c = 2\,X_{fs} \left[V_f + V_m \frac{E_m}{E_{1f}} \right] \tag{3.29}$$

where X_{fs} represents the shear strength of the fibre.

Transverse Tensile Strength

Consider a transversely loaded composite, the residual stresses and strains due to curing of the matrix, or thermal stresses and strains due to thermal expansion mismatch, must be taken into account in predicting failure. Assuming a maximum tensile stress or strain failure criterion and linear elastic behaviour and linear elastic behaviour to failure for the matrix, one can predict the transverse composite tensile strength for a unidirectional composite using Equation 3.30 [Daniel and Ishai (2006)].

$$Y_t = \frac{X_{mt} - \sigma_{rm}}{k_\sigma} \tag{3.30}$$

where X_{mt} represents the matrix tensile strength, k_σ represents the stress concentration factor and σ_{rm} represents the radial (maximum) residual stress.

Transverse Compressive Strength

Consider a unidirectional composite under a transverse compressive force, the high compressive stress concentration at the interface may cause compressive failure in the matrix and/or fibre crushing. The predicted transverse composite compressive strength for this failure mechanism is given by Equation 3.31 [Daniel and Ishai (2006)].

$$Y_c = \frac{X_{mc} + \sigma_{rm}}{k_\sigma}$$
(3.31)

where X_{mc} represents the matrix compressive strength.

In-plane Shear Strength

Consider a composite under in-plane shear force, a high shear stress concentration develops at the fibre-matrix interface. The high shear stress at the interface can cause shear failure in the matrix and/or fibre-matrix debonding. The in-plane shear strength of the composite based on matrix shear failure can be predicted with Equation 3.32 [Daniel and Ishai (2006)].

$$S = \frac{X_{ms}}{k_\tau}$$
(3.32)

where X_{ms} is the matrix shear strength, k_τ is the shear stress concentration factor.

3.3 Fibre Distribution Techniques

It describes the micromechanics algorithm and the fibre distribution techniques such as manual fibre distribution, average fibre distribution and smooth fibre distribution technique developed in this work. This section explains the implementation of fibre distribution in the FE code that was developed for this work. Equation 3.33 is used to implement fibre distribution in the FE code.

$$V_f(\xi) = V_1 + (V_2 - V_1)\xi^P \tag{3.33}$$

where

V_1 = fibre volume fraction at x_1, y_1 or r_1 or gradation offset

V_2 = fibre volume fraction at x_2, y_2 or r_2

P = gradation exponent

$$\xi = \frac{x - x_1}{x_2 - x_1}, \quad \text{for case 1}$$

$$\xi = \frac{y - y_1}{y_2 - y_1}, \quad \text{for case 2}$$

$$\xi = \frac{r - r_1}{r_2 - r_1}, \quad \text{for case 3}$$

x_1, y_1 or r_1 = End "1" of the functionally graded domain

x_2, y_2 or r_2 = End "2" of the functionally graded domain

x, y or r = the position in the domain

Manual Fibre Distribution

This fibre distribution technique enables the code user to manually specify the fibre volume fraction for each element along the direction of fibre volume fraction variation.

Average Fibre Distribution

This fibre distribution technique enables the code user to either specify the fibre volume fractions such as V_1 and V_2 or the mean fibre volume fraction $\overline{V}$ and fibre volume fraction, V_1. The fibre volume fractions are then computed at the midpoint of each element using equations, which will be derived later in this section.

Smooth Fibre Distribution

This fibre distribution technique enables the code user to either specify fibre volume fractions such as V_1 and V_2 or the mean fibre volume fraction $\overline{V}$ and fibre volume fraction, V_1. The fibre volume fractions are then computed at each Gaussian quadrature point using equations which are derived subsequently in this section.

Derivation of mean fibre volume fraction $\overline{V}$ for specified V_1 and V_2

Using the fibre distribution equation below:

$$V_f(\xi) = V_1 + (V_2 - V_1)\xi^P \tag{3.34}$$

And the mean fibre volume fraction is as given below:

$$\overline{V}_f(\xi) = \frac{\displaystyle\int_{\xi_{min}}^{\xi_{max}} V(\xi)\,d\xi}{\xi_{max} - \xi_{min}} \tag{3.35}$$

It can be shown that:

$$\overline{V}_f(\xi) = \frac{V_1(\xi_{max} - \xi_{min}) + \dfrac{(V_2 - V_1)(\xi_{max}^{P+1} - \xi_{min}^{P+1})}{P+1}}{\xi_{max} - \xi_{min}} \tag{3.36}$$

Derivation of fibre volume fraction V_2 for specified V_1 and $\overline{V}$

Rearranging Equation 3.34 gives.

$$\overline{V}_f(\xi) = V_1 + (V_2 - V_1)\frac{(\xi_{max}^{P+1} - \xi_{min}^{P+1})}{(\xi_{max} - \xi_{min})(P+1)}$$

$$\overline{V}_f(\xi) = V_1 + (V_2 - V_1)Q$$

$$\text{where } Q = \frac{(\xi_{max}^{P+1} - \xi_{min}^{P+1})}{(\xi_{max} - \xi_{min})(P+1)} \tag{3.37}$$

$$\overline{V}_f(\xi) = V_2 Q + V_1(1-Q)$$

Rearranging the above equation gives:

$$V_2 = \frac{\overline{V}_f - V_1(1-Q)}{Q} \tag{3.38}$$

The plots of the fibre distribution for all ten optimisation cases considered in this thesis were obtained using Equation 3.33 and they are as shown below. It should be noted that

each of the ten optimisation cases have a mean fibre volume fraction of 0.4. The case with gradation exponent of zero (i.e. P=0) represents the traditional composite case.
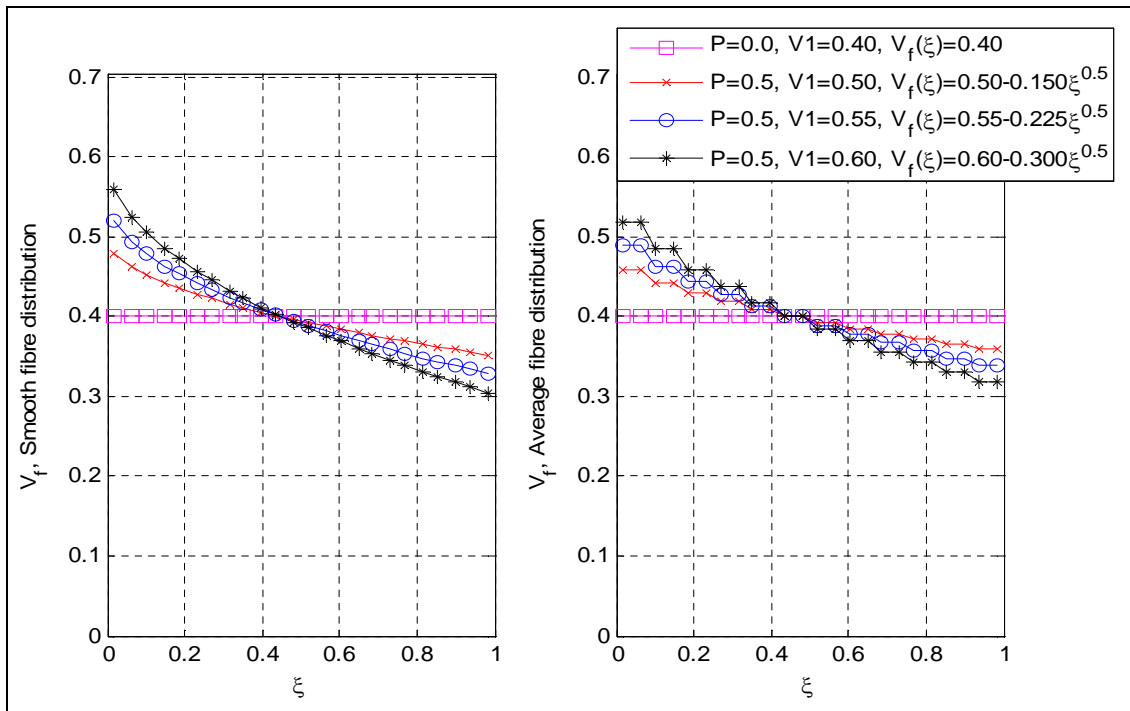
Figure 3-5: Fibre ratio distribution plot for cases with P=0 and P=0.5
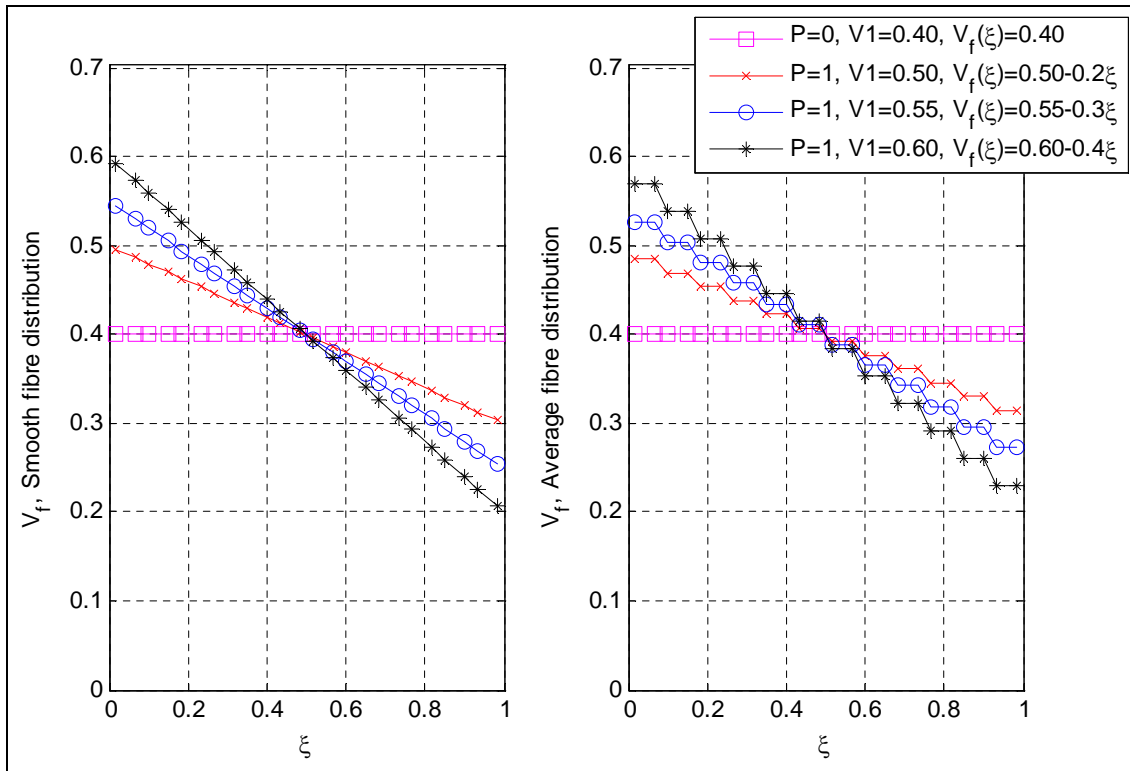
Figure 3-6: Fibre ratio distribution plot for cases with P=0 and P=1
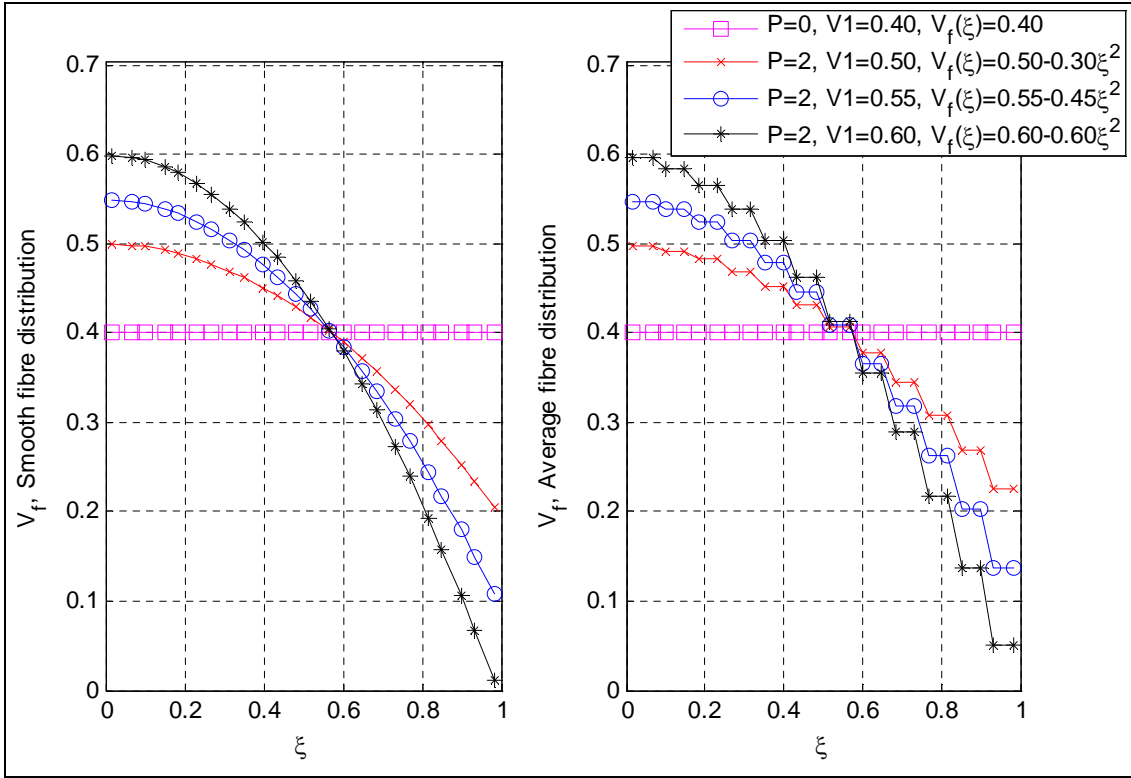
Figure 3-7: Fibre ratio distribution plot for cases with P=0 and P=2

3.4 Failure Criteria and Damage Mechanisms

Progressive damage analysis is based on the assumption that the damaged material can be substituted with an equivalent material with degraded properties. A comprehensive literature review on progressive damage analysis was undertaken by Padhi et al (1998). Most property degradation models can be grouped into three categories such as total discount approach, limited discount method and residual property method as shown in the diagram below. The total discount approach reduces the stiffness and strength of a failed ply to zero, although the ply is physically present. The limited discount method reduces stiffness based on the failure mode in action. For fibre failure, the longitudinal stiffness is degraded whereas for matrix failure, zero stiffness and strength are assigned to the failed ply for the transverse mode. The limited discount method was employed by Chang and Chang (1987), Chang and Lessard (1991) and Shahid and Chang (1995). The residual property method as described by Lo et al (1996) uses continuum damage models to predict progressive damage and the stiffness drop in the laminate.
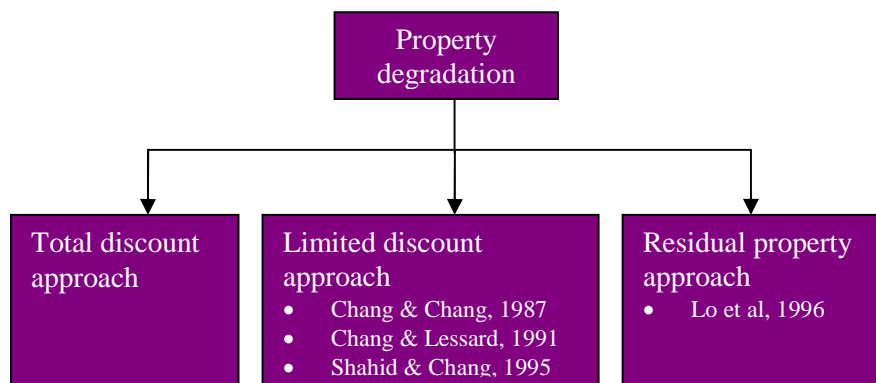
Figure 3-8: Types of property degradation

Chang and Lessard (1991) assume that after failure occurs, the stresses in the failed directions drop to zero immediately, which corresponds to brittle failure with no energy absorption. This kind of failure model usually leads to immediate, unstable failure of the composite. This assumption is not very realistic. In reality, the stress-carrying capacity degrades gradually with increasing strain after failure occurs. Hence the behaviour of the composite after onset of failure is not likely to be captured well by this model. Moreover, the instantaneous loss of stress-carrying capacity also makes the post-failure analysis results strongly dependent on the refinement of the FE mesh and

the finite element type used. Further details on progressive damage analysis can be found in Reddy & Reddy (1993), Kim et al (1996), Kam & Sher (1995), Echaabi et al (1996) and Tolson & Zabaras (1991).

In this thesis, a damage mechanism based on the material degradation model found in Spottswood and Palazotto (2001) was employed in the finite element programs. The damage mechanism involves carrying out a failure check at the node of element at every load increment by using any of the interactive failure criteria. If failure is detected, material properties of the failed element are degraded and equilibrium is re-established. The failed element is degraded by multiplying the element stiffness properties in the finite element code with a strength reduction factor which is given by the equation below.

$$\text{Stiffness Reduction Factor} = 1.0 - \frac{\text{No. of failed nodes per element}}{\text{No. of nodes per element}} \qquad (3.39)$$

Failure criteria for composite materials are often classified into two groups: namely, non-interactive failure criteria and interactive failure criteria. Further details can be found in a publication by Sleight (1999).

Non-Interactive Failure Criteria

A non-interactive failure criterion is defined as one having no interactions between the stress or strain components. These criteria, sometimes called independent failure criteria, compare the individual stress or strain components with the corresponding material allowable strength values. The maximum stress and maximum strain criteria belong to this category. Both failure criteria indicate the type of failure mode. The failure surfaces for these criteria are rectangular in stress and strain space, respectively.

Interactive Failure Criteria

Interactive failure criteria involve interactions between stress and strain components. Interactive failure criteria are mathematical in their formulation. Interactive failure criteria fall into three categories: (1) polynomial theories, (2) direct-mode determining theories, and (3) strain energy theories. The polynomial theories use a polynomial based upon the material strengths to describe a failure surface. The direct-mode determining theories are usually polynomial equations based on the material strengths

and use separate equations to describe each mode of failure. Finally, the strain energy theories are based on local strain energy levels determined during a nonlinear analysis.

Most of the interactive failure criteria are polynomials based on curve-fitting data from composite material tests. The most general polynomial failure criterion for composite materials is the tensor polynomial criterion proposed by Tsai and Wu (1971). Other popular quadratic failure criteria include those by Tsai-Hill, Azzi and Tsai, Hoffman, and Chamis. The failure surfaces for these quadratic criteria are elliptical in shape. One of the disadvantages of these quadratic failure criteria is that they predict the initiation of failure but say nothing about the failure mode or how the composite fails.

Using strength parameter defined earlier in this chapter, in conjunction with the interactive failure criteria, it can be determined whether an FGM component has failed or not. The commonly used interactive failure criteria include:

1) Tsai-Hill Failure Criterion

The Tsai-Hill failure criterion is based on the distortion energy failure theory of Von-Mises distortional energy yield criterion for isotropic materials. Hill (1950) adapted the Von-Mises distortional energy yield criterion to anisotropic materials. Then Tsai (1968) adapted it to a unidirectional lamina. Distortion energy is a part of the total strain energy in a body which is due to a change in the body shape. It is assumed that failure in the material takes place only when the distortion energy is greater than the failure distortion energy of the material. Failure occurs when the failure index (F.I.) given by Tsai-Hill failure criterion exceeds 1 i.e. the following inequality [Kaw (1997)] must be satisfied to ensure no failure has occurred:

$$\text{F.I.} = \left[\frac{\sigma_{11}}{X}\right]^2 + \left[\frac{\sigma_{22}}{Y}\right]^2 + \left[\frac{\tau_{12}}{S}\right]^2 - \left[\frac{\sigma_{11}}{X}\right]\left[\frac{\sigma_{22}}{X}\right] < 1 \qquad (3.40)$$

where

$X = X_t$ or X_c and $Y = Y_t$ or Y_c depending on the signs of σ_{11} and σ_{22} (i.e. if the applied stress is tension, use the tensile strength and if the applied stress is compressive, use the compressive strength).

X_c and Y_c are absolute values.

X_t and Y_t = Longitudinal and transverse compressive strength respectively

X_c and Y_c = Longitudinal and transverse compressive strength respectively

31

σ_{11} = Stress in the fibre, "1" or longitudinal direction of the material axis.

σ_{22} = Stress in the "2" or transverse direction of the material axis

τ_{12} = In-plane shear stress in the material axis.

S = Shear strength

This criterion considers the interaction of the stresses in the material axes directions unlike the maximum strain and maximum stress failure criteria. The criterion will not indicate the mode of failure as the maximum stress and maximum strain failure criteria will do.

2) Hoffman Failure Criterion

As in Tsai-Hill failure criterion, the Hoffman failure criterion is an interactive failure criterion which indicate whether failure has occurred or not, but it does not indicate the mode of failure. Failure occurs when the failure index (F.I.) given by Hoffman failure criterion exceeds 1 i.e. the following inequality [Kaw (1997)] must be satisfied to ensure no failure has occurred:

$$\text{F.I.} = F_1\sigma_{11} + F_2\sigma_{22} + F_{11}\sigma_{11}^2 + F_{22}\sigma_{22}^2 + F_{33}\tau_{12}^2 + 2F_{12}\sigma_{11}\sigma_{22} < 1 \qquad (3.41)$$

where

$$F_1 = \frac{1}{X_t} - \frac{1}{X_c}, \qquad F_2 = \frac{1}{Y_t} - \frac{1}{Y_c}, \qquad F_{11} = \frac{1}{X_t X_c}$$

$$F_{22} = \frac{1}{Y_t Y_c}, \qquad F_{33} = \frac{1}{S^2}, \qquad F_{12} = \frac{-1}{2X_t X_c}$$

3) Tsai-Wu Failure Criterion

The Tsai-Wu failure criterion is based on the total strain energy failure theory of Beltrami. Tsai and Wu (1971) applied the failure criterion to a lamina in plane stress. As in Tsai-Hill and Hoffman failure criteria, the Tsai-Wu failure criterion is an interactive failure criterion which indicate whether failure has occurred or not, but it does not indicate the mode of failure. This criterion is very similar to the Hoffman failure criterion except for the value of the coefficient F_{12}. Failure occurs when the failure index (F.I.) given by Tsai-Wu failure criterion exceeds 1 i.e. the following inequality [Kaw (1997)] must be satisfied to ensure no failure has occurred.

$$\text{F.I.} = F_1\sigma_{11} + F_2\sigma_{22} + F_{11}\sigma_{11}^2 + F_{22}\sigma_{22}^2 + F_{33}\tau_{12}^2 + 2F_{12}\sigma_{11}\sigma_{22} < 1 \qquad (3.42)$$

where

$$F_1 = \frac{1}{X_t} - \frac{1}{X_c}, \qquad F_2 = \frac{1}{Y_t} - \frac{1}{Y_c}, \qquad F_{11} = \frac{1}{X_t X_c}$$

$$F_{22} = \frac{1}{Y_t Y_c}, \qquad F_{33} = \frac{1}{S^2}, \qquad F_{12} = F_{12}^* \sqrt{F_{11} F_{22}} = \frac{F_{12}^*}{\sqrt{X_t X_c Y_t Y_c}}$$

The coefficient F_{12}^* has to be determined from a biaxial test. Performing such a biaxial test on a laminate is not straightforward and the value of the coefficient is usually estimated. Tsai and Hahn (1980) have shown that the value of the coefficient must be between the limits -1 and 1. In the absence of a measured value, the coefficient is generally set to -0.5.

4 Mindlin-type Element Theory

This section explains the Mindlin-type plate bending element theory and derives the equation used in the finite element programming. The finite element formulation of displacement equation, strain equation, stress equation, strain energy variation and generalised equation of equilibrium have been summarised in this section. The generalised equation of equilibrium is then linearised in-order to obtain the Mindlin element equation. The material non-linearity and geometrical non-linearity have been considered, and integrations through plate thickness have been carried out analytically.

4.1 Stress and Strain Equations

Displacement Components

The composite plate is represented by N_l layers, which are parallel to the x-y plane such that for layer l:

$$z = Z_L^{(l)}, \quad z = Z_U^{(l)} \tag{4.1}$$

are the equations of its lower and upper surfaces, and its thickness is given by:

$$h^{(l)} = Z_U^{(l)} - Z_L^{(l)} \tag{4.2}$$

The total thickness of the composite plate can be obtained as follows:

$$h = \sum_{l=1}^{N_l} h^{(l)} \tag{4.3}$$

The mid-plane of the plate $(z = 0)$ is assumed to be the bending neutral plane.

Transverse shear modelling is based on the following equations which can be found in a publication by Attia and El-Zafrany (1999):

$$\gamma_{xz}(x,y,z) = \gamma_{xz}^{o}(x,y)\left[1 - \frac{4z^2}{h^2}\right] \equiv \frac{3}{2}\bar{\gamma}_{xz}\left[1 - \frac{4z^2}{h^2}\right] \tag{4.4}$$

$$\gamma_{yz}(x,y,z) = \gamma_{yz}^{o}(x,y)\left[1 - \frac{4z^2}{h^2}\right] \equiv \frac{3}{2}\bar{\gamma}_{yz}\left[1 - \frac{4z^2}{h^2}\right] \tag{4.5}$$

where $\gamma_{xz}^{o}, \gamma_{yz}^{o}$ represent the values of transverse shear strains at the mid-plane, and:

$$\bar{\gamma}_{xz}(x,y) = \frac{1}{h}\int_{-h/2}^{h/2} \gamma_{xz}\, dz \equiv \frac{2}{3}\gamma_{xz}^{o} \tag{4.6}$$

$$\bar{\gamma}_{yz}(x,y) \;=\; \frac{1}{h}\int\limits_{-h/2}^{h/2}\gamma_{yz}\,dz \;\equiv\; \frac{2}{3}\gamma_{yz}^{o} \tag{4.7}$$

Approximate (z-linearised) distributions of u,v, (the displacement components in x and y directions) can be assumed such that:

$$\bar{\gamma}_{xz} \approx \frac{\partial u}{\partial z}+\frac{\partial w}{\partial x}, \quad \bar{\gamma}_{yz} \approx \frac{\partial v}{\partial z}+\frac{\partial w}{\partial y} \tag{4.8}$$

The lateral displacement (in z-direction) w is assumed to be independent of z, i.e.

$$w(x,y,z) \approx w(x,y) \tag{4.9}$$

Hence, it can be deduced from equations (4.8) and (4.9) that:

$$u(x,y,z) \;=\; u^{o}(x,y)+z\theta_{y}(x,y) \tag{4.10}$$

$$v(x,y,z) \;=\; v^{o}(x,y)-z\theta_{x}(x,y) \tag{4.11}$$

where u^{o}, v^{o} represent displacement values at the mid-plane of the plate and θ_{x}, θ_{y} are average slope angles defined as follows:

$$\theta_{x} \;=\; +\left[\frac{\partial w}{\partial y}-\bar{\gamma}_{yz}\right], \quad \theta_{y} \;=\; -\left[\frac{\partial w}{\partial x}-\bar{\gamma}_{xz}\right] \tag{4.12}$$

Strain Components

The transverse strain components at any point inside the plate are assumed infinitesimal, they are negligible for thin plates, other components are defined in the x-y plane and they may assume finite values. The strain component ε_{z} will always be assumed negligible.

Transverse shear strains

Using Equations (4.4) and (4.5), the transverse shear strains can be represented by the following vector:

$$\boldsymbol{\gamma} \;=\; \begin{bmatrix}\gamma_{xz}\\[1mm]\gamma_{yz}\end{bmatrix} \equiv \frac{3}{2}\left(1-\frac{4z^{2}}{h^{2}}\right)\begin{bmatrix}\bar{\gamma}_{xz}\\[1mm]\bar{\gamma}_{yz}\end{bmatrix} \tag{4.13}$$

and from Equation (4.13) it can be deduced that:

$$\boldsymbol{\gamma} \;=\; f_{\gamma}(z)\hat{\boldsymbol{\gamma}} \tag{4.14}$$

where

$$\hat{\gamma} = \begin{bmatrix} \bar{\gamma}_{xz} \\ \bar{\gamma}_{yz} \end{bmatrix} \equiv \begin{bmatrix} \dfrac{\partial w}{\partial x} + \theta_y \\ \dfrac{\partial w}{\partial y} - \theta_x \end{bmatrix} \tag{4.15}$$

and

$$f_\gamma(z) = \frac{3}{2}\left(1 - \frac{4z^2}{h^2}\right) \tag{4.16}$$

The *x-y* strain components

These are $\varepsilon_x, \varepsilon_y, \gamma_{xy}$ and are represented with the following vector:

$$\boldsymbol{\varepsilon} = \begin{bmatrix} \varepsilon_x \\ \varepsilon_y \\ \gamma_{xy} \end{bmatrix} \tag{4.17}$$

Using Green's strain-displacement equations, then:

$$\varepsilon_x = \frac{\partial u}{\partial x} + \frac{1}{2}\left[\left(\frac{\partial u}{\partial x}\right)^2 + \left(\frac{\partial v}{\partial x}\right)^2 + \left(\frac{\partial w}{\partial x}\right)^2\right] \tag{4.18}$$

$$\varepsilon_y = \frac{\partial v}{\partial y} + \frac{1}{2}\left[\left(\frac{\partial u}{\partial y}\right)^2 + \left(\frac{\partial v}{\partial y}\right)^2 + \left(\frac{\partial w}{\partial y}\right)^2\right] \tag{4.19}$$

$$\gamma_{xy} = \frac{\partial u}{\partial y} + \frac{\partial v}{\partial x} + \left[\frac{\partial u}{\partial x}\frac{\partial u}{\partial y} + \frac{\partial v}{\partial x}\frac{\partial v}{\partial y} + \frac{\partial w}{\partial x}\frac{\partial w}{\partial y}\right] \tag{4.20}$$

Using the previous equations, the *x-y* strain vector can be partitioned and represented in terms of different vectors and matrices as follows:

$$\begin{bmatrix} \varepsilon_x \\ \varepsilon_y \\ \gamma_{xy} \end{bmatrix} = \boldsymbol{\varepsilon}_o - z\boldsymbol{\varepsilon}_b + \frac{1}{2}\begin{bmatrix} \mathbf{A}_m - z\mathbf{A}_\theta \\ \mathbf{A}_w \\ -z\mathbf{A}_m + z^2\mathbf{A}_\theta \end{bmatrix}^T \begin{bmatrix} \boldsymbol{\theta}_m \\ \boldsymbol{\theta}_w \\ \boldsymbol{\theta}_\theta \end{bmatrix} \tag{4.21}$$

where the vectors and matrices in the above equation are defined as follows:

$$\boldsymbol{\theta}_m(x,y) = \begin{bmatrix} \dfrac{\partial u^o}{\partial x} & \dfrac{\partial v^o}{\partial x} & \dfrac{\partial u^o}{\partial y} & \dfrac{\partial v^o}{\partial y} \end{bmatrix}^T \tag{4.22}$$

$$\boldsymbol{\theta}_w(x,y) = \begin{bmatrix} \dfrac{\partial w}{\partial x} & \dfrac{\partial w}{\partial y} \end{bmatrix}^T \tag{4.23}$$

$$\boldsymbol{\theta}_\theta(x,y) = \begin{bmatrix} -\dfrac{\partial \theta_y}{\partial x} & \dfrac{\partial \theta_x}{\partial x} & -\dfrac{\partial \theta_y}{\partial y} & \dfrac{\partial \theta_x}{\partial y} \end{bmatrix}^T \tag{4.24}$$

$$\mathbf{A}_m(x,y) = \begin{bmatrix} \dfrac{\partial u^o}{\partial x} & \dfrac{\partial v^o}{\partial x} & 0 & 0 \\[2mm] 0 & 0 & \dfrac{\partial u^o}{\partial y} & \dfrac{\partial v^o}{\partial y} \\[2mm] \dfrac{\partial u^o}{\partial y} & \dfrac{\partial v^o}{\partial y} & \dfrac{\partial u^o}{\partial x} & \dfrac{\partial v^o}{\partial x} \end{bmatrix} \tag{4.25}$$

$$\mathbf{A}_w(x,y) = \begin{bmatrix} \dfrac{\partial w}{\partial x} & 0 \\[2mm] 0 & \dfrac{\partial w}{\partial y} \\[2mm] \dfrac{\partial w}{\partial y} & \dfrac{\partial w}{\partial y} \end{bmatrix} \tag{4.26}$$

$$\mathbf{A}_\theta(x,y) = \begin{bmatrix} -\dfrac{\partial \theta_y}{\partial x} & \dfrac{\partial \theta_x}{\partial x} & 0 & 0 \\[2mm] 0 & 0 & -\dfrac{\partial \theta_y}{\partial y} & \dfrac{\partial \theta_x}{\partial y} \\[2mm] -\dfrac{\partial \theta_y}{\partial y} & \dfrac{\partial \theta_x}{\partial y} & -\dfrac{\partial \theta_y}{\partial x} & \dfrac{\partial \theta_x}{\partial x} \end{bmatrix} \tag{4.27}$$

$$\boldsymbol{\varepsilon}_o(x,y) = \begin{bmatrix} \dfrac{\partial u^o}{\partial x} & \dfrac{\partial v^o}{\partial y} & \dfrac{\partial u^o}{\partial y} + \dfrac{\partial v^o}{\partial x} \end{bmatrix}^T \tag{4.28}$$

$$\boldsymbol{\varepsilon}_b(x,y) = \begin{bmatrix} -\dfrac{\partial \theta_y}{\partial x} & \dfrac{\partial \theta_x}{\partial y} & \dfrac{\partial \theta_x}{\partial x} - \dfrac{\partial \theta_y}{\partial y} \end{bmatrix}^T \tag{4.29}$$

Also the variation of the total *x-y* strain vector can be represented in matrix form as shown below:

$$\begin{bmatrix} d\varepsilon_x \\ d\varepsilon_y \\ d\gamma_{xy} \end{bmatrix} = d\boldsymbol{\varepsilon}_o - z\,d\boldsymbol{\varepsilon}_b + \begin{bmatrix} \mathbf{A}_m - z\mathbf{A}_\theta \\ \mathbf{A}_w \\ -z\mathbf{A}_m + z^2\mathbf{A}_\theta \end{bmatrix}^T \begin{bmatrix} \mathbf{d\theta}_m \\ \mathbf{d\theta}_w \\ \mathbf{d\theta}_\theta \end{bmatrix} \tag{4.30a}$$

And the variation of the transverse shear strain vector is derived from Equation (4.14) as:

$$d\boldsymbol{\gamma} \;=\; f_\gamma(z)\,d\hat{\boldsymbol{\gamma}} \tag{4.30b}$$

Stress Components

The relevant stress components at any point inside the lth layer of a composite layered plate can be represented in terms of two vectors defined as follows:

(a) The transverse shear stress vector

$$\boldsymbol{\tau}^{(l)} = \begin{bmatrix} \tau_{xz} \\[6pt] \tau_{yz} \end{bmatrix} \tag{4.31}$$

(b) The *x-y* stress vector

$$\boldsymbol{\sigma}^{(l)} = \begin{bmatrix} \sigma_x \\[6pt] \sigma_y \\[6pt] \tau_{xy} \end{bmatrix} \tag{4.32}$$

Using constitutive equations for the lth layer, as explained in Appendix A, the stress vectors can be expressed in terms of strain vectors as follows:

$$\boldsymbol{\tau}^{(l)} = \boldsymbol{\mu}^{(l)}\,\boldsymbol{\gamma} \;\equiv\; f_\gamma(z)\,\boldsymbol{\mu}^{(l)}\,\hat{\boldsymbol{\gamma}} \tag{4.33}$$

$$\boldsymbol{\sigma}^{(l)} = \mathbf{D}^{(l)}\,\boldsymbol{\varepsilon} \tag{4.34}$$

Strain Energy Variation

The variation of strain energy density (strain energy per unit volume) due to a variation of displacement at any point inside the lth layer of the plate can be expressed as follows:

$$d\overline{U}^{(l)} = \sigma_x^{(l)}\,d\varepsilon_x + \sigma_y^{(l)}\,d\varepsilon_y + \tau_{xy}^{(l)}\,d\gamma_{xy} + \tau_{yz}^{(l)}\,d\gamma_{yz} + \tau_{xz}^{(l)}\,d\gamma_{xz} \tag{4.35}$$

which can be represented in the following matrix form:

$$d\overline{U}^{(l)} = d\boldsymbol{\gamma}^t\,\boldsymbol{\tau}^{(l)} + d\boldsymbol{\varepsilon}^t\,\boldsymbol{\sigma}^{(l)} \tag{4.36}$$

The variation of strain energy per unit area of the plate surface is defined as follows:

$$dU' = \int_{-h/2}^{h/2} (d\overline{U}^{(l)})\,dz \tag{4.37}$$

and the variation of the strain energy of the plate is given by:

$$dU = \iint_{x-y\,\text{surface}} (dU')\,dx\,dy \tag{4.38}$$

Substituting from Equations (4.30) into (4.36), it can be deduced that:

$$d\overline{U}^{(l)} = f_\gamma(z) d\hat{\boldsymbol{\gamma}}^t \boldsymbol{\tau}^{(l)} + \left[d\boldsymbol{\varepsilon}_o + \mathbf{A}_m d\boldsymbol{\theta}_m + \mathbf{A}_w d\boldsymbol{\theta}_w \right.$$
$$\left. - z\left(d\boldsymbol{\varepsilon}_b + \mathbf{A}_m d\boldsymbol{\theta}_\theta + \mathbf{A}_\theta d\boldsymbol{\theta}_m \right) + z^2 \mathbf{A}_\theta d\boldsymbol{\theta}_\theta \right] \boldsymbol{\sigma}^{(l)}$$

(4.39a)

i.e.

$$d\overline{U}^{(l)} = f_\gamma(z) d\hat{\boldsymbol{\gamma}}^t \boldsymbol{\tau}^{(l)} + \left[d\boldsymbol{\varepsilon}_o^t + d\boldsymbol{\theta}_m^t \mathbf{A}_m^t + d\boldsymbol{\theta}_w^t \mathbf{A}_w^t \right.$$
$$\left. - z\left(d\boldsymbol{\varepsilon}_b^t + d\boldsymbol{\theta}_\theta^t \mathbf{A}_m^t + d\boldsymbol{\theta}_m^t \mathbf{A}_\theta^t \right) + z^2 d\boldsymbol{\theta}_\theta^t \mathbf{A}_\theta \right] \boldsymbol{\sigma}^{(l)}$$

(4.39b)

4.2 Interpolated Equations of Displacement and Strain

Displacement Components

Mindlin-type elements are based on Lagrangian interpolation, and for an n-node element the mid-plane displacement components and average slope angles at any point (x, y) in the mid-plane of the plate can be interpolated as follows:

$$u^o(x, y) = \sum_{i=1}^{n} N_i(x, y) u_i \tag{4.40}$$

$$v^o(x, y) = \sum_{i=1}^{n} N_i(x, y) v_i \tag{4.41}$$

$$w(x, y) = \sum_{i=1}^{n} N_i(x, y) w_i \tag{4.42}$$

$$\theta_x(x, y) = \sum_{i=1}^{n} N_i(x, y) (\theta_x)_i \tag{4.43}$$

$$\theta_y(x, y) = \sum_{i=1}^{n} N_i(x, y) (\theta_y)_i \tag{4.44}$$

where $u_i, v_i, w_i, (\theta_x)_i, (\theta_y)_i$ are values at node i (x_i, y_i) and $N_i(x, y)$ represents Lagrangian shape functions.

Usually, the two-dimensional Lagrangian shape functions are expressed in terms of intrinsic coordinates (ξ, η), and the relationships between Cartesian coordinates (x, y) and intrinsic coordinates (ξ, η) are obtained via the following iso-parametric equations:

$$x(\xi, \eta) = \sum_{i=1}^{n} N_i(\xi, \eta) x_i \tag{4.45}$$

$$y(\xi, \eta) = \sum_{i=1}^{n} N_i(\xi, \eta) y_i \tag{4.46}$$

The nodal displacement vector for in-plane components can be defined as:

$$\boldsymbol{\delta}_o = \{ u_1 \quad v_1 \quad u_2 \quad v_2 \quad \cdots \quad u_n \quad v_n \} \tag{4.47}$$

The nodal displacement vector for out-of-plane components can be defined as:

$$\boldsymbol{\delta}_b = \{ w_1 \quad (\theta_x)_1 \quad (\theta_y)_1 \quad \cdots \quad w_n \quad (\theta_x)_n \quad (\theta_y)_n \} \tag{4.48}$$

Strain Components

Transverse shear strains

Substituting from Equations (4.42)-(4.44) into Equation (4.14), then:

$$\boldsymbol{\gamma}(x,y,z) = f_\gamma(z) \, \mathbf{B}_\gamma(x,y) \, \boldsymbol{\delta}_b \tag{4.49a}$$

where

$$\mathbf{B}_\gamma(x,y) = \begin{bmatrix} \cdots & \dfrac{\partial N_i}{\partial x} & 0 & N_i & \cdots \\[3mm] \cdots & \dfrac{\partial N_i}{\partial y} & -N_i & 0 & \cdots \end{bmatrix} \tag{4.49b}$$

Also the variation of transverse shear strains can be obtained from Equation (4.49a) as follows:

$$d\boldsymbol{\gamma}(x,y,z) = f_\gamma(z) \, \mathbf{B}_\gamma(x,y) \, d\boldsymbol{\delta}_b \tag{4.50}$$

Total x-y strain vector and its variation

The total strain vector of x-y components can be represented in terms of nodal parameters as:

$$\begin{bmatrix} \varepsilon_x \\ \varepsilon_y \\ \gamma_{xy} \end{bmatrix} = \begin{bmatrix} \mathbf{B_o} + \dfrac{1}{2}\mathbf{A}_m\mathbf{G}_m - \dfrac{z}{2}\mathbf{A}_\theta\mathbf{G}_m \\[3mm] \dfrac{1}{2}\mathbf{A}_w\mathbf{G}_w - z\left(\mathbf{B_b} + \dfrac{1}{2}\mathbf{A}_m\mathbf{G}_\theta\right) + \dfrac{z^2}{2}\mathbf{A}_\theta\mathbf{G}_\theta \end{bmatrix}^T \begin{bmatrix} \boldsymbol{\delta}_o \\ \boldsymbol{\delta}_b \end{bmatrix} \tag{4.51}$$

Hence it can be shown that:

$$\mathbf{B}_o(x,y) = \begin{bmatrix} \cdots & \dfrac{\partial N_i}{\partial x} & 0 & \cdots \\[3mm] \cdots & 0 & \dfrac{\partial N_i}{\partial y} & \cdots \\[3mm] \cdots & \dfrac{\partial N_i}{\partial y} & \dfrac{\partial N_i}{\partial x} & \cdots \end{bmatrix} \tag{4.52}$$

$$
\mathbf{B}_b(x, y) = \begin{bmatrix} \cdots & 0 & 0 & -\dfrac{\partial N_i}{\partial x} & \cdots \\[3mm] \cdots & 0 & \dfrac{\partial N_i}{\partial y} & 0 & \cdots \\[3mm] \cdots & 0 & \dfrac{\partial N_i}{\partial x} & -\dfrac{\partial N_i}{\partial y} & \cdots \end{bmatrix} \tag{4.53}
$$

$$
\mathbf{G}_m(x, y) = \begin{bmatrix} \cdots & \dfrac{\partial N_i}{\partial x} & 0 & \cdots \\[3mm] \cdots & 0 & \dfrac{\partial N_i}{\partial x} & \cdots \\[3mm] \cdots & \dfrac{\partial N_i}{\partial y} & 0 & \cdots \\[3mm] \cdots & 0 & \dfrac{\partial N_i}{\partial y} & \cdots \end{bmatrix} \tag{4.54}
$$

$$
\mathbf{G}_w(x, y) = \begin{bmatrix} \cdots & \dfrac{\partial N_i}{\partial x} & 0 & 0 & \cdots \\[3mm] \cdots & \dfrac{\partial N_i}{\partial y} & 0 & 0 & \cdots \end{bmatrix} \tag{4.55}
$$

$$
\mathbf{G}_\theta(x, y) = \begin{bmatrix} \cdots & 0 & 0 & -\dfrac{\partial N_i}{\partial x} & \cdots \\[3mm] \cdots & 0 & \dfrac{\partial N_i}{\partial x} & 0 & \cdots \\[3mm] \cdots & 0 & 0 & -\dfrac{\partial N_i}{\partial y} & \cdots \\[3mm] \cdots & 0 & \dfrac{\partial N_i}{\partial y} & 0 & \cdots \end{bmatrix} \tag{4.56}
$$

Also the variation of the x-y strain vector can be represented in terms of nodal parameters as shown below:

$$
\begin{bmatrix} d\varepsilon_x \\ d\varepsilon_y \\ d\gamma_{xy} \end{bmatrix} = \begin{bmatrix} \mathbf{B_o} + \mathbf{A}_m\mathbf{G}_m - z\mathbf{A}_\theta\mathbf{G}_m \\ \mathbf{A}_w\mathbf{G}_w - z(\mathbf{B_b} + \mathbf{A}_m\mathbf{G}_\theta) + z^2\mathbf{A}_\theta\mathbf{G}_\theta \end{bmatrix}^T \begin{bmatrix} \mathbf{d\delta}_o \\ \mathbf{d\delta}_b \end{bmatrix} \tag{4.57}
$$

Define the following non-linear **B** matrices:

$$
\mathbf{B}_{pq} = \mathbf{A}_p\mathbf{G}_q \tag{4.58}
$$

with $\qquad p \equiv m, w, \theta, \quad q \equiv m, w, \theta$

Define also:

$$\tilde{\mathbf{B}}_o = \mathbf{B}_o + \mathbf{A}_m \mathbf{G}_m \equiv \mathbf{B}_o + \mathbf{B}_{mm} \tag{4.59}$$

and

$$\tilde{\mathbf{B}}_b = \mathbf{B}_b + \mathbf{A}_m \mathbf{G}_\theta \equiv \mathbf{B}_b + \mathbf{B}_{m\theta} \tag{4.60}$$

Hence, Equation (4.57) can be rewritten as follows:

$$\begin{bmatrix} d\varepsilon_x \\ d\varepsilon_y \\ d\gamma_{xy} \end{bmatrix} = \begin{bmatrix} \tilde{\mathbf{B}}_o - z\mathbf{B}_{\theta\mathbf{m}} \\ \mathbf{B}_{\mathbf{ww}} - z\tilde{\mathbf{B}}_{\mathbf{b}} + z^2\mathbf{B}_{\theta\theta} \end{bmatrix}^T \begin{bmatrix} \mathbf{d\delta}_o \\ \mathbf{d\delta}_b \end{bmatrix} \tag{4.61}$$

Variation of Strain Energy

Substituting from Equations (4.50) and (4.61) into (4.36), then the variation of strain energy density at any point inside the lth layer of the plate can be expressed as follows:

$$d\overline{U}^{(l)}(x,y,z) = \begin{bmatrix} d\boldsymbol{\delta}_\psi^t \, \mathbf{B}_\gamma^t \end{bmatrix} \left(f_\gamma(z)\, \boldsymbol{\tau}^{(l)} \right)$$

$$+ \begin{bmatrix} d\boldsymbol{\delta}_o \\ d\boldsymbol{\delta}_b \end{bmatrix}^T \begin{bmatrix} \mathbf{B}_o^t + \mathbf{G}_m^t \mathbf{A}_m^t - z\mathbf{G}_m^t \mathbf{A}_\theta^t \\ \mathbf{G}_w^t \mathbf{A}_w^t - z\left(\mathbf{B}_b^t + \mathbf{G}_\theta^t \mathbf{A}_m^t\right) + z^2 \mathbf{G}_\theta^t \mathbf{A}_\theta^t \end{bmatrix}^T \begin{bmatrix} \sigma_x^{(L)} \\ \sigma_y^{(L)} \\ \sigma_{xy}^{(L)} \end{bmatrix} \tag{4.62}$$

<u>Integrated stress vectors</u>

(a) *Integrated transverse shear stress*

This is defined as follows:

$$\tilde{\boldsymbol{\tau}} = \int_{-h/2}^{h/2} f_\gamma(z)\, \boldsymbol{\tau}^{(l)}\, dz \tag{4.63}$$

Substituting from Equation (4.33) into (4.63), then it can be deduced that:

$$\tilde{\boldsymbol{\tau}} = \begin{bmatrix} \int_{-h/2}^{h/2} f_\gamma^2(z) \boldsymbol{\mu}^{(l)}\, dz \end{bmatrix} \hat{\boldsymbol{\gamma}} \tag{4.64}$$

Define an integrated $\boldsymbol{\mu}$ matrix as follows:

$$\boldsymbol{\mu}_{\gamma\gamma} = \int_{-h/2}^{h/2} f_\gamma^2(z) \boldsymbol{\mu}^{(l)}\, dz \equiv \int_{-h/2}^{h/2} \tfrac{9}{4}\left(1 - \frac{4z^2}{h^2}\right)^2 \boldsymbol{\mu}^{(l)}\, dz \tag{4.65}$$

and for the special case of transversely isotropic plate, where all layers have the same $\boldsymbol{\mu}$ matrix, it can be proved that:

$$\boldsymbol{\mu}_{\gamma\gamma} = \tfrac{6}{5} h \boldsymbol{\mu} \tag{4.66}$$

Hence, it can be deduced that:

$$\tilde{\boldsymbol{\tau}} \; = \; \boldsymbol{\mu}_{\gamma\gamma} \, \hat{\boldsymbol{\gamma}} \; \equiv \; \boldsymbol{\mu}_{\gamma\gamma} \, \mathbf{B}_\gamma \, \boldsymbol{\delta}_b \tag{4.67}$$

(b) *Integrated x-y stress vectors*

These can be defined generally as follows:

$$\boldsymbol{\sigma}_n \; = \; (-1)^n \int_{-h/2}^{h/2} z^n \, \boldsymbol{\sigma}^{(l)} \, dz \; \equiv \; \begin{bmatrix} \sigma_x^{(n)} \\[1em] \sigma_y^{(n)} \\[1em] \tau_{xy}^{(n)} \end{bmatrix} \tag{4.68}$$

Equation (4.68) can also be expressed as:

$$\boldsymbol{\sigma}_n \; = \; (-1)^n \left[\int_{-h/2}^{h/2} z^n \, \mathbf{D}^{(l)} dz \right] \left(\boldsymbol{\varepsilon}_o + \boldsymbol{\varepsilon}_m + \boldsymbol{\varepsilon}_w \right)$$
$$+ (-1)^{n+1} \left[\int_{-h/2}^{h/2} z^{n+1} \, \mathbf{D}^{(l)} dz \right] \left(\boldsymbol{\varepsilon}_b + \boldsymbol{\varepsilon}_{m\theta} \right) \tag{4.69}$$
$$+ (-1)^{n+2} \left[\int_{-h/2}^{h/2} z^{n+2} \, \mathbf{D}^{(l)} dz \right] \left(\boldsymbol{\varepsilon}_\theta \right)$$

Defining integrated **D** matrices generally as follows:

$$\mathbf{D}_n \; = \; \int_{-h/2}^{h/2} z^n \, \mathbf{D}^{(l)} dz \tag{4.70}$$

then Equation (4.69) can be simplified as follows:

$$\boldsymbol{\sigma}_n \; = \; (-1)^n \left[\mathbf{D}_n \left(\boldsymbol{\varepsilon}_o + \boldsymbol{\varepsilon}_m + \boldsymbol{\varepsilon}_w \right) - \mathbf{D}_{n+1} \left(\boldsymbol{\varepsilon}_b + \boldsymbol{\varepsilon}_{m\theta} \right) + \mathbf{D}_{n+2} \, \boldsymbol{\varepsilon}_\theta \right] \tag{4.71}$$

with the following special cases:

$$\boldsymbol{\sigma}_o \; = \; \mathbf{D}_o \left(\boldsymbol{\varepsilon}_o + \boldsymbol{\varepsilon}_m + \boldsymbol{\varepsilon}_w \right) - \mathbf{D}_1 \left(\boldsymbol{\varepsilon}_b + \boldsymbol{\varepsilon}_{m\theta} \right) + \mathbf{D}_2 \, \boldsymbol{\varepsilon}_\theta \tag{4.72}$$

$$\boldsymbol{\sigma}_1 \; = \; - \left[\mathbf{D}_1 \left(\boldsymbol{\varepsilon}_o + \boldsymbol{\varepsilon}_m + \boldsymbol{\varepsilon}_w \right) - \mathbf{D}_2 \left(\boldsymbol{\varepsilon}_b + \boldsymbol{\varepsilon}_{m\theta} \right) + \mathbf{D}_3 \, \boldsymbol{\varepsilon}_\theta \right] \tag{4.73}$$

$$\boldsymbol{\sigma}_2 \; = \; \mathbf{D}_2 \left(\boldsymbol{\varepsilon}_o + \boldsymbol{\varepsilon}_m + \boldsymbol{\varepsilon}_w \right) - \mathbf{D}_3 \left(\boldsymbol{\varepsilon}_b + \boldsymbol{\varepsilon}_{m\theta} \right) + \mathbf{D}_4 \, \boldsymbol{\varepsilon}_\theta \tag{4.74}$$

Integrating Equation (4.62) over the layers with respect to z, then it can be deduced that:

$$dU' \; = \; d\boldsymbol{\delta}_b^t \, \mathbf{B}_\gamma^t \, \tilde{\boldsymbol{\tau}} + \left(d\boldsymbol{\delta}_o^t \, \tilde{\mathbf{B}}_o^t + d\boldsymbol{\delta}_b^t \, \mathbf{B}_{ww}^t \right) \boldsymbol{\sigma}_o$$
$$+ \left(d\boldsymbol{\delta}_o^t \, \mathbf{B}_{\theta m}^t + d\boldsymbol{\delta}_b^t \, \tilde{\mathbf{B}}_b^t \right) \boldsymbol{\sigma}_1 + d\boldsymbol{\delta}_b^t \, \mathbf{B}_{\theta\theta}^t \, \boldsymbol{\sigma}_2 \tag{4.75}$$

4.3 Derivation of FE Equations for Mindlin-type Element

Generalized Equations of Equilibrium

The wok done by actual external loads can be expressed in terms of equivalent nodal loading represented with the following vector:

$$\mathbf{F} \equiv \begin{bmatrix} \mathbf{F}_o \\ \\ \mathbf{F}_b \end{bmatrix} \tag{4.76}$$

where

$$\mathbf{F}_o = \left\{ (F_x)_1 \quad (F_y)_1 \quad (F_x)_2 \quad (F_y)_2 \quad \cdots \quad (F_x)_m \quad (F_y)_m \right\} \tag{4.77}$$

$$\mathbf{F}_b = \left\{ (F_z)_1 \quad (M_x)_1 \quad (M_y)_1 \quad \cdots \quad (F_z)_m \quad (M_x)_m \quad (M_y)_m \right\} \tag{4.78}$$

and m is the total number of finite element mesh nodes.

From the principle of virtual work due to a variation of displacement:

$$d\chi = dU - dW = 0 \tag{4.79}$$

Equation (4.79) can be expressed as:

$$\sum_{e=1}^{N_e} \int_{-h/2}^{h/2} \iint_e \left\{ \begin{bmatrix} d\boldsymbol{\delta}_o \\ d\boldsymbol{\delta}_b \end{bmatrix}^T \begin{bmatrix} \mathbf{B}_o^t + \mathbf{G}_m^t \mathbf{A}_m^t - z\mathbf{G}_m^t \mathbf{A}_\theta^t \\ \mathbf{G}_w^t \mathbf{A}_w^t - z\left(\mathbf{B}_b^t + \mathbf{G}_\theta^t \mathbf{A}_m^t\right) + z^2 \mathbf{G}_\theta^t \mathbf{A}_\theta^t \end{bmatrix}^T \begin{bmatrix} \sigma_x^{(L)} \\ \sigma_y^{(L)} \\ \sigma_{xy}^{(L)} \end{bmatrix} \right\} dxdydz \tag{4.80}$$
$$+ d\boldsymbol{\delta}_b^t \mathbf{B}_\gamma^t f_\gamma \boldsymbol{\tau}^{(L)}$$
$$- d\boldsymbol{\delta}_o^t \mathbf{F}_o^t - d\boldsymbol{\delta}_b^t \mathbf{F}_b^t = \mathbf{0}$$

Since $d\boldsymbol{\delta}_o, d\boldsymbol{\delta}_b$ represent arbitrary parameters, then their coefficients in the above equation vanish, leading to:

$$\sum_{e=1}^{N_e} \int_{-h/2}^{h/2} \iint_e \left\{ \begin{bmatrix} \mathbf{B}_o^t + \mathbf{G}_m^t \mathbf{A}_m^t - z\mathbf{G}_m^t \mathbf{A}_\theta^t \\ \mathbf{G}_w^t \mathbf{A}_w^t - z\left(\mathbf{B}_b^t + \mathbf{G}_\theta^t \mathbf{A}_m^t\right) + z^2 \mathbf{G}_\theta^t \mathbf{A}_\theta^t \end{bmatrix}^T \begin{bmatrix} \sigma_x^{(L)} \\ \sigma_y^{(L)} \\ \sigma_{xy}^{(L)} \end{bmatrix} + \mathbf{B}_\gamma^t f_\psi \boldsymbol{\tau}^{(L)} \right\} dxdydz \tag{4.81}$$
$$- \begin{bmatrix} \mathbf{F}_o & \mathbf{F}_b \end{bmatrix}^T = \mathbf{0}$$

which represent the generalized equations of equilibrium.

If an approximate solution is employed then the previous equations will lead to the following residual vectors:

$$\sum_{e=1}^{N_e} \int_{-h/2}^{h/2} \iint_e \left\{ \begin{bmatrix} \mathbf{B}_o^t + \mathbf{G}_m^t \mathbf{A}_m^t - z\mathbf{G}_m^t \mathbf{A}_\theta^t \\ \mathbf{G}_w^t \mathbf{A}_w^t - z(\mathbf{B}_b^t + \mathbf{G}_\theta^t \mathbf{A}_m^t) + z^2 \mathbf{G}_\theta^t \mathbf{A}_\theta^t \end{bmatrix}^T \begin{bmatrix} \sigma_x^{(L)} \\ \sigma_y^{(L)} \\ \sigma_{xy}^{(L)} \end{bmatrix} + \mathbf{B}_\gamma^t f_\psi \boldsymbol{\tau}^{(L)} \right\} dxdydz \tag{4.82}$$

$$-\begin{bmatrix} \mathbf{F}_o & \mathbf{F}_b \end{bmatrix}^T = -\begin{bmatrix} \mathbf{R}_o & \mathbf{R}_b \end{bmatrix}^T$$

When calculating the residual forces, the equation above is integrated analytically with respect to z, leading to:

$$\mathbf{R}_o = \mathbf{F}_o - \sum_{e=1}^{N_e} \iint_e \left\{ \left(\mathbf{B}_o^t + \mathbf{G}_m^t \mathbf{A}_m^t \right) \boldsymbol{\sigma}_0 + \left(\mathbf{G}_m^t \mathbf{A}_\theta^t \right) \boldsymbol{\sigma}_1 \right\} dx\, dy \tag{4.83}$$

$$\mathbf{R}_b = \mathbf{F}_b - \sum_{e=1}^{N_e} \iint_e \left\{ \mathbf{B}_\gamma^t \tilde{\tau} + \left(\mathbf{G}_w^t \mathbf{A}_w^t \right) \boldsymbol{\sigma}_0 + \left(\mathbf{B}_b^t + \mathbf{G}_\theta^t \mathbf{A}_m^t \right) \boldsymbol{\sigma}_1 \right. $$
$$\left. + \left(\mathbf{G}_\theta^t \mathbf{A}_\theta^t \right) \boldsymbol{\sigma}_2 \right\} dx\, dy \tag{4.84}$$

Linearization of Equations of Equilibrium

To restore equilibrium, i.e. to make the residual vectors vanish we assume:

$$\boldsymbol{\delta}_{new} = \boldsymbol{\delta}_{old} + \Delta\boldsymbol{\delta}$$
$$\boldsymbol{\sigma}_{new}^{(l)} = \boldsymbol{\sigma}_{old}^{(l)} + \Delta\boldsymbol{\sigma} \tag{4.85}$$
$$\mathbf{A}_{new} = \mathbf{A}_{old} + \Delta\mathbf{A}$$

such that $\qquad \mathbf{R}_o \to \mathbf{O}, \quad \mathbf{R}_b \to \mathbf{O}$

Substituting from Equations (4.85) into (4.82), then it can be deduced that:

$$\sum_{e=1}^{N_e} \iiint_e \left\{ \left[\mathbf{B}_o^t + \mathbf{G}_m^t \left(\mathbf{A}_m^t + \Delta\mathbf{A}_m^t \right) \right] \left(\boldsymbol{\sigma}^{(l)} + \Delta\boldsymbol{\sigma}^{(l)} \right) \right. $$
$$\left. + \mathbf{G}_m^t \left(\mathbf{A}_\theta^t + \Delta\mathbf{A}_\theta^t \right) (-z) \left(\boldsymbol{\sigma}^{(l)} + \Delta\boldsymbol{\sigma}^{(l)} \right) \right\} dx\, dy\, dz - \mathbf{F}_o = \mathbf{O} \tag{4.86}$$

$$\sum_{e=1}^{N_e} \iiint_e \left\{ \mathbf{B}_\gamma^t f_\gamma (z) \left(\boldsymbol{\tau}^{(l)} + \Delta\boldsymbol{\tau}^{(l)} \right) + \mathbf{G}_w^t \left(\mathbf{A}_w^t + \Delta\mathbf{A}_w^t \right) \left(\boldsymbol{\sigma}^{(l)} + \Delta\boldsymbol{\sigma}^{(l)} \right) \right. $$
$$+ \left[\mathbf{B}_b^t + \mathbf{G}_\theta^t \left(\mathbf{A}_m^t + \Delta\mathbf{A}_m^t \right) \right] (-z) \left(\boldsymbol{\sigma}^{(l)} + \Delta\boldsymbol{\sigma}^{(l)} \right)$$
$$\left. + \mathbf{G}_\theta^t \left(\mathbf{A}_\theta^t + \Delta\mathbf{A}_\theta^t \right) (z^2) \left(\boldsymbol{\sigma}^{(l)} + \Delta\boldsymbol{\sigma}^{(l)} \right) \right\} dx\, dy\, dz - \mathbf{F}_b = \mathbf{O} \tag{4.87}$$

Expanding the previous expressions and ignoring high order terms, and using the definitions of $\mathbf{R}_o, \mathbf{R}_b$ given in Equations (4.82), then Equations (4.86) and (4.87) can be reduced to:

$$\sum_{e=1}^{N_e} \iiint_e \left\{ \left[\mathbf{B}_o^t + \mathbf{G}_m^t \mathbf{A}_m^t \right] \Delta\boldsymbol{\sigma}^{(l)} + \mathbf{G}_m^t \mathbf{A}_\theta^t \left(-z\Delta\boldsymbol{\sigma}^{(l)} \right) \right. $$
$$\left. + \mathbf{G}_m^t \Delta\mathbf{A}_m^t \boldsymbol{\sigma}^{(l)} + \mathbf{G}_m^t \Delta\mathbf{A}_\theta^t \left(-z\boldsymbol{\sigma}^{(l)} \right) \right\} dx\, dy\, dz = \mathbf{R}_o \tag{4.88}$$

$$\sum_{e=1}^{N_e} \iiint_e \Big\{ \mathbf{B}_\gamma^t \, f_\gamma(z) \Delta \boldsymbol{\tau}^{(l)} + \mathbf{G}_w^t \, \mathbf{A}_w^t \, \Delta \boldsymbol{\sigma}^{(l)} + \big[\mathbf{B}_b^t + \mathbf{G}_\theta^t \, \mathbf{A}_m^t \big] \big(- z \Delta \boldsymbol{\sigma}^{(l)} \big)$$

$$+ \, \mathbf{G}_\theta^t \, \mathbf{A}_\theta^t \left(z^2 \, \Delta \boldsymbol{\sigma}^{(l)} \right) + \mathbf{G}_w^t \, \Delta \mathbf{A}_w^t \, \boldsymbol{\sigma}^{(l)} + \mathbf{G}_\theta^t \, \Delta \mathbf{A}_m^t \, (-z) \boldsymbol{\sigma}^{(l)} \tag{4.89}$$

$$+ \, \mathbf{G}_\theta^t \, \Delta \mathbf{A}_\theta^t \, (z^2) \boldsymbol{\sigma}^{(l)} \Big\} \, dx\, dy\, dz \;=\; \mathbf{R}_b$$

Equations (4.88) and (4.89) can be divided into two parts each. The first part contains the terms which include $\Delta\boldsymbol{\sigma}$ and the second part has the terms with $\Delta\mathbf{A}$'s, as follows:

$$\sum_{e=1}^{N_e} \Big[\big(\mathbf{R}_o^e \big)_{\Delta\boldsymbol{\sigma}} + \big(\mathbf{R}_o^e \big)_{\Delta\mathbf{A}} \Big] \;=\; \mathbf{R}_o \tag{4.90}$$

$$\sum_{e=1}^{N_e} \Big[\big(\mathbf{R}_b^e \big)_{\Delta\boldsymbol{\sigma}} + \big(\mathbf{R}_b^e \big)_{\Delta\mathbf{A}} \Big] \;=\; \mathbf{R}_b \tag{4.91}$$

where, with the use of non-linear $\mathbf{B}$ matrices:

$$\big(\mathbf{R}_o^e \big)_{\Delta\boldsymbol{\sigma}} \;=\; \int_{-h/2}^{h/2} \iint_e \Big[\tilde{\mathbf{B}}_o^t \, \Delta \boldsymbol{\sigma}^{(l)} + \mathbf{B}_{\theta m}^t \big(- z \Delta \boldsymbol{\sigma}^{(l)} \big) \Big] \, dx\, dy\, dz \tag{4.92}$$

$$\big(\mathbf{R}_b^e \big)_{\Delta\boldsymbol{\sigma}} \;=\; \int_{-h/2}^{h/2} \iint_e \Big[\mathbf{B}_\gamma^t \, f_\gamma(z) \Delta \boldsymbol{\tau}^{(l)} + \mathbf{B}_{ww}^t \, \Delta \boldsymbol{\sigma}^{(l)}$$

$$+ \tilde{\mathbf{B}}_b^t \big(- z \Delta \boldsymbol{\sigma}^{(l)} \big) + \mathbf{B}_{\theta\theta}^t \left(z^2 \, \Delta \boldsymbol{\sigma}^{(l)} \right) \Big] \, dx\, dy\, dz \tag{4.93}$$

$$\big(\mathbf{R}_o^e \big)_{\Delta\mathbf{A}} \;=\; \int_{-h/2}^{h/2} \iint_e \Big[\mathbf{G}_m^t \, \Delta \mathbf{A}_m^t \, \boldsymbol{\sigma}^{(l)} + \mathbf{G}_m^t \, \Delta \mathbf{A}_\theta^t \, (-z) \, \boldsymbol{\sigma}^{(l)} \Big] \, dx\, dy\, dz \tag{4.94}$$

$$\big(\mathbf{R}_b^e \big)_{\Delta\mathbf{A}} \;=\; \int_{-h/2}^{h/2} \iint_e \Big[\mathbf{G}_w^t \, \Delta \mathbf{A}_w^t \, \boldsymbol{\sigma}^{(l)} + \mathbf{G}_\theta^t \, \Delta \mathbf{A}_m^t (-z) \boldsymbol{\sigma}^{(l)} + \mathbf{G}_\theta^t \, \Delta \mathbf{A}_\theta^t (z^2) \boldsymbol{\sigma}^{(l)} \Big] \, dx\, dy\, dz \tag{4.95}$$

Analysis of $\Delta\boldsymbol{\sigma}$ Terms

Using Equations (4.33) and (4.50), the increment of transverse shear stress can be expressed as follows:

$$\Delta \boldsymbol{\tau}^{(l)} \;=\; f_\gamma(z) \boldsymbol{\mu}^{(l)} \, \Delta \hat{\boldsymbol{\gamma}} \;\equiv\; f_\gamma(z) \boldsymbol{\mu}^{(l)} \, \mathbf{B}_\gamma \, \Delta \boldsymbol{\delta}_b \tag{4.96}$$

Hence, it can be deduced that:

$$\int_{-h/2}^{h/2} f_\gamma(z) \Delta \boldsymbol{\tau}^{(l)} \, dz \;=\; \boldsymbol{\mu}_{\gamma\gamma} \, \mathbf{B}_\gamma \, \Delta \boldsymbol{\delta}_b \tag{4.97}$$

Similarly the increment of x-y stress can be obtained from Equations (4.34) and (4.61), as follows:

$$\Delta \boldsymbol{\sigma}^{(l)} = \mathbf{D}^{(l)} \Delta \boldsymbol{\varepsilon} \equiv \mathbf{D}^{(l)} \left[\widetilde{\mathbf{B}}_o \Delta \boldsymbol{\delta}_o + \mathbf{B}_{ww} \Delta \boldsymbol{\delta}_b \right.$$
$$\left. - z \left(\mathbf{B}_{\theta m} \Delta \boldsymbol{\delta}_o + \widetilde{\mathbf{B}}_b \Delta \boldsymbol{\delta}_b \right) + z^2 \mathbf{B}_{\theta\theta} \Delta \boldsymbol{\delta}_b \right] \tag{4.98}$$

Using Equation (4.70), the following integrated stress increments can be deduced:

$$\int_{-h/2}^{h/2} \Delta \boldsymbol{\sigma}^{(l)} dz = \mathbf{D}_o \left(\widetilde{\mathbf{B}}_o \Delta \boldsymbol{\delta}_o + \mathbf{B}_{ww} \Delta \boldsymbol{\delta}_b \right) - \mathbf{D}_1 \left(\mathbf{B}_{\theta m} \Delta \boldsymbol{\delta}_o + \widetilde{\mathbf{B}}_b \Delta \boldsymbol{\delta}_b \right)$$
$$+ \mathbf{D}_2 \left(\mathbf{B}_{\theta\theta} \Delta \boldsymbol{\delta}_b \right) \tag{4.99}$$

$$\int_{-h/2}^{h/2} z \Delta \boldsymbol{\sigma}^{(l)} dz = \mathbf{D}_1 \left(\widetilde{\mathbf{B}}_o \Delta \boldsymbol{\delta}_o + \mathbf{B}_{ww} \Delta \boldsymbol{\delta}_b \right) - \mathbf{D}_2 \left(\mathbf{B}_{\theta m} \Delta \boldsymbol{\delta}_o + \widetilde{\mathbf{B}}_b \Delta \boldsymbol{\delta}_b \right)$$
$$+ \mathbf{D}_3 \left(\mathbf{B}_{\theta\theta} \Delta \boldsymbol{\delta}_b \right) \tag{4.100}$$

$$\int_{-h/2}^{h/2} z^2 \Delta \boldsymbol{\sigma}^{(l)} dz = \mathbf{D}_2 \left(\widetilde{\mathbf{B}}_o \Delta \boldsymbol{\delta}_o + \mathbf{B}_{ww} \Delta \boldsymbol{\delta}_b \right) - \mathbf{D}_3 \left(\mathbf{B}_{\theta m} \Delta \boldsymbol{\delta}_o + \widetilde{\mathbf{B}}_b \Delta \boldsymbol{\delta}_b \right)$$
$$+ \mathbf{D}_4 \left(\mathbf{B}_{\theta\theta} \Delta \boldsymbol{\delta}_b \right) \tag{4.101}$$

Using Equations (3.97) and (3.99)-(3.101) then Equations (3.92) and (3.93) can be reduced as follows:

$$\left(\mathbf{R}_o^e \right)_{\Delta\boldsymbol{\sigma}} = \mathbf{K}_{oo} \Delta \boldsymbol{\delta}_o + \mathbf{K}_{ob} \Delta \boldsymbol{\delta}_b \tag{4.102}$$

$$\left(\mathbf{R}_b^e \right)_{\Delta\boldsymbol{\sigma}} = \mathbf{K}_{bo} \Delta \boldsymbol{\delta}_o + \mathbf{K}_{bb} \Delta \boldsymbol{\delta}_b + \mathbf{K}_{\gamma\gamma} \Delta \boldsymbol{\delta}_b \tag{4.103}$$

where

$$\mathbf{K}_{oo} = \iint_e \left[\widetilde{\mathbf{B}}_o^t \mathbf{D}_o \widetilde{\mathbf{B}}_o - \widetilde{\mathbf{B}}_o^t \mathbf{D}_1 \mathbf{B}_{\theta m} - \mathbf{B}_{\theta m}^t \mathbf{D}_1 \widetilde{\mathbf{B}}_o + \mathbf{B}_{\theta m}^t \mathbf{D}_2 \mathbf{B}_{\theta m} \right] dx\, dy \tag{4.104}$$

$$\mathbf{K}_{ob} = \iint_e \left[\widetilde{\mathbf{B}}_o^t \mathbf{D}_o \mathbf{B}_{ww} - \widetilde{\mathbf{B}}_o^t \mathbf{D}_1 \widetilde{\mathbf{B}}_b - \mathbf{B}_{\theta m}^t \mathbf{D}_1 \mathbf{B}_{ww} \right.$$
$$\left. + \widetilde{\mathbf{B}}_o^t \mathbf{D}_2 \mathbf{B}_{\theta\theta} + \mathbf{B}_{\theta m}^t \mathbf{D}_2 \widetilde{\mathbf{B}}_b - \mathbf{B}_{\theta m}^t \mathbf{D}_3 \mathbf{B}_{\theta\theta} \right] dx\, dy \tag{4.105}$$

$$\mathbf{K}_{bo} = \iint_e \left[\mathbf{B}_{ww}^t \mathbf{D}_o \widetilde{\mathbf{B}}_o - \widetilde{\mathbf{B}}_b^t \mathbf{D}_1 \widetilde{\mathbf{B}}_o - \mathbf{B}_{ww}^t \mathbf{D}_1 \mathbf{B}_{\theta m} \right.$$
$$\left. + \mathbf{B}_{\theta\theta}^t \mathbf{D}_2 \widetilde{\mathbf{B}}_o + \widetilde{\mathbf{B}}_b^t \mathbf{D}_2 \mathbf{B}_{\theta m} - \mathbf{B}_{\theta\theta}^t \mathbf{D}_3 \mathbf{B}_{\theta m} \right] dx\, dy \equiv \mathbf{K}_{ob}^t \tag{4.106}$$

$$\mathbf{K}_{\gamma\gamma} = \iint_e \mathbf{B}_\gamma^t \boldsymbol{\mu}_{\gamma\gamma} \mathbf{B}_\gamma \, dx\, dy \tag{4.107}$$

$$\mathbf{K}_{bb} = \iint_e \left[\mathbf{B}_{ww}^t \mathbf{D}_o \mathbf{B}_{ww} - \mathbf{B}_{ww}^t \mathbf{D}_1 \widetilde{\mathbf{B}}_b - \widetilde{\mathbf{B}}_b^t \mathbf{D}_1 \mathbf{B}_{ww} \right.$$
$$+ \widetilde{\mathbf{B}}_b^t \mathbf{D}_2 \widetilde{\mathbf{B}}_b + \mathbf{B}_{ww}^t \mathbf{D}_2 \mathbf{B}_{\theta\theta} + \mathbf{B}_{\theta\theta}^t \mathbf{D}_2 \mathbf{B}_{ww}$$
$$\left. - \widetilde{\mathbf{B}}_b^t \mathbf{D}_3 \mathbf{B}_{\theta\theta} - \mathbf{B}_{\theta\theta}^t \mathbf{D}_3 \widetilde{\mathbf{B}}_b + \mathbf{B}_{\theta\theta}^t \mathbf{D}_4 \mathbf{B}_{\theta\theta} \right] dx\, dy \tag{4.108}$$

Analysis of ΔA Terms

Using the integrated stress defined by Equation (4.68), then Equations (4.94) and (4.95) can be simplified as follows:

$$\left(\mathbf{R}_o^e\right)_{\Delta\mathbf{A}} = \iint_e \left[\mathbf{G}_m^t \,\Delta\mathbf{A}_m^t \,\boldsymbol{\sigma}_o + \mathbf{G}_m^t \,\Delta\mathbf{A}_\theta^t \,\boldsymbol{\sigma}_1\right] dx\,dy \tag{4.109}$$

$$\left(\mathbf{R}_b^e\right)_{\Delta\mathbf{A}} = \iint_e \left[\mathbf{G}_w^t \,\Delta\mathbf{A}_w^t \,\boldsymbol{\sigma}_o + \mathbf{G}_\theta^t \,\Delta\mathbf{A}_m^t \,\boldsymbol{\sigma}_1 + \mathbf{G}_\theta^t \,\Delta\mathbf{A}_\theta^t \,\boldsymbol{\sigma}_2\right] dx\,dy \tag{4.110}$$

Using matrix manipulations, the following theorems can be proved:

$$\Delta\mathbf{A}_m^t \,\boldsymbol{\sigma}_n \equiv \mathbf{S}_n \,\Delta\boldsymbol{\theta}_m = \mathbf{S}_n \,\mathbf{G}_m \,\Delta\boldsymbol{\delta}_o \tag{4.111}$$

$$\Delta\mathbf{A}_\theta^t \,\boldsymbol{\sigma}_n \equiv \mathbf{S}_n \,\Delta\boldsymbol{\theta}_\theta = \mathbf{S}_n \,\mathbf{G}_\theta \,\Delta\boldsymbol{\delta}_b \tag{4.112}$$

$$\Delta\mathbf{A}_w^t \,\boldsymbol{\sigma}_o \equiv \mathbf{S}_w \,\Delta\boldsymbol{\theta}_w = \mathbf{S}_w \,\mathbf{G}_w \,\Delta\boldsymbol{\delta}_b \tag{4.113}$$

where

$$\mathbf{S}_n = \begin{bmatrix} \sigma_x^{(n)} & 0 & \tau_{xy}^{(n)} & 0 \\ 0 & \sigma_x^{(n)} & 0 & \tau_{xy}^{(n)} \\ \tau_{xy}^{(n)} & 0 & \sigma_y^{(n)} & 0 \\ 0 & \tau_{xy}^{(n)} & 0 & \sigma_y^{(n)} \end{bmatrix} \tag{4.114}$$

and

$$\mathbf{S}_w = \begin{bmatrix} \sigma_x^{(0)} & \tau_{xy}^{(0)} \\ \tau_{xy}^{(0)} & \sigma_y^{(0)} \end{bmatrix} \tag{4.115}$$

Substituting from Equations (4.111)-(4.113) into (4.109) and (4.110), then it can be deduced that:

$$\left(\mathbf{R}_o\right)_{\Delta\mathbf{A}} = \mathbf{K}_{mm}^\sigma \,\Delta\boldsymbol{\delta}_o + \mathbf{K}_{m\theta}^\sigma \,\Delta\boldsymbol{\delta}_b \tag{4.116}$$

$$\left(\mathbf{R}_b\right)_{\Delta\mathbf{A}} = \mathbf{K}_{\theta m}^\sigma \,\Delta\boldsymbol{\delta}_o + (\mathbf{K}_{ww}^\sigma + \mathbf{K}_{\theta\theta}^\sigma)\,\Delta\boldsymbol{\delta}_b \tag{4.117}$$

where

$$\mathbf{K}_{mm}^\sigma = \iint_e \mathbf{G}_m^t \,\mathbf{S}_o \,\mathbf{G}_m \,dx\,dy \tag{4.118}$$

$$\mathbf{K}_{m\theta}^\sigma = \iint_e \mathbf{G}_m^t \,\mathbf{S}_1 \,\mathbf{G}_\theta \,dx\,dy \tag{4.119}$$

$$\mathbf{K}_{\theta m}^\sigma = \iint_e \mathbf{G}_\theta^t \,\mathbf{S}_1 \,\mathbf{G}_m \,dx\,dy \tag{4.120}$$

$$\mathbf{K}_{ww}^{\sigma} = \iint_{e} \mathbf{G}_{w}^{t} \mathbf{S}_{w} \mathbf{G}_{w} \, dx \, dy \tag{4.121}$$

$$\mathbf{K}_{\theta\theta}^{\sigma} = \iint_{e} \mathbf{G}_{\theta}^{t} \mathbf{S}_{2} \mathbf{G}_{\theta} \, dx \, dy \tag{4.122}$$

Final Matrix Equations of the Element

Substituting from Equations (4.102), (4.103), (4.116), (4.117) into (4.90) and (4.91), it can be deduced that:

$$\sum_{e=1}^{N_e} \left\{ \mathbf{K}_{oo} \, \Delta\boldsymbol{\delta}_o + \mathbf{K}_{ob} \, \Delta\boldsymbol{\delta}_b + \mathbf{K}_{mm}^{\sigma} \, \Delta\boldsymbol{\delta}_o + \mathbf{K}_{m\theta}^{\sigma} \, \Delta\boldsymbol{\delta}_b \right\} = \mathbf{R}_o \tag{4.123}$$

$$\sum_{e=1}^{N_e} \left\{ \mathbf{K}_{bo} \, \Delta\boldsymbol{\delta}_o + \left(\mathbf{K}_{\gamma\gamma} + \mathbf{K}_{bb} \right) \Delta\boldsymbol{\delta}_b \right. \\ \left. + \mathbf{K}_{\theta m}^{\sigma} \, \Delta\boldsymbol{\delta}_o + \left(\mathbf{K}_{ww}^{\sigma} + \mathbf{K}_{\theta\theta}^{\sigma} \right) \Delta\boldsymbol{\delta}_b \right\} = \mathbf{R}_b \tag{4.124}$$

which can be rewritten as follows:

$$\sum_{e=1}^{N_e} \left\{ \left(\mathbf{K} + \mathbf{K}^{\sigma} \right) \begin{bmatrix} \Delta\boldsymbol{\delta}_o \\ \Delta\boldsymbol{\delta}_b \end{bmatrix} \right\} = \begin{bmatrix} \mathbf{R}_o \\ \mathbf{R}_b \end{bmatrix} \tag{4.125}$$

and the element stiffness matrices are defined as follow:

$$\mathbf{K} = \begin{bmatrix} \mathbf{K}_{oo} & \mathbf{K}_{ob} \\ \mathbf{K}_{bo} & \mathbf{K}_{bb} + \mathbf{K}_{\gamma\gamma} \end{bmatrix} \tag{4.126}$$

$$\mathbf{K}^{\sigma} = \begin{bmatrix} \mathbf{K}_{mm}^{\sigma} & \mathbf{K}_{m\theta}^{\sigma} \\ \mathbf{K}_{\theta m}^{\sigma} & \mathbf{K}_{ww}^{\sigma} + \mathbf{K}_{\theta\theta}^{\sigma} \end{bmatrix} \tag{4.127}$$

4.4 Derivation of Mass Matrix for Mindlin-type Element

It is assumed that different layers are made of the same composite material but with different fibre orientations, i.e. the density of every layer is the same i.e.

$$\rho^{(L)} = \rho \tag{4.128}$$

Using D'Alembert's principle, the inertial force vector acting at an infinitesimal volume due to an acceleration vector is:

$$d\bar{F} = -\rho\,\bar{a}\,dxdydz \tag{4.129}$$

Hence, the work done by the inertia force due to an infinitesimal virtual displacement field is:

$$dW_a = -\iiint\limits_{volume} \rho\,d\bar{q}.\bar{a}\,dxdydz \equiv -\iiint\limits_{volume} \rho\,d\mathbf{q}^t\,\ddot{\mathbf{q}}\,dxdydz \tag{4.130}$$

Using the expression below

$$q(x,y,z,t) = \begin{bmatrix} \mathbf{q}_{uv} \\ \mathbf{q}_w \end{bmatrix} = \begin{bmatrix} \mathbf{q}_o - z\mathbf{q}_\theta \\ \mathbf{q}_w \end{bmatrix} \tag{4.131}$$

It can be shown that

$$d\mathbf{q}^t\,\ddot{\mathbf{q}} = \left(d\mathbf{q}_o^t - zd\mathbf{q}_\theta^t\right)*\left(\ddot{\mathbf{q}}_o - z\ddot{\mathbf{q}}_\theta\right) + d\mathbf{q}_w^t\,\ddot{\mathbf{q}}_w \tag{4.132}$$

Expanding the equation above and integrating with respect to z gives:

$$\int\limits_{-h/2}^{h/2} d\mathbf{q}^t\,\ddot{\mathbf{q}}\,dz = h\left(d\mathbf{q}_o^t\,\ddot{\mathbf{q}}_o + d\mathbf{q}_w^t\,\ddot{\mathbf{q}}_w\right) + \frac{h^3}{12}d\mathbf{q}_\theta^t\,\ddot{\mathbf{q}}_\theta \tag{4.133}$$

Defining the following displacement components:

$$\mathbf{q}_o(x,y,t) = \mathbf{N}_o(x,y)\,\boldsymbol{\delta}_o(t) \tag{4.134}$$

$$\mathbf{q}_\theta(x,y,t) = \mathbf{N}_\theta(x,y)\,\boldsymbol{\delta}_b(t) \tag{4.135}$$

$$\mathbf{q}_w(x,y,t) = \mathbf{N}_w(x,y)\,\boldsymbol{\delta}_b(t) \tag{4.136}$$

$$\mathbf{N}_o(x,y) \equiv \mathbf{N}_o(\xi,\eta) = \begin{bmatrix} \cdots & \mathbf{N}_i(\xi,\eta) & 0 & \cdots \\ \cdots & 0 & \mathbf{N}_i(\xi,\eta) & \cdots \end{bmatrix} \tag{4.137}$$

$$\mathbf{N}_\theta(x,y) \equiv \mathbf{N}_\theta(\xi,\eta) = \begin{bmatrix} \cdots & 0 & 0 & -\mathbf{N}_i(\xi,\eta) & \cdots \\ \cdots & 0 & \mathbf{N}_i(\xi,\eta) & 0 & \cdots \end{bmatrix} \tag{4.138}$$

$$\mathbf{N}_w(x,y) \equiv \mathbf{N}_w(\xi,\eta) = \begin{bmatrix} \cdots & \mathbf{N}_i(\xi,\eta) & 0 & 0 & \cdots \end{bmatrix} \tag{4.139}$$

Equation (4.130) can be rewritten as:

$$dW_a = -\iint_{x-y} \left\{ \begin{array}{l} \rho\, h\, d\boldsymbol{\delta}_o^t\, \mathbf{N}_o^t\, \mathbf{N}_o\, \ddot{\boldsymbol{\delta}}_o + \rho\, h\, d\boldsymbol{\delta}_b^t\, \mathbf{N}_w^t\, \mathbf{N}_w\, \ddot{\boldsymbol{\delta}}_b \\ + \dfrac{\rho\, h^3}{12}\, d\boldsymbol{\delta}_b^t\, \mathbf{N}_\theta^t\, \mathbf{N}_\theta\, \ddot{\boldsymbol{\delta}}_b \end{array} \right\} dxdy \qquad (4.140)$$

Defining the following mass matrices:

$$\mathbf{M}_{oo} = \iint_{x-y} \rho\, h\, \mathbf{N}_o^t(\xi,\ \eta)\, \mathbf{N}_o(\xi,\ \eta)\, dxdy \qquad (4.141)$$

$$\mathbf{M}_{ww} = \iint_{x-y} \rho\, h\, \mathbf{N}_w^t(\xi,\ \eta)\, \mathbf{N}_w(\xi,\ \eta)\, dxdy \qquad (4.142)$$

$$\mathbf{M}_{\theta\theta} = \iint_{x-y} \frac{\rho\, h^3}{12}\, \mathbf{N}_\theta^t(\xi,\ \eta)\, \mathbf{N}_\theta(\xi,\ \eta)\, dxdy \qquad (4.143)$$

Equation (4.140) can be rewritten as:

$$dW_a = -\left\{ d\boldsymbol{\delta}_o^t\, \mathbf{M}_{oo}\, \ddot{\boldsymbol{\delta}}_o + d\boldsymbol{\delta}_b^t\, [\mathbf{M}_{ww} + \mathbf{M}_{\theta\theta}]\ddot{\boldsymbol{\delta}}_b \right\}$$

$$\equiv -d\boldsymbol{\delta}^t \mathbf{M}\, \ddot{\boldsymbol{\delta}} \qquad (4.144)$$

Hence it can be shown that the element mass matrix is as given below:

$$\mathbf{M} = \begin{bmatrix} \mathbf{M}_{oo} & 0 \\ 0 & \mathbf{M}_{ww} + \mathbf{M}_{\theta\theta} \end{bmatrix} \qquad (4.145)$$

5 Reissner-type Element Theory

This chapter explains the Reissner-type plate bending element theory and derives the equation used in the finite element programming. The Reissner-type element theory defines the displacement equation, strain equation, stress equation, strain energy variation and generalised equation of equilibrium. These are based upon parabolic distributions of transverse shear strains over the plate thickness. The transverse shear strains are assumed infinitesimal whilst the x-y strain components are considered finite, according to Green's strain-displacement equations. The generalised equation of equilibrium is then linearised in-order to obtain the Reissner-type element equation. The element interpolations are based on Lagrangian and Hermitian shape functions, with 7 degrees-of-freedom per node for non-conforming elements, and 8 degrees-of-freedom per node for the conforming elements. All integrations through the plate thickness (i.e. with respect to z) are carried out analytically.

5.1 Stress and Strain Equations

Modelling of Transverse Shear Strains

The composite plate consists of N_l layers, which are parallel to the x-y plane such that for layer l:

$$z = Z_L^{(l)}, \quad z = Z_U^{(l)} \tag{5.1}$$

are the equations of its lower and upper surfaces, and its thickness is given by:

$$h^{(l)} = Z_U^{(l)} - Z_L^{(l)} \tag{5.2}$$

The total thickness of the composite plate can be obtained as follows:

$$h = \sum_{l=1}^{N_l} h^{(l)} \tag{5.3}$$

The midplane of the plate $(z = 0)$ is assumed to be the bending neutral plane.

Consider the composite plate to be transversely isotropic, which means continuous transverse shear strains all over the thickness of the plate. Using a three-point Lagrangian interpolation (Attia & El-Zafrany, 1999), the distributions of transverse shear strains over the plate thickness can be expressed as follows:

$$\gamma_{xz}(x,y,z) = \gamma_{xz}^o(x,y)\left[1-\frac{4z^2}{h^2}\right] \tag{5.4}$$

$$\gamma_{yz}(x,y,z) = \gamma_{yz}^o(x,y)\left[1-\frac{4z^2}{h^2}\right] \tag{5.5}$$

where $\gamma_{xz}^o, \gamma_{yz}^o$ represent the values of transverse shear strains at the midplane.

The average values of transverse shear strains over the plate thickness can be defined as follows:

$$\bar{\gamma}_{xz}(x,y) = \frac{1}{h}\int_{-h/2}^{h/2}\gamma_{xz}\,dz \equiv \frac{2}{3}\gamma_{xz}^o \tag{5.6}$$

$$\bar{\gamma}_{yz}(x,y) = \frac{1}{h}\int_{-h/2}^{h/2}\gamma_{yz}\,dz \equiv \frac{2}{3}\gamma_{yz}^o \tag{5.7}$$

and Equations (5.4) and (5.5) can be rewritten as follows:

$$\gamma_{xz}(x,y,z) = \tfrac{3}{2}\bar{\gamma}_{xz}(x,y)\left[1-\frac{4z^2}{h^2}\right] \tag{5.8}$$

$$\gamma_{yz}(x,y,z) = \tfrac{3}{2}\bar{\gamma}_{yz}(x,y)\left[1-\frac{4z^2}{h^2}\right] \tag{5.9}$$

From Mindlin's plate-bending theory, average slope angles are defined as follows:

$$\theta_x = \frac{\partial w}{\partial y} - \bar{\gamma}_{yz} \equiv \frac{\partial w}{\partial y} - \psi_x \tag{5.10}$$

$$\theta_y = -\frac{\partial w}{\partial x} + \bar{\gamma}_{xz} \equiv -\frac{\partial w}{\partial x} - \psi_y \tag{5.11}$$

where

$$\psi_x = \bar{\gamma}_{yz}, \quad \psi_y = -\bar{\gamma}_{xz} \tag{5.12}$$

Hence, Equations (5.8) and (5.9) can be rewritten as follows:

$$\gamma_{xz}(x,y,z) = -\tfrac{3}{2}\psi_y(x,y)\left[1-\frac{4z^2}{h^2}\right] \tag{5.13}$$

$$\gamma_{yz}(x,y,z) = \tfrac{3}{2}\psi_x(x,y)\left[1-\frac{4z^2}{h^2}\right] \tag{5.14}$$

Equations (5.13) and (5.14) can be expressed in the following matrix form:

$$\boldsymbol{\gamma}(x,y,z) = \begin{bmatrix} \gamma_{xz} \\ \gamma_{yz} \end{bmatrix} \equiv f_\gamma(z)\,\hat{\boldsymbol{\gamma}}(x,y) \qquad (5.15)$$

where

$$f_\gamma(z) = \frac{3}{2}\left[1 - \frac{4z^2}{h^2}\right] \qquad (5.16\text{a})$$

$$\hat{\boldsymbol{\gamma}}(x,z) = \begin{bmatrix} -\psi_y \\ \psi_x \end{bmatrix} \qquad (5.16\text{b})$$

Notice also that the variation of transverse strain vector is:

$$d\boldsymbol{\gamma} = f_\gamma\, d\hat{\boldsymbol{\gamma}} \qquad (5.17)$$

Displacement Components

The following approximations are considered in this theory:

(a)   The lateral deflection w is independent of z, the distance along the plate thickness.

(b)   The transverse shear strains are infinitesimal.

The second approximation will lead to:

$$\gamma_{xz} = \frac{\partial w}{\partial x} + \frac{\partial u}{\partial z}, \quad \gamma_{yz} = \frac{\partial w}{\partial y} + \frac{\partial v}{\partial z} \tag{5.18}$$

Substituting from Equations (5.13) and (5.14) into (5.18), then it can be deduced that:

$$\frac{\partial u}{\partial z} = -\frac{\partial w}{\partial x} - \frac{3}{2}\psi_y\left(1 - \frac{4z^2}{h^2}\right) \tag{5.19}$$

$$\frac{\partial v}{\partial z} = -\frac{\partial w}{\partial y} + \frac{3}{2}\psi_x\left(1 - \frac{4z^2}{h^2}\right) \tag{5.20}$$

Integrating Equations (5.19) and (5.20) with respect to z, then:

$$u(x,y,z) = u^o(x,y) - z\frac{\partial w}{\partial x} - f_\psi(z)\psi_y \tag{5.21}$$

$$v(x,y,z) = v^o(x,y) - z\frac{\partial w}{\partial y} + f_\psi(z)\psi_x \tag{5.22}$$

with

$$w(x,y,z) \approx w(x,y) \tag{5.23}$$

where

$$f_\psi(z) = \frac{3}{2}z - \frac{2z^3}{h^2} \tag{5.24}$$

and u^o, v^o represent the values of u, v at the midplane ($z = 0$).

The *x-y* Strain Components

<u>General definitions</u>

These are $\varepsilon_x, \varepsilon_y, \gamma_{xy}$ and are represented with the following vector:

$$\boldsymbol{\varepsilon} = \begin{bmatrix} \varepsilon_x \\ \varepsilon_y \\ \gamma_{xy} \end{bmatrix} \tag{5.25}$$

Using Green's strain-displacement equations, then:

$$\varepsilon_x = \frac{\partial u}{\partial x} + \frac{1}{2}\left[\left(\frac{\partial u}{\partial x}\right)^2 + \left(\frac{\partial v}{\partial x}\right)^2 + \left(\frac{\partial w}{\partial x}\right)^2\right] \tag{5.26}$$

$$\varepsilon_y = \frac{\partial v}{\partial y} + \frac{1}{2}\left[\left(\frac{\partial u}{\partial y}\right)^2 + \left(\frac{\partial v}{\partial y}\right)^2 + \left(\frac{\partial w}{\partial y}\right)^2\right] \tag{5.27}$$

$$\gamma_{xy} = \frac{\partial u}{\partial y} + \frac{\partial v}{\partial x} + \left[\frac{\partial u}{\partial x}\frac{\partial u}{\partial y} + \frac{\partial v}{\partial x}\frac{\partial v}{\partial y} + \frac{\partial w}{\partial x}\frac{\partial w}{\partial y}\right] \tag{5.28}$$

Using the previous equations, the *x-y* strain vector can be partitioned as follows:

$$\boldsymbol{\varepsilon} = \boldsymbol{\varepsilon}_S + \boldsymbol{\varepsilon}_L \tag{5.29}$$

where $\boldsymbol{\varepsilon}_S$ represents the first order terms, or the infinitesimal strain vector, i.e.

$$\boldsymbol{\varepsilon}_S = \begin{bmatrix} \dfrac{\partial u}{\partial x} \\[2ex] \dfrac{\partial v}{\partial y} \\[2ex] \dfrac{\partial u}{\partial y} + \dfrac{\partial v}{\partial x} \end{bmatrix} \tag{5.30}$$

and $\boldsymbol{\varepsilon}_L$ represents the additional non-linear terms in Green's equations, i.e.

$$\boldsymbol{\varepsilon}_L = \frac{1}{2} \begin{bmatrix} \left(\dfrac{\partial u}{\partial x}\right)^2 + \left(\dfrac{\partial v}{\partial x}\right)^2 + \left(\dfrac{\partial w}{\partial x}\right)^2 \\[3mm] \left(\dfrac{\partial u}{\partial y}\right)^2 + \left(\dfrac{\partial v}{\partial y}\right)^2 + \left(\dfrac{\partial w}{\partial y}\right)^2 \\[3mm] 2\left(\dfrac{\partial u}{\partial x}\dfrac{\partial u}{\partial y} + \dfrac{\partial v}{\partial x}\dfrac{\partial v}{\partial y} + \dfrac{\partial w}{\partial x}\dfrac{\partial w}{\partial y}\right) \end{bmatrix} \qquad (5.31)$$

Infinitesimal strain components

Substituting from Equations (5.21) and (5.22) into (5.30), then it can be deduced that:

$$\boldsymbol{\varepsilon}_S(x,y,z) = \boldsymbol{\varepsilon}_o(x,y) - z\,\boldsymbol{\varepsilon}_b(x,y) + f_\psi(z)\,\boldsymbol{\varepsilon}_\psi(x,y) \qquad (5.32)$$

where

$$\boldsymbol{\varepsilon}_o(x,y) = \begin{bmatrix} \dfrac{\partial u^o}{\partial x} \\[4mm] \dfrac{\partial v^o}{\partial y} \\[4mm] \dfrac{\partial u^o}{\partial y} + \dfrac{\partial v^o}{\partial x} \end{bmatrix} \qquad (5.33)$$

$$\boldsymbol{\varepsilon}_b(x,y) = \begin{bmatrix} \dfrac{\partial^2 w}{\partial x^2} \\[4mm] \dfrac{\partial^2 w}{\partial y^2} \\[4mm] 2\dfrac{\partial^2 w}{\partial x\,\partial y} \end{bmatrix} \qquad (5.34)$$

$$\boldsymbol{\varepsilon}_\psi(x,y) = \begin{bmatrix} -\dfrac{\partial \psi_y}{\partial x} \\[4mm] \dfrac{\partial \psi_x}{\partial y} \\[4mm] \dfrac{\partial \psi_x}{\partial x} - \dfrac{\partial \psi_y}{\partial y} \end{bmatrix} \qquad (5.35)$$

<u>Additional large strain components</u>

Substituting from Equations (5.21) and (5.22) into (5.31), then it can be proved that:

$$\begin{aligned}
\varepsilon_L(x, y, z) &= \varepsilon_{mm}(x, y) + \varepsilon_{ww}(x, y) + z^2 \varepsilon_{\theta\theta}(x, y) + f_\psi^2 \varepsilon_{\psi\psi} \\
&\quad - z\,\varepsilon_{m\theta}(x, y) + f_\psi\,\varepsilon_{m\psi}(x, y) - z\,f_\psi\,\varepsilon_{\theta\psi}(x, y)
\end{aligned} \tag{5.36}$$

where

$$\varepsilon_{mm}(x, y) = \frac{1}{2}\begin{bmatrix} \left(\dfrac{\partial u^o}{\partial x}\right)^2 + \left(\dfrac{\partial v^o}{\partial x}\right)^2 \\[2mm] \left(\dfrac{\partial u^o}{\partial y}\right)^2 + \left(\dfrac{\partial v^o}{\partial y}\right)^2 \\[2mm] 2\left(\dfrac{\partial u^o}{\partial x}\dfrac{\partial u^o}{\partial y} + \dfrac{\partial v^o}{\partial x}\dfrac{\partial v^o}{\partial y}\right) \end{bmatrix} \tag{5.37}$$

$$\varepsilon_{ww}(x, y) = \frac{1}{2}\begin{bmatrix} \left(\dfrac{\partial w}{\partial x}\right)^2 \\[2mm] \left(\dfrac{\partial w}{\partial y}\right)^2 \\[2mm] 2\left(\dfrac{\partial w}{\partial x}\dfrac{\partial w}{\partial y}\right) \end{bmatrix} \tag{5.38}$$

$$\varepsilon_{\theta\theta}(x, y) = \frac{1}{2}\begin{bmatrix} \left(\dfrac{\partial^2 w}{\partial x^2}\right)^2 + \left(\dfrac{\partial^2 w}{\partial x \partial y}\right)^2 \\[2mm] \left(\dfrac{\partial^2 w}{\partial x \partial y}\right)^2 + \left(\dfrac{\partial^2 w}{\partial y^2}\right)^2 \\[2mm] 2\left(\dfrac{\partial^2 w}{\partial x^2}\dfrac{\partial^2 w}{\partial x \partial y} + \dfrac{\partial^2 w}{\partial x \partial y}\dfrac{\partial^2 w}{\partial y^2}\right) \end{bmatrix} \tag{5.39}$$

$$\varepsilon_{\psi\psi}(x, y) = \frac{1}{2}\begin{bmatrix} \left(\dfrac{\partial \psi_x}{\partial x}\right)^2 + \left(\dfrac{\partial \psi_y}{\partial x}\right)^2 \\[2mm] \left(\dfrac{\partial \psi_x}{\partial y}\right)^2 + \left(\dfrac{\partial \psi_y}{\partial y}\right)^2 \\[2mm] 2\left(\dfrac{\partial \psi_x}{\partial x}\dfrac{\partial \psi_x}{\partial y} + \dfrac{\partial \psi_y}{\partial x}\dfrac{\partial \psi_y}{\partial y}\right) \end{bmatrix} \tag{5.40}$$

$$\varepsilon_{m\theta}(x,y) = \begin{bmatrix} \dfrac{\partial u^o}{\partial x}\dfrac{\partial^2 w}{\partial x^2} + \dfrac{\partial v^o}{\partial x}\dfrac{\partial^2 w}{\partial x \partial y} \\[3mm] \dfrac{\partial u^o}{\partial y}\dfrac{\partial^2 w}{\partial x \partial y} + \dfrac{\partial v^o}{\partial y}\dfrac{\partial^2 w}{\partial y^2} \\[3mm] \dfrac{\partial u^o}{\partial x}\dfrac{\partial^2 w}{\partial x \partial y} + \dfrac{\partial u^o}{\partial y}\dfrac{\partial^2 w}{\partial x^2} + \dfrac{\partial v^o}{\partial x}\dfrac{\partial^2 w}{\partial y^2} + \dfrac{\partial v^o}{\partial y}\dfrac{\partial^2 w}{\partial x \partial y} \end{bmatrix} \qquad (5.41)$$

$$\varepsilon_{m\psi}(x,y) = \begin{bmatrix} -\dfrac{\partial u^o}{\partial x}\dfrac{\partial \psi_y}{\partial x} + \dfrac{\partial v^o}{\partial x}\dfrac{\partial \psi_x}{\partial x} \\[3mm] -\dfrac{\partial u^o}{\partial y}\dfrac{\partial \psi_y}{\partial y} + \dfrac{\partial v^o}{\partial y}\dfrac{\partial \psi_x}{\partial y} \\[3mm] -\dfrac{\partial u^o}{\partial x}\dfrac{\partial \psi_y}{\partial y} - \dfrac{\partial u^o}{\partial y}\dfrac{\partial \psi_y}{\partial x} + \dfrac{\partial v^o}{\partial x}\dfrac{\partial \psi_x}{\partial y} + \dfrac{\partial v^o}{\partial y}\dfrac{\partial \psi_x}{\partial x} \end{bmatrix} \qquad (5.42)$$

$$\varepsilon_{\theta\psi}(x,y) = \begin{bmatrix} -\dfrac{\partial^2 w}{\partial x^2}\dfrac{\partial \psi_y}{\partial x} + \dfrac{\partial^2 w}{\partial x \partial y}\dfrac{\partial \psi_x}{\partial x} \\[3mm] -\dfrac{\partial^2 w}{\partial x \partial y}\dfrac{\partial \psi_y}{\partial y} + \dfrac{\partial^2 w}{\partial y^2}\dfrac{\partial \psi_x}{\partial y} \\[3mm] -\dfrac{\partial^2 w}{\partial x \partial y}\dfrac{\partial \psi_y}{\partial x} - \dfrac{\partial^2 w}{\partial x^2}\dfrac{\partial \psi_y}{\partial y} + \dfrac{\partial^2 w}{\partial y^2}\dfrac{\partial \psi_x}{\partial x} + \dfrac{\partial^2 w}{\partial x \partial y}\dfrac{\partial \psi_x}{\partial y} \end{bmatrix} \qquad (5.43)$$

Matrix representation of additional large strain components

This can be achieved in terms of the following rotation vectors:

$$\boldsymbol{\theta}_m(x, y) = \begin{bmatrix} \dfrac{\partial u^o}{\partial x} \\[2ex] \dfrac{\partial v^o}{\partial x} \\[2ex] \dfrac{\partial u^o}{\partial y} \\[2ex] \dfrac{\partial v^o}{\partial y} \end{bmatrix} \tag{5.44}$$

$$\boldsymbol{\theta}_w(x, y) = \begin{bmatrix} \dfrac{\partial w}{\partial x} \\[2ex] \dfrac{\partial w}{\partial y} \end{bmatrix} \tag{5.45}$$

$$\boldsymbol{\theta}_\theta(x, y) = \begin{bmatrix} \dfrac{\partial^2 w}{\partial x^2} \\[2ex] \dfrac{\partial^2 w}{\partial x \partial y} \\[2ex] \dfrac{\partial^2 w}{\partial y \partial x} \\[2ex] \dfrac{\partial^2 w}{\partial y^2} \end{bmatrix} \tag{5.46}$$

$$\boldsymbol{\theta}_\psi(x, y) = \begin{bmatrix} -\dfrac{\partial \psi_y}{\partial x} \\[2ex] \dfrac{\partial \psi_x}{\partial x} \\[2ex] -\dfrac{\partial \psi_y}{\partial y} \\[2ex] \dfrac{\partial \psi_x}{\partial y} \end{bmatrix} \tag{5.47}$$

Hence, by matrix manipulation it can be proved that:

(i) $\qquad \boldsymbol{\varepsilon}_{mm} = \tfrac{1}{2}\mathbf{A}_m\boldsymbol{\theta}_m, \quad d\boldsymbol{\varepsilon}_{mm} = \mathbf{A}_m\, d\boldsymbol{\theta}_m$ \hfill (5.48)

where

$$\mathbf{A}_m(x,y) = \begin{bmatrix} \dfrac{\partial u^o}{\partial x} & \dfrac{\partial v^o}{\partial x} & 0 & 0 \\[3mm] 0 & 0 & \dfrac{\partial u^o}{\partial y} & \dfrac{\partial v^o}{\partial y} \\[3mm] \dfrac{\partial u^o}{\partial y} & \dfrac{\partial v^o}{\partial y} & \dfrac{\partial u^o}{\partial x} & \dfrac{\partial v^o}{\partial x} \end{bmatrix} \tag{5.49}$$

(ii) $\qquad \boldsymbol{\varepsilon}_{ww} = \tfrac{1}{2}\mathbf{A}_w\,\boldsymbol{\theta}_w\,, \quad d\boldsymbol{\varepsilon}_{ww} = \mathbf{A}_w\,d\boldsymbol{\theta}_w \tag{5.50}$

where

$$\mathbf{A}_w(x,y) = \begin{bmatrix} \dfrac{\partial w}{\partial x} & 0 \\[3mm] 0 & \dfrac{\partial w}{\partial y} \\[3mm] \dfrac{\partial w}{\partial y} & \dfrac{\partial w}{\partial y} \end{bmatrix} \tag{5.51}$$

(iii) $\qquad \boldsymbol{\varepsilon}_{\theta\theta} = \tfrac{1}{2}\mathbf{A}_\theta\,\boldsymbol{\theta}_\theta\,, \quad d\boldsymbol{\varepsilon}_{\theta\theta} = \mathbf{A}_\theta\,d\boldsymbol{\theta}_\theta \tag{5.52}$

where

$$\mathbf{A}_\theta(x,y) = \begin{bmatrix} \dfrac{\partial^2 w}{\partial x^2} & \dfrac{\partial^2 w}{\partial x \partial y} & 0 & 0 \\[3mm] 0 & 0 & \dfrac{\partial^2 w}{\partial y \partial x} & \dfrac{\partial^2 w}{\partial y^2} \\[3mm] \dfrac{\partial^2 w}{\partial y \partial x} & \dfrac{\partial^2 w}{\partial y^2} & \dfrac{\partial^2 w}{\partial x^2} & \dfrac{\partial^2 w}{\partial x \partial y} \end{bmatrix} \tag{5.53}$$

(iv) $\qquad \boldsymbol{\varepsilon}_{\psi\psi} = \tfrac{1}{2}\mathbf{A}_\psi\,\boldsymbol{\theta}_\psi\,, \quad d\boldsymbol{\varepsilon}_{\psi\psi} = \mathbf{A}_\psi\,d\boldsymbol{\theta}_\psi \tag{5.54}$

where

$$\mathbf{A}_\psi(x,y) = \begin{bmatrix} -\dfrac{\partial \psi_y}{\partial x} & \dfrac{\partial \psi_x}{\partial x} & 0 & 0 \\[3mm] 0 & 0 & -\dfrac{\partial \psi_y}{\partial y} & \dfrac{\partial \psi_x}{\partial y} \\[3mm] -\dfrac{\partial \psi_y}{\partial y} & \dfrac{\partial \psi_x}{\partial y} & -\dfrac{\partial \psi_y}{\partial x} & \dfrac{\partial \psi_x}{\partial x} \end{bmatrix} \tag{5.55}$$

(v)
$$\boldsymbol{\varepsilon}_{m\theta} = \tfrac{1}{2}\left(\mathbf{A}_m\,\boldsymbol{\theta}_\theta + \mathbf{A}_\theta\,\boldsymbol{\theta}_m\right),$$
$$d\boldsymbol{\varepsilon}_{m\theta} = \mathbf{A}_m\,d\boldsymbol{\theta}_\theta + \mathbf{A}_\theta\,d\boldsymbol{\theta}_m \qquad (5.56)$$

(vi)
$$\boldsymbol{\varepsilon}_{m\psi} = \tfrac{1}{2}\left(\mathbf{A}_m\,\boldsymbol{\theta}_\psi + \mathbf{A}_\psi\,\boldsymbol{\theta}_m\right),$$
$$d\boldsymbol{\varepsilon}_{m\psi} = \mathbf{A}_m\,d\boldsymbol{\theta}_\psi + \mathbf{A}_\psi\,d\boldsymbol{\theta}_m \qquad (5.57)$$

(vii)
$$\boldsymbol{\varepsilon}_{\theta\psi} = \tfrac{1}{2}\left(\mathbf{A}_\theta\,\boldsymbol{\theta}_\psi + \mathbf{A}_\psi\,\boldsymbol{\theta}_\theta\right),$$
$$d\boldsymbol{\varepsilon}_{\theta\psi} = \mathbf{A}_\theta\,d\boldsymbol{\theta}_\psi + \mathbf{A}_\psi\,d\boldsymbol{\theta}_\theta \qquad (5.58)$$

Total strain vector and its variation

From previous equations, the total *x-y* strain vector can be expressed as follows:

$$\boldsymbol{\varepsilon}(x,y,z) = \boldsymbol{\varepsilon}_o(x,y) + \boldsymbol{\varepsilon}_{mm}(x,y) + \boldsymbol{\varepsilon}_{ww}(x,y)$$
$$- z\left[\boldsymbol{\varepsilon}_b(x,y) + \boldsymbol{\varepsilon}_{m\theta}(x,y)\right] + f_\psi(z)\left[\boldsymbol{\varepsilon}_\psi(x,y) + \boldsymbol{\varepsilon}_{m\psi}(x,y)\right] \qquad (5.59)$$
$$- z\,f_\psi(z)\,\boldsymbol{\varepsilon}_{\theta\psi}(x,y) + z^2\,\boldsymbol{\varepsilon}_{\theta\theta}(x,y) + f_\psi^2(z)\,\boldsymbol{\varepsilon}_{\psi\psi}(x,y)$$

which can also be written as follows:

$$\boldsymbol{\varepsilon}(x,y,z) = \boldsymbol{\varepsilon}_o + \tfrac{1}{2}\left(\mathbf{A}_m\,\boldsymbol{\theta}_m + \mathbf{A}_w\,\boldsymbol{\theta}_w\right) - z\left[\boldsymbol{\varepsilon}_b + \tfrac{1}{2}\left(\mathbf{A}_m\,\boldsymbol{\theta}_\theta + \mathbf{A}_\theta\,\boldsymbol{\theta}_m\right)\right]$$
$$+ f_\psi\left[\boldsymbol{\varepsilon}_\psi + \tfrac{1}{2}\left(\mathbf{A}_m\,\boldsymbol{\theta}_\psi + \mathbf{A}_\psi\,\boldsymbol{\theta}_m\right)\right] - \tfrac{1}{2}z\,f_\psi\left(\mathbf{A}_\psi\,\boldsymbol{\theta}_\theta + \mathbf{A}_\theta\,\boldsymbol{\theta}_\psi\right) \qquad (5.60)$$
$$+ \tfrac{1}{2}z^2\left(\mathbf{A}_\theta\,\boldsymbol{\theta}_\theta\right) + \tfrac{1}{2}f_\psi^2\left(\mathbf{A}_\psi\,\boldsymbol{\theta}_\psi\right)$$

The variation of the total *x-y* strain vector can be obtained from the previous equation as follows:

$$d\boldsymbol{\varepsilon}(x,y,z) = d\boldsymbol{\varepsilon}_o + \left(\mathbf{A}_m\,d\boldsymbol{\theta}_m + \mathbf{A}_w\,d\boldsymbol{\theta}_w\right) - z\left[d\boldsymbol{\varepsilon}_b + \left(\mathbf{A}_m\,d\boldsymbol{\theta}_\theta + \mathbf{A}_\theta\,d\boldsymbol{\theta}_m\right)\right]$$
$$+ f_\psi\left[d\boldsymbol{\varepsilon}_\psi + \left(\mathbf{A}_m\,d\boldsymbol{\theta}_\psi + \mathbf{A}_\psi\,d\boldsymbol{\theta}_m\right)\right] - z\,f_\psi\left(\mathbf{A}_\psi\,d\boldsymbol{\theta}_\theta + \mathbf{A}_\theta\,d\boldsymbol{\theta}_\psi\right) \qquad (5.61)$$
$$+ z^2\left(\mathbf{A}_\theta\,d\boldsymbol{\theta}_\theta\right) + f_\psi^2\left(\mathbf{A}_\psi\,d\boldsymbol{\theta}_\psi\right)$$

Stress Components

The relevant stress components at any point inside the lth layer of a composite layered plate can be represented in terms of two vectors defined as follows:

(a) The transverse shear stress vector

$$\boldsymbol{\tau}^{(l)} = \begin{bmatrix} \tau_{xz} \\[4pt] \tau_{yz} \end{bmatrix} \qquad (5.62)$$

(b) The *x-y* stress vector

$$\boldsymbol{\sigma}^{(l)} = \begin{bmatrix} \sigma_x \\ \sigma_y \\ \tau_{xy} \end{bmatrix} \tag{5.63}$$

Using constitutive equations for the lth layer, as explained in Appendix A, the stress vectors can be expressed in terms of strain vectors as follows:

$$\boldsymbol{\tau}^{(l)} = \boldsymbol{\mu}^{(l)} \boldsymbol{\gamma} \equiv f_\gamma(z) \boldsymbol{\mu}^{(l)} \hat{\boldsymbol{\gamma}} \tag{5.64}$$

$$\boldsymbol{\sigma}^{(l)} = \mathbf{D}^{(l)} \boldsymbol{\varepsilon} \tag{5.65a}$$

Substituting from Equation (5.60) into (5.65a) then it can be deduced that:

$$\begin{aligned}
\boldsymbol{\sigma}^{(l)} = \mathbf{D}^{(l)} \Big\{ &\boldsymbol{\varepsilon}_o + \tfrac{1}{2}\big(\mathbf{A}_m \boldsymbol{\theta}_m + \mathbf{A}_w \boldsymbol{\theta}_w\big) - z\big[\boldsymbol{\varepsilon}_b + \tfrac{1}{2}\big(\mathbf{A}_m \boldsymbol{\theta}_\theta + \mathbf{A}_\theta \boldsymbol{\theta}_m\big)\big] \\
&+ f_\psi \big[\boldsymbol{\varepsilon}_\psi + \tfrac{1}{2}\big(\mathbf{A}_m \boldsymbol{\theta}_\psi + \mathbf{A}_\psi \boldsymbol{\theta}_m\big)\big] - \tfrac{1}{2} z f_\psi \big(\mathbf{A}_\psi \boldsymbol{\theta}_\theta + \mathbf{A}_\theta \boldsymbol{\theta}_\psi\big) \\
&+ \tfrac{1}{2} z^2 \big(\mathbf{A}_\theta \boldsymbol{\theta}_\theta\big) + \tfrac{1}{2} f_\psi^2 \big(\mathbf{A}_\psi \boldsymbol{\theta}_\psi\big) \Big\}
\end{aligned} \tag{5.65b}$$

Strain Energy Variation

<u>General</u>

The variation of strain energy density (strain energy per unit volume) due to a variation of displacement at any point inside the lth layer of the plate can be expressed as follows:

$$d\overline{U}^{(l)} = \sigma_x^{(l)} d\varepsilon_x + \sigma_y^{(l)} d\varepsilon_y + \tau_{xy}^{(l)} d\gamma_{xy} + \tau_{yz}^{(l)} d\gamma_{yz} + \tau_{xz}^{(l)} d\gamma_{xz} \tag{5.66}$$

which can be represented in the following matrix form:

$$d\overline{U}^{(l)} = d\boldsymbol{\gamma}^t \boldsymbol{\tau}^{(l)} + d\boldsymbol{\varepsilon}^t \boldsymbol{\sigma}^{(l)} \equiv d\overline{U}_\gamma^{(l)} + d\overline{U}_\varepsilon^{(l)} \tag{5.67}$$

where

$$d\overline{U}_\gamma^{(l)} = d\boldsymbol{\gamma}^t \boldsymbol{\tau}^{(l)} \equiv f_\gamma(z) d\hat{\boldsymbol{\gamma}}^t \boldsymbol{\tau}^{(l)} \tag{5.68}$$

$$d\overline{U}_\varepsilon^{(l)} = d\boldsymbol{\varepsilon}^t \boldsymbol{\sigma}^{(l)} \tag{5.69}$$

Substituting from Equation (5.61) into (5.69) then it can be deduced that:

$$\begin{aligned} d\overline{U}_\varepsilon^{(l)} = &\left\{ d\boldsymbol{\varepsilon}_o^t + \left(d\boldsymbol{\theta}_m^t \mathbf{A}_m^t + d\boldsymbol{\theta}_w^t \mathbf{A}_w^t \right) - z \left[d\boldsymbol{\varepsilon}_b^t + \left(d\boldsymbol{\theta}_\theta^t \mathbf{A}_m^t + d\boldsymbol{\theta}_m^t \mathbf{A}_\theta^t \right) \right] \right. \\ &+ f_\psi \left[d\boldsymbol{\varepsilon}_\psi^t + \left(d\boldsymbol{\theta}_\psi^t \mathbf{A}_m^t + d\boldsymbol{\theta}_m^t \mathbf{A}_\psi^t \right) \right] - z f_\psi \left(d\boldsymbol{\theta}_\theta^t \mathbf{A}_\psi^t + d\boldsymbol{\theta}_\psi^t \mathbf{A}_\theta^t \right) \\ &\left. + z^2 \left(d\boldsymbol{\theta}_\theta^t \mathbf{A}_\theta^t \right) + f_\psi^2 \left(d\boldsymbol{\theta}_\psi^t \mathbf{A}_\psi^t \right) \right\} \boldsymbol{\sigma}^{(l)} \end{aligned} \tag{5.70}$$

The variation of strain energy per unit area of the plate surface is defined as follows:

$$dU' = \int_{-h/2}^{h/2} (d\overline{U}^{(l)}) dz \tag{5.71}$$

and the variation of the strain energy of the plate is given by:

$$dU = \iint_{x-y\,\text{surface}} (dU') dx\,dy \tag{5.72}$$

<u>Integrated stress matrices</u>

These are used in the expressions of dU' and the integrated transverse shear stress is defined as follows:

$$\tilde{\boldsymbol{\tau}} = \int_{-h/2}^{h/2} f_\gamma(z) \boldsymbol{\tau}^{(l)} dz \equiv \int_{-h/2}^{h/2} f_\gamma^2(z) \boldsymbol{\mu}^{(l)} \hat{\boldsymbol{\gamma}} dz \tag{5.73}$$

Defining

$$\boldsymbol{\mu}_{\gamma\gamma} = \int_{-h/2}^{h/2} f_\gamma^2(z) \boldsymbol{\mu}^{(l)} dz \tag{5.74}$$

then Equation (5.73) can be rewritten as follows:

$$\tilde{\boldsymbol{\tau}} = \boldsymbol{\mu}_{\gamma\gamma}\,\hat{\boldsymbol{\gamma}} \tag{5.75}$$

Notice also that for transversely isotropic composites:

$$\mu_{xz} = \mu_{yz} \equiv \mu \tag{5.76}$$

then

$$\boldsymbol{\mu}^{(l)} = \mu \begin{bmatrix} 1 & 0 \\ 0 & 1 \end{bmatrix} \tag{5.77}$$

which is the same for every layer. Hence, Equation (5.74) is reduced to:

$$\boldsymbol{\mu}_{\gamma\gamma} = \int_{-h/2}^{h/2} f_\gamma^2(z)\,dz\,\boldsymbol{\mu}^{(l)} = \frac{6\mu h}{5} \begin{bmatrix} 1 & 0 \\ 0 & 1 \end{bmatrix} \tag{5.78}$$

For *x-y* stress components, we define the following integrated stress vectors:

$$\begin{aligned} \boldsymbol{\sigma}_n &= (-1)^n \int_{-h/2}^{h/2} z^n\,\boldsymbol{\sigma}^{(l)}\,dz \\ &\equiv \left\{ \sigma_x^{(n)} \quad \sigma_y^{(n)} \quad \tau_{xy}^{(n)} \right\} \end{aligned} \tag{5.79}$$

$$\begin{aligned} \boldsymbol{\sigma}_{\psi n} &= (-1)^n \int_{-h/2}^{h/2} z^n\,f_\psi(z)\,\boldsymbol{\sigma}^{(l)}\,dz \\ &\equiv \left\{ \sigma_x^{(\psi n)} \quad \sigma_y^{(\psi n)} \quad \tau_{xy}^{(\psi n)} \right\} \end{aligned} \tag{5.80}$$

$$\begin{aligned} \boldsymbol{\sigma}_{\psi\psi} &= \int_{-h/2}^{h/2} f_\psi^2(z)\,\boldsymbol{\sigma}^{(l)}\,dz \\ &\equiv \left\{ \sigma_x^{(\psi\psi)} \quad \sigma_y^{(\psi\psi)} \quad \tau_{xy}^{(\psi\psi)} \right\} \end{aligned} \tag{5.81}$$

Substitute Equation (5.65b) in the previous definitions to obtain explicit expressions for the integrated stress vectors. It can be seen that the parts of the integrated terms that depend on *z* will lead to the following integrated **D** matrices:

$$\mathbf{D}_n = \int_{-h/2}^{h/2} z^n\,\mathbf{D}^{(l)}\,dz \tag{5.82}$$

$$\mathbf{D}_{\psi n} = \int_{-h/2}^{h/2} z^n\,f_\psi(z)\,\mathbf{D}^{(l)}\,dz \tag{5.83}$$

$$\mathbf{D}_{\psi\psi n} = \int_{-h/2}^{h/2} z^n\,f_\psi^2(z)\,\mathbf{D}^{(l)}\,dz \tag{5.84}$$

$$\mathbf{D}_{\psi\psi\psi n} = \int_{-h/2}^{h/2} z^n\,f_\psi^3(z)\,\mathbf{D}^{(l)}\,dz \tag{5.85}$$

$$\mathbf{D}_{\psi\psi\psi\psi} = \int\limits_{-h/2}^{h/2} f_\psi^4(z)\mathbf{D}^{(l)}\,dz \tag{5.86}$$

with

$$\mathbf{D}_{\psi\psi} \equiv \mathbf{D}_{\psi\psi 0}, \quad \mathbf{D}_{\psi\psi\psi} \equiv \mathbf{D}_{\psi\psi\psi 0} \tag{5.87}$$

Explicit forms of integrated $\mathbf{D}$ matrices are given in Appendix B.

Hence, Equations (5.79)-(5.81) can be expressed as follows:

$$\begin{aligned}
\boldsymbol{\sigma}_n = (-1)^n \Big\{ &\mathbf{D}_n\left[\boldsymbol{\varepsilon}_o + \tfrac{1}{2}\left(\mathbf{A}_m\boldsymbol{\theta}_m + \mathbf{A}_w\boldsymbol{\theta}_w\right)\right] - \mathbf{D}_{n+1}\left[\boldsymbol{\varepsilon}_b + \tfrac{1}{2}\left(\mathbf{A}_m\boldsymbol{\theta}_\theta + \mathbf{A}_\theta\boldsymbol{\theta}_m\right)\right] \\
&+ \mathbf{D}_{\psi n}\left[\boldsymbol{\varepsilon}_\psi + \tfrac{1}{2}\left(\mathbf{A}_m\boldsymbol{\theta}_\psi + \mathbf{A}_\psi\boldsymbol{\theta}_m\right)\right] - \tfrac{1}{2}\mathbf{D}_{\psi(n+1)}\left(\mathbf{A}_\psi\boldsymbol{\theta}_\theta + \mathbf{A}_\theta\boldsymbol{\theta}_\psi\right) \\
&+ \tfrac{1}{2}\mathbf{D}_{n+2}\left(\mathbf{A}_\theta\boldsymbol{\theta}_\theta\right) + \tfrac{1}{2}\mathbf{D}_{\psi\psi n}\left(\mathbf{A}_\psi\boldsymbol{\theta}_\psi\right) \Big\}
\end{aligned} \tag{5.88}$$

$$\begin{aligned}
\boldsymbol{\sigma}_{\psi n} = (-1)^n \Big\{ &\mathbf{D}_{\psi n}\left[\boldsymbol{\varepsilon}_o + \tfrac{1}{2}\left(\mathbf{A}_m\boldsymbol{\theta}_m + \mathbf{A}_w\boldsymbol{\theta}_w\right)\right] - \mathbf{D}_{\psi(n+1)}\left[\boldsymbol{\varepsilon}_b + \tfrac{1}{2}\left(\mathbf{A}_m\boldsymbol{\theta}_\theta + \mathbf{A}_\theta\boldsymbol{\theta}_m\right)\right] \\
&+ \mathbf{D}_{\psi\psi n}\left[\boldsymbol{\varepsilon}_\psi + \tfrac{1}{2}\left(\mathbf{A}_m\boldsymbol{\theta}_\psi + \mathbf{A}_\psi\boldsymbol{\theta}_m\right)\right] - \tfrac{1}{2}\mathbf{D}_{\psi\psi(n+1)}\left(\mathbf{A}_\psi\boldsymbol{\theta}_\theta + \mathbf{A}_\theta\boldsymbol{\theta}_\psi\right) \\
&+ \tfrac{1}{2}\mathbf{D}_{\psi(n+2)}\left(\mathbf{A}_\theta\boldsymbol{\theta}_\theta\right) + \tfrac{1}{2}\mathbf{D}_{\psi\psi\psi n}\left(\mathbf{A}_\psi\boldsymbol{\theta}_\psi\right) \Big\}
\end{aligned} \tag{5.89}$$

$$\begin{aligned}
\boldsymbol{\sigma}_{\psi\psi} = \Big\{ &\mathbf{D}_{\psi\psi}\left[\boldsymbol{\varepsilon}_o + \tfrac{1}{2}\left(\mathbf{A}_m\boldsymbol{\theta}_m + \mathbf{A}_w\boldsymbol{\theta}_w\right)\right] - \mathbf{D}_{\psi\psi 1}\left[\boldsymbol{\varepsilon}_b + \tfrac{1}{2}\left(\mathbf{A}_m\boldsymbol{\theta}_\theta + \mathbf{A}_\theta\boldsymbol{\theta}_m\right)\right] \\
&+ \mathbf{D}_{\psi\psi\psi}\left[\boldsymbol{\varepsilon}_\psi + \tfrac{1}{2}\left(\mathbf{A}_m\boldsymbol{\theta}_\psi + \mathbf{A}_\psi\boldsymbol{\theta}_m\right)\right] - \tfrac{1}{2}\mathbf{D}_{\psi\psi\psi 1}\left(\mathbf{A}_\psi\boldsymbol{\theta}_\theta + \mathbf{A}_\theta\boldsymbol{\theta}_\psi\right) \\
&+ \tfrac{1}{2}\mathbf{D}_{\psi\psi 2}\left(\mathbf{A}_\theta\boldsymbol{\theta}_\theta\right) + \tfrac{1}{2}\mathbf{D}_{\psi\psi\psi\psi}\left(\mathbf{A}_\psi\boldsymbol{\theta}_\psi\right) \Big\}
\end{aligned} \tag{5.90}$$

Variation of strain energy due to transverse shear components

The variation of strain energy density due to transverse shear components is given by Equation (5.68), and from which it can be deduced that:

$$dU_\gamma' = \int\limits_{-h/2}^{h/2}\left[d\overline{U}_\gamma^{(l)}\right]dz \equiv d\hat{\boldsymbol{\gamma}}^t\,\tilde{\boldsymbol{\tau}} \tag{5.91a}$$

with

$$dU_\gamma = \iint\limits_{x-y} dU_\gamma'\,dx\,dy \tag{5.91b}$$

Variation of strain energy due to *x-y* components

The variation of strain energy density due to *x-y* stress and strain components is given by Equation (5.70), and from which it can be deduced that:

66

$$dU'_\varepsilon = \int_{-h/2}^{h/2} d\overline{U}_\varepsilon^{(l)} \, dz \equiv \left[d\boldsymbol{\varepsilon}_o^t + \left(d\boldsymbol{\theta}_m^t \mathbf{A}_m^t + d\boldsymbol{\theta}_w^t \mathbf{A}_w^t \right) \right] \boldsymbol{\sigma}_0$$

$$+ \left[d\boldsymbol{\varepsilon}_b^t + \left(d\boldsymbol{\theta}_\theta^t \mathbf{A}_m^t + d\boldsymbol{\theta}_m^t \mathbf{A}_\theta^t \right) \right] \boldsymbol{\sigma}_1 \qquad (5.92a)$$

$$+ \left[d\boldsymbol{\varepsilon}_\psi^t + \left(d\boldsymbol{\theta}_\psi^t \mathbf{A}_m^t + d\boldsymbol{\theta}_m^t \mathbf{A}_\psi^t \right) \right] \boldsymbol{\sigma}_{\psi 0} + \left(d\boldsymbol{\theta}_\theta^t \mathbf{A}_\psi^t + d\boldsymbol{\theta}_\psi^t \mathbf{A}_\theta^t \right) \boldsymbol{\sigma}_{\psi 1}$$

$$+ \left(d\boldsymbol{\theta}_\theta^t \mathbf{A}_\theta^t \right) \boldsymbol{\sigma}_2 + \left(d\boldsymbol{\theta}_\psi^t \mathbf{A}_\psi^t \right) \boldsymbol{\sigma}_{\psi\psi}$$

with

$$dU_\varepsilon = \iint_{x-y} dU'_\varepsilon \, dx \, dy \qquad (5.92b)$$

5.2 Interpolated Equations of Displacement and Strain

Degrees of Freedom for a Plate Element

Based on displacement distributions given by Equations (5.21)-(5.23), the degrees of freedom for a plate element with respect to its local axes, at its midplane, are as follows:

u^o, v^o the in-plane displacement components,

$w, \dfrac{\partial w}{\partial x}, \dfrac{\partial w}{\partial y}$ the bending components for non-conformining elements, and

$w, \dfrac{\partial w}{\partial x}, \dfrac{\partial w}{\partial y}, \dfrac{\partial^2 w}{\partial x \partial y}$ the bending components for conforming elements,

ψ_x, ψ_y the transverse shear strain components.

For an *n*-node element the nodal displacement vector is defined as follows:

$$\boldsymbol{\delta} = \begin{bmatrix} \boldsymbol{\delta}_o \\ \boldsymbol{\delta}_b \\ \boldsymbol{\delta}_\psi \end{bmatrix} \tag{5.93}$$

where

$$\boldsymbol{\delta}_o = \left\{ u_1^o \quad v_1^o \quad u_2^o \quad v_2^o \quad \cdots \quad u_n^o \quad v_n^o \right\} \tag{5.94}$$

$$\boldsymbol{\delta}_b = \left\{ w_1 \quad w_{1,x} \quad w_{1,y} \quad \cdots \quad w_n \quad w_{n,x} \quad w_{n,y} \right\}$$
for non-conforming elements   (5.95a)

$$\boldsymbol{\delta}_b = \left\{ w_1 \quad w_{1,x} \quad w_{1,y} \quad w_{1,xy} \quad \cdots \quad w_n \quad w_{n,x} \quad w_{n,y} \quad w_{n,xy} \right\}$$
for conforming elements   (5.95b)

$$\boldsymbol{\delta}_\psi = \left\{ (\psi_x)_1 \quad (\psi_y)_1 \quad (\psi_x)_2 \quad (\psi_y)_2 \quad \cdots \quad (\psi_x)_n \quad (\psi_y)_n \right\} \tag{5.96}$$

with

$$w_{i,x} \equiv \left. \frac{\partial w}{\partial x} \right|_{at\,(x_i, y_i)} , \quad w_{i,y} \equiv \left. \frac{\partial w}{\partial y} \right|_{at\,(x_i, y_i)} , \quad w_{i,xy} \equiv \left. \frac{\partial^2 w}{\partial x \partial y} \right|_{at\,(x_i, y_i)}$$

Interpolation of Displacement

The displacement components at the midplane of an *n*-node element are interpolated as follows:

$$u^o(x, y) = \sum_{i=1}^{n} N_i(x, y)\, u_i^o \tag{5.97}$$

$$v^o(x, y) = \sum_{i=1}^{n} N_i(x, y)\, v_i^o \tag{5.98}$$

$$\psi_x(x, y) = \sum_{i=1}^{n} N_i(x, y)\, (\psi_x)_i \tag{5.99}$$

$$\psi_y(x, y) = \sum_{i=1}^{n} N_i(x, y)\, (\psi_y)_i \tag{5.100}$$

where N_i represents Lagrangian shape functions.

There are two types of interpolation for the lateral deflection w as described in a publication by El-Zafrany and Cookson (1986a, b):

(a) Non-conforming elements

$$w(x, y) = \sum_{i=1}^{n} \left[F_i(x, y)\, w_i + G_i(x, y)\, w_{i,x} + H_i(x, y)\, w_{i,y} \right] \tag{5.101}$$

(b) Conforming elements

$$w(x, y) = \sum_{i=1}^{n} \left[F_i(x, y)\, w_i + G_i(x, y)\, w_{i,x} + H_i(x, y)\, w_{i,y} + P_i(x, y)\, w_{i,xy} \right] \tag{5.102}$$

where F_i, G_i, H_i, P_i represent Hermitian shape functions.

Interpolation of Strain

Interpolation of transverse shear strain

Substituting from Equations (5.99) and (5.100) into (5.16b), then it can be deduced that:

$$\hat{\boldsymbol{\gamma}}(x,y) = \begin{bmatrix} -\psi_y \\ \psi_x \end{bmatrix} \equiv \mathbf{B}_\gamma(x,y)\,\boldsymbol{\delta}_\psi \qquad (5.103)$$

where

$$\mathbf{B}_\gamma(x,y) = \begin{bmatrix} \cdots & 0 & -N_i(x,y) & \cdots \\ \cdots & N_i(x,y) & 0 & \cdots \end{bmatrix} \qquad (5.104)$$

Infinitesimal strain parts

Substituting from Equations (5.97) and (5.98) into (5.33), then it can be shown that:

$$\boldsymbol{\varepsilon}_o(x,y) = \begin{bmatrix} \dfrac{\partial u^o}{\partial x} \\[2ex] \dfrac{\partial v^o}{\partial y} \\[2ex] \dfrac{\partial u^o}{\partial y} + \dfrac{\partial v^o}{\partial x} \end{bmatrix} \equiv \mathbf{B}_o(x,y)\,\boldsymbol{\delta}_o \qquad (5.105)$$

where

$$\mathbf{B}_o(x,y) = \begin{bmatrix} \cdots & \dfrac{\partial N_i}{\partial x} & 0 & \cdots \\[2ex] \cdots & 0 & \dfrac{\partial N_i}{\partial y} & \cdots \\[2ex] \cdots & \dfrac{\partial N_i}{\partial y} & \dfrac{\partial N_i}{\partial x} & \cdots \end{bmatrix} \qquad (5.106)$$

Similarly, substituting from Equations (5.99) and (5.100) into (5.35), then it can be deduced that:

$$\boldsymbol{\varepsilon}_\psi(x,y) = \begin{bmatrix} -\dfrac{\partial \psi_y}{\partial x} \\[3mm] \dfrac{\partial \psi_x}{\partial y} \\[3mm] \dfrac{\partial \psi_x}{\partial x} - \dfrac{\partial \psi_y}{\partial y} \end{bmatrix} \equiv \mathbf{B}_\psi(x,y)\,\boldsymbol{\delta}_\psi \tag{5.107}$$

where

$$\mathbf{B}_\psi(x,y) = \begin{bmatrix} \cdots & 0 & -\dfrac{\partial N_i}{\partial x} & \cdots \\[3mm] \cdots & \dfrac{\partial N_i}{\partial y} & 0 & \cdots \\[3mm] \cdots & \dfrac{\partial N_i}{\partial x} & -\dfrac{\partial N_i}{\partial y} & \cdots \end{bmatrix} \tag{5.108}$$

Substituting from Equation (5.101) or (5.102) into (5.34), then it can be proved that:

$$\boldsymbol{\varepsilon}_b(x,y) = \begin{bmatrix} \dfrac{\partial^2 w}{\partial x^2} \\[3mm] \dfrac{\partial^2 w}{\partial y^2} \\[3mm] 2\dfrac{\partial^2 w}{\partial x\,\partial y} \end{bmatrix} \equiv \mathbf{B}_b(x,y)\,\boldsymbol{\delta}_b \tag{5.109}$$

where for non-conforming elements:

$$\mathbf{B}_b(x,y) = \begin{bmatrix} \cdots & \dfrac{\partial^2 F_i}{\partial x^2} & \dfrac{\partial^2 G_i}{\partial x^2} & \dfrac{\partial^2 H_i}{\partial x^2} & \cdots \\[3mm] \cdots & \dfrac{\partial^2 F_i}{\partial y^2} & \dfrac{\partial^2 G_i}{\partial y^2} & \dfrac{\partial^2 H_i}{\partial y^2} & \cdots \\[3mm] \cdots & 2\dfrac{\partial^2 F_i}{\partial x\,\partial y} & 2\dfrac{\partial^2 G_i}{\partial x\,\partial y} & 2\dfrac{\partial^2 H_i}{\partial x\,\partial y} & \cdots \end{bmatrix} \tag{5.110a}$$

and for conforming elements:

$$\mathbf{B}_b(x,y) = \begin{bmatrix} \cdots & \dfrac{\partial^2 F_i}{\partial x^2} & \dfrac{\partial^2 G_i}{\partial x^2} & \dfrac{\partial^2 H_i}{\partial x^2} & \dfrac{\partial^2 P_i}{\partial x^2} & \cdots \\[2ex] \cdots & \dfrac{\partial^2 F_i}{\partial y^2} & \dfrac{\partial^2 G_i}{\partial y^2} & \dfrac{\partial^2 H_i}{\partial y^2} & \dfrac{\partial^2 P_i}{\partial y^2} & \cdots \\[2ex] \cdots & 2\dfrac{\partial^2 F_i}{\partial x \partial y} & 2\dfrac{\partial^2 G_i}{\partial x \partial y} & 2\dfrac{\partial^2 H_i}{\partial x \partial y} & 2\dfrac{\partial^2 P_i}{\partial x \partial y} & \cdots \end{bmatrix} \qquad (5.111b)$$

Substituting from Equations (5.105), (5.107), (5.109) into (5.32) then it can be deduced that:

$$\boldsymbol{\varepsilon}_S(x,y,z) = \mathbf{B}_o(x,y)\boldsymbol{\delta}_o - z\mathbf{B}_b(x,y)\boldsymbol{\delta}_b + f_\psi(z)\mathbf{B}_\psi(x,y)\boldsymbol{\delta}_\psi \qquad (5.112)$$

Interpolation of rotation vector

Substituting from Equations (5.97) and (5.98) into (5.44), then it can be shown that:

$$\boldsymbol{\theta}_m(x,y) = \begin{bmatrix} \dfrac{\partial u^o}{\partial x} \\[2ex] \dfrac{\partial v^o}{\partial x} \\[2ex] \dfrac{\partial u^o}{\partial y} \\[2ex] \dfrac{\partial v^o}{\partial y} \end{bmatrix} \equiv \mathbf{G}_m(x,y)\,\boldsymbol{\delta}_o \qquad (5.113)$$

where
$$\mathbf{G}_m(x,y) = \begin{bmatrix} \cdots & \dfrac{\partial N_i}{\partial x} & 0 & \cdots \\[2ex] \cdots & 0 & \dfrac{\partial N_i}{\partial x} & \cdots \\[2ex] \cdots & \dfrac{\partial N_i}{\partial y} & 0 & \cdots \\[2ex] \cdots & 0 & \dfrac{\partial N_i}{\partial y} & \cdots \end{bmatrix} \qquad (5.114)$$

Similarly by substituting from Equations (5.99) and (5.100) into (5.47), it can be deduced that:

$$\boldsymbol{\theta}_\psi(x,y) = \begin{bmatrix} -\dfrac{\partial \psi_y}{\partial x} \\[2ex] \dfrac{\partial \psi_x}{\partial x} \\[2ex] -\dfrac{\partial \psi_y}{\partial y} \\[2ex] \dfrac{\partial \psi_x}{\partial y} \end{bmatrix} \equiv \mathbf{G}_\psi(x,y)\,\boldsymbol{\delta}_\psi \qquad (5.115)$$

where
$$\mathbf{G}_\psi(x,y) = \begin{bmatrix} \cdots & 0 & -\dfrac{\partial N_i}{\partial x} & \cdots \\[2ex] \cdots & \dfrac{\partial N_i}{\partial x} & 0 & \cdots \\[2ex] \cdots & 0 & -\dfrac{\partial N_i}{\partial y} & \cdots \\[2ex] \cdots & \dfrac{\partial N_i}{\partial y} & 0 & \end{bmatrix} \qquad (5.116)$$

Substituting from Equation (5.101) or (5.102) into Equations (5.45) and (5.44), then it can be proved that:

$$\boldsymbol{\theta}_w(x,y) = \begin{bmatrix} \dfrac{\partial w}{\partial x} \\[2ex] \dfrac{\partial w}{\partial y} \end{bmatrix} \equiv \mathbf{G}_w(x,y)\,\boldsymbol{\delta}_b \qquad (5.117)$$

$$\boldsymbol{\theta}_\theta(x,y) = \begin{bmatrix} \dfrac{\partial^2 w}{\partial x^2} \\[2ex] \dfrac{\partial^2 w}{\partial x\,\partial y} \\[2ex] \dfrac{\partial^2 w}{\partial y\,\partial x} \\[2ex] \dfrac{\partial^2 w}{\partial y^2} \end{bmatrix} \equiv \mathbf{G}_\theta(x,y)\,\boldsymbol{\delta}_b \qquad (5.118)$$

where for non-conforming elements:

$$\mathbf{G}_w(x, y) = \begin{bmatrix} \cdots & \dfrac{\partial F_i}{\partial x} & \dfrac{\partial G_i}{\partial x} & \dfrac{\partial H_i}{\partial x} & \cdots \\[2ex] \cdots & \dfrac{\partial F_i}{\partial y} & \dfrac{\partial G_i}{\partial y} & \dfrac{\partial H_i}{\partial y} & \cdots \end{bmatrix} \tag{5.119}$$

$$\mathbf{G}_\theta(x, y) = \begin{bmatrix} \cdots & \dfrac{\partial^2 F_i}{\partial x^2} & \dfrac{\partial^2 G_i}{\partial x^2} & \dfrac{\partial^2 H_i}{\partial x^2} & \cdots \\[2ex] \cdots & \dfrac{\partial^2 F_i}{\partial x \partial y} & \dfrac{\partial^2 G_i}{\partial x \partial y} & \dfrac{\partial^2 H_i}{\partial x \partial y} & \cdots \\[2ex] \cdots & \dfrac{\partial^2 F_i}{\partial x \partial y} & \dfrac{\partial^2 G_i}{\partial x \partial y} & \dfrac{\partial^2 H_i}{\partial x \partial y} & \cdots \\[2ex] \cdots & \dfrac{\partial^2 F_i}{\partial y^2} & \dfrac{\partial^2 G_i}{\partial y^2} & \dfrac{\partial^2 H_i}{\partial y^2} & \cdots \end{bmatrix} \tag{5.120}$$

and for conforming elements:

$$\mathbf{G}_w(x, y) = \begin{bmatrix} \cdots & \dfrac{\partial F_i}{\partial x} & \dfrac{\partial G_i}{\partial x} & \dfrac{\partial H_i}{\partial x} & \dfrac{\partial P_i}{\partial x} & \cdots \\[2ex] \cdots & \dfrac{\partial F_i}{\partial y} & \dfrac{\partial G_i}{\partial y} & \dfrac{\partial H_i}{\partial y} & \dfrac{\partial P_i}{\partial y} & \cdots \end{bmatrix} \tag{5.121}$$

$$\mathbf{G}_\theta(x, y) = \begin{bmatrix} \cdots & \dfrac{\partial^2 F_i}{\partial x^2} & \dfrac{\partial^2 G_i}{\partial x^2} & \dfrac{\partial^2 H_i}{\partial x^2} & \dfrac{\partial^2 P_i}{\partial x^2} & \cdots \\[2ex] \cdots & \dfrac{\partial^2 F_i}{\partial x \partial y} & \dfrac{\partial^2 G_i}{\partial x \partial y} & \dfrac{\partial^2 H_i}{\partial x \partial y} & \dfrac{\partial^2 P_i}{\partial x \partial y} & \cdots \\[2ex] \cdots & \dfrac{\partial^2 F_i}{\partial x \partial y} & \dfrac{\partial^2 G_i}{\partial x \partial y} & \dfrac{\partial^2 H_i}{\partial x \partial y} & \dfrac{\partial^2 P_i}{\partial x \partial y} & \cdots \\[2ex] \cdots & \dfrac{\partial^2 F_i}{\partial y^2} & \dfrac{\partial^2 G_i}{\partial y^2} & \dfrac{\partial^2 H_i}{\partial y^2} & \dfrac{\partial^2 P_i}{\partial y^2} & \cdots \end{bmatrix}$$

$$\tag{5.122}$$

Total strain vector and its variation

Using equations from sections 2.3.2 and 2.3.3 then the total x-y strain vector, as defined by Equation (5.60), can be expresses as follows:

$$
\begin{aligned}
\boldsymbol{\varepsilon}(x,y,z) = & \left[\mathbf{B}_o(x,y)\boldsymbol{\delta}_o + \tfrac{1}{2}\mathbf{A}_m(x,y)\mathbf{G}_m(x,y)\boldsymbol{\delta}_o + \tfrac{1}{2}\mathbf{A}_w(x,y)\mathbf{G}_w(x,y)\boldsymbol{\delta}_b \right] \\
& - z\left[\mathbf{B}_b(x,y)\boldsymbol{\delta}_b + \tfrac{1}{2}\mathbf{A}_m(x,y)\mathbf{G}_\theta(x,y)\boldsymbol{\delta}_b + \tfrac{1}{2}\mathbf{A}_\theta(x,y)\mathbf{G}_m(x,y)\boldsymbol{\delta}_o \right] \\
& + f_\psi(z)\left[\mathbf{B}_\psi(x,y)\boldsymbol{\delta}_\psi + \tfrac{1}{2}\mathbf{A}_m(x,y)\mathbf{G}_\psi(x,y)\boldsymbol{\delta}_\psi + \tfrac{1}{2}\mathbf{A}_\psi(x,y)\mathbf{G}_m(x,y)\boldsymbol{\delta}_o \right] \\
& - z\,f_\psi(z)\left[\tfrac{1}{2}\mathbf{A}_\psi(x,y)\mathbf{G}_\theta(x,y)\boldsymbol{\delta}_b + \tfrac{1}{2}\mathbf{A}_\theta(x,y)\mathbf{G}_\psi(x,y)\boldsymbol{\delta}_\psi \right] \\
& + \tfrac{1}{2}z^2\,\mathbf{A}_\theta(x,y)\mathbf{G}_\theta(x,y)\boldsymbol{\delta}_b + \tfrac{1}{2}f_\psi^2(z)\mathbf{A}_\psi(x,y)\mathbf{G}_\psi(x,y)\boldsymbol{\delta}_\psi
\end{aligned}
$$

(5.123)

Hence, the variation of the x-y strain vector can be expressed as follows:

$$
\begin{aligned}
d\boldsymbol{\varepsilon}(x,y,z) = & \left[\mathbf{B}_o(x,y)d\boldsymbol{\delta}_o + \mathbf{A}_m(x,y)\mathbf{G}_m(x,y)d\boldsymbol{\delta}_o + \mathbf{A}_w(x,y)\mathbf{G}_w(x,y)d\boldsymbol{\delta}_b \right] \\
& - z\left[\mathbf{B}_b(x,y)d\boldsymbol{\delta}_b + \mathbf{A}_m(x,y)\mathbf{G}_\theta(x,y)d\boldsymbol{\delta}_b + \mathbf{A}_\theta(x,y)\mathbf{G}_m(x,y)d\boldsymbol{\delta}_o \right] \\
& + f_\psi(z)\left[\mathbf{B}_\psi(x,y)d\boldsymbol{\delta}_\psi + \mathbf{A}_m(x,y)\mathbf{G}_\psi(x,y)d\boldsymbol{\delta}_\psi + \mathbf{A}_\psi(x,y)\mathbf{G}_m(x,y)d\boldsymbol{\delta}_o \right] \\
& - z\,f_\psi(z)\left[\mathbf{A}_\psi(x,y)\mathbf{G}_\theta(x,y)d\boldsymbol{\delta}_b + \mathbf{A}_\theta(x,y)\mathbf{G}_\psi(x,y)d\boldsymbol{\delta}_\psi \right] \\
& + z^2\,\mathbf{A}_\theta(x,y)\mathbf{G}_\theta(x,y)d\boldsymbol{\delta}_b + f_\psi^2(z)\mathbf{A}_\psi(x,y)\mathbf{G}_\psi(x,y)d\boldsymbol{\delta}_\psi
\end{aligned}
$$

(5.124)

5.3 Derivation of FE Equations for Reissner-type Element

Strain Energy and Work Variations

The variation of strain energy density at any point in the *l*th layer of a composite plate is given by Equation (5.67). Substituting from Equations (5.103) and (5.123) into (5.67) then:

$$
\begin{aligned}
d\overline{U}^{(l)}(x,y,z) &= \left[d\boldsymbol{\delta}_o^t \left(\mathbf{B}_o^t + \mathbf{G}_m^t \mathbf{A}_m^t \right) + d\boldsymbol{\delta}_b^t \, \mathbf{G}_w^t \mathbf{A}_w^t \right] \left(\boldsymbol{\sigma}^{(l)} \right) \\
&\quad + \left[d\boldsymbol{\delta}_o^t \, \mathbf{G}_m^t \mathbf{A}_\theta^t + d\boldsymbol{\delta}_b^t \left(\mathbf{B}_b^t + \mathbf{G}_\theta^t \mathbf{A}_m^t \right) \right] \left(- z \, \boldsymbol{\sigma}^{(l)} \right) \\
&\quad + \left[d\boldsymbol{\delta}_o^t \, \mathbf{G}_m^t \mathbf{A}_\psi^t + d\boldsymbol{\delta}_\psi^t \left(\mathbf{B}_\psi^t + \mathbf{G}_\psi^t \mathbf{A}_m^t \right) \right] \left(f_\psi(z) \boldsymbol{\sigma}^{(l)} \right) \\
&\quad + \left[d\boldsymbol{\delta}_b^t \, \mathbf{G}_\theta^t \mathbf{A}_\psi^t + d\boldsymbol{\delta}_\psi^t \, \mathbf{G}_\psi^t \mathbf{A}_\theta^t \right] \left(- z \, f_\psi(z) \boldsymbol{\sigma}^{(l)} \right) \\
&\quad + \left[d\boldsymbol{\delta}_b^t \, \mathbf{G}_\theta^t \mathbf{A}_\theta^t \right] \left(z^2 \, \boldsymbol{\sigma}^{(l)} \right) + \left[d\boldsymbol{\delta}_\psi^t \, \mathbf{G}_\psi^t \mathbf{A}_\psi^t \right] \left(f_\psi^2(z) \, \boldsymbol{\sigma}^{(l)} \right) \\
&\quad + \left[d\boldsymbol{\delta}_\psi^t \, \mathbf{B}_\gamma^t \right] \left(f_\gamma(z) \, \boldsymbol{\tau}^{(l)} \right)
\end{aligned}
\tag{5.125}
$$

The equivalent nodal loading is assumed to have the same variation as the work done by actual loads. Hence, the variation of the work done by actual loads can be expressed as follows:

$$
dW = d\boldsymbol{\delta}^t \, \mathbf{F} \equiv d\boldsymbol{\delta}_o^t \, \mathbf{F}_o + d\boldsymbol{\delta}_b^t \, \mathbf{F}_b + d\boldsymbol{\delta}_\psi^t \, \mathbf{F}_\psi
\tag{5.126}
$$

where $\mathbf{F}$ represents the equivalent nodal loading vector.

Derivation of Generalized Equations of Equilibrium

From the principle of virtual work due to a variation of displacement:

$$
d\chi = dU - dW = 0
\tag{5.127}
$$

Substituting from Equations (5.125) and (5.126) into (5.127), it can be deduced that:

$$
\begin{aligned}
\sum_{e=1}^{N_e} \int_{-h/2}^{h/2} \iint_e &\left\{ \left[d\boldsymbol{\delta}_o^t \left(\mathbf{B}_o^t + \mathbf{G}_m^t \mathbf{A}_m^t \right) + d\boldsymbol{\delta}_b^t \, \mathbf{G}_w^t \mathbf{A}_w^t \right] \left(\boldsymbol{\sigma}^{(l)} \right) \right. \\
&\quad + \left[d\boldsymbol{\delta}_o^t \, \mathbf{G}_m^t \mathbf{A}_\theta^t + d\boldsymbol{\delta}_b^t \left(\mathbf{B}_b^t + \mathbf{G}_\theta^t \mathbf{A}_m^t \right) \right] \left(- z \, \boldsymbol{\sigma}^{(l)} \right) \\
&\quad + \left[d\boldsymbol{\delta}_o^t \, \mathbf{G}_m^t \mathbf{A}_\psi^t + d\boldsymbol{\delta}_\psi^t \left(\mathbf{B}_\psi^t + \mathbf{G}_\psi^t \mathbf{A}_m^t \right) \right] \left(f_\psi(z) \boldsymbol{\sigma}^{(l)} \right) \\
&\quad + \left[d\boldsymbol{\delta}_b^t \, \mathbf{G}_\theta^t \mathbf{A}_\psi^t + d\boldsymbol{\delta}_\psi^t \, \mathbf{G}_\psi^t \mathbf{A}_\theta^t \right] \left(- z \, f_\psi(z) \boldsymbol{\sigma}^{(l)} \right) \\
&\quad + \left[d\boldsymbol{\delta}_b^t \, \mathbf{G}_\theta^t \mathbf{A}_\theta^t \right] \left(z^2 \, \boldsymbol{\sigma}^{(l)} \right) + \left[d\boldsymbol{\delta}_\psi^t \, \mathbf{G}_\psi^t \mathbf{A}_\psi^t \right] \left(f_\psi^2(z) \, \boldsymbol{\sigma}^{(l)} \right) \\
&\quad \left. + \left[d\boldsymbol{\delta}_\psi^t \, \mathbf{B}_\gamma^t \right] \left(f_\gamma(z) \, \boldsymbol{\tau}^{(l)} \right) \right\} dx\, dy\, dz - d\boldsymbol{\delta}_o^t \, \mathbf{F}_o - d\boldsymbol{\delta}_b^t \, \mathbf{F}_b - d\boldsymbol{\delta}_\psi^t \, \mathbf{F}_\psi = 0
\end{aligned}
\tag{5.128}
$$

The variations represent small arbitrary changes; hence the coefficients of displacement variations in Equation (5.128) vanish, leading to:

$$\sum_{e=1}^{N_e} \int_{-h/2}^{h/2} \iint_e \left\{ \left(\mathbf{B}_o^t + \mathbf{G}_m^t \mathbf{A}_m^t \right) \boldsymbol{\sigma}^{(l)} + \mathbf{G}_m^t \mathbf{A}_\theta^t \left(-z \boldsymbol{\sigma}^{(l)} \right) \right.$$
$$\left. + \mathbf{G}_m^t \mathbf{A}_\psi^t \left(f_\psi (z) \, \boldsymbol{\sigma}^{(l)} \right) \right\} dx\,dy\,dz - \mathbf{F}_o = \mathbf{O} \tag{5.129}$$

$$\sum_{e=1}^{N_e} \int_{-h/2}^{h/2} \iint_e \left\{ \mathbf{G}_w^t \mathbf{A}_w^t \boldsymbol{\sigma}^{(l)} + \left(\mathbf{B}_b^t + \mathbf{G}_\theta^t \mathbf{A}_m^t \right) \left(-z \boldsymbol{\sigma}^{(l)} \right) \right.$$
$$\left. + \mathbf{G}_\theta^t \mathbf{A}_\psi^t \left(-z\, f_\psi \, \boldsymbol{\sigma}^{(l)} \right) + \mathbf{G}_\theta^t \mathbf{A}_\theta^t \left(z^2 \, \boldsymbol{\sigma}^{(l)} \right) \right\} dx\,dy\,dz - \mathbf{F}_b = \mathbf{O} \tag{5.130}$$

$$\sum_{e=1}^{N_e} \int_{-h/2}^{h/2} \iint_e \left\{ \mathbf{B}_\gamma^t \, f_\gamma(z)\, \boldsymbol{\tau}^{(l)} + \left(\mathbf{B}_\psi^t + \mathbf{G}_\psi^t \mathbf{A}_m^t \right) \left(f_\psi \, \boldsymbol{\sigma}^{(l)} \right) \right.$$
$$\left. + \mathbf{G}_\psi^t \mathbf{A}_\theta^t \left(-z\, f_\psi \, \boldsymbol{\sigma}^{(l)} \right) + \mathbf{G}_\psi^t \mathbf{A}_\psi^t \left(f_\psi^2 \, \boldsymbol{\sigma}^{(l)} \right) \right\} dx\,dy\,dz - \mathbf{F}_\psi = \mathbf{O} \tag{5.131}$$

Equations (5.129)-(5.131) represent the generalized equations of equilibrium.

If an approximate solution is employed then the previous equations will lead to the following residual vectors:

$$\mathbf{R}_o = \mathbf{F}_o - \sum_{e=1}^{N_e} \int_{-h/2}^{h/2} \iint_e \left\{ \left(\mathbf{B}_o^t + \mathbf{G}_m^t \mathbf{A}_m^t \right) \boldsymbol{\sigma}^{(l)} + \mathbf{G}_m^t \mathbf{A}_\theta^t \left(-z \boldsymbol{\sigma}^{(l)} \right) \right.$$
$$\left. + \mathbf{G}_m^t \mathbf{A}_\psi^t \left(f_\psi (z) \, \boldsymbol{\sigma}^{(l)} \right) \right\} dx\,dy\,dz \tag{5.132}$$

$$\mathbf{R}_b = \mathbf{F}_b - \sum_{e=1}^{N_e} \int_{-h/2}^{h/2} \iint_e \left\{ \mathbf{G}_w^t \mathbf{A}_w^t \boldsymbol{\sigma}^{(l)} + \left(\mathbf{B}_b^t + \mathbf{G}_\theta^t \mathbf{A}_m^t \right) \left(-z \boldsymbol{\sigma}^{(l)} \right) \right.$$
$$\left. + \mathbf{G}_\theta^t \mathbf{A}_\psi^t \left(-z\, f_\psi \, \boldsymbol{\sigma}^{(l)} \right) + \mathbf{G}_\theta^t \mathbf{A}_\theta^t \left(z^2 \, \boldsymbol{\sigma}^{(l)} \right) \right\} dx\,dy\,dz \tag{5.133}$$

$$\mathbf{R}_\psi = \mathbf{F}_\psi - \sum_{e=1}^{N_e} \int_{-h/2}^{h/2} \iint_e \left\{ \mathbf{B}_\gamma^t \, f_\gamma(z)\, \boldsymbol{\tau}^{(l)} + \left(\mathbf{B}_\psi^t + \mathbf{G}_\psi^t \mathbf{A}_m^t \right) \left(f_\psi \, \boldsymbol{\sigma}^{(l)} \right) \right.$$
$$\left. + \mathbf{G}_\psi^t \mathbf{A}_\theta^t \left(-z\, f_\psi \, \boldsymbol{\sigma}^{(l)} \right) + \mathbf{G}_\psi^t \mathbf{A}_\psi^t \left(f_\psi^2 \, \boldsymbol{\sigma}^{(l)} \right) \right\} dx\,dy\,dz \tag{5.134}$$

When calculating the residual forces Equations (5.132)-(5.134) are integrated analytically with respect to z, leading to:

$$\mathbf{R}_o = \mathbf{F}_o - \sum_{e=1}^{N_e} \iint_e \left\{ \left(\mathbf{B}_o^t + \mathbf{G}_m^t \mathbf{A}_m^t \right) \boldsymbol{\sigma}_0 + \left(\mathbf{G}_m^t \mathbf{A}_\theta^t \right) \boldsymbol{\sigma}_1 \right.$$
$$\left. + \left(\mathbf{G}_m^t \mathbf{A}_\psi^t \right) \boldsymbol{\sigma}_{\psi 0} \right\} dx\,dy \tag{5.135}$$

$$\mathbf{R}_b = \mathbf{F}_b - \sum_{e=1}^{N_e} \iint_e \left\{ \left(\mathbf{G}_w^t \mathbf{A}_w^t \right) \boldsymbol{\sigma}_0 + \left(\mathbf{B}_b^t + \mathbf{G}_\theta^t \mathbf{A}_m^t \right) \boldsymbol{\sigma}_1 \right.$$
$$\left. + \left(\mathbf{G}_\theta^t \mathbf{A}_\psi^t \right) \boldsymbol{\sigma}_{\psi 1} + \left(\mathbf{G}_\theta^t \mathbf{A}_\theta^t \right) \boldsymbol{\sigma}_2 \right\} dx\,dy \tag{5.136}$$

$$\mathbf{R}_{\psi} = \mathbf{F}_{\psi} - \sum_{e=1}^{N_e} \iint_{e} \left\{ \mathbf{B}_{\gamma}^{t}\, \tilde{\boldsymbol{\tau}} + \left(\mathbf{B}_{\psi}^{t} + \mathbf{G}_{\psi}^{t}\, \mathbf{A}_{m}^{t} \right) \boldsymbol{\sigma}_{\psi 0} \right.$$

$$\left. + \left(\mathbf{G}_{\psi}^{t}\, \mathbf{A}_{\theta}^{t} \right) \boldsymbol{\sigma}_{\psi 1} + \left(\mathbf{G}_{\psi}^{t}\, \mathbf{A}_{\psi}^{t} \right) \boldsymbol{\sigma}_{\psi\psi} \right\} dx\,dy \tag{5.137}$$

Linearization of Equations of Equilibrium

To restore equilibrium, i.e. to make the residual vectors vanish we assume:

$$\boldsymbol{\delta}_{new} = \boldsymbol{\delta}_{old} + \Delta\boldsymbol{\delta}$$

$$\boldsymbol{\sigma}_{new}^{(l)} = \boldsymbol{\sigma}_{old}^{(l)} + \Delta\boldsymbol{\sigma} \tag{5.138}$$

$$\mathbf{A}_{new} = \mathbf{A}_{old} + \Delta\mathbf{A}$$

such that
$$\mathbf{R}_{o} \to \mathbf{O}, \quad \mathbf{R}_{b} \to \mathbf{O}, \quad \mathbf{R}_{\psi} \to \mathbf{O}$$

Substituting from Equations (5.138) into (5.132) - (5.134), then it can be deduced that:

$$\mathbf{O} = \mathbf{F}_{o} - \sum_{e=1}^{N_e} \int_{-h/2}^{h/2} \iint_{e} \left\{ \left[\mathbf{B}_{o}^{t} + \mathbf{G}_{m}^{t} \left(\mathbf{A}_{m}^{t} + \Delta\mathbf{A}_{m}^{t} \right) \right] \left(\boldsymbol{\sigma}^{(l)} + \Delta\boldsymbol{\sigma}^{(l)} \right) \right.$$

$$+ \mathbf{G}_{m}^{t} \left(\mathbf{A}_{\theta}^{t} + \Delta\mathbf{A}_{\theta}^{t} \right)(-z) \left(\boldsymbol{\sigma}^{(l)} + \Delta\boldsymbol{\sigma}^{(l)} \right) \tag{5.139}$$

$$\left. + \mathbf{G}_{m}^{t} \left(\mathbf{A}_{\psi}^{t} + \Delta\mathbf{A}_{\psi}^{t} \right) f_{\psi}(z) \left(\boldsymbol{\sigma}^{(l)} + \Delta\boldsymbol{\sigma}^{(l)} \right) \right\} dx\,dy\,dz$$

$$\mathbf{O} = \mathbf{F}_{b} - \sum_{e=1}^{N_e} \int_{-h/2}^{h/2} \iint_{e} \left\{ \mathbf{G}_{w}^{t} \left(\mathbf{A}_{w}^{t} + \Delta\mathbf{A}_{w}^{t} \right) \left(\boldsymbol{\sigma}^{(l)} + \Delta\boldsymbol{\sigma}^{(l)} \right) \right.$$

$$+ \left[\mathbf{B}_{b}^{t} + \mathbf{G}_{\theta}^{t} \left(\mathbf{A}_{m}^{t} + \Delta\mathbf{A}_{m}^{t} \right) \right](-z) \left(\boldsymbol{\sigma}^{(l)} + \Delta\boldsymbol{\sigma}^{(l)} \right)$$

$$+ \mathbf{G}_{\theta}^{t} \left(\mathbf{A}_{\psi}^{t} + \Delta\mathbf{A}_{\psi}^{t} \right) \left(-z\, f_{\psi} \right) \left(\boldsymbol{\sigma}^{(l)} + \Delta\boldsymbol{\sigma}^{(l)} \right) \tag{5.140}$$

$$\left. + \mathbf{G}_{\theta}^{t} \left(\mathbf{A}_{\theta}^{t} + \Delta\mathbf{A}_{\theta}^{t} \right)(z^2) \left(\boldsymbol{\sigma}^{(l)} + \Delta\boldsymbol{\sigma}^{(l)} \right) \right\} dx\,dy\,dz$$

$$\mathbf{O} = \mathbf{F}_{\psi} - \sum_{e=1}^{N_e} \int_{-h/2}^{h/2} \iint_{e} \left\{ \mathbf{B}_{\gamma}^{t}\, f_{\gamma}(z) \left(\boldsymbol{\tau}^{(l)} + \Delta\boldsymbol{\tau}^{(l)} \right) \right.$$

$$+ \left[\mathbf{B}_{\psi}^{t} + \mathbf{G}_{\psi}^{t} \left(\mathbf{A}_{m}^{t} + \Delta\mathbf{A}_{m}^{t} \right) \right] (f_{\psi}) \left(\boldsymbol{\sigma}^{(l)} + \Delta\boldsymbol{\sigma}^{(l)} \right)$$

$$+ \mathbf{G}_{\psi}^{t} \left(\mathbf{A}_{\theta}^{t} + \Delta\mathbf{A}_{\theta}^{t} \right) \left(-z\, f_{\psi} \right) \left(\boldsymbol{\sigma}^{(l)} + \Delta\boldsymbol{\sigma}^{(l)} \right) \tag{5.141}$$

$$\left. + \mathbf{G}_{\psi}^{t} \left(\mathbf{A}_{\psi}^{t} + \Delta\mathbf{A}_{\psi}^{t} \right) \left(f_{\psi}^{2} \right) \left(\boldsymbol{\sigma}^{(l)} + \Delta\boldsymbol{\sigma}^{(l)} \right) \right\} dx\,dy\,dz$$

Expanding Equations (5.139)-(5.141), using the definitions of residual vectors given by Equations (5.132)-(5.134), and ignoring $\Delta\mathbf{A} \cdot \Delta\boldsymbol{\sigma}$ terms, then it can be deduced that:

$$\sum_{e=1}^{N_e} \int_{-h/2}^{h/2} \iint_{e} \left\{ \left[\left(\mathbf{B}_{o}^{t} + \mathbf{G}_{m}^{t}\, \mathbf{A}_{m}^{t} \right) + \mathbf{G}_{m}^{t}\, \mathbf{A}_{\theta}^{t}\,(-z) + \mathbf{G}_{m}^{t}\, \mathbf{A}_{\psi}^{t}\,(f_{\psi}) \right] \Delta\boldsymbol{\sigma}^{(l)} \right.$$

$$\left. + \left[\mathbf{G}_{m}^{t}\, \Delta\mathbf{A}_{m}^{t} + \mathbf{G}_{m}^{t}\, \Delta\mathbf{A}_{\theta}^{t}\,(-z) + \mathbf{G}_{m}^{t}\, \Delta\mathbf{A}_{\psi}^{t}\,(f_{\psi}) \right] \boldsymbol{\sigma}^{(l)} \right\} dx\,dy\,dz = \mathbf{R}_{o} \tag{5.142}$$

$$\sum_{e=1}^{N_e} \int_{-h/2}^{h/2} \iint_e \left\{ \left[\mathbf{G}_w^t \mathbf{A}_w^t + \left(\mathbf{B}_b^t + \mathbf{G}_\theta^t \mathbf{A}_m^t \right)(-z) \right. \right.$$
$$\left. + \mathbf{G}_\theta^t \mathbf{A}_\psi^t (-z f_\psi) + \mathbf{G}_\theta^t \mathbf{A}_\theta^t (z^2) \right] \Delta\boldsymbol{\sigma}^{(l)} \tag{5.143}$$
$$+ \left[\mathbf{G}_w^t \Delta\mathbf{A}_w^t + \mathbf{G}_\theta^t \Delta\mathbf{A}_m^t (-z) \right.$$
$$\left. \left. + \mathbf{G}_\theta^t \Delta\mathbf{A}_\psi^t (-z f_\psi) + \mathbf{G}_\theta^t \Delta\mathbf{A}_\theta^t (z^2) \right] \boldsymbol{\sigma}^{(l)} \right\} dx\,dy\,dz = \mathbf{R}_\psi$$

$$\sum_{e=1}^{N_e} \int_{-h/2}^{h/2} \iint_e \left\{ \mathbf{B}_\gamma^t f_\gamma \Delta\boldsymbol{\tau}^{(l)} + \left[\left(\mathbf{B}_\psi^t + \mathbf{G}_\psi^t \mathbf{A}_m^t \right) f_\psi \right. \right.$$
$$\left. + \mathbf{G}_\psi^t \mathbf{A}_\theta^t (-z f_\psi) + \mathbf{G}_\psi^t \mathbf{A}_\psi^t \left(f_\psi^2 \right) \right] \Delta\boldsymbol{\sigma}^{(l)} \tag{5.144}$$
$$+ \left[\mathbf{G}_\psi^t \Delta\mathbf{A}_m^t f_\psi + \mathbf{G}_\psi^t \Delta\mathbf{A}_\theta^t (-z f_\psi) \right.$$
$$\left. \left. + \mathbf{G}_\psi^t \Delta\mathbf{A}_\psi^t \left(f_\psi^2 \right) \right] \boldsymbol{\sigma}^{(l)} \right\} dx\,dy\,dz = \mathbf{R}_\psi$$

which can be rewritten as follows:

$$\sum_{e=1}^{N_e} \left[\left(\mathbf{R}_o^e \right)_{\Delta\boldsymbol{\sigma}} + \left(\mathbf{R}_o^e \right)_{\Delta\mathbf{A}} \right] = \mathbf{R}_o \tag{5.145}$$

$$\sum_{e=1}^{N_e} \left[\left(\mathbf{R}_b^e \right)_{\Delta\boldsymbol{\sigma}} + \left(\mathbf{R}_b^e \right)_{\Delta\mathbf{A}} \right] = \mathbf{R}_b \tag{5.146}$$

$$\sum_{e=1}^{N_e} \left[\left(\mathbf{R}_\psi^e \right)_{\Delta\boldsymbol{\sigma}} + \left(\mathbf{R}_\psi^e \right)_{\Delta\mathbf{A}} \right] = \mathbf{R}_\psi \tag{5.147}$$

where

$$\left(\mathbf{R}_o^e \right)_{\Delta\boldsymbol{\sigma}} = \sum_{e=1}^{N_e} \int_{-h/2}^{h/2} \iint_e \left\{ \left[\left(\mathbf{B}_o^t + \mathbf{G}_m^t \mathbf{A}_m^t \right) + \mathbf{G}_m^t \mathbf{A}_\theta^t (-z) + \mathbf{G}_m^t \mathbf{A}_\psi^t (f_\psi) \right] \Delta\boldsymbol{\sigma}^{(l)} \right\} dx\,dy\,dz$$
$$\tag{5.148}$$

$$\left(\mathbf{R}_b^e \right)_{\Delta\boldsymbol{\sigma}} = \sum_{e=1}^{N_e} \int_{-h/2}^{h/2} \iint_e \left\{ \left[\mathbf{G}_w^t \mathbf{A}_w^t + \left(\mathbf{B}_b^t + \mathbf{G}_\theta^t \mathbf{A}_m^t \right)(-z) \right. \right.$$
$$\left. \left. + \mathbf{G}_\theta^t \mathbf{A}_\psi^t (-z f_\psi) + \mathbf{G}_\theta^t \mathbf{A}_\theta^t (z^2) \right] \Delta\boldsymbol{\sigma}^{(l)} \right\} dx\,dy\,dz \tag{5.149}$$

$$\left(\mathbf{R}_\psi^e \right)_{\Delta\boldsymbol{\sigma}} = \sum_{e=1}^{N_e} \int_{-h/2}^{h/2} \iint_e \left\{ \mathbf{B}_\gamma^t f_\gamma \Delta\boldsymbol{\tau}^{(l)} + \left[\left(\mathbf{B}_\psi^t + \mathbf{G}_\psi^t \mathbf{A}_m^t \right) f_\psi \right. \right.$$
$$\left. \left. + \mathbf{G}_\psi^t \mathbf{A}_\theta^t (-z f_\psi) + \mathbf{G}_\psi^t \mathbf{A}_\psi^t \left(f_\psi^2 \right) \right] \Delta\boldsymbol{\sigma}^{(l)} \right\} dx\,dy\,dz \tag{5.150}$$

$$\left(\mathbf{R}_o^e \right)_{\Delta\mathbf{A}} = \sum_{e=1}^{N_e} \int_{-h/2}^{h/2} \iint_e \left\{ \left[\mathbf{G}_m^t \Delta\mathbf{A}_m^t + \mathbf{G}_m^t \Delta\mathbf{A}_\theta^t (-z) + \mathbf{G}_m^t \Delta\mathbf{A}_\psi^t (f_\psi) \right] \boldsymbol{\sigma}^{(l)} \right\} dx\,dy\,dz \tag{5.151}$$

$$\left(\mathbf{R}_b^e\right)_{\Delta\mathbf{A}} = \sum_{e=1}^{N_e} \int_{-h/2}^{h/2} \iint_e \left\{\left[\mathbf{G}_w^t\,\Delta\mathbf{A}_w^t + \mathbf{G}_\theta^t\,\Delta\mathbf{A}_m^t(-z)\right.\right.$$
$$\left.\left. + \mathbf{G}_\theta^t\,\Delta\mathbf{A}_\psi^t(-z\,f_\psi) + \mathbf{G}_\theta^t\,\Delta\mathbf{A}_\theta^t(z^2)\right]\boldsymbol{\sigma}^{(l)}\right\}dx\,dy\,dz \tag{5.152}$$

$$\left(\mathbf{R}_\psi^e\right)_{\Delta\mathbf{A}} = \sum_{e=1}^{N_e} \int_{-h/2}^{h/2} \iint_e \left\{\left[\mathbf{G}_\psi^t\,\Delta\mathbf{A}_m^t\,f_\psi + \mathbf{G}_\psi^t\,\Delta\mathbf{A}_\theta^t(-z\,f_\psi)\right.\right.$$
$$\left.\left. + \mathbf{G}_\psi^t\,\Delta\mathbf{A}_\psi^t\left(f_\psi^2\right)\right]\boldsymbol{\sigma}^{(l)}\right\}dx\,dy\,dz \tag{5.153}$$

Analysis of $\Delta\boldsymbol{\sigma}$ Terms

Notice that it can be deduced from Equations (5.65) and (5.123) that:

$$\begin{aligned}
\Delta\boldsymbol{\sigma}^{(l)} = \mathbf{D}^{(l)}\Big\{ & \left[\mathbf{B}_o\Delta\boldsymbol{\delta}_o + \mathbf{A}_m\mathbf{G}_m\Delta\boldsymbol{\delta}_o + \mathbf{A}_w\mathbf{G}_w\Delta\boldsymbol{\delta}_b\right] \\
& - z\left[\mathbf{B}_b\Delta\boldsymbol{\delta}_b + \mathbf{A}_m\mathbf{G}_\theta\Delta\boldsymbol{\delta}_b + \mathbf{A}_\theta\mathbf{G}_m\Delta\boldsymbol{\delta}_o\right] \\
& + f_\psi(z)\left[\mathbf{B}_\psi\Delta\boldsymbol{\delta}_\psi + \mathbf{A}_m\mathbf{G}_\psi\Delta\boldsymbol{\delta}_\psi + \mathbf{A}_\psi\mathbf{G}_m\Delta\boldsymbol{\delta}_o\right] \\
& - z\,f_\psi(z)\left[\mathbf{A}_\psi\mathbf{G}_\theta\Delta\boldsymbol{\delta}_b + \mathbf{A}_\theta\mathbf{G}_\psi\Delta\boldsymbol{\delta}_\psi\right] \\
& + z^2\,\mathbf{A}_\theta\mathbf{G}_\theta\Delta\boldsymbol{\delta}_b + f_\psi^2(z)\,\mathbf{A}_\psi\mathbf{G}_\psi\Delta\boldsymbol{\delta}_\psi\Big\}
\end{aligned} \tag{5.154a}$$

which can be rewritten as follows:

$$\begin{aligned}
\Delta\boldsymbol{\sigma}^{(l)} = & \left[\mathbf{D}^{(l)}\left(\mathbf{B}_o + \mathbf{A}_m\mathbf{G}_m\right) - z\,\mathbf{D}^{(l)}\mathbf{A}_\theta\mathbf{G}_m + f_\psi(z)\mathbf{D}^{(l)}\mathbf{A}_\psi\mathbf{G}_m\right]\Delta\boldsymbol{\delta}_o \\
& + \left[\mathbf{D}^{(l)}\mathbf{A}_w\mathbf{G}_w - z\,\mathbf{D}^{(l)}\left(\mathbf{B}_b + \mathbf{A}_m\mathbf{G}_\theta\right) - z\,f_\psi(z)\mathbf{D}^{(l)}\mathbf{A}_\psi\mathbf{G}_\theta + z^2\,\mathbf{D}^{(l)}\mathbf{A}_\theta\mathbf{G}_\theta\right]\Delta\boldsymbol{\delta}_b \\
& + \left[f_\psi(z)\mathbf{D}^{(l)}\left(\mathbf{B}_\psi + \mathbf{A}_m\mathbf{G}_\psi\right) - z\,f_\psi(z)\mathbf{D}^{(l)}\mathbf{A}_\theta\mathbf{G}_\psi + f_\psi^2(z)\mathbf{D}^{(l)}\mathbf{A}_\psi\mathbf{G}_\psi\right]\Delta\boldsymbol{\delta}_\psi
\end{aligned} \tag{5.154b}$$

We will require integrated stress or stress increment, and from Equation (5.154) we can deduce the following general form:

$$\int_{-h/2}^{h/2} f(z)\Delta\boldsymbol{\sigma}^{(l)}dz = \left\{ \left[\int_{-h/2}^{h/2} f(z)\mathbf{D}^{(l)}dz \right] \left(\mathbf{B}_o + \mathbf{A}_m \mathbf{G}_m \right) - \left[\int_{-h/2}^{h/2} z\, f(z)\mathbf{D}^{(l)}dz \right] \mathbf{A}_\theta \mathbf{G}_m \right.$$

$$+ \left. \left[\int_{-h/2}^{h/2} f(z)\, f_\psi(z)\mathbf{D}^{(l)}dz \right] \mathbf{A}_\psi \mathbf{G}_m \right\} \Delta\boldsymbol{\delta}_o$$

$$+ \left\{ \left[\int_{-h/2}^{h/2} f(z)\mathbf{D}^{(l)}dz \right] \mathbf{A}_w \mathbf{G}_w - \left[\int_{-h/2}^{h/2} z\, f(z)\mathbf{D}^{(l)}dz \right] \left(\mathbf{B}_b + \mathbf{A}_m \mathbf{G}_\theta \right) \right.$$

$$- \left[\int_{-h/2}^{h/2} z\, f(z)\, f_\psi(z)\mathbf{D}^{(l)}dz \right] \mathbf{A}_\psi \mathbf{G}_\theta + \left. \left[\int_{-h/2}^{h/2} z^2\, f(z)\mathbf{D}^{(l)}dz \right] \mathbf{A}_\theta \mathbf{G}_\theta \right\} \Delta\boldsymbol{\delta}_b$$

$$+ \left\{ \left[\int_{-h/2}^{h/2} f(z)\, f_\psi(z)\mathbf{D}^{(l)}dz \right] \left(\mathbf{B}_\psi + \mathbf{A}_m \mathbf{G}_\psi \right) - \left[\int_{-h/2}^{h/2} z\, f(z)\, f_\psi(z)\mathbf{D}^{(l)}dz \right] \mathbf{A}_\theta \mathbf{G}_\psi \right.$$

$$+ \left. \left[\int_{-h/2}^{h/2} f(z)\, f_\psi^2(z)\mathbf{D}^{(l)}dz \right] \mathbf{A}_\psi \mathbf{G}_\psi \right\} \Delta\boldsymbol{\delta}_\psi$$

$$(5.155)$$

<u>Terms of Equation (5.24)</u>

Using Equation (5.155) then it can be deduced that:

$$\int_{-h/2}^{h/2} \Delta\boldsymbol{\sigma}^{(l)}\, dz = \left[\mathbf{D}_0 \left(\mathbf{B}_o + \mathbf{A}_m \mathbf{G}_m \right) - \mathbf{D}_1 \mathbf{A}_\theta \mathbf{G}_m + \mathbf{D}_{\psi 0} \mathbf{A}_\psi \mathbf{G}_m \right] \Delta\boldsymbol{\delta}_o$$

$$+ \left[\mathbf{D}_0 \mathbf{A}_w \mathbf{G}_w - \mathbf{D}_1 \left(\mathbf{B}_b + \mathbf{A}_m \mathbf{G}_\theta \right) - \mathbf{D}_{\psi 1} \mathbf{A}_\psi \mathbf{G}_\theta + \mathbf{D}_2 \mathbf{A}_\theta \mathbf{G}_\theta \right] \Delta\boldsymbol{\delta}_b \qquad (5.156)$$

$$+ \left[\mathbf{D}_{\psi 0} \left(\mathbf{B}_\psi + \mathbf{A}_m \mathbf{G}_\psi \right) - \mathbf{D}_{\psi 1} \mathbf{A}_\theta \mathbf{G}_\psi + \mathbf{D}_{\psi\psi} \mathbf{A}_\psi \mathbf{G}_\psi \right] \Delta\boldsymbol{\delta}_\psi$$

$$- \int_{-h/2}^{h/2} z\Delta\boldsymbol{\sigma}^{(l)}\, dz = \left[-\mathbf{D}_1 \left(\mathbf{B}_o + \mathbf{A}_m \mathbf{G}_m \right) + \mathbf{D}_2 \mathbf{A}_\theta \mathbf{G}_m - \mathbf{D}_{\psi 1} \mathbf{A}_\psi \mathbf{G}_m \right] \Delta\boldsymbol{\delta}_o$$

$$+ \left[-\mathbf{D}_1 \mathbf{A}_w \mathbf{G}_w + \mathbf{D}_2 \left(\mathbf{B}_b + \mathbf{A}_m \mathbf{G}_\theta \right) + \mathbf{D}_{\psi 2} \mathbf{A}_\psi \mathbf{G}_\theta - \mathbf{D}_3 \mathbf{A}_\theta \mathbf{G}_\theta \right] \Delta\boldsymbol{\delta}_b \qquad (5.157)$$

$$+ \left[-\mathbf{D}_{\psi 1} \left(\mathbf{B}_\psi + \mathbf{A}_m \mathbf{G}_\psi \right) + \mathbf{D}_{\psi 2} \mathbf{A}_\theta \mathbf{G}_\psi - \mathbf{D}_{\psi\psi 1} \mathbf{A}_\psi \mathbf{G}_\psi \right] \Delta\boldsymbol{\delta}_\psi$$

$$\int_{-h/2}^{h/2} f_\psi \Delta\boldsymbol{\sigma}^{(l)}\, dz = \left[\mathbf{D}_{\psi 0} \left(\mathbf{B}_o + \mathbf{A}_m \mathbf{G}_m \right) - \mathbf{D}_{\psi 1} \mathbf{A}_\theta \mathbf{G}_m + \mathbf{D}_{\psi\psi} \mathbf{A}_\psi \mathbf{G}_m \right] \Delta\boldsymbol{\delta}_o$$

$$+ \left[\mathbf{D}_{\psi 0} \mathbf{A}_w \mathbf{G}_w - \mathbf{D}_{\psi 1} \left(\mathbf{B}_b + \mathbf{A}_m \mathbf{G}_\theta \right) - \mathbf{D}_{\psi\psi 1} \mathbf{A}_\psi \mathbf{G}_\theta + \mathbf{D}_{\psi 2} \mathbf{A}_\theta \mathbf{G}_\theta \right] \Delta\boldsymbol{\delta}_b \qquad (5.158)$$

$$+ \left[\mathbf{D}_{\psi\psi} \left(\mathbf{B}_\psi + \mathbf{A}_m \mathbf{G}_\psi \right) - \mathbf{D}_{\psi\psi 1} \mathbf{A}_\theta \mathbf{G}_\psi + \mathbf{D}_{\psi\psi\psi} \mathbf{A}_\psi \mathbf{G}_\psi \right] \Delta\boldsymbol{\delta}_\psi$$

Substituting from Equations (5.156)-(5.158) into (5.148), then it can be deduced that:

$$\left(\mathbf{R}_o^e \right)_{\Delta\boldsymbol{\sigma}} = \mathbf{K}_{oo}\, \Delta\boldsymbol{\delta}_o + \mathbf{K}_{ob}\, \Delta\boldsymbol{\delta}_b + \mathbf{K}_{o\psi}\, \Delta\boldsymbol{\delta}_\psi \qquad (5.159)$$

where

$$\mathbf{K}_{oo} = \iint_e \left\{ \left(\mathbf{B}_o^t + \mathbf{G}_m^t \, \mathbf{A}_m^t \right) \left[\mathbf{D}_o \left(\mathbf{B}_o + \mathbf{A}_m \, \mathbf{G}_m \right) - \mathbf{D}_1 \, \mathbf{A}_\theta \, \mathbf{G}_m + \mathbf{D}_{\psi 0} \, \mathbf{A}_\psi \, \mathbf{G}_m \right] \right.$$

$$+ \left(\mathbf{G}_m^t \, \mathbf{A}_\theta^t \right) \left[- \mathbf{D}_1 \left(\mathbf{B}_o + \mathbf{A}_m \, \mathbf{G}_m \right) + \mathbf{D}_2 \, \mathbf{A}_\theta \, \mathbf{G}_m - \mathbf{D}_{\psi 1} \, \mathbf{A}_\psi \, \mathbf{G}_m \right] \qquad (5.160)$$

$$\left. + \left(\mathbf{G}_m^t \, \mathbf{A}_\psi^t \right) \left[\mathbf{D}_{\psi 0} \left(\mathbf{B}_o + \mathbf{A}_m \, \mathbf{G}_m \right) - \mathbf{D}_{\psi 1} \, \mathbf{A}_\theta \, \mathbf{G}_m + \mathbf{D}_{\psi \psi} \, \mathbf{A}_\psi \, \mathbf{G}_m \right] \right\} dx \, dy$$

$$\mathbf{K}_{ob} = \iint_e \left\{ \left(\mathbf{B}_o^t + \mathbf{G}_m^t \, \mathbf{A}_m^t \right) \left[\mathbf{D}_0 \, \mathbf{A}_w \, \mathbf{G}_w - \mathbf{D}_1 \left(\mathbf{B}_b + \mathbf{A}_m \, \mathbf{G}_\theta \right) - \mathbf{D}_{\psi 1} \, \mathbf{A}_\psi \, \mathbf{G}_\theta + \mathbf{D}_2 \, \mathbf{A}_\theta \, \mathbf{G}_\theta \right] \right.$$

$$+ \left(\mathbf{G}_m^t \, \mathbf{A}_\theta^t \right) \left[- \mathbf{D}_1 \, \mathbf{A}_w \, \mathbf{G}_w + \mathbf{D}_2 \left(\mathbf{B}_b + \mathbf{A}_m \, \mathbf{G}_\theta \right) + \mathbf{D}_{\psi 2} \, \mathbf{A}_\psi \, \mathbf{G}_\theta - \mathbf{D}_3 \, \mathbf{A}_\theta \, \mathbf{G}_\theta \right]$$

$$\left. + \left(\mathbf{G}_m^t \, \mathbf{A}_\psi^t \right) \left[\mathbf{D}_{\psi 0} \, \mathbf{A}_w \, \mathbf{G}_w - \mathbf{D}_{\psi 1} \left(\mathbf{B}_b + \mathbf{A}_m \, \mathbf{G}_\theta \right) - \mathbf{D}_{\psi \psi 1} \, \mathbf{A}_\psi \, \mathbf{G}_\theta + \mathbf{D}_{\psi 2} \, \mathbf{A}_\theta \, \mathbf{G}_\theta \right] \right\} dx \, dy$$

$$(5.161)$$

$$\mathbf{K}_{o\psi} = \iint_e \left\{ \left(\mathbf{B}_o^t + \mathbf{G}_m^t \, \mathbf{A}_m^t \right) \left[\mathbf{D}_{\psi 1} \left(\mathbf{B}_\psi + \mathbf{A}_m \, \mathbf{G}_\psi \right) - \mathbf{D}_{\psi 1} \, \mathbf{A}_\theta \, \mathbf{G}_\psi + \mathbf{D}_{\psi \psi} \, \mathbf{A}_\psi \, \mathbf{G}_\psi \right] \right.$$

$$+ \left(\mathbf{G}_m^t \, \mathbf{A}_\theta^t \right) \left[- \mathbf{D}_{\psi 1} \left(\mathbf{B}_\psi + \mathbf{A}_m \, \mathbf{G}_\psi \right) + \mathbf{D}_{\psi 2} \, \mathbf{A}_\theta \, \mathbf{G}_\psi - \mathbf{D}_{\psi \psi 1} \, \mathbf{A}_\psi \, \mathbf{G}_\psi \right] \qquad (5.162)$$

$$\left. + \left(\mathbf{G}_m^t \, \mathbf{A}_\psi^t \right) \left[\mathbf{D}_{\psi \psi} \left(\mathbf{B}_\psi + \mathbf{A}_m \, \mathbf{G}_\psi \right) - \mathbf{D}_{\psi \psi 1} \, \mathbf{A}_\theta \, \mathbf{G}_\psi + \mathbf{D}_{\psi \psi \psi} \, \mathbf{A}_\psi \, \mathbf{G}_\psi \right] \right\} dx \, dy$$

<u>Terms of Equation (5.149)</u>

Using Equation (5.155) then it can also be shown that:

$$\int_{-h/2}^{h/2} z^2 \, \Delta \boldsymbol{\sigma}^{(l)} \, dz = \left[\mathbf{D}_2 \left(\mathbf{B}_o + \mathbf{A}_m \, \mathbf{G}_m \right) - \mathbf{D}_3 \, \mathbf{A}_\theta \, \mathbf{G}_m + \mathbf{D}_{\psi 2} \, \mathbf{A}_\psi \, \mathbf{G}_m \right] \Delta \boldsymbol{\delta}_o$$

$$+ \left[\mathbf{D}_2 \, \mathbf{A}_w \, \mathbf{G}_w - \mathbf{D}_3 \left(\mathbf{B}_b + \mathbf{A}_m \, \mathbf{G}_\theta \right) - \mathbf{D}_{\psi 3} \, \mathbf{A}_\psi \, \mathbf{G}_\theta + \mathbf{D}_2 \, \mathbf{A}_\theta \, \mathbf{G}_\theta \right] \Delta \boldsymbol{\delta}_b \qquad (5.163)$$

$$+ \left[\mathbf{D}_{\psi 2} \left(\mathbf{B}_\psi + \mathbf{A}_m \, \mathbf{G}_\psi \right) - \mathbf{D}_{\psi 3} \, \mathbf{A}_\theta \, \mathbf{G}_\psi + \mathbf{D}_{\psi \psi 2} \, \mathbf{A}_\psi \, \mathbf{G}_\psi \right] \Delta \boldsymbol{\delta}_\psi$$

$$- \int_{-h/2}^{h/2} z \, f_\psi \, \Delta \boldsymbol{\sigma}^{(l)} \, dz = \left[- \mathbf{D}_{\psi 1} \left(\mathbf{B}_o + \mathbf{A}_m \, \mathbf{G}_m \right) + \mathbf{D}_{\psi 2} \, \mathbf{A}_\theta \, \mathbf{G}_m - \mathbf{D}_{\psi \psi 1} \, \mathbf{A}_\psi \, \mathbf{G}_m \right] \Delta \boldsymbol{\delta}_o$$

$$+ \left[- \mathbf{D}_{\psi 1} \, \mathbf{A}_w \, \mathbf{G}_w + \mathbf{D}_{\psi 2} \left(\mathbf{B}_b + \mathbf{A}_m \, \mathbf{G}_\theta \right) + \mathbf{D}_{\psi \psi 2} \, \mathbf{A}_\psi \, \mathbf{G}_\theta - \mathbf{D}_{\psi 3} \, \mathbf{A}_\theta \, \mathbf{G}_\theta \right] \Delta \boldsymbol{\delta}_b \qquad (5.164)$$

$$+ \left[- \mathbf{D}_{\psi \psi 1} \left(\mathbf{B}_\psi + \mathbf{A}_m \, \mathbf{G}_\psi \right) + \mathbf{D}_{\psi \psi 2} \, \mathbf{A}_\theta \, \mathbf{G}_\psi - \mathbf{D}_{\psi \psi \psi 1} \, \mathbf{A}_\psi \, \mathbf{G}_\psi \right] \Delta \boldsymbol{\delta}_\psi$$

Substituting from Equations (5.156)-(5.158), (5.163) and (5.164) into (5.149) it can be proved that:

$$\left(\mathbf{R}_b^e \right)_{\Delta \boldsymbol{\sigma}} = \mathbf{K}_{bo} \, \Delta \boldsymbol{\delta}_o + \mathbf{K}_{bb} \, \Delta \boldsymbol{\delta}_b + \mathbf{K}_{b\psi} \, \Delta \boldsymbol{\delta}_\psi \qquad (5.165)$$

where

$$\mathbf{K}_{bo} = \iint_e \left\{ \left(\mathbf{G}_w^t \, \mathbf{A}_w^t \right) \left[\mathbf{D}_o \left(\mathbf{B}_o + \mathbf{A}_m \, \mathbf{G}_m \right) - \mathbf{D}_1 \, \mathbf{A}_\theta \, \mathbf{G}_m + \mathbf{D}_{\psi 0} \, \mathbf{A}_\psi \, \mathbf{G}_m \right] \right.$$
$$+ \left(\mathbf{B}_b^t + \mathbf{G}_\theta^t \, \mathbf{A}_m^t \right) \left[-\mathbf{D}_1 \left(\mathbf{B}_o + \mathbf{A}_m \, \mathbf{G}_m \right) + \mathbf{D}_2 \, \mathbf{A}_\theta \, \mathbf{G}_m - \mathbf{D}_{\psi 1} \, \mathbf{A}_\psi \, \mathbf{G}_m \right]$$
$$+ \left(\mathbf{G}_\theta^t \, \mathbf{A}_\theta^t \right) \left[\mathbf{D}_2 \left(\mathbf{B}_o + \mathbf{A}_m \, \mathbf{G}_m \right) - \mathbf{D}_3 \, \mathbf{A}_\theta \, \mathbf{G}_m + \mathbf{D}_{\psi 2} \, \mathbf{A}_\psi \, \mathbf{G}_m \right]$$
$$\left. + \left(\mathbf{G}_\theta^t \, \mathbf{A}_\psi^t \right) \left[-\mathbf{D}_{\psi 1} \left(\mathbf{B}_o + \mathbf{A}_m \, \mathbf{G}_m \right) + \mathbf{D}_{\psi 2} \, \mathbf{A}_\theta \, \mathbf{G}_m - \mathbf{D}_{\psi \psi 1} \, \mathbf{A}_\psi \, \mathbf{G}_m \right] \right\} dx\, dy$$

$$(5.166)$$

$$\mathbf{K}_{bb} = \iint_e \left\{ \left(\mathbf{G}_w^t \, \mathbf{A}_w^t \right) \left[\mathbf{D}_o \, \mathbf{A}_w \mathbf{G}_w - \mathbf{D}_1 \left(\mathbf{B}_b + \mathbf{A}_m \, \mathbf{G}_\theta \right) - \mathbf{D}_{\psi 1} \, \mathbf{A}_\psi \, \mathbf{G}_\theta + \mathbf{D}_2 \, \mathbf{A}_\theta \, \mathbf{G}_\theta \right] \right.$$
$$+ \left(\mathbf{B}_b^t + \mathbf{G}_\theta^t \, \mathbf{A}_m^t \right) \left[-\mathbf{D}_1 \, \mathbf{A}_w \mathbf{G}_w + \mathbf{D}_2 \left(\mathbf{B}_b + \mathbf{A}_m \, \mathbf{G}_\theta \right) + \mathbf{D}_{\psi 2} \, \mathbf{A}_\psi \, \mathbf{G}_\theta - \mathbf{D}_3 \, \mathbf{A}_\theta \, \mathbf{G}_\theta \right]$$
$$+ \left(\mathbf{G}_\theta^t \, \mathbf{A}_\theta^t \right) \left[\mathbf{D}_2 \, \mathbf{A}_w \mathbf{G}_w - \mathbf{D}_3 \left(\mathbf{B}_b + \mathbf{A}_m \, \mathbf{G}_\theta \right) - \mathbf{D}_{\psi 3} \, \mathbf{A}_\psi \, \mathbf{G}_\theta + \mathbf{D}_4 \, \mathbf{A}_\theta \, \mathbf{G}_\theta \right]$$
$$\left. + \left(\mathbf{G}_\theta^t \, \mathbf{A}_\psi^t \right) \left[-\mathbf{D}_{\psi 1} \, \mathbf{A}_w \mathbf{G}_w + \mathbf{D}_{\psi 2} \left(\mathbf{B}_b + \mathbf{A}_m \, \mathbf{G}_\theta \right) + \mathbf{D}_{\psi \psi 2} \, \mathbf{A}_\psi \, \mathbf{G}_\theta - \mathbf{D}_{\psi 3} \, \mathbf{A}_\theta \, \mathbf{G}_\theta \right] \right\} dx\, dy$$

$$(5.167)$$

$$\mathbf{K}_{b\psi} = \iint_e \left\{ \left(\mathbf{G}_w^t \, \mathbf{A}_w^t \right) \left[\mathbf{D}_{\psi 0} \left(\mathbf{B}_\psi + \mathbf{A}_m \, \mathbf{G}_\psi \right) - \mathbf{D}_{\psi 1} \, \mathbf{A}_\theta \, \mathbf{G}_\psi + \mathbf{D}_{\psi \psi} \, \mathbf{A}_\psi \, \mathbf{G}_\psi \right] \right.$$
$$+ \left(\mathbf{B}_b^t + \mathbf{G}_\theta^t \, \mathbf{A}_m^t \right) \left[-\mathbf{D}_{\psi 1} \left(\mathbf{B}_\psi + \mathbf{A}_m \, \mathbf{G}_\psi \right) + \mathbf{D}_{\psi 2} \, \mathbf{A}_\theta \, \mathbf{G}_\psi - \mathbf{D}_{\psi \psi 1} \, \mathbf{A}_\psi \, \mathbf{G}_\psi \right]$$
$$+ \left(\mathbf{G}_\theta^t \, \mathbf{A}_\psi^t \right) \left[\mathbf{D}_{\psi 2} \left(\mathbf{B}_\psi + \mathbf{A}_m \, \mathbf{G}_\psi \right) - \mathbf{D}_{\psi 3} \, \mathbf{A}_\theta \, \mathbf{G}_\psi + \mathbf{D}_{\psi \psi 2} \, \mathbf{A}_\psi \, \mathbf{G}_\psi \right]$$
$$\left. + \left(\mathbf{G}_\theta^t \, \mathbf{A}_\psi^t \right) \left[-\mathbf{D}_{\psi \psi 1} \left(\mathbf{B}_\psi + \mathbf{A}_m \, \mathbf{G}_\psi \right) - \mathbf{D}_{\psi \psi 2} \, \mathbf{A}_\theta \, \mathbf{G}_\psi - \mathbf{D}_{\psi \psi \psi 1} \, \mathbf{A}_\psi \, \mathbf{G}_\psi \right] \right\} dx\, dy$$

$$(5.168)$$

Terms of Equation (5.150)

Using Equation (5.155) then it can also be proved that:

$$\int_{-h/2}^{h/2} f_\psi^2 \, \Delta \boldsymbol{\sigma}^{(l)} \, dz = \left[\mathbf{D}_{\psi \psi} \left(\mathbf{B}_o + \mathbf{A}_m \, \mathbf{G}_m \right) - \mathbf{D}_{\psi \psi 1} \, \mathbf{A}_\theta \, \mathbf{G}_m + \mathbf{D}_{\psi \psi \psi} \, \mathbf{A}_\psi \, \mathbf{G}_m \right] \Delta \boldsymbol{\delta}_o$$
$$+ \left[\mathbf{D}_{\psi \psi} \, \mathbf{A}_w \, \mathbf{G}_w - \mathbf{D}_{\psi \psi 1} \left(\mathbf{B}_b + \mathbf{A}_m \, \mathbf{G}_\theta \right) - \mathbf{D}_{\psi \psi \psi 1} \, \mathbf{A}_\psi \, \mathbf{G}_\theta + \mathbf{D}_{\psi \psi 2} \, \mathbf{A}_\theta \, \mathbf{G}_\theta \right] \Delta \boldsymbol{\delta}_b \quad (5.169)$$
$$+ \left[\mathbf{D}_{\psi \psi \psi} \left(\mathbf{B}_\psi + \mathbf{A}_m \, \mathbf{G}_\psi \right) - \mathbf{D}_{\psi \psi \psi 1} \, \mathbf{A}_\theta \, \mathbf{G}_\psi + \mathbf{D}_{\psi \psi \psi \psi} \, \mathbf{A}_\psi \, \mathbf{G}_\psi \right] \Delta \boldsymbol{\delta}_\psi$$

The transverse shear stress term in Equation (5.150) can also be integrated with respect to z as follows:

$$\int_{-h/2}^{h/2} \mathbf{B}_\gamma^t \, f_\gamma(z) \, \Delta \boldsymbol{\tau}^{(l)} \, dz = \int_{-h/2}^{h/2} \mathbf{B}_\gamma^t \left[f_\gamma^2(z) \boldsymbol{\mu}^{(l)} \right] \mathbf{B}_\gamma \, \Delta \boldsymbol{\delta}_\psi \, dz$$
$$\equiv \mathbf{B}_\gamma^t \, \boldsymbol{\mu}_{\gamma \gamma} \, \mathbf{B}_\gamma \, \Delta \boldsymbol{\delta}_\psi$$

$$(5.170)$$

Hence, Equation (5.150) can be simplified as follows:

$$\left(\mathbf{R}_\psi^e \right)_{\Delta \boldsymbol{\sigma}} = \mathbf{K}_{\psi o} \, \Delta \boldsymbol{\delta}_o + \mathbf{K}_{\psi b} \, \Delta \boldsymbol{\delta}_b + \left(\mathbf{K}_{\psi \psi} + \mathbf{K}_{\gamma \gamma} \right) \Delta \boldsymbol{\delta}_\psi \qquad (5.171)$$

where

$$\mathbf{K}_{\psi o} = \iint_e \left\{ \left(\mathbf{B}_\psi^t + \mathbf{G}_\psi^t \, \mathbf{A}_m^t \right) \left[\mathbf{D}_{\psi 0} \left(\mathbf{B}_o + \mathbf{A}_m \, \mathbf{G}_m \right) - \mathbf{D}_{\psi 1} \, \mathbf{A}_\theta \, \mathbf{G}_m + \mathbf{D}_{\psi \psi} \, \mathbf{A}_\psi \, \mathbf{G}_m \right] \right.$$
$$+ \left(\mathbf{G}_\psi^t \, \mathbf{A}_\theta^t \right) \left[-\mathbf{D}_{\psi 1} \left(\mathbf{B}_o + \mathbf{A}_m \, \mathbf{G}_m \right) + \mathbf{D}_{\psi 2} \, \mathbf{A}_\theta \, \mathbf{G}_m - \mathbf{D}_{\psi \psi 1} \, \mathbf{A}_\psi \, \mathbf{G}_m \right] \tag{5.172}$$
$$\left. + \left(\mathbf{G}_\psi^t \, \mathbf{A}_\psi^t \right) \left[\mathbf{D}_{\psi \psi} \left(\mathbf{B}_o + \mathbf{A}_m \, \mathbf{G}_m \right) - \mathbf{D}_{\psi \psi 1} \, \mathbf{A}_\theta \, \mathbf{G}_m + \mathbf{D}_{\psi \psi \psi} \, \mathbf{A}_\psi \, \mathbf{G}_m \right] \right\} dx \, dy$$

$$\mathbf{K}_{\psi b} = \iint_e \left\{ \left(\mathbf{B}_\psi^t + \mathbf{G}_\psi^t \, \mathbf{A}_m^t \right) \left[\mathbf{D}_{\psi 0} \, \mathbf{A}_w \, \mathbf{G}_w - \mathbf{D}_{\psi 1} \left(\mathbf{B}_b + \mathbf{A}_m \, \mathbf{G}_\theta \right) - \mathbf{D}_{\psi \psi 1} \, \mathbf{A}_\psi \, \mathbf{G}_\theta + \mathbf{D}_{\psi 2} \, \mathbf{A}_\theta \, \mathbf{G}_\theta \right] \right.$$
$$+ \left(\mathbf{G}_\psi^t \, \mathbf{A}_\theta^t \right) \left[-\mathbf{D}_{\psi 1} \, \mathbf{A}_w \, \mathbf{G}_w + \mathbf{D}_{\psi 2} \left(\mathbf{B}_b + \mathbf{A}_m \, \mathbf{G}_\theta \right) + \mathbf{D}_{\psi \psi 2} \, \mathbf{A}_\psi \, \mathbf{G}_\theta - \mathbf{D}_{\psi 3} \, \mathbf{A}_\theta \, \mathbf{G}_\theta \right]$$
$$\left. + \left(\mathbf{G}_\psi^t \, \mathbf{A}_\psi^t \right) \left[\mathbf{D}_{\psi \psi} \, \mathbf{A}_w \, \mathbf{G}_w - \mathbf{D}_{\psi \psi 1} \left(\mathbf{B}_b + \mathbf{A}_m \, \mathbf{G}_\theta \right) - \mathbf{D}_{\psi \psi \psi 1} \, \mathbf{A}_\psi \, \mathbf{G}_\theta + \mathbf{D}_{\psi \psi 2} \, \mathbf{A}_\theta \, \mathbf{G}_\theta \right] \right\} dx \, dy$$
$$\tag{5.173}$$

$$\mathbf{K}_{\psi \psi} = \iint_e \left\{ \left(\mathbf{B}_\psi^t + \mathbf{G}_\psi^t \, \mathbf{A}_m^t \right) \left[\mathbf{D}_{\psi \psi} \left(\mathbf{B}_\psi + \mathbf{A}_m \, \mathbf{G}_\psi \right) - \mathbf{D}_{\psi \psi 1} \, \mathbf{A}_\theta \, \mathbf{G}_\psi + \mathbf{D}_{\psi \psi \psi} \, \mathbf{A}_\psi \, \mathbf{G}_\psi \right] \right.$$
$$+ \left(\mathbf{G}_\psi^t \, \mathbf{A}_\theta^t \right) \left[-\mathbf{D}_{\psi \psi 1} \left(\mathbf{B}_\psi + \mathbf{A}_m \, \mathbf{G}_\psi \right) + \mathbf{D}_{\psi \psi 2} \, \mathbf{A}_\theta \, \mathbf{G}_\psi - \mathbf{D}_{\psi \psi \psi 1} \, \mathbf{A}_\psi \, \mathbf{G}_\psi \right]$$
$$\left. + \left(\mathbf{G}_\psi^t \, \mathbf{A}_\psi^t \right) \left[\mathbf{D}_{\psi \psi \psi} \left(\mathbf{B}_\psi + \mathbf{A}_m \, \mathbf{G}_\psi \right) - \mathbf{D}_{\psi \psi \psi 1} \, \mathbf{A}_\theta \, \mathbf{G}_\psi + \mathbf{D}_{\psi \psi \psi \psi} \, \mathbf{A}_\psi \, \mathbf{G}_\psi \right] \right\} dx \, dy$$
$$\tag{5.174}$$

$$\mathbf{K}_{\gamma \gamma} = \iint_e \mathbf{B}_\gamma^t \, \boldsymbol{\mu}_{\gamma \gamma} \, \mathbf{B}_\gamma \, dx \, dy \tag{5.175}$$

Analysis of $\Delta\mathbf{A}$ Terms

Using the integrated stress vectors, as defined by Equations (5.79)-(5.81), then the residual vectors defined by Equations (5.151)-(5.153) can be expressed as follows:

$$\left(\mathbf{R}_o^e \right)_{\Delta\mathbf{A}} = \iint_e \left[\mathbf{G}_m^t \, \Delta\mathbf{A}_m^t \, \boldsymbol{\sigma}_0 + \mathbf{G}_m^t \, \Delta\mathbf{A}_\theta^t \, \boldsymbol{\sigma}_1 + \mathbf{G}_m^t \, \Delta\mathbf{A}_\psi^t \, \boldsymbol{\sigma}_\psi \right] dx \, dy \tag{5.176}$$

$$\left(\mathbf{R}_b^e \right)_{\Delta\mathbf{A}} = \iint_e \left[\mathbf{G}_w^t \, \Delta\mathbf{A}_w^t \, \boldsymbol{\sigma}_0 + \mathbf{G}_\theta^t \, \Delta\mathbf{A}_m^t \, \boldsymbol{\sigma}_1 + \mathbf{G}_\theta^t \, \Delta\mathbf{A}_\psi^t \, \boldsymbol{\sigma}_{\psi 1} + \mathbf{G}_\theta^t \, \Delta\mathbf{A}_\theta^t \, \boldsymbol{\sigma}_2 \right] dx \, dy \tag{5.177}$$

$$\left(\mathbf{R}_\psi^e \right)_{\Delta\mathbf{A}} = \iint_e \left[\mathbf{G}_\psi^t \, \Delta\mathbf{A}_m^t \, \boldsymbol{\sigma}_{\psi 0} + \mathbf{G}_\psi^t \, \Delta\mathbf{A}_\theta^t \, \boldsymbol{\sigma}_{\psi 1} + \mathbf{G}_\psi^t \, \Delta\mathbf{A}_\psi^t \, \boldsymbol{\sigma}_{\psi \psi} \right] dx \, dy \tag{5.178}$$

Using matrix manipulations, the following theorem can be proved:

$$\Delta\mathbf{A}_p^t \, \boldsymbol{\sigma}_q = \mathbf{S}_q \, \Delta\boldsymbol{\theta}_p \tag{5.179}$$

where

$$p \equiv m, \theta, \psi, \qquad q \equiv n, \psi n, \psi \psi$$

and

$$\mathbf{S}_q = \begin{bmatrix} \sigma_x^{(q)} & 0 & \tau_{xy}^{(q)} & 0 \\ 0 & \sigma_x^{(q)} & 0 & \tau_{xy}^{(q)} \\ & & & \\ \tau_{xy}^{(q)} & 0 & \sigma_y^{(q)} & 0 \\ 0 & \tau_{xy}^{(q)} & 0 & \sigma_y^{(q)} \end{bmatrix} \tag{5.180}$$

Similarly, it can be proved that:

$$\Delta \mathbf{A}_w^t \, \boldsymbol{\sigma}_0 = \mathbf{S}_w \, \Delta \boldsymbol{\theta}_w \equiv \mathbf{S}_w \, \mathbf{G}_w \, \Delta \boldsymbol{\delta}_b \tag{5.181}$$

where

$$\mathbf{S}_w = \begin{bmatrix} \sigma_x^{(0)} & \tau_{xy}^{(0)} \\ & \\ \tau_{xy}^{(0)} & \sigma_y^{(0)} \end{bmatrix}$$

Notice also that:

$$\Delta \boldsymbol{\theta}_m = \mathbf{G}_m \, \Delta \boldsymbol{\delta}_o, \quad \Delta \boldsymbol{\theta}_\theta = \mathbf{G}_\theta \, \Delta \boldsymbol{\delta}_b, \quad \Delta \boldsymbol{\theta}_\psi = \mathbf{G}_\psi \, \Delta \boldsymbol{\delta}_\psi \tag{5.182}$$

Hence, Equation (5.176) can be rewritten as follows:

$$\begin{aligned} \left(\mathbf{R}_o^e \right)_{\Delta\mathbf{A}} &= \iint_e \left[\mathbf{G}_m^t \, \mathbf{S}_0 \, \mathbf{G}_m \, \Delta \boldsymbol{\delta}_o + \mathbf{G}_m^t \, \mathbf{S}_1 \, \mathbf{G}_\theta \, \Delta \boldsymbol{\delta}_b + \mathbf{G}_m^t \, \mathbf{S}_\psi \, \mathbf{G}_\psi \, \Delta \boldsymbol{\delta}_\psi \right] dx\,dy \\ &\equiv \mathbf{K}_{mm}^\sigma \, \Delta \boldsymbol{\delta}_o + \mathbf{K}_{m\theta}^\sigma \, \Delta \boldsymbol{\delta}_b + \mathbf{K}_{m\psi}^\sigma \, \Delta \boldsymbol{\delta}_\psi \end{aligned} \tag{5.183}$$

where

$$\mathbf{K}_{mm}^\sigma = \iint_e \mathbf{G}_m^t \, \mathbf{S}_0 \, \mathbf{G}_m \, dx\,dy \tag{5.184}$$

$$\mathbf{K}_{m\theta}^\sigma = \iint_e \mathbf{G}_m^t \, \mathbf{S}_1 \, \mathbf{G}_\theta \, dx\,dy \tag{5.185}$$

$$\mathbf{K}_{mm}^\sigma = \iint_e \mathbf{G}_m^t \, \mathbf{S}_\psi \, \mathbf{G}_\psi \, dx\,dy \tag{5.186}$$

Similarly, Equation (5.177) can be expressed as follows:

$$\begin{aligned} \left(\mathbf{R}_b^e \right)_{\Delta\mathbf{A}} &= \iint_e \left[\mathbf{G}_\theta^t \, \mathbf{S}_1 \, \mathbf{G}_m \, \Delta \boldsymbol{\delta}_o + \left(\mathbf{G}_w^t \, \mathbf{S}_0 \, \mathbf{G}_w + \mathbf{G}_\theta^t \, \mathbf{S}_2 \, \mathbf{G}_\theta \right) \Delta \boldsymbol{\delta}_b + \mathbf{G}_\theta^t \, \mathbf{S}_{\psi 1} \, \mathbf{G}_\psi \, \Delta \boldsymbol{\delta}_\psi \right] dx\,dy \\ &\equiv \mathbf{K}_{\theta m}^\sigma \, \Delta \boldsymbol{\delta}_o + \left(\mathbf{K}_{ww}^\sigma + \mathbf{K}_{\theta\theta}^\sigma \right) \Delta \boldsymbol{\delta}_b + \mathbf{K}_{\theta\psi}^\sigma \, \Delta \boldsymbol{\delta}_\psi \end{aligned}$$
$$\tag{5.187}$$

where

$$\mathbf{K}_{\theta m}^\sigma = \iint_e \mathbf{G}_\theta^t \, \mathbf{S}_1 \, \mathbf{G}_m \, dx\,dy \tag{5.188}$$

$$\mathbf{K}_{\theta\theta}^\sigma = \iint_e \mathbf{G}_\theta^t \, \mathbf{S}_2 \, \mathbf{G}_\theta \, dx\,dy \tag{5.189}$$

$$\mathbf{K}_{ww}^{\sigma} = \iint_{e} \mathbf{G}_{w}^{t}\,\mathbf{S}_{0}\,\mathbf{G}_{w}\,dx\,dy \tag{5.190}$$

$$\mathbf{K}_{\theta\psi}^{\sigma} = \iint_{e} \mathbf{G}_{\theta}^{t}\,\mathbf{S}_{\psi 1}\,\mathbf{G}_{\psi}\,dx\,dy \tag{5.191}$$

Equation (5.178) can also be expressed as follows:

$$\left(\mathbf{R}_{\psi}^{e}\right)_{\Delta\mathbf{A}} = \iint_{e}\left[\mathbf{G}_{\psi}^{t}\,\mathbf{S}_{\psi 0}\,\mathbf{G}_{m}\,\Delta\boldsymbol{\delta}_{o} + \mathbf{G}_{\psi}^{t}\,\mathbf{S}_{\psi 1}\,\mathbf{G}_{\theta}\,\Delta\boldsymbol{\delta}_{b} + \mathbf{G}_{\psi}^{t}\,\mathbf{S}_{\psi\psi}\,\mathbf{G}_{\psi}\,\Delta\boldsymbol{\delta}_{\psi}\right]dx\,dy$$

$$\equiv \quad \mathbf{K}_{\psi m}^{\sigma}\,\Delta\boldsymbol{\delta}_{o} + \mathbf{K}_{\psi\theta}^{\sigma}\,\Delta\boldsymbol{\delta}_{b} + \mathbf{K}_{\psi\psi}^{\sigma}\,\Delta\boldsymbol{\delta}_{\psi} \tag{5.192}$$

where

$$\mathbf{K}_{\psi m}^{\sigma} = \iint_{e} \mathbf{G}_{\psi}^{t}\,\mathbf{S}_{\psi 0}\,\mathbf{G}_{m}\,dx\,dy \tag{5.193}$$

$$\mathbf{K}_{\psi\theta}^{\sigma} = \iint_{e} \mathbf{G}_{\psi}^{t}\,\mathbf{S}_{\psi 1}\,\mathbf{G}_{\theta}\,dx\,dy \tag{5.194}$$

$$\mathbf{K}_{\psi\psi}^{\sigma} = \iint_{e} \mathbf{G}_{\psi}^{t}\,\mathbf{S}_{\psi\psi}\,\mathbf{G}_{\psi}\,dx\,dy \tag{5.195}$$

Final Matrix Equations of the Element

Using the results of Equations (5.159), (5.165), (5.171), (5.183), (5.187), and (5.192), then Equations (5.145), (5.146), and (5.147) can be rewritten as follows:

$$\sum_{e=1}^{N_e}\left\{\left(\mathbf{K}_{oo} + \mathbf{K}_{mm}^{\sigma}\right)\Delta\boldsymbol{\delta}_{o} + \left(\mathbf{K}_{ob} + \mathbf{K}_{m\theta}^{\sigma}\right)\Delta\boldsymbol{\delta}_{b} + \left(\mathbf{K}_{o\psi} + \mathbf{K}_{m\psi}^{\sigma}\right)\Delta\boldsymbol{\delta}_{\psi}\right\} = \mathbf{R}_{o} \tag{5.196}$$

$$\sum_{e=1}^{N_e}\left\{\left(\mathbf{K}_{bo} + \mathbf{K}_{\theta m}^{\sigma}\right)\Delta\boldsymbol{\delta}_{o} + \left(\mathbf{K}_{bb} + \mathbf{K}_{ww}^{\sigma} + \mathbf{K}_{\theta\theta}^{\sigma}\right)\Delta\boldsymbol{\delta}_{b} + \left(\mathbf{K}_{b\psi} + \mathbf{K}_{\theta\psi}^{\sigma}\right)\Delta\boldsymbol{\delta}_{\psi}\right\} = \mathbf{R}_{b} \tag{5.197}$$

$$\sum_{e=1}^{N_e}\left\{\left(\mathbf{K}_{\psi o} + \mathbf{K}_{\psi m}^{\sigma}\right)\Delta\boldsymbol{\delta}_{o} + \left(\mathbf{K}_{\psi b} + \mathbf{K}_{\psi\theta}^{\sigma}\right)\Delta\boldsymbol{\delta}_{b} + \left(\mathbf{K}_{\psi\psi} + \mathbf{K}_{\gamma\gamma} + \mathbf{K}_{\psi\psi}^{\sigma}\right)\Delta\boldsymbol{\delta}_{\psi}\right\} = \mathbf{R}_{\psi}$$

$$\tag{5.198}$$

which can be rewritten as follows:

$$\sum_{e=1}^{N_e}\left\{\left(\mathbf{K} + \mathbf{K}_{\sigma}\right)\begin{bmatrix}\Delta\boldsymbol{\delta}_{o}\\ \Delta\boldsymbol{\delta}_{b}\\ \Delta\boldsymbol{\delta}_{\psi}\end{bmatrix}\right\} = \begin{bmatrix}\mathbf{R}_{o}\\ \mathbf{R}_{b}\\ \mathbf{R}_{\psi}\end{bmatrix} \tag{5.199}$$

where the element stiffness matrices are defined as follows:

$$\mathbf{K} = \begin{bmatrix} \mathbf{K}_{oo} & \mathbf{K}_{ob} & \mathbf{K}_{o\psi} \\ \mathbf{K}_{bo} & \mathbf{K}_{bb} & \mathbf{K}_{b\psi} \\ \mathbf{K}_{\psi o} & \mathbf{K}_{\psi b} & \mathbf{K}_{\psi\psi} + \mathbf{K}_{\gamma\gamma} \end{bmatrix} \qquad (5.200)$$

$$\mathbf{K}^{\sigma} = \begin{bmatrix} \mathbf{K}^{\sigma}_{mm} & \mathbf{K}^{\sigma}_{m\theta} & \mathbf{K}^{\sigma}_{m\psi} \\ \mathbf{K}^{\sigma}_{\theta m} & \mathbf{K}^{\sigma}_{ww} + \mathbf{K}^{\sigma}_{\theta\theta} & \mathbf{K}^{\sigma}_{\theta\psi} \\ \mathbf{K}^{\sigma}_{\psi m} & \mathbf{K}^{\sigma}_{\psi\theta} & \mathbf{K}^{\sigma}_{\psi\psi} \end{bmatrix} \qquad (5.201)$$

5.4 Derivation of Mass Matrix for Reissner-type Element

It is assumed that different layers are made of the same composite material but with different fibre orientations, i.e. the density of every layer is the same i.e.

$$\rho^{(L)} = \rho \qquad (5.202)$$

Using D'Alembert's principle, the inertial force vector acting at an infinitesimal volume due to an acceleration vector is:

$$d\vec{F} = -\rho\, \vec{a}\, dxdydz \qquad (5.203)$$

Hence, the work done by the inertia force due to an infinitesimal virtual displacement field is:

$$dW_a = -\iiint\limits_{volume} \rho\, d\vec{q}.\vec{a}\, dxdydz \;\equiv\; -\iiint\limits_{volume} \rho\, d\mathbf{q}^t\, \ddot{\mathbf{q}}\, dxdydz \qquad (5.204)$$

Using the expression below

$$q(x,y,z,t) = \begin{bmatrix} \mathbf{q}_{uv} \\ \mathbf{q}_w \end{bmatrix} = \begin{bmatrix} \mathbf{q}_o - z\mathbf{q}_\theta - f_\psi \mathbf{q}_\psi \\ \mathbf{q}_w \end{bmatrix} \qquad (5.205)$$

It can be shown that

$$d\mathbf{q}^t\,\ddot{\mathbf{q}} = \left(d\mathbf{q}^t_o - zd\,\mathbf{q}^t_\theta - f_\psi d\mathbf{q}^t_\psi\right)*\left(\ddot{\mathbf{q}}_o - z\,\ddot{\mathbf{q}}_\theta - f_\psi\,\ddot{\mathbf{q}}_\psi\right) + d\mathbf{q}^t_w\,\ddot{\mathbf{q}}_w \qquad (5.206)$$

Expanding the equation above and integrating with respect to z gives:

$$\int\limits_{-h/2}^{h/2} d\mathbf{q}^t\,\ddot{\mathbf{q}}\, dz = h\left(d\mathbf{q}^t_o\,\ddot{\mathbf{q}}_o + d\mathbf{q}^t_w\,\ddot{\mathbf{q}}_w\right) + \frac{h^3}{12} d\mathbf{q}^t_\theta\,\ddot{\mathbf{q}}_\theta + \frac{17\,h^3}{140} d\mathbf{q}^t_\psi\,\ddot{\mathbf{q}}_\psi$$
$$+ \frac{h^3}{10}\left(d\mathbf{q}^t_\theta\,\ddot{\mathbf{q}}_\psi + d\mathbf{q}^t_\psi\,\ddot{\mathbf{q}}_\theta\right) \qquad (5.207)$$

Defining the following displacement components:

$$\mathbf{q}_o(x,y,t) = \mathbf{N}_o(x,y)\,\boldsymbol{\delta}_o(t) \qquad (5.208)$$

$$\mathbf{q}_\theta(x,y,t) = \mathbf{N}_\theta(x,y)\,\boldsymbol{\delta}_b(t) \qquad (5.209)$$

$$\mathbf{q}_\psi(x,y,t) = \mathbf{N}_\psi(x,y)\,\boldsymbol{\delta}_t(t) \tag{5.210}$$

$$\mathbf{q}_w(x,y,t) = \mathbf{N}_w(x,y)\,\boldsymbol{\delta}_b(t) \tag{5.211}$$

$$\mathbf{N}_o(x,y) \equiv \mathbf{N}_o(\xi,\eta) = \begin{bmatrix} \dots & \mathbf{N}_i(\xi,\eta) & 0 & \dots \\ \dots & 0 & \mathbf{N}_i(\xi,\eta) & \dots \end{bmatrix} \tag{5.212}$$

$$\mathbf{N}_\psi(x,y) \equiv \mathbf{N}_\psi(\xi,\eta) = \begin{bmatrix} \dots & 0 & \mathbf{N}_i(\xi,\eta) & \dots \\ \dots & -\mathbf{N}_i(\xi,\eta) & 0 & \dots \end{bmatrix} \tag{5.213}$$

$$\mathbf{N}_w(x,y) \equiv \mathbf{N}_w(\xi,\eta) = \begin{bmatrix} \dots & F_i & H_i & -G_i & P_i & \dots \end{bmatrix}$$

for conforming elements (5.214a)

$$\mathbf{N}_w(x,y) \equiv \mathbf{N}_w(\xi,\eta) = \begin{bmatrix} \dots & F_i & H_i & -G_i & \dots \end{bmatrix}$$

for non-conforming elements (5.214b)

$$\mathbf{N}_\theta(x,y) = \begin{bmatrix} \dfrac{\partial v}{\partial x} \\ \dfrac{\partial w}{\partial y} \end{bmatrix} = \begin{bmatrix} \dots & F_{i,x} & H_{i,x} & -G_{i,x} & P_{i,x} & \dots \\ \dots & F_{i,y} & H_{i,y} & -G_{i,y} & P_{i,y} & \dots \end{bmatrix}$$

for conforming elements (5.215a)

$$\mathbf{N}_\theta(x,y) = \begin{bmatrix} \dfrac{\partial v}{\partial x} \\ \dfrac{\partial w}{\partial y} \end{bmatrix} = \begin{bmatrix} \dots & F_{i,x} & H_{i,x} & -G_{i,x} & \dots \\ \dots & F_{i,y} & H_{i,y} & -G_{i,y} & \dots \end{bmatrix}$$

for non-conforming elements (5.215b)

Equation (5.204) can be rewritten as:

$$dW_a = -\iint_{x-y} \left\{ \begin{array}{l} \rho\, h\, d\boldsymbol{\delta}_o^t \mathbf{N}_o^t \mathbf{N}_o\,\ddot{\boldsymbol{\delta}}_o + \rho\, h\, d\boldsymbol{\delta}_b^t \mathbf{N}_w^t \mathbf{N}_w\,\ddot{\boldsymbol{\delta}}_b \\ + \dfrac{\rho\, h^3}{12} d\boldsymbol{\delta}_b^t \mathbf{N}_\theta^t \mathbf{N}_\theta\,\ddot{\boldsymbol{\delta}}_b + \dfrac{17\,\rho\, h^3}{140} d\boldsymbol{\delta}_t^t \mathbf{N}_\psi^t \mathbf{N}_\psi\,\ddot{\boldsymbol{\delta}}_t \\ + \dfrac{\rho\, h^3}{10}\left(d\boldsymbol{\delta}_b^t \mathbf{N}_\theta^t \mathbf{N}_\psi\,\ddot{\boldsymbol{\delta}}_t + d\boldsymbol{\delta}_t^t \mathbf{N}_\psi^t \mathbf{N}_\theta\,\ddot{\boldsymbol{\delta}}_b \right) \end{array} \right\} dxdy \tag{5.216}$$

Defining the following mass matrices:

$$\mathbf{M}_{oo} = \iint_{x-y} \rho\, h\, \mathbf{N}_o^t(\xi,\eta)\,\mathbf{N}_o(\xi,\eta)\, dxdy \tag{5.217}$$

$$\mathbf{M}_{ww} = \iint_{x-y} \rho\, h\, \mathbf{N}_w^t(\xi,\eta)\,\mathbf{N}_w(\xi,\eta)\, dxdy \tag{5.218}$$

$$\mathbf{M}_{\theta\theta} = \iint_{x-y} \frac{\rho\, h^3}{12}\, \mathbf{N}_\theta^t(\xi,\eta)\,\mathbf{N}_\theta(\xi,\eta)\, dxdy \tag{5.219}$$

$$\mathbf{M}_{\psi\psi} = \iint_{x-y} \frac{17\,\rho\,h^3}{140}\,\mathbf{N}_{\psi}^{t}\,(\xi,\,\eta)\,\mathbf{N}_{\psi}\,(\xi,\,\eta)\,dxdy \tag{5.220}$$

$$\mathbf{M}_{\psi\theta} = \iint_{x-y} \frac{\rho\,h^3}{10}\,\mathbf{N}_{\psi}^{t}\,(\xi,\,\eta)\,\mathbf{N}_{\theta}\,(\xi,\,\eta)\,dxdy \tag{5.221}$$

$$\mathbf{M}_{\theta\psi} = \iint_{x-y} \frac{\rho\,h^3}{10}\,\mathbf{N}_{\theta}^{t}\,(\xi,\,\eta)\,\mathbf{N}_{\psi}\,(\xi,\,\eta)\,dxdy \equiv \mathbf{M}_{\psi\theta}^{t} \tag{5.222}$$

Equation (5.216) can be rewritten as:

$$dW_a = -\left\{ \begin{array}{l} d\boldsymbol{\delta}_{o}^{t}\mathbf{M}_{oo}\,\ddot{\boldsymbol{\delta}}_{o} + d\boldsymbol{\delta}_{b}^{t}\big[\mathbf{M}_{ww} + \mathbf{M}_{\theta\theta}\big]\ddot{\boldsymbol{\delta}}_{b} + d\boldsymbol{\delta}_{t}^{t}\mathbf{M}_{\psi\psi}\,\ddot{\boldsymbol{\delta}}_{t} \\[2mm] + \left(d\boldsymbol{\delta}_{b}^{t}\mathbf{M}_{\theta\psi}\,\ddot{\boldsymbol{\delta}}_{t} + d\boldsymbol{\delta}_{t}^{t}\mathbf{M}_{\psi\theta}\,\ddot{\boldsymbol{\delta}}_{b} \right) \end{array} \right\} \tag{5.223}$$

$$\equiv -d\boldsymbol{\delta}^{t}\mathbf{M}\,\ddot{\boldsymbol{\delta}}$$

Hence it can be shown that the element mass matrix is as given below:

$$\mathbf{M} = \begin{bmatrix} \mathbf{M}_{oo} & \mathbf{0} & \mathbf{0} \\ \mathbf{0} & \mathbf{M}_{ww} + \mathbf{M}_{\theta\theta} & \mathbf{M}_{\theta\psi} \\ \mathbf{0} & \mathbf{M}_{\psi\theta} & \mathbf{M}_{\psi\psi} \end{bmatrix} \tag{5.224}$$

6 Finite Element Programming

This chapter explains the unique and innovative programming concepts developed for the FE analysis of functionally graded composites. During the literature review for this work, it was discovered that there were very little literature on FE analysis of functionally graded composites. Chen and Liew (2004) actually admitted that FE method for functionally graded composites leads to complicated numerical procedures. A breakdown of the innovative concepts in this work is given below.

- A special FGM element has been derived which is a modification of the Reissner and Mindlin plate bending element. This special element further develops the Reissner and Mindlin plate bending element theory to account for the D-matrix in the element stiffness matrix as a function of fibre ratio distribution. The advantage of this special element is not only in its usefulness in analysing FGMs but also in its capability to be interfaced into existing commercial software for the analysis of FGMs.

- Two techniques were employed in computing the element stiffness matrix. These techniques include the averaging technique and smoothing technique. The averaging technique is a simple concept which involves computing an average fibre ratio per element. While the smoothing technique involves the computation of the fibre ratio at the Gaussian quadrature points which is then used directly in the computation of the element stiffness matrix. During the case studies, it was demonstrated that as the mesh becomes finer, the result of the averaging technique converges to the result of the smoothing technique.

The structure of the FE code implemented in this thesis is as shown below. The aim of this chapter is to give an in-depth explanation of the FE code. As a result, this chapter focuses on the explanation of each block in the flow chart shown below.
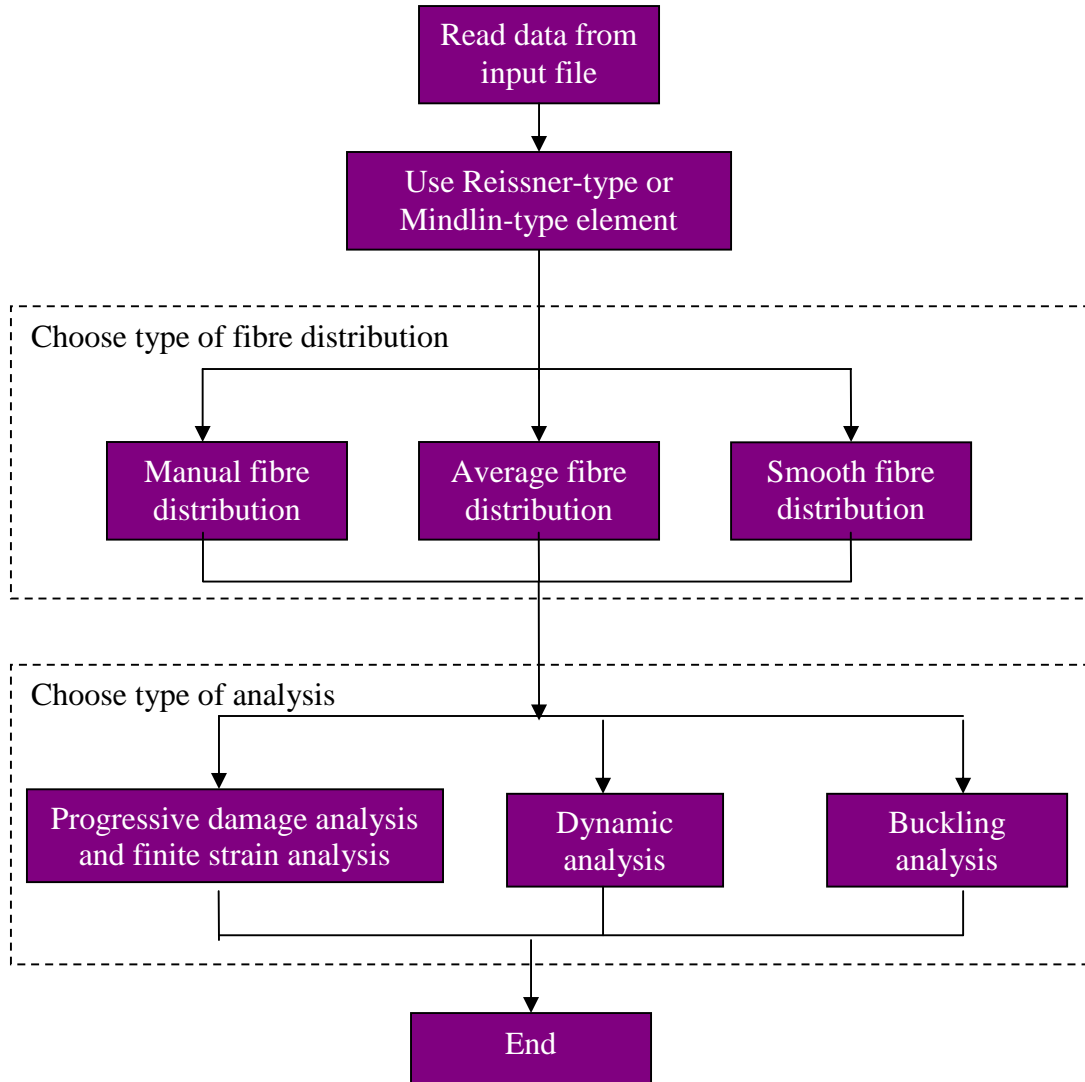
Figure 6-1: FE code structure

6.1 Static Analysis Algorithm

In order to carry out static analysis of composites, the code user needs to identify a suitable element to use in solving the problem. Table 6-1 shows the description of different types of static analysis codes developed in this thesis.

Table 6-1: Static analysis code description

Code	Description
AV-CONF-STA.FOR	Static analysis of composites using average conforming Reissner-type element.
AV-NONCONF-STA.FOR	Static analysis of composites using average non-conforming Reissner-type element.
SM-CONF-STA.FOR	Static analysis of composites using smooth conforming Reissner-type element.
SM-NONCONF-STA.FOR	Static analysis of composites using smooth non-conforming Reissner-type element.
AV-MIND-STA.FOR	Static analysis of composites using average Mindlin-type element.
SM-MIND-STA.FOR	Static analysis of composites using smooth Mindlin-type element.

The subroutines used in developing the static analysis codes will now be explained. In the static analysis codes, there are calls to subroutines which have been listed below in the order of calling sequence.

- SET FILE
- DATA
- LINEARAN
- NONLINEAR

SET FILE

This subroutine sets input and output files.

<u>DATA</u>

The input file (*.DAT) is divided into a number of modules, each is recognized by a single control word. The DATA subroutine reads the input file and recognizes its modules through the calls of different subroutine for each input module, as follows:

ELEMID: Identifies the number of coordinates, number of degree of freedom and element type.

NODE: Reads the nodal coordinates from the input data file (*.DAT) and writes out this coordinates to an output data file (*.OUT).

ELEMENT: Reads the element topology from the input data file and writes out this element topology to an output data file.

COMPOS: Reads the fibre and matrix properties. It also reads the number of layers, thickness of layers and fibre direction.

FUNGRADED: Reads the fibre distribution and calculates the average fibre ratio for every element as shown below.

- Computes V_{f2} using $V_{f2} = V_{f1} + (P+1)*(\overline{V}_f - V_{f1})$

- Computes the average fibre ratio per element $\overline{V}_f(\xi)$ using

$$\overline{V}_f(\xi) = V_1 + (V_2 - V_1)\frac{(\xi_{max}^{p+1} - \xi_{min}^{p+1})}{(\xi_{max} - \xi_{min})(p+1)}$$

- Calls MICROMECHANICS subroutine to calculate composite material properties using micromechanics equations.

BOUNDARY: Reads the number of boundary conditions, number of degree of freedom, prescribed displacement, number of nodes with boundary conditions and list of nodes with boundary conditions.

LOAD: Reads the number of loaded nodes, number of load increments and direction of rotation. It also reads the list of loaded nodes and the corresponding applied loads.

STATIC: Reads the type of analysis, maximum number of iteration, permissible error and relaxation factor.

DYNAMIC: Reads the type of eigenvalue analysis, number of eigenvalues, maximum number of iterations and permissible error.

GAUSSDATA: Reads the number of Gauss quadrature points.

SOUT: Reads the list of nodes for displacement output and stress output.

FACETS: This subroutine is used for facet elements.

SET AXES: Defines local axes for facet elements.

BWF: This is subroutine is based upon calculating MD, the maximum difference between node numbers inside an element, for all of the elements. The bandwidth for assembled matrices is the calculated from MD, and the number of degrees-of-freedom per node.

DLOAD: Computes the element equivalent loading to a uniformly distributed pressure.

RLOAD: Computes the element equivalent loading to rotation with uniform speed.

<u>LINEARAN</u>

The flow chart for linear static analysis of composites using is as shown below.

```
┌─────────────────────────────────┐
│     Read data from input file   │
└─────────────────────────────────┘
                 │
                 ▼
┌─────────────────────────────────┐
│       K_G = ASSEMBLER           │
└─────────────────────────────────┘
                 │
                 ▼
┌─────────────────────────────────┐
│       K_R = REDUCER             │
└─────────────────────────────────┘
       │         │         │
       ▼         ▼         ▼
┌───────────┐ ┌───────────┐ ┌───────────┐
│ Gaussian  │ │  Banded   │ │  Frontal  │
│Elimination│ │ Gaussian  │ │ Gaussian  │
│  Solver   │ │  Solver   │ │  Solver   │
└───────────┘ └───────────┘ └───────────┘
                 │
                 ▼
┌─────────────────────────────────────────┐
│ ε_S = LNSTRAING and ε_S = LNSTRAINN     │
└─────────────────────────────────────────┘
                 │
                 ▼
┌─────────────────────────────────────────┐
│ ε_L = NLSTRAING and ε_L = NLSTRAINN     │
└─────────────────────────────────────────┘
                 │
                 ▼
┌─────────────────────────────────┐
│       R_G = RESIDUAL            │
└─────────────────────────────────┘
                 │
                 ▼
┌─────────────────────────────────┐
│       F_G = REACT               │
└─────────────────────────────────┘
                 │
                 ▼
┌─────────────────────────────────┐
│        ε = STRAIN               │
└─────────────────────────────────┘
                 │
                 ▼
┌─────────────────────────────────┐
│        σ = STRESS               │
└─────────────────────────────────┘
                 │
                 ▼
┌─────────────────────────────────┐
│            End                  │
└─────────────────────────────────┘
```
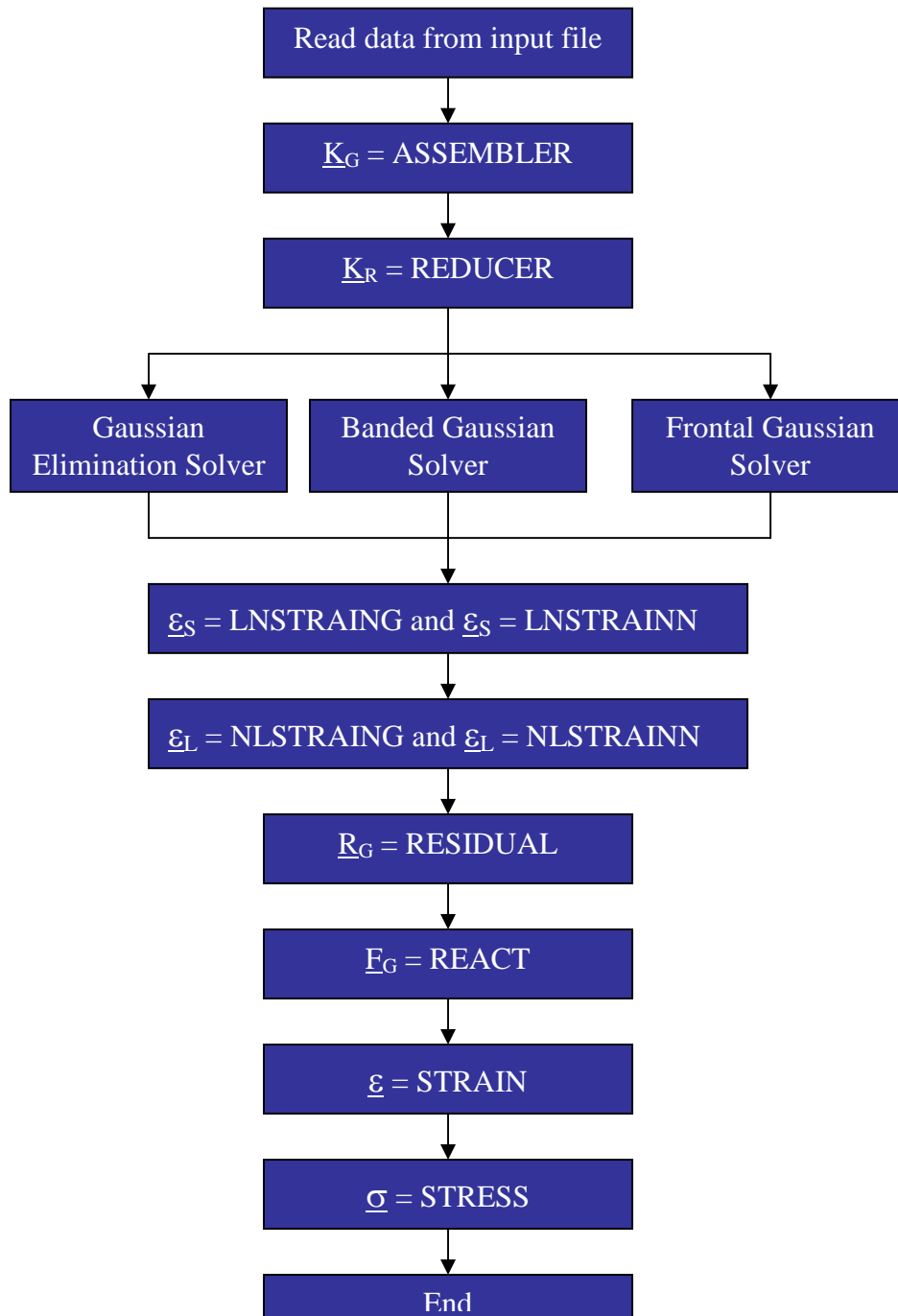
Figure 6-2: Linear static analysis flowchart

In the LINEARAN subroutine, there were calls to subroutines which have been listed below in the order of calling sequence.

ELEM1D: Identifies the number of coordinates, number of degree of freedom and element type.

ASSEMBLER: Assembles the global stiffness matrix.

REDUCER: Computes the reduced force vector and the reduced stiffness matrix by applying the prescribed displacements of the boundary condition to the equation of the whole domain.

SOLVER: Computes the reduced displacement vector by using Gaussian elimination method.

OEXPANDERL: Assembles the global displacement vector by combining the reduced displacement vector and the prescribed displacements.

DISP: Writes the nodal displacement results into an output file.

LNSTRAING: Computes midplane infinitesimal strains at Gaussian quadrature points.

LNSTRAINN: Computes midplane infinitesimal strains averaged at nodes.

RESIDUAL: Computes the global residual vector.

REACT: Writes the nodal forces and nodal reactions to an output file.

STRAIN: Writes the nodal strain results with respect to the material axis and the local axis to an output file.

STRESS: Writes the nodal stress results with respect to the material axes and the local axes to an output file.

The flow chart for non-linear static analysis of composites with material degradation and geometric non-linearity is as shown below.
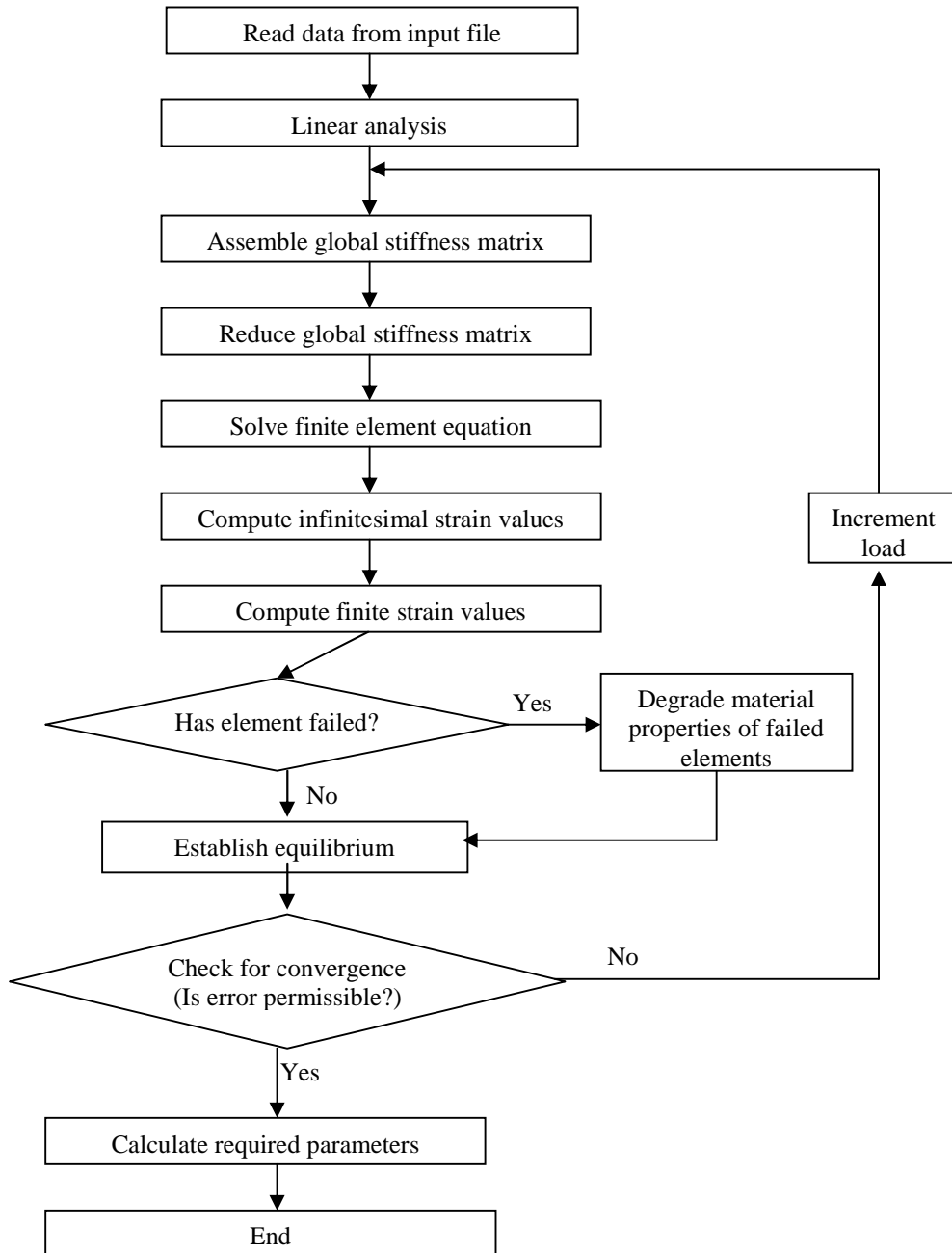

Figure 6-3: Nonlinear static analysis flowchart

In the NONLINEAR subroutine, there were calls to subroutines which have been listed below in the order of calling sequence.

ELEM1D: Identifies the number of coordinates, number of degree of freedom and element type.

ASSEMBLER: Assembles the global stiffness matrix.

REDUCER: Computes the reduced force vector and the reduced stiffness matrix by applying the prescribed displacements of the boundary condition to the equation of the whole domain.

SOLVER: Computes the reduced displacement vector by using Gaussian elimination method.

OEXPANDER: Assembles the global displacement vector by combining the reduced displacement vector and the prescribed displacements. It also uses load increment and relaxation factor parameters to assemble the global displacement vector.

LNSTRAING: Computes midplane infinitesimal strains at Gaussian quadrature points.

LNSTRAINN: Computes midplane infinitesimal strains averaged at nodes.

NLSTRAING: Computes midplane finite strains at Gaussian quadrature points.

NLSTRAINN: Computes midplane finite strains averaged at nodes.

FAIL ASSESS: Performs failure assessment by using either Tsai-Hill criteria, Tsai-Wu criteria either Hoffman criteria.

RESIDUAL: Computes the global residual vector.

CONVERGENCE: Performs convergence check for nonlinear static iterations.

UPDATE: Updates the global force vector by removing the global residual vector values from the global force vector values.

DISP: Writes the nodal displacement results into an output file.

REACT: Writes the nodal forces and nodal reactions to an output file.

STRAIN: Writes the nodal strain results with respect to the material axis and the local axis to an output file.

STRESS: Writes the nodal stress results with respect to the material axes and the local axes to an output file.

6.2 Buckling Analysis Algorithm

Buckling occurs at infinitesimal strains.

$$\begin{aligned}
\boldsymbol{\sigma}_{\text{L}} &\Rightarrow \mathbf{0} \\
\mathbf{F}_{\text{L}} &\Rightarrow \mathbf{0} \\
\boldsymbol{\sigma}_{\text{m}} &= \mathbf{D}_{\text{oo}}\boldsymbol{\varepsilon}_{\text{o}} - \mathbf{D}_{\text{ob}}\boldsymbol{\varepsilon}_{\text{b}} \\
\boldsymbol{\sigma}_{\theta} &= \mathbf{D}_{\text{bb}}\boldsymbol{\varepsilon}_{\text{o}} - \mathbf{D}_{(3)}\boldsymbol{\varepsilon}_{\text{b}} \\
\boldsymbol{\sigma}_{\text{m}\theta} &= -\mathbf{D}_{\text{ob}}\boldsymbol{\varepsilon}_{\text{o}} - \mathbf{D}_{\text{bb}}\boldsymbol{\varepsilon}_{\text{b}}
\end{aligned}$$

(6.1)

A small deflection analysis can be carried out with a small load representing the distribution of actual load, and has equivalent nodal loading vector $\mathbf{F}_{\text{o}}$ which is defined below.

$$\mathbf{F}_{\text{o}} = \mathbf{K}\boldsymbol{\delta}_{\text{o}}$$

(6.2)

Just before the onset of instability, the strains can be considered infinitesimal, and if instability occurs at:

$$\mathbf{F} = \lambda\mathbf{F}_{\text{o}}$$

(6.3)

Hence

$$\begin{aligned}
\left\{\mathbf{K} + \lambda\mathbf{K}^{\sigma}(\sigma_{\text{o}})\right\}\boldsymbol{\delta} &\Rightarrow \mathbf{0} \\
\left|\mathbf{K} + \lambda\mathbf{K}^{\sigma}(\sigma_{\text{o}})\right| &= 0
\end{aligned}$$

(6.4)

This gives a characteristic equation and its smallest real roots define the critical buckling load.

$$\mathbf{F}_{\text{critical}} = \lambda_{\min}\mathbf{F}_{\text{o}}$$

(6.5)

Buckling analysis to find $\lambda_{\min}$ is similar to natural frequency analysis with a hypothetical mass matrix defined as: $\mathbf{M} = -\mathbf{K}^{o}$.

Table 6-2 shows the description of different types of buckling analysis codes developed in this report.

Table 6-2: Buckling analysis code description

Code	Description
AV-NONC-BUC.FOR	Buckling analysis of composites using average non-conforming Reissner-type element.
AV-CONF-BUC.FOR	Buckling analysis of composites using average conforming Reissner-type element.
SM-NONC-BUC.FOR	Buckling analysis of composites using smooth non-conforming Reissner-type element.
SM-CONF-BUC.FOR	Buckling analysis of composites using smooth conforming Reissner-type element.
AV-MIND-BUC.FOR	Buckling analysis of composites using average Mindlin-type element.
SM-MIND-BUC.FOR	Buckling analysis of composites using smooth Mindlin-type element.

The subroutines used in developing the buckling analysis codes will now be explain. In the buckling analysis codes, there were calls to subroutines which have been listed below in the order of calling sequence.

- SET FILE
- DATA
- LINEARAN
- SUBSPACE

SET FILE

This subroutine has been explained in the static analysis algorithm.

DATA

This subroutine has been explained in the static analysis algorithm.

<u>LINEARAN</u>

This subroutine has been explained in the static analysis algorithm.

<u>SUBSPACE</u>

In the SUBSPACE subroutine, there were calls to subroutines which have been listed below in the order of calling sequence.

DASSEMBLER: Assembles the global mass matrix.

DREDUCER: Computes the reduced force vector and the reduced stiffness matrix by applying the prescribed displacements of the boundary condition to the equation of the whole domain.

DSOLVER: Solves the simultaneous equations using Choleski direct procedure.

TPRODUCT: computes the subspace stiffness matrix and the outer-shifted stiffness matrix. It also computes the subspace mass matrix and the reduced banded mass matrix.

EIGENV: Computes eigenvalues using simple iteration algorithm.

TRANSF: Computes the band product.

DOUTPUT: Writes the dynamic result values into an output file.

Further explanation of the subspace iteration algorithm will be described now. If the matrix equation

$$\underline{K} \, \tilde{\underline{\delta}} = \lambda \, \underline{M} \, \tilde{\underline{\delta}}$$ (6.6)

has $\underline{K}$ and $\underline{M}$ with a very large order and only relatively few eigenvalues are required, subspace, or simultaneous iteration provides a very economical eigenvalue solver. The method is based upon reducing $\underline{K}$ and $\underline{M}$ whilst restraining the lowest eigenvalues.

The subspace iteration algorithm consists of the following steps.

1. Assume a set of load vectors:

$$\underline{Y}_{m*p} = [\, y_1 \quad y_2 \quad ... \quad y_p \,]$$ (6.7)

where y_r is a vector of order m, r = 1, 2, …, p

m is the total number of unknowns, or the order of the stiffness and mass matrices of the component,

p is the number of the required lowest eigenvalues.

A reasonable guess is to take $Y_{rs} = \delta_{rs}$.

2. Solve the following p sets of equations, using a static analysis solver.

$$\underline{K}_{m*m}\ \underline{\delta}_r = y_r \tag{6.8}$$

for   r = 1, 2, ..., p

3. Form the following rectangular matrix of eigenvectors:

$$\underline{X}_{m*p} = [\tilde{\delta}_1 \quad \tilde{\delta}_2 \quad ... \quad \tilde{\delta}_p] \tag{6.9}$$

4. Obtain the reduced or subspace stiffness and mass matrices as follows:

$$\underline{K}^*_{p*p} = (\underline{X}^t)_{p*m}\ \underline{K}_{m*m}\ \underline{X}_{m*p}$$
$$\underline{M}^*_{p*p} = (\underline{X}^t)_{p*m}\ \underline{M}_{m*m}\ \underline{X}_{m*p} \tag{6.10}$$

5. Solve the subspace, or reduced, eigenvalue problem:

$$\underline{K}^*_{p*p}\ \tilde{\underline{\delta}}^*_{p*1} = \lambda\ \underline{M}^*_{p*p}\ \tilde{\underline{\delta}}^*_{p*1} \tag{6.11}$$

using any standard eigenvalue solver, such as simple iteration algorithm.

6. Form the following square matrix of the reduced eigenvectors:

$$\underline{X}_{p*p} = [\tilde{\delta}_1^* \quad \tilde{\delta}_2^* \quad ... \quad \tilde{\delta}_9^*] \tag{6.12}$$

7. Transform back to the original space, i.e.

$$(\underline{X}_{m*p})_{new} = (\underline{X}_{m*p})_{old}\ \underline{X}^*_{p*p} \tag{6.13}$$

8. Update the load vectors, using:

$$(\underline{Y}_{m*p})_{new} = \underline{M}_{m*m}\ (\underline{X}_{m*p})_{new} \tag{6.14}$$

9. Iteration decision:

- Calculate the maximum error in the eigenvalues i.e.

$$e_{max} = Max\ \left(\left|\lambda_{i_{new}} - \lambda_{i_{old}}\right|, i = 1, 2, ..., p\right) \tag{6.15}$$

- If the maximum error is greater than a given permissible error then go to step-2.

6.3 Dynamic Analysis Algorithm

Consider an ideal structure with no damping forces, the dynamic finite element matrix equation can be reduced to the expression below.

$$\mathbf{M}\ddot{\boldsymbol{\delta}}(t) + \mathbf{K}\boldsymbol{\delta}(t) = \mathbf{F}(t) \qquad (6.17)$$

In a natural mode, each point of a structure executes harmonic motion about the position of static equilibrium at the same frequency. Hence it can be assumed that, at a natural mode of vibration:

$$\boldsymbol{\delta}(t) = \tilde{\boldsymbol{\delta}}\cos(\omega t) \qquad (6.18)$$

where $\underset{\sim}{\tilde{\delta}}$ represents the vector of nodal amplitudes.

The matrix equation represents a system of homogenous simultaneous equations which can have a non-trivial solution, if the value of λ satisfies the condition below:

$$|\mathbf{K} - \lambda\mathbf{M}| = 0 \qquad (6.19)$$

where $\lambda = \omega^2$

The matrix equation of the dynamic eigenvalue problem was solved in this report. This report employed two techniques which include the simple iteration and subspace iteration techniques. Further details on these techniques can be found in publications of Clint and Jennings (1970), Corr and Jennings (1976), Bathe and Wilson (1976).

Table 6-3 shows the description of different types of dynamic analysis codes developed in this thesis.

Table 6-3: Dynamic analysis code description

Code	Description
AV-NONC-DYN.FOR	Dynamic analysis of composites using average non-conforming Reissner-type element.
AV-CONF-DYN.FOR	Dynamic analysis of composites using average conforming Reissner-type element.
SM-NONC-DYN.FOR	Dynamic analysis of composites using smooth non-conforming Reissner-type element.
SM-CONF-DYN.FOR	Dynamic analysis of composites using smooth conforming Reissner-type element.
AV-MIND-DYN.FOR	Dynamic analysis of composites using average Mindlin-type element.
SM-MIND-DYN.FOR	Dynamic analysis of composites using smooth Mindlin-type element.

The subroutines used in developing the dynamic analysis codes will now be explain. In the dynamic analysis codes, there were calls to subroutines which have been listed below in the order of calling sequence and they have similar descriptions as that of the buckling analysis subroutines.

- SET FILE
- DATA
- LINEARAN
- NONLINEAR
- ELEMID
- SUBSPACE

7 Mindlin and Reissner Program Validation

In this chapter, the Mindlin programs (i.e. Average and Smooth Mindlin program) and Reissner programs (i.e. Average and Smooth Reissner program) were validated. These programs were validated in three stages which include program validation against analytical solutions, program validation against a commercial package called Abaqus and program validation against Ordinary FE programs (i.e. Ordinary Mindlin program and Ordinary Reissner program). The Ordinary FE programs are programs developed in-house for the finite element analysis of structures made of composite materials without functional gradation. This chapter aims to present the three stages of validation exercises.

7.1 Program Validation against Analytical Solution

In this section, the Mindlin programs (i.e. Average and Smooth Mindlin program) were validated against analytical solution. The analytical solution presented in this section is often referred to as the classical lamination theory (CLT). A more in-depth explanation of the theory can be found in a publication by Agarwal et al (2006). The analytical solution could only be used to validate the infinitesimal strain part of the Mindlin programs for the analysis of composite without functional gradation. Also, the progressive damage capability of the Average Mindlin program was not validated because damage prediction in the Mindlin programs uses a different approach in comparison to the analytical technique. In the Mindlin programs, damage prediction is done for each element but the analytical technique can only predict damage for each composite lamina. In this section, some numerical examples will be presented for this validation exercise. These numerical examples include composite plate subjected to tensile load, composite plate subjected to buckling load, free vibration of composite plate and composite plate with a central hole subjected to tensile load. In order to solve these numerical examples, the following solution technique is employed.

Consider a lamina parallel to the x-y plane with (x-y-z) being the geometrical axes. Axes (1-2-3) represent the material axes, where 1 is usually in the fibre direction. The lamina

is orthotropic with respect to (1-2-3) axes. Using generalised Hooke's equations, it can be deduced that:

$$\begin{bmatrix} \sigma_1 \\ \sigma_2 \\ \tau_{12} \end{bmatrix} = Q \begin{bmatrix} \varepsilon_1 \\ \varepsilon_2 \\ \gamma_{12} \end{bmatrix} \tag{7.1}$$

where

$$Q = \frac{1}{1 - \nu_{12}\nu_{21}} \begin{bmatrix} E_{11} & \nu_{21}E_{11} & 0 \\ \nu_{12}E_{22} & E_{22} & 0 \\ 0 & 0 & (1 - \nu_{12}\nu_{21})\mu_{12} \end{bmatrix} \tag{7.2}$$

where E_{11} is the Young's modulus in the "1" or fibre direction.

                E_{22} is the Young's modulus in the "2" direction.

                μ_{12} is the shear modulus in the material axes (i.e. axes 1-2).

                ν_{12} and ν_{21} are the major and minor Poisson's ratio respectively.

Using planar transformation for a lamina, it can be deduced that:

$$\overline{Q}_{11} = l^4 Q_{11} + m^4 Q_{22} + 2l^2 m^2 \left(Q_{12} + 2Q_{33} \right) \tag{7.3}$$

$$\overline{Q}_{22} = l^4 Q_{22} + m^4 Q_{11} + 2l^2 m^2 \left(Q_{12} + 2Q_{33} \right) \tag{7.4}$$

$$\overline{Q}_{12} = \overline{Q}_{21} = \left(l^4 + m^4 \right)Q_{12} + l^2 m^2 \left(Q_{11} + Q_{22} - 4Q_{33} \right) \tag{7.5}$$

$$\overline{Q}_{33} = \left(l^2 - m^2 \right)^2 Q_{33} + l^2 m^2 \left(Q_{11} + Q_{22} - 2Q_{12} \right) \tag{7.6}$$

$$\overline{Q}_{13} = \overline{Q}_{31} = l\,m \left[l^2 Q_{11} - m^2 Q_{22} - \left(l^2 - m^2 \right)(Q_{12} + 2Q_{33}) \right] \tag{7.7}$$

$$\overline{Q}_{23} = \overline{Q}_{32} = l\,m \left[m^2 Q_{11} - l^2 Q_{22} + \left(l^2 - m^2 \right)(Q_{12} + 2Q_{33}) \right] \tag{7.8}$$

where $l = \cos\theta$ and $m = \sin\theta$

                θ = fibre orientation of lamina

Composite laminates are constructed of an arbitrary number of orthotropic lamina with planes elastic symmetry in the plane of the laminate. In order to describe the behaviour of the laminate, it is necessary to define the laminate force and moment resultants.

Three force resultants:

$$(N_x, N_y, N_{xy}) = \int_{-h/2}^{h/2} (\sigma_x, \sigma_y, \tau_{xy})\, dz \qquad (7.9)$$

Three moment resultants:

$$(M_x, M_y, M_{xy}) = \int_{-h/2}^{h/2} (\sigma_x, \sigma_y, \tau_{xy})\, z\, dz \qquad (7.10)$$

where h is the laminate thickness and z is the normal coordinate measured from the laminate mid-surface.

Since laminate strains are assumed in classical lamination theory to vary linearly through the laminate thickness, the strain at any point through the laminate thickness can be expressed as a function of laminate midplane strains, ε^o and curvatures, $\boldsymbol{k}$.

$$\varepsilon = \varepsilon^o + z\,\boldsymbol{k} \qquad (7.11)$$

Now the force and moment resultants can be expressed in terms of the midplane strains and curvatures of the laminate.

$$\begin{aligned} \boldsymbol{N} &= \boldsymbol{A}\,\varepsilon^o + \boldsymbol{B}\,\boldsymbol{k} \\ \boldsymbol{M} &= \boldsymbol{B}\,\varepsilon^o + \boldsymbol{D}\,\boldsymbol{k} \end{aligned} \qquad (7.12)$$

where the laminate stiffness matrix terms are defined in terms of the lamina properties.

$$\begin{aligned} A_{ij} &= \sum_{l=1}^{N_l} \overline{Q}_{ij}^{\,l} (h_l - h_{l-1}) \\ B_{ij} &= \frac{1}{2} \sum_{l=1}^{N_l} \overline{Q}_{ij}^{\,l} (h_l^2 - h_{l-1}^2) \\ D_{ij} &= \frac{1}{3} \sum_{l=1}^{N_l} \overline{Q}_{ij}^{\,l} (h_l^3 - h_{l-1}^3) \end{aligned} \qquad (7.13)$$

7.1.1 Traditional composite plate under tensile loading

Example 7.1.1: A rectangular traditional composite plate with a "[[-45/0/45]$_2$]$_s$" stacking sequence was subjected to a tensile loading of 240kN. The task is to validate the displacement and stress result of the Average Mindlin program against the result of the classical lamination theory. The FE modelling procedure and the analytical solution procedure is presented for this example.

The geometrical properties, micro-mechanical properties and loading condition are as given below. The micromechanical data were obtained from a textbook by Kaw (1997).

Table 7-1: Tensile case data

Geometry					
L (m)	2.000	w (m)	1.000		
t (m)	0.0300	No. of ply	12		
Fibre and matrix properties					
E_f (Pa)	2.300E+11	v_f	3.500E-01	μ_f (Pa)	8.519E+10
E_m (Pa)	3.400E+09	v_m	3.000E-01	μ_m (Pa)	1.308E+09
V_f	0.4	V_m	0.6		
Applied Force					
F_x (N)	2.400E+05	N_x (N/m)	2.400E+05		
N_y (N/m)	0.000E+00	N_{xy} (N/m)	0.000E+00		

The notations used in Table 7-1 are as described below.

L, w, and t, represent the length, width, thickness of ply respectively.

E_f and E_m represent the Young's modulus of the fibre and matrix respectively.

v_f and v_m represent the Poisson's ratio of the fibre and matrix respectively.

μ_f and μ_m represent the shear modulus of the fibre and matrix respectively.

V_f and V_m represent the volume fraction of the fibre and matrix respectively.

F_x represents the applied force in the x-direction.

N represents the distributed load.

The composite plate has a mid-plane as shown in Figure 7-1. Different meshes were employed in this example to check for convergence. A mesh with 72 four-noded Mindlin-type elements was selected and is as shown in Figure 7-1. A tensile load of 240kN was applied as an equivalent nodal loads at the nodes on the x=2 edge with reduced load at the corner nodes. For example, in the 72 element case, the load was applied equally at nodes on the x=2 edge but with half the loads at the corner nodes on the x=2 edge as shown in Figure 7-1. Hence the equivalent nodal loading for the 72 element case was 40kN at each nodes on the x=2 edge with 20kN at corner nodes on the x=2 edge. The boundary condition shown in Table 7-2 was applied to the FE model.

Table 7-2: Boundary condition for the tensile case

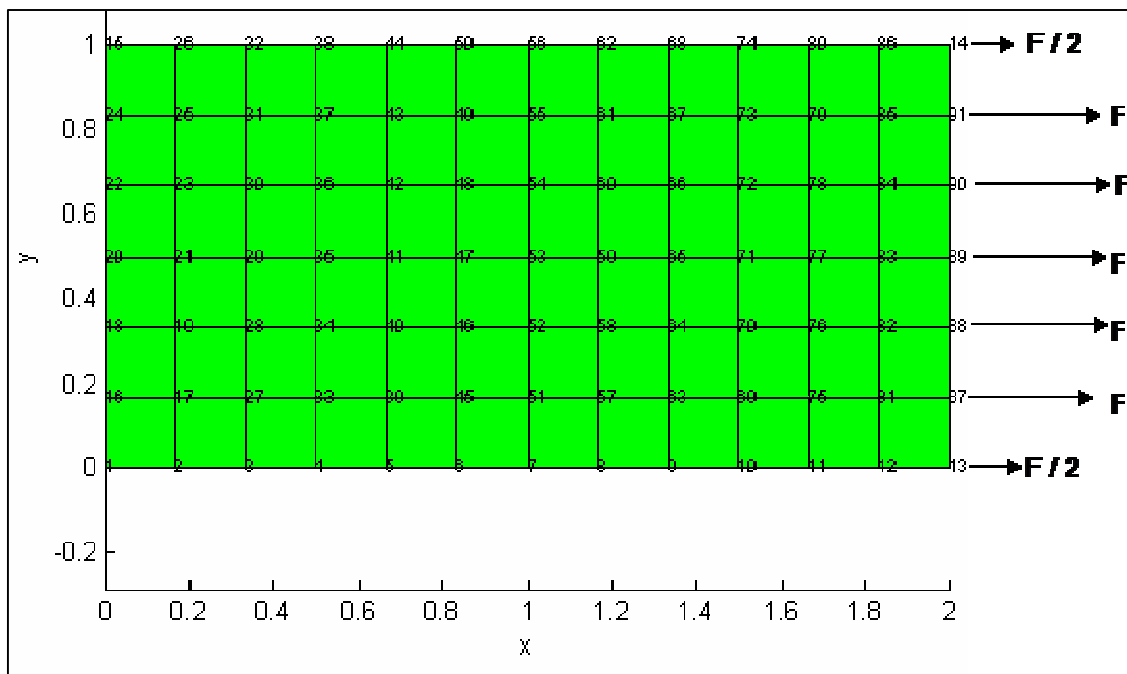| Nodes	Boundary condition
Node 20	$u = v = w = \theta_x = \theta_y = 0$
Nodes on the x=0 edge excluding node 20	$u = 0$

Figure 7-1: 4-noded element mesh for the tensile case

<u>Analytical Solution</u>

Using the macro-mechanical equations (i.e. Equations 3.1 to 3.4) and the classical lamination theory (i.e. Equations (7.1) – (7.13)), the deformation of the composite plate was computed with Excel Spreadsheet as shown in Table 7-3.

Table 7-3: Analytical solution for the tensile case

Elastic constants						
	E_{11} (Pa)	9.404E+10	ν_{12}	3.200E-01	μ_{12} (Pa)	2.157E+09
	E_{22} (Pa)	5.611E+09	ν_{21}	1.909E-02		

Stiffness matrix						
	Q (Pa)	9.462E+10	1.807E+09	0.000E+00		
		1.807E+09	5.646E+09	0.000E+00		
		0.000E+00	0.000E+00	2.157E+09		

Ply p	1	2	3	4	5	6
θ (°)	-45	0	45	-45	0	45
Z_{p-1} (m)	-0.015	-0.0125	-0.01	-0.0075	-0.005	-0.0025
Z_p (m)	-0.0125	-0.01	-0.0075	-0.005	-0.0025	0
$Z_p - Z_{p-1}$ (m)	0.0025	0.0025	0.0025	0.0025	0.0025	0.0025
$Z_p^2 - Z_{p-1}^2$ (m)	-6.875E-05	-5.625E-05	-4.375E-05	-3.125E-05	-1.875E-05	-6.250E-06
$Z_p^3 - Z_{p-1}^3$ (m)	1.422E-06	9.531E-07	5.781E-07	2.969E-07	1.094E-07	1.563E-08
$Q_{11\_}$ (Pa)	2.813E+10	9.462E+10	2.813E+10	2.813E+10	9.462E+10	2.813E+10
$Q_{22\_}$ (Pa)	2.813E+10	5.646E+09	2.813E+10	2.813E+10	5.646E+09	2.813E+10
$Q_{12\_}$ (Pa)	2.381E+10	1.807E+09	2.381E+10	2.381E+10	1.807E+09	2.381E+10
$Q_{66\_}$ (Pa)	2.416E+10	2.157E+09	2.416E+10	2.416E+10	2.157E+09	2.416E+10
$Q_{16\_}$ (Pa)	-2.224E+10	0.000E+00	2.224E+10	-2.224E+10	0.000E+00	2.224E+10
$Q_{26\_}$ (Pa)	-2.224E+10	0.000E+00	2.224E+10	-2.224E+10	0.000E+00	2.224E+10

Table 7-3: Analytical solution for the tensile case (continued)

Ply p	7	8	9	10	11	12
θ (^{o})	45	0	-45	45	0	-45
Z_{p-1} (m)	0	0.0025	0.005	0.0075	0.01	0.0125
Z_p (m)	0.0025	0.005	0.0075	0.01	0.0125	0.015
$Z_p - Z_{p-1}$ (m)	0.0025	0.0025	0.0025	0.0025	0.0025	0.0025
$Z_p^2 - Z_{p-1}^2$ (m)	6.250E-06	1.875E-05	3.125E-05	4.375E-05	5.625E-05	6.875E-05
$Z_p^3 - Z_{p-1}^3$ (m)	1.563E-08	1.094E-07	2.969E-07	5.781E-07	9.531E-07	1.422E-06
$Q_{11\_}$ (Pa)	2.813E+10	9.462E+10	2.813E+10	2.813E+10	9.462E+10	2.813E+10
$Q_{22\_}$ (Pa)	2.813E+10	5.646E+09	2.813E+10	2.813E+10	5.646E+09	2.813E+10
$Q_{12\_}$ (Pa)	2.381E+10	1.807E+09	2.381E+10	2.381E+10	1.807E+09	2.381E+10
$Q_{66\_}$ (Pa)	2.416E+10	2.157E+09	2.416E+10	2.416E+10	2.157E+09	2.416E+10
$Q_{16\_}$ (Pa)	2.224E+10	0.000E+00	-2.224E+10	2.224E+10	0.000E+00	-2.224E+10
$Q_{26\_}$ (Pa)	2.224E+10	0.000E+00	-2.224E+10	2.224E+10	0.000E+00	-2.224E+10

Extensional stiffness matrix						
A (N/m)		1.509E+09	4.943E+08	-5.960E-08		
		4.943E+08	6.190E+08	-6.706E-08		
		-5.960E-08	-6.706E-08	5.048E+08		

Midplane strain						
ε		2.154E-04				
		-1.720E-04				
		2.585E-21				

Deformation						
u (m)		4.309E-04				

Layer *l*	1	2	3	4	5	6
σ_{xx} (Pa)	1.963E+06	2.007E+07	1.963E+06	1.963E+06	2.007E+07	1.963E+06
σ_{yy} (Pa)	2.911E+05	-5.821E+05	2.911E+05	2.911E+05	-5.821E+05	2.911E+05
τ_{xy} (Pa)	-9.653E+05	5.577E-12	9.653E+05	-9.653E+05	5.577E-12	9.653E+05

Layer *l*	7	8	9	10	11	12
σ_{xx} (Pa)	1.963E+06	2.007E+07	1.963E+06	1.963E+06	2.007E+07	1.963E+06
σ_{yy} (Pa)	2.911E+05	-5.821E+05	2.911E+05	2.911E+05	-5.821E+05	2.911E+05
τ_{xy} (Pa)	9.653E+05	5.577E-12	-9.653E+05	9.653E+05	5.577E-12	-9.653E+05

The notations used in Table 7-3 are as described below.

E_{11} and E_{22} represent the Young's modulus in the "1" and "2" direction of the material axes respectively.

v_{12} and v_{21} are the major and minor Poisson's ratio respectively.

μ_{12} represent the shear modulus in the material axes (i.e. axes 1-2).

Q represents the stiffness matrix of the composite plate.

θ represents the fibre orientation of the ply.

Z represents the ply location in the out-plane direction.

Q_ represents the transformed stiffness matrix of the composite plate which contains $Q_{11\_}$, $Q_{22\_}$, $Q_{12\_}$, $Q_{66\_}$, $Q_{16\_}$ and $Q_{26\_}$.

A represents the extensional stiffness matrix of the composite plate.

ε represents the midplane strain vector of the composite plate

u represents the deformation of the composite plate in the x-direction of the geometric axis.

Validation results

Figure 7-2 shows the nodal displacement result along the y=0.5 line for the Average Mindlin Program. The displacement result of the classical lamination theory which has been computed in Table 7-3 was plotted with the displacement results of the Average Mindlin program as shown in Figure 7-2 for validation purpose. The displacement results of the Average Mindlin program for different mesh cases show good convergence and they also show good agreement with the result of the classical lamination theory.
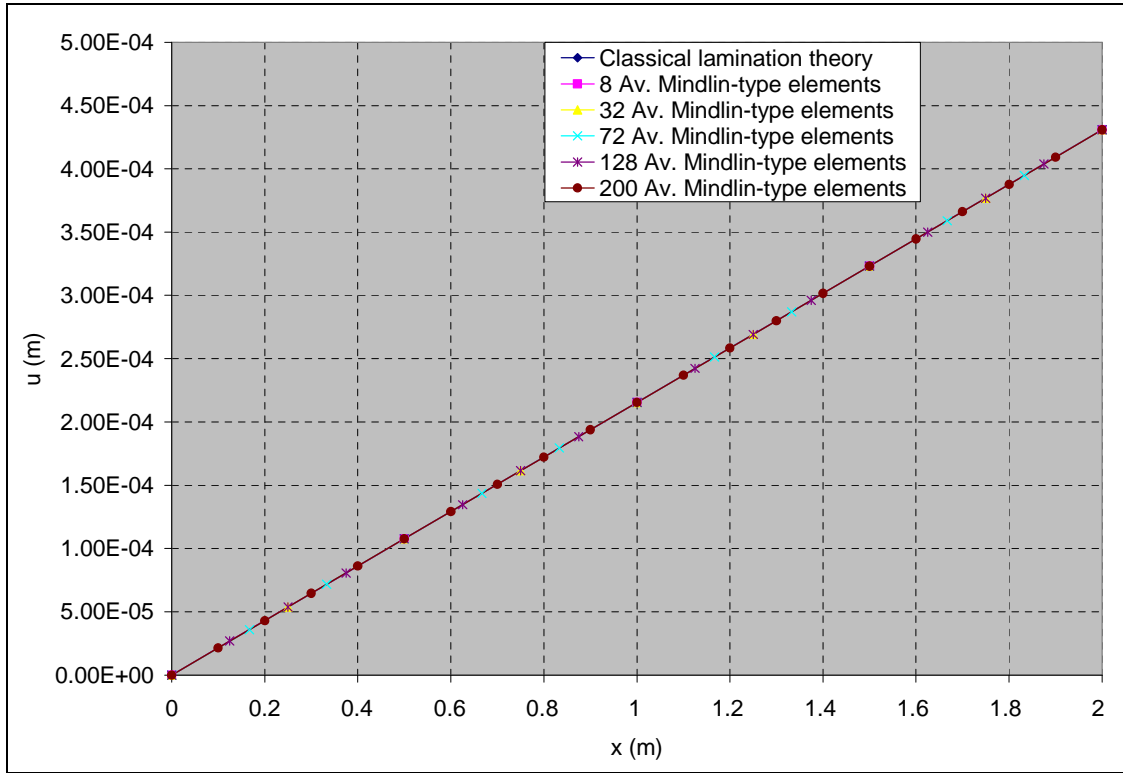
Figure 7-2: u-displacement validation against analytical solution for the tension case

Figure 7-3 to 7-5 show the stresses with respect to the material axes at x=0 and y=0.5. The stress result of the classical lamination theory which has been computed in Table 7-3 was also validated against the stress results of the Average Mindlin program as shown in Figures 7-3 to 7-5. The stress result of the Average Mindlin program shows good agreement (all data points overlap) with the result of the classical lamination theory. Figure 7-3 shows that the 0° plies have the highest σ_{xx} relative to the 45° plies and -45° plies. This is due to the fact that the fibres in the 0° plies are aligned in the tensile force direction. Hence they carry a higher share of the load relative to the share of load of fibres in the 45° plies and -45° plies. Figure 7-4 shows that the 0° plies have compressive σ_{yy} values which are expected because the fibres are aligned in the direction of the tensile load. Figure 7-5 shows that the 0° plies have no shear stress (τ_{xy}) which is expected because the fibres are aligned in the direction of the tensile load. It can be seen that the 45° plies exhibit an equal but opposite shear stress in comparison with the -45° plies which is due to the stacking sequence of the composite.
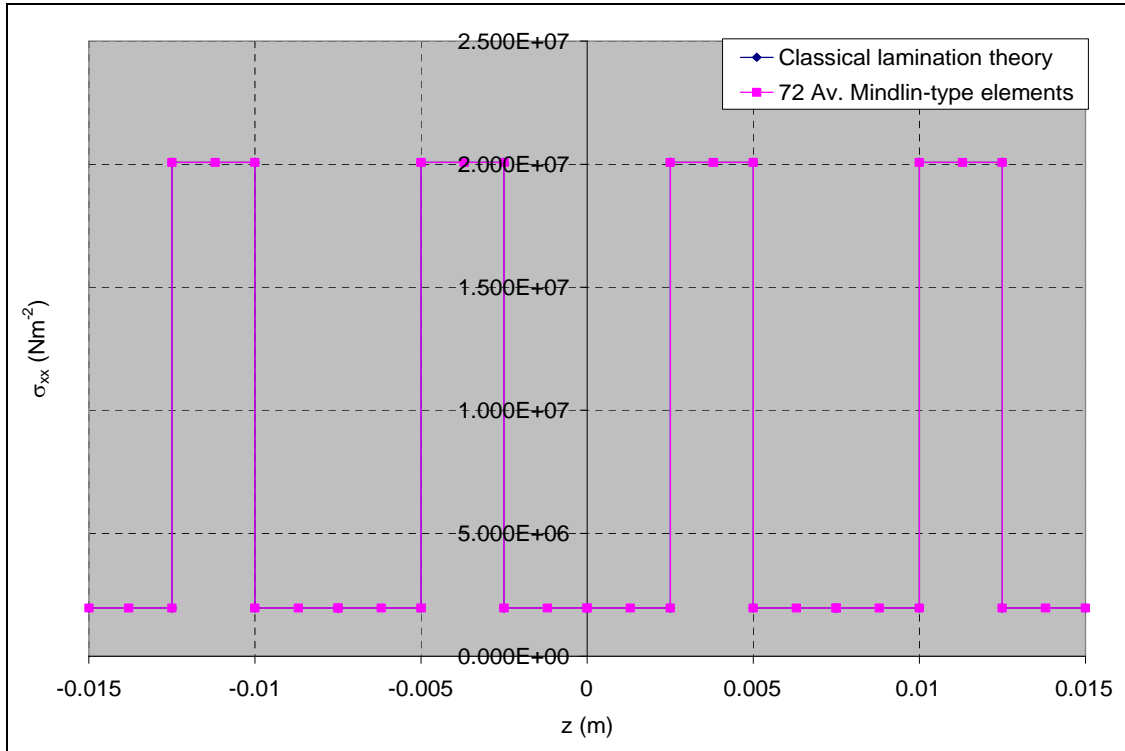
Figure 7-3: σ_{xx} validation against analytical solution for the tension case
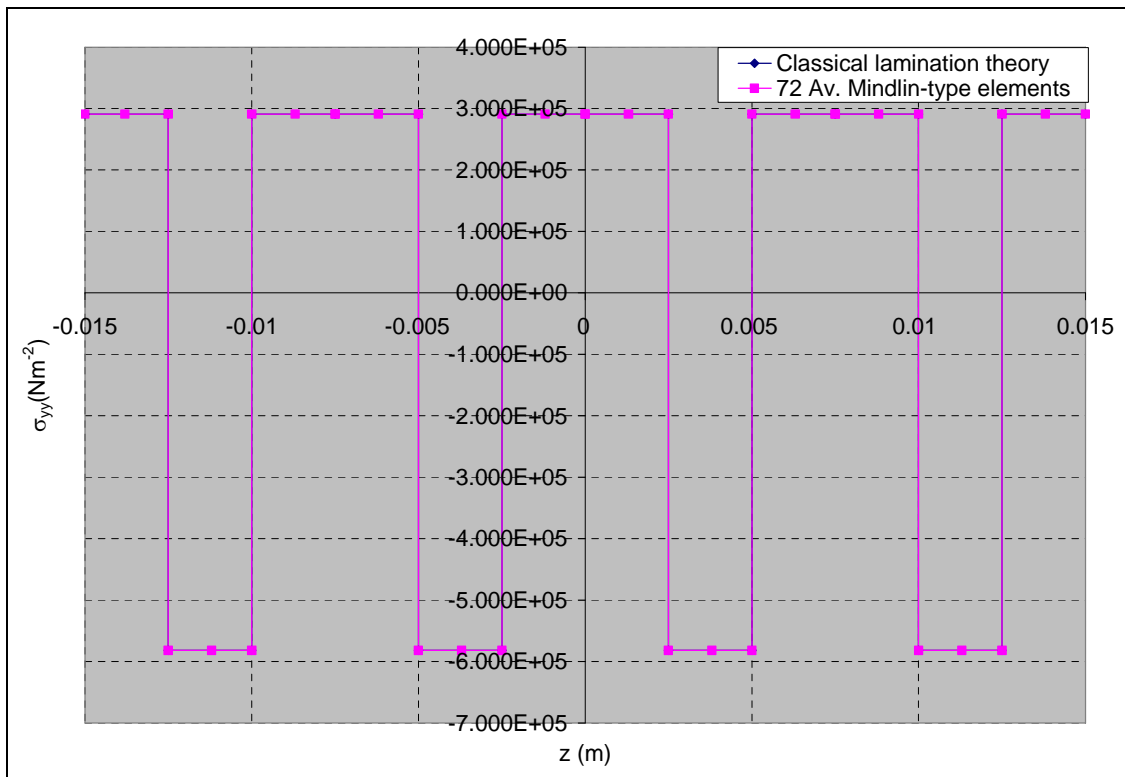
Figure 7-4: σ_{yy} validation against analytical solution for the tension case

114
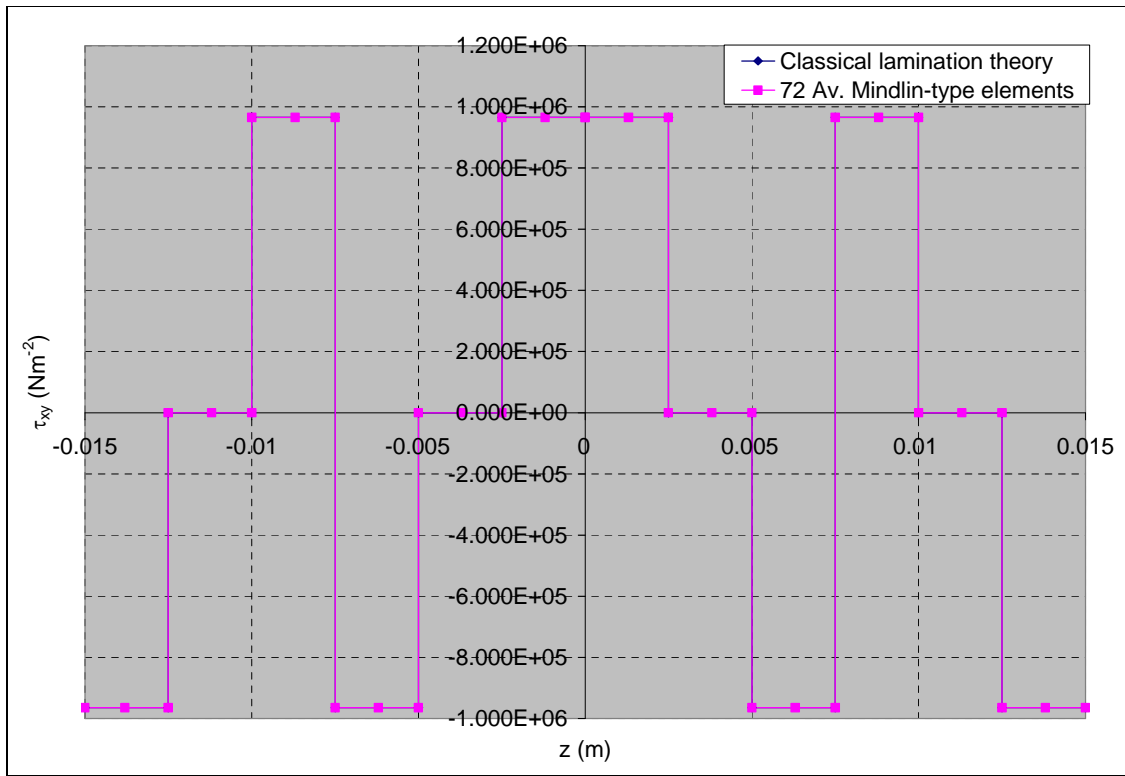
Figure 7-5: τ_{xy} validation against analytical solution for the tension case

7.1.2   Traditional composite under compressive loading

<u>Example 7.1.2</u>: A rectangular traditional composite plate with a "[0/90]$_s$" stacking sequence was subjected to a uniaxial compression. It is simply supported along its four edges. The task is to compute the critical buckling load using classical laminate theory and the result is then used to validate the result of the Average Mindlin program. The FE modelling procedure and the analytical solution procedure is presented for this example.

The geometrical properties and micro-mechanical properties are as given below. The micromechanical data were obtained from a textbook by Kaw (1997).

Table 7-4: Buckling case data

Geometry					
L (m)	2.000	w (m)	1.000		
t (m)	0.0100	No. of ply	4		
Fibre and matrix properties					
E_f (Pa)	2.300E+11	ν_f	3.500E-01	μ_f (Pa)	8.519E+10
E_m (Pa)	3.400E+09	ν_m	3.000E-01	μ_m (Pa)	1.308E+09
V_f	0.4	ρ_f (Kg m^{-3})	1.800E+03		
V_m	0.6	ρ_m (Kg m^{-3})	1.200E+03		

The notations used in Table 7-4 are as described below.

> L, w, and t, represent the length, width, thickness of ply respectively.
>
> E_f and E_m represent the Young's modulus of the fibre and matrix respectively.
>
> ν_f and ν_m represent the Poisson's ratio of the fibre and matrix respectively.
>
> μ_f and μ_m represent the shear modulus of the fibre and matrix respectively.
>
> V_f and V_m represent the volume fraction of the fibre and matrix respectively.
>
> ρ_f and ρ_m represent the density of the fibre and matrix respectively.

<u>FE Modelling</u>

The composite plate case has a mid-plane as shown in Figure 7-6. Different meshes were employed in this example to check for convergence. A mesh with 72 four-noded Mindlin-type elements was selected and is as shown in Figure 7-6. A compressive load of 24kN was applied as an equivalent nodal loads at the nodes on the x=2 edge with reduced load at the corner nodes. For example, in the 72 element case, the load was

applied equally at nodes on the x=2 edge but with half the loads at the corner nodes on the x=2 edge as shown in Figure 7-6. Hence the equivalent nodal loading for the 72 element case was 4kN at each nodes on the x=2 edge with 2kN at the corner nodes on the x=2 edge. The boundary condition shown in Table 7-5 was applied to the FE model. The Average Mindlin FE program is then used to perform buckling eigenvalue analysis on the model.

Table 7-5: Boundary condition for the buckling case

Nodes	Boundary condition
Nodes on the x=0 edge	u = 0
Nodes on all four edges	w = 0
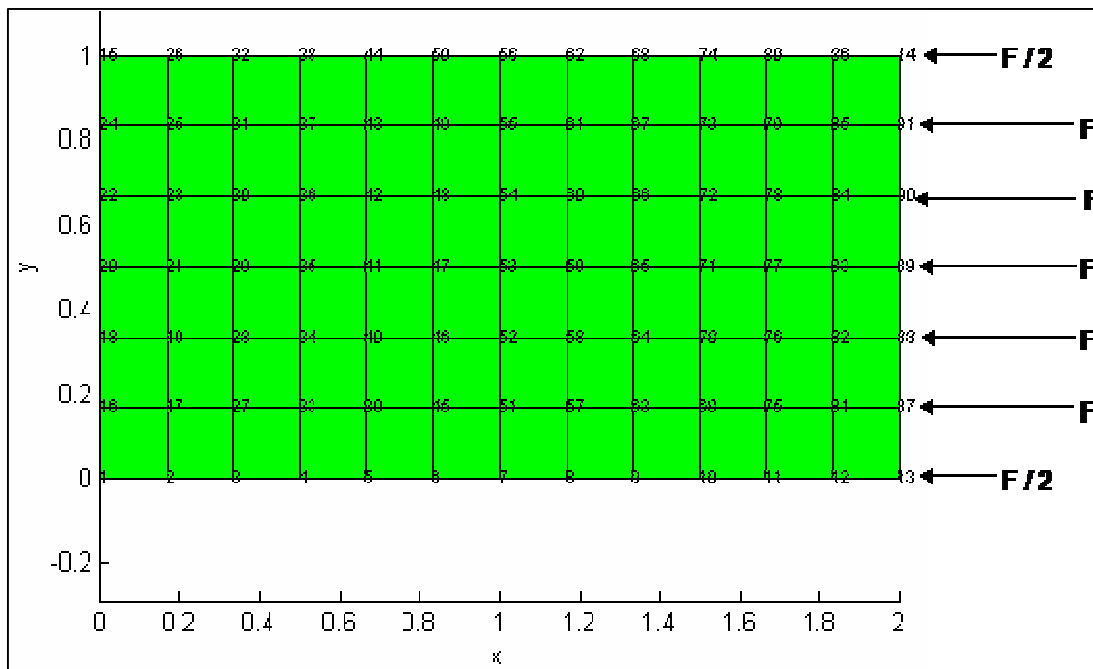
Figure 7-6: 4-noded element mesh for the buckling case

Analytical Solution

In order to determine the critical buckling load of the rectangular plate, it is assumed that the laminate is specially orthotropic i.e. they satisfy the following three conditions.

- The in-plane stiffness matrix, A, is orthotropic with the direct and shear stiffness terms uncoupled so that A_{16} and A_{26} are zero.

117

- The bending stiffness matrix, D, is orthotropic with the bending and twisting stiffness terms uncoupled so that D_{16} and D_{26} are zero.

- The in-plane and bending stiffness matrices are uncoupled, that is B=0.

The buckling loads can be computed using the equation below which can be found in a textbook by Agarwal et. al. (2006).

$$N_o(m,n) = \pi^2 \left[D_{11}\left(\frac{m}{a}\right)^2 + 2(D_{12} + 2D_{66})\left(\frac{n}{b}\right)^2 + D_{22}\left(\frac{n}{b}\right)^4\left(\frac{a}{m}\right)^2 \right] \qquad (7.14)$$

Using the transformed stiffness matrix computed in Example 7.1.1 and Equation (7.13 – 7.14), the buckling loads can be computed with the following spreadsheet.

Table 7-6: Analytical solution for the buckling case

Elastic constants					
E_{11} (Pa)	9.404E+10		v_{12}	3.200E-01	
E_{22} (Pa)	5.611E+09		v_{21}	1.909E-02	
ρ (Kg m^{-3})	1.440E+03		μ_{12} (Pa)	2.157E+09	
ρ_o (Kg m^{-2})	1.440E+01				

Stiffness matrix				
Q (Pa)	9.462E+10	1.807E+09	0.000E+00	
	1.807E+09	5.646E+09	0.000E+00	
	0.000E+00	0.000E+00	2.157E+09	

Layer l	1	2	3	4
θ (^{o})	0	90	90	0
Z_{p-1} (m)	-0.005	-0.0025	0	0.0025
Z_p (m)	-0.0025	0	0.0025	0.005
$Z_p - Z_{p-1}$ (m)	2.500E-03	2.500E-03	2.500E-03	2.500E-03
$Z_p^2 - Z_{p-1}^2$ (m)	-1.875E-05	-6.250E-06	6.250E-06	1.875E-05
$Z_p^3 - Z_{p-1}^3$ (m)	1.094E-07	1.563E-08	1.563E-08	1.094E-07
$Q_{11\_}$ (Pa)	9.462E+10	5.646E+09	5.646E+09	9.462E+10
$Q_{22\_}$ (Pa)	5.646E+09	9.462E+10	9.462E+10	5.646E+09
$Q_{12\_}$ (Pa)	1.807E+09	1.807E+09	1.807E+09	1.807E+09
$Q_{66\_}$ (Pa)	2.157E+09	2.157E+09	2.157E+09	2.157E+09
$Q_{16\_}$ (Pa)	0.000E+00	2.914E-08	2.914E-08	0.000E+00
$Q_{26\_}$ (Pa)	0.000E+00	5.421E-06	5.421E-06	0.000E+00

Table 7-6: Analytical solution for the buckling case (continued)

Bending stiffness matrix (N m)			
D	6.958E+03	1.506E+02	3.035E-16
	1.506E+02	1.397E+03	5.647E-14
	3.035E-16	5.647E-14	1.798E+02

Buckling loads (N m^{-1})						
N(m,n)	1	2	3	4	5	6
1	8.240E+04	9.400E+05	4.576E+06	1.430E+07	3.475E+07	7.187E+07
2	9.253E+04	3.296E+05	1.276E+06	3.760E+06	8.940E+06	1.830E+07
3	1.707E+05	2.929E+05	7.416E+05	1.885E+06	4.237E+06	8.460E+06
4	2.882E+05	3.701E+05	6.446E+05	1.318E+06	2.681E+06	5.105E+06
5	4.415E+05	5.048E+05	6.986E+05	1.155E+06	2.060E+06	3.651E+06
6	6.297E+05	6.829E+05	8.328E+05	1.171E+06	1.827E+06	2.966E+06

The notations used in Table 7-6 are as described below.

E_{11} and E_{22} represent the Young's modulus in the "1" and "2" direction of the material axes respectively.

ρ represents the density of the composite plate

ρ_o represents the mass per unit area of the composite plate.

v_{12} and v_{21} are the major and minor Poisson's ratio respectively.

μ_{12} represent the shear modulus in the material axes (i.e. axes 1-2).

Q represents the stiffness matrix of the composite plate.

θ represents the fibre orientation of the ply.

Z represents the ply location in the out-plane direction.

Q_ represents the transformed stiffness matrix of the composite plate which contains $Q_{11\_}$, $Q_{22\_}$, $Q_{12\_}$, $Q_{66\_}$, $Q_{16\_}$ and $Q_{26\_}$.

D represents the bending stiffness matrix of the composite plate.

N(m,n) represents the buckling load.

m and n represent the buckling load indices

The critical buckling load is the lowest of all the values. It can be seen from the spreadsheet that the critical buckling load occurs when m=1 and n=1. Hence the critical buckling load is 82.4kN m^{-1}.

The critical buckling load result of the classical lamination theory was then validated against the results of the Average Mindlin program as shown in Table 7-7. The critical buckling load results of the Average Mindlin program for different mesh cases show good convergence and they converge to the analytical solution. It can be seen from Table 7-7 that the results of the model with 200 elements agree well with the analytical results in predicting the buckling loads for all the 3 buckling modes.

Table 7-7: Analytical validation result for the buckling case

Buckling mode	Buckling load (N m^{-1})					
	8 Elements	32 Elements	72 Elements	128 Elements	200 Elements	Analytical solution
1st mode	1.117E+05	9.067E+04	8.588E+04	8.429E+04	8.356E+04	8.240E+04
2nd mode	1.222E+05	1.007E+05	9.598E+04	9.432E+04	9.356E+04	9.253E+04
3rd mode	4.818E+05	2.114E+05	1.865E+05	1.788E+05	1.754E+05	1.707E+05

7.1.3 Traditional composite plate under free vibration

Example 7.1.3: The rectangular traditional composite plate considered in Example 7.1.2 is now under free vibration. It is simply supported along its four edges. The task is to compute the first three natural frequencies using the classical lamination theory and the result is then used to validate the result of the Average Mindlin program. The FE modelling procedure and the analytical solution procedure is presented for this example. The geometrical properties and micro-mechanical properties are as given in Example 7.1.2.

FE Modelling

Different meshes were employed in this example to check for convergence. The boundary condition shown in Table 7-8 was applied to the FE model. The Average Mindlin program is then used to perform free vibration eigenvalue analysis on the model.

Table 7-8: Boundary condition for free vibration case

Nodes	Boundary condition
Nodes on all four edges	w = 0
Nodes on all four corners of the rectangular traditional composite plate	$u = v = w = \theta_x = \theta_y = 0$

Analytical Solution

The natural frequencies can be computed using the equation below which can be found in a textbook by Agarwal et. al. (2006).

$$\omega_{mn} = \sqrt{\frac{\pi^4}{\rho_o}\left[D_{11}\left(\frac{m}{a}\right)^4 + 2(D_{12} + 2D_{66})\left(\frac{m}{a}\right)^2\left(\frac{n}{b}\right)^2 + D_{22}\left(\frac{n}{b}\right)^4\right]} \qquad (7.14)$$

where

ρ$_o$ represents the mass per unit area of the composite plate.

D represents the bending stiffness matrix of the composite plate

m and n represent the natural frequency indices.

Using the bending stiffness matrix computed in Example 7.1.2, the buckling loads can be computed with the following spreadsheet.

Table 7-9: Analytical solution for the free vibration case

Natural frequencies (rad s^{-1})						
ω_{mn}	1	2	3	4	5	6
1	118.82	401.34	885.48	1565.33	2439.99	3509.24
2	251.84	475.29	935.30	1605.36	2475.29	3541.93
3	513.09	672.03	1069.41	1704.83	2556.16	3612.07
4	888.90	1007.34	1329.34	1901.18	2711.22	3741.21
5	1375.20	1470.50	1729.86	2224.51	2970.59	3954.89
6	1970.80	2052.36	2266.52	2688.12	3357.50	4277.65

The fundamental frequency is the lowest of all the values. It can be seen from the spreadsheet that the fundamental frequency occurs when m=1 and n=1. Hence the fundamental frequency is 118.82 rad s^{-1}.

FE Convergence and Validation Results

The natural frequency results of the classical lamination theory were then validated against the results of the Average Mindlin program as shown in Table 7-10. The natural frequency results of the Average Mindlin program for different mesh cases show good convergence and they converge to the analytical solution. It can be seen from Table 7-10 that the results of the model with 200 elements agrees well with the analytical results in

predicting the natural frequencies for all the 3 free vibration modes. The results also show that finer meshes are needed to accurately predict higher natural frequency modes.

Table 7-10: Analytical validation result for the free vibration case

Vibration mode	Natural frequencies (rad s^{-1})					
	8 Elements	32 Elements	72 Elements	128 Elements	200 Elements	Analytical solution
1st mode	154.49	125.93	121.80	120.43	119.81	118.82
2nd mode	314.69	270.07	259.62	256.00	254.34	251.84
3rd mode	1071.09	555.58	459.59	432.23	420.45	401.34

7.1.4 Traditional composite plate with a central hole under tension

Example 7.1.4: A rectangular traditional composite plate with a central hole and a "[[-45/0/45]$_2$]$_s$" stacking sequence was subjected to a tensile loading of 24kN. The task is to validate the stress result of the Average Mindlin program against the result of the classical lamination theory. The FE modelling procedure and the analytical solution procedure is presented for this example.

The geometrical properties, micro-mechanical properties and loading condition are as given below. The micromechanical data were obtained from a textbook by Kaw (1997).

Table 7-11: Data for the traditional composite plate case with a central hole

Geometry					
L (m)	2.000	w (m)	1.000	R (m)	0.1
t (m)	0.0300	No. of ply	12		
Fibre and matrix properties					
E_f (Pa)	2.300E+11	v_f	3.500E-01	μ_f (Pa)	8.519E+10
E_m (Pa)	3.400E+09	v_m	3.000E-01	μ_m (Pa)	1.308E+09
V_f	0.4	V_m	0.6		
Applied Force					
F_x (N)	2.400E+04	N_x (N/m)	2.400E+04		
N_y (N/m)	0.000E+00	N_z (N/m)	0.000E+00		

The notations used in Table 7-11 are as described below.

L, w, and t, represent the length, width, thickness of ply respectively.

R represents the radius of the hole.

E_f and E_m represent the Young's modulus of the fibre and matrix respectively.

v_f and v_m represent the Poisson's ratio of the fibre and matrix respectively.

μ_f and μ_m represent the shear modulus of the fibre and matrix respectively.

V_f and V_m represent the volume fraction of the fibre and matrix respectively.

F_x represents the applied force in the x-direction.

N represents the distributed load.

FE Modelling

In order to model the composite plate with a central hole under uniaxial tensile loading, the model was divided into four equal quarters. One of the quarter models was then used in the FE modelling by applying boundary conditions which takes advantage of symmetrical nature of the full model. The composite plate with a central hole has a mid-plane as shown in Figure 7-7. Different meshes were employed in this example to check for convergence. A mesh with 180 four-noded Mindlin-type elements was selected and is as shown in Figure 7-7. A tensile load of 24kN was applied as an equivalent nodal loads at the nodes on the x=2 edge with reduced load at the corner nodes. For example, in the 180 element case, the load was applied equally at nodes on the x=2 edge but with half the loads at the corner nodes on the x=2 edge as shown in Figure 7-7. Hence the equivalent nodal loading for the 180 element case was 4.8kN at each nodes on the x=2 edge with 2.4kN at corner nodes on the x=2 edge. The boundary condition shown in Table 7-12 was applied to the FE model. The Average Mindlin FE program is then used to perform linear static analysis on the model.

Table 7-12: Boundary condition for the traditional composite plate case with a hole

Nodes	Boundary condition
Nodes on the x=0 edge	u = 0
Nodes on the y=0 edge	v = 0
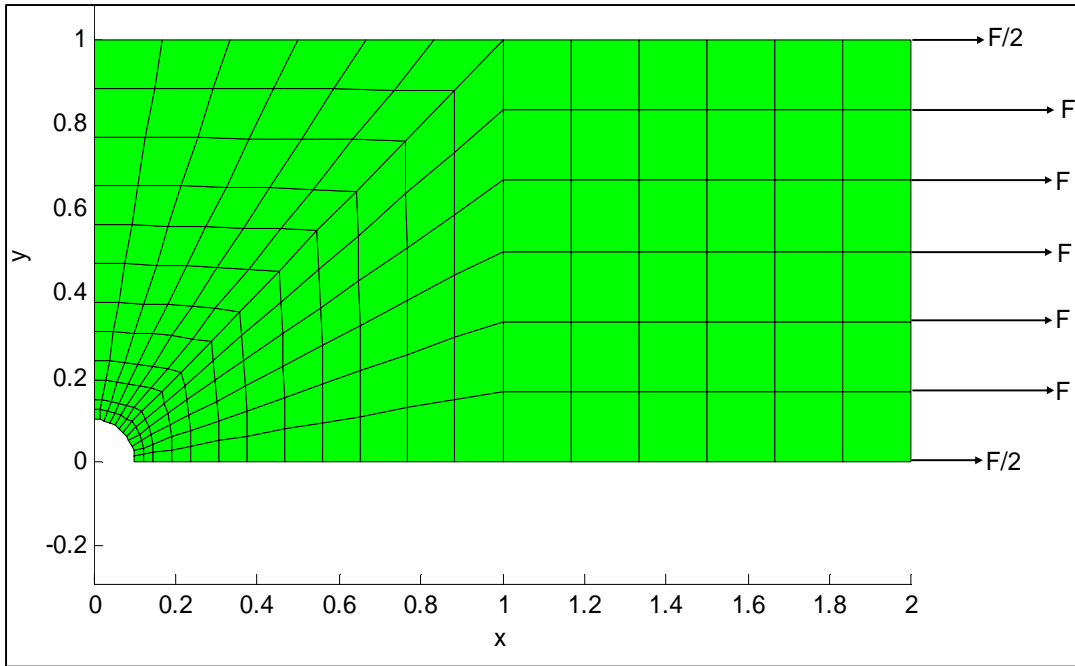
Figure 7-7: 4-noded element mesh for a traditional composite plate with a hole

Analytical Solution

In order to determine the stress field in the vicinity of the central hole in the rectangular traditional composite plate, it is assumed that the laminate is balanced i.e. it has equal number of lamina with $+\theta^{o}$ and $-\theta^{o}$ fibre orientation. For such a laminate, the shear coupling stiffness terms, A_{16} and A_{26} are zero. It is also assumed that the lamina within the laminate are positioned symmetrically with respect to the laminate midplane, hence the coupling terms B_{ij} become zero.

The stress field in the vicinity of a circular hole of radius, R, in an orthotropic laminate under uniaxial loading, σ_x^{∞} can be computed using the equation below which can be found in a textbook by Whitney et. al. (1984).

$$\sigma_x(0, y) = \frac{\sigma_x^{\infty}}{2}\left\{2 + \left(\frac{R}{y}\right)^2 + 3\left(\frac{R}{y}\right)^2 - \left(K_T^{\infty} - 3\right)\left[5\left(\frac{R}{y}\right)^6 - 7\left(\frac{R}{y}\right)^8\right]\right\} \qquad (7.15)$$

where
$$\sigma_x^{\infty} = N_x^{\infty}/t$$

$$K_T^{\infty} = 1 + n$$

$$n = \sqrt{\frac{2}{A_{11}}\left(\sqrt{A_{11}A_{22} - A_{12}} + \frac{A_{11}A_{22} - A_{12}^2}{2A_{66}}\right)}$$

FE Convergence and Validation Results

Using the extensional stiffness matrix computed in Example 7.1.1 and the above equation, the effective stress results were plotted as shown below. The effective stress $\sigma_x(0,y)$ computed using the classical lamination theory was then validated against the results of the Average Mindlin program as shown in Figure 7-8. The results of the Average Mindlin program for different mesh cases show good convergence. The FE results and the result of the classical lamination theory show similar trends.
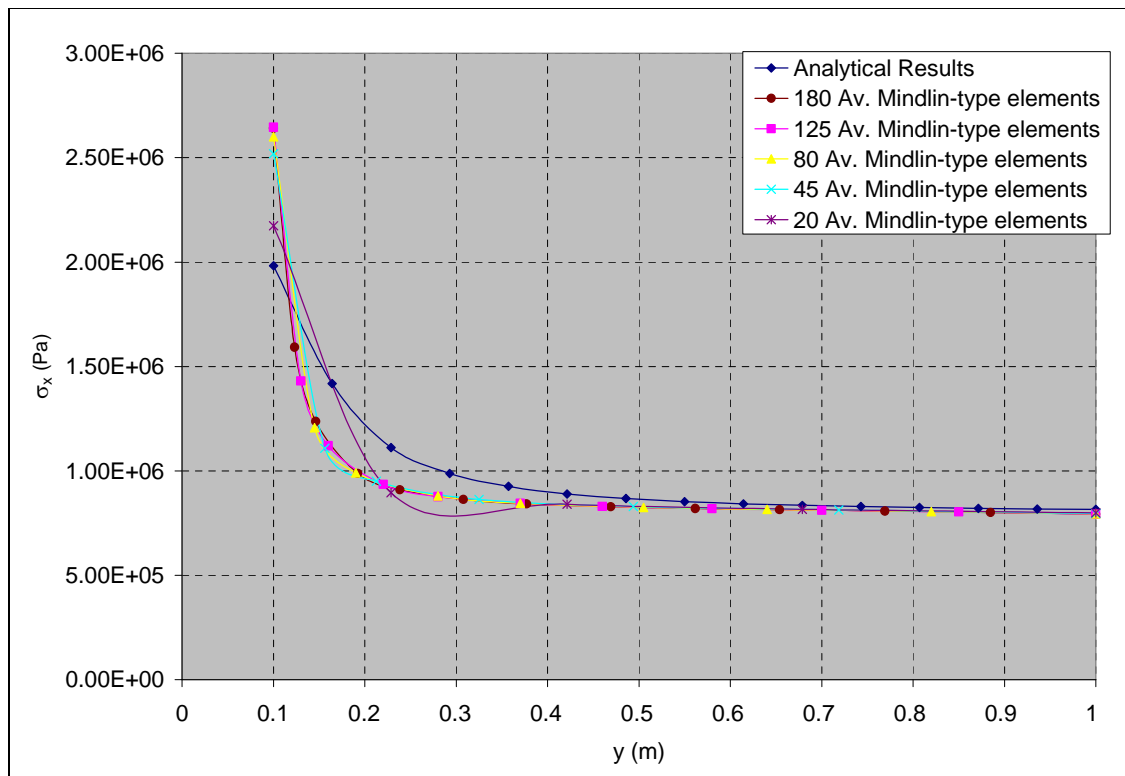
Figure 7-8: σ_x validation against analytical solution for the tension case

7.2 Program Validation against Abaqus Program

In this section, the Mindlin programs were validated against a commercial FE package called Abaqus. The Abaqus package was used to validate the infinitesimal strain part of the Mindlin programs for the analysis of functionally graded composite (FGC). Also, the progressive damage capabilities of the Mindlin FE programs were not validated against the Abaqus package in this section but they were validated against the Ordinary FE program in the next section. In this section, some numerical examples were presented for this validation exercise. These numerical examples include composite plate subjected to tensile load, out-of-plane load; buckling load and free vibration; a simply supported ring subjected to uniform out-of-plane load; and a clamped ring subjected to uniform out-of-plane load.

7.2.1 FGC plate under tensile loading

Example 7.2.1: A rectangular FGC plate with a "[[-45/0/45]$_2$]$_s$" stacking sequence was subjected to a tensile loading of 240kN. The task is to validate the displacement and stress result of the Average Mindlin program against the result of the Abaqus package. The FE modelling procedure is presented for this example.

The geometrical properties, micro-mechanical properties and loading condition are as given below. The micromechanical data were obtained from a textbook by Kaw (1997).

Table 7-13: Tensile case data

Geometry					
L (m)	2.000	w (m)	1.000		
t (m)	0.0300	No. of ply	12		
Fibre and matrix properties					
E_f (Pa)	2.300E+11	v_f	3.500E-01	μ_f (Pa)	8.519E+10
E_m (Pa)	3.400E+09	v_m	3.000E-01	μ_m (Pa)	1.308E+09
Applied Force					
F_x (N)	2.400E+05				

The notations used in Table 7-13 are as described below.

L, w, and t, represent the length, width, thickness of ply respectively.

E_f and E_m represent the Young's modulus of the fibre and matrix respectively.

v_f and v_m represent the Poisson's ratio of the fibre and matrix respectively.

μ_f and μ_m represent the shear modulus of the fibre and matrix respectively.

F_x represents the applied force in the x-direction.

<u>FE Modelling</u>

Different meshes were employed in this example to check for convergence. A mesh with 72 four-noded Mindlin-type elements was selected. A tensile load of 240kN was applied as an equivalent nodal loads at the nodes on the x=2 edge with reduced load at the corner nodes. For example, in the 72 element case, the load was applied equally at nodes on the x=2 edge but with half the loads at the corner nodes on the x=2 edge. Hence the equivalent nodal loading for the 72 element case was 40kN at each nodes on the x=2 edge with 20kN at corner nodes on the x=2 edge. The horizontal displacement of all the nodes on the x=0 edge was fixed. The node at the (0, 0.5) coordinate was clamped (i.e. fixed in all degrees of freedom).

In order to model the functional gradation of the FGC plate in the Abaqus package, the fibre and matrix volume fractions were computed for each element at their midpoints by using the fibre distribution equations (i.e. Equation 3.34 and 3.38) developed in chapter 3. The macro-mechanical properties were then computed for each element by substituting the fibre and matrix volume fractions into the macro-mechanical equations developed in chapter 3. For example in the case of the mesh with 72 elements, the composite plate has 12 divisions in the x-direction. Hence the macro-mechanical properties at the 12 positions along the x-direction were computed using the Excel Spreadsheet as shown in Table 7-14. Each macro-mechanical property was then assigned to each element in the Abaqus package based on the location of each element midpoint.

Table 7-14: Computation of macro-mechanical properties

Functional gradation properties				
P	1	$V_{f\_}$	0.4	
V_1	0.5			
x_1 (m)	0	x_2 (m)	2	
ξ_{min}	0	ξ_{max}	1	
Q	0.5			
V_2	0.3			

Macro-mechanical properties							
x (m)	ξ	V_f	V_m	E_{11} (Pa)	E_{22} (Pa)	ν_{12}	μ_{12} (Pa)
0.083	0.042	0.492	0.508	1.148E+11	6.594E+09	0.325	2.535E+09
0.250	0.125	0.475	0.525	1.110E+11	6.391E+09	0.324	2.457E+09
0.417	0.208	0.458	0.542	1.073E+11	6.199E+09	0.323	2.383E+09
0.583	0.292	0.442	0.558	1.035E+11	6.019E+09	0.322	2.314E+09
0.750	0.375	0.425	0.575	9.971E+10	5.849E+09	0.321	2.249E+09
0.917	0.458	0.408	0.592	9.593E+10	5.688E+09	0.320	2.187E+09
1.083	0.542	0.392	0.608	9.215E+10	5.536E+09	0.320	2.129E+09
1.250	0.625	0.375	0.625	8.838E+10	5.392E+09	0.319	2.073E+09
1.417	0.708	0.358	0.642	8.460E+10	5.255E+09	0.318	2.021E+09
1.583	0.792	0.342	0.658	8.082E+10	5.125E+09	0.317	1.971E+09
1.750	0.875	0.325	0.675	7.705E+10	5.001E+09	0.316	1.923E+09
1.917	0.958	0.308	0.692	7.327E+10	4.883E+09	0.315	1.878E+09

The notations used in Table 7-14 are as described below.

P represents the gradation exponent of the FGC plate.

$V_{f\_}$ represents the average volume fraction of fibre in the composite plate.

x_1 and x_2 represents the x=0 and x=2 edge respectively.

ξ_{min} and ξ_{max} represents the non-dimensional representation of the x=0 and x=2 edge respectively.

Q represents a constant term in the fibre distribution equation.

V_2 represents the volume fraction of the fibre at the x=2 edge.

x represents the position in the x-direction

ξ represents the non-dimensional position in the x-direction.

V_f and V_m represent the volume fraction of the fibre and matrix respectively.

E_{11} and E_{22} represent the Young's modulus in the "1" and "2" direction of the material axes respectively.

ν_{12} represents the major Poisson's ratio of the composite plate.

μ_{12} represents the shear modulus in the material axes (i.e. axes 1-2).

FE convergence results

The displacement results of the Average Mindlin program and the Abaqus package were analysed for different mesh cases and the results showed good convergence as shown in Figures 7-9 to 7-10.
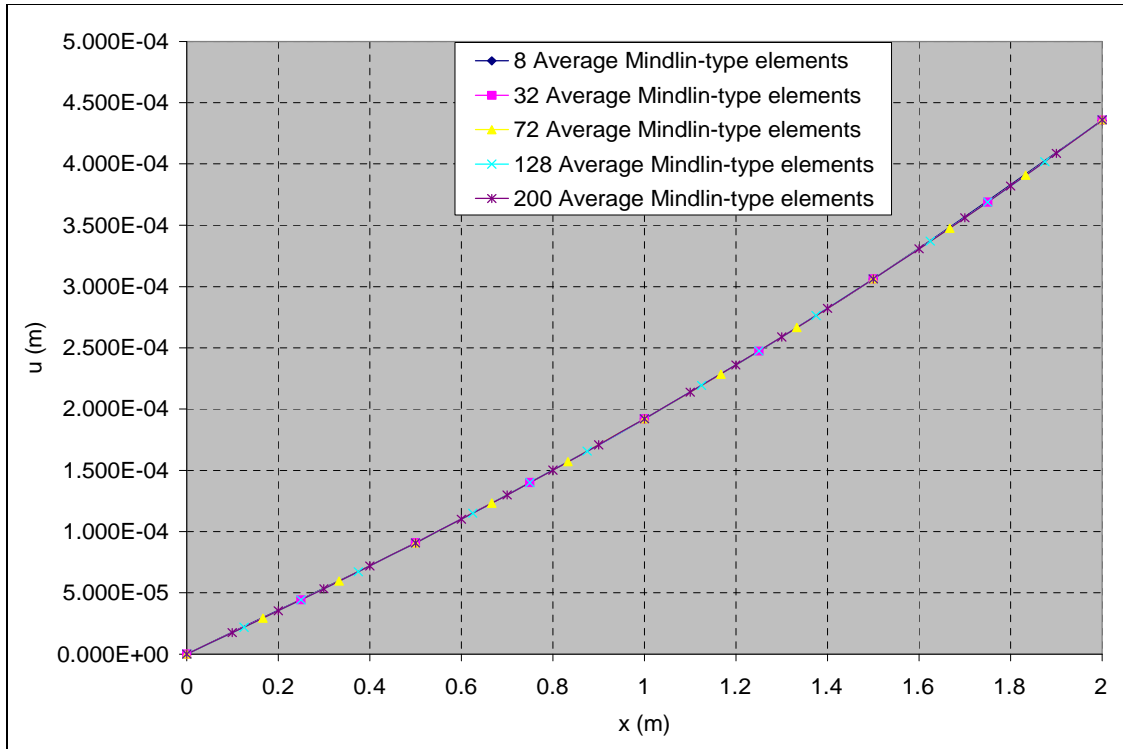
Figure 7-9: Mindlin program convergence check for the tension case
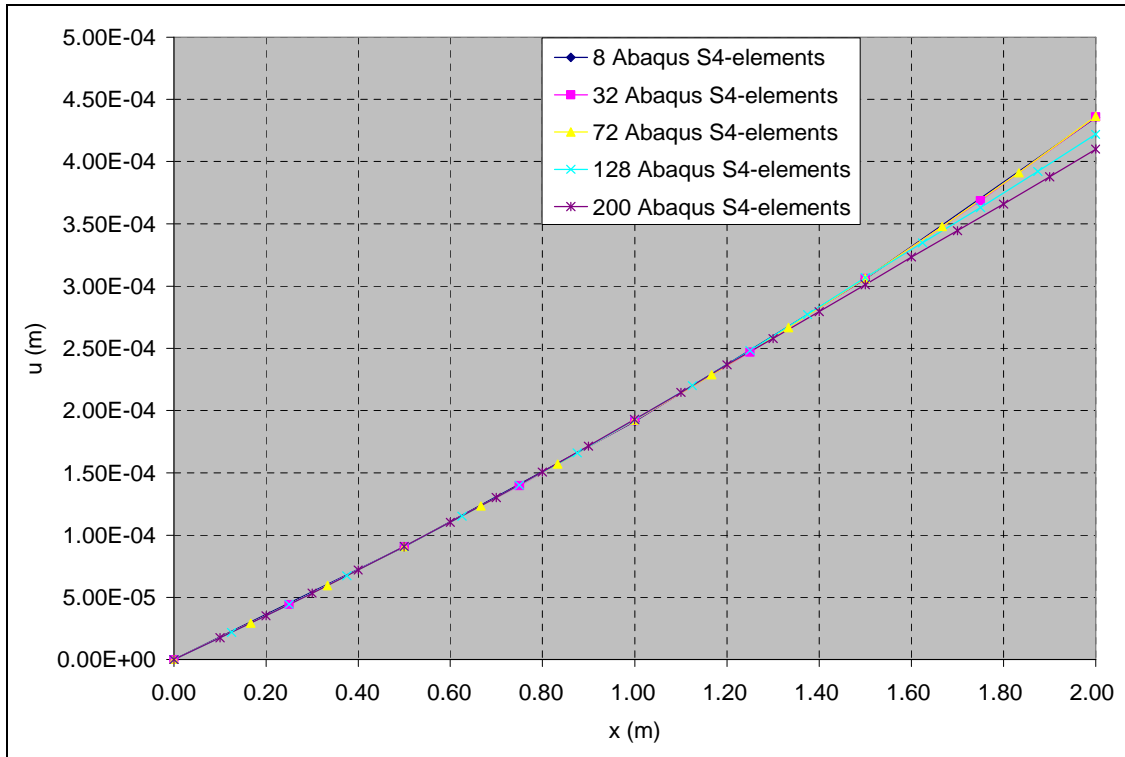
Figure 7-10: Abaqus program convergence check for the tension case

Mindlin program validation results

All the Mindlin programs including the independent validation program (i.e. the Ordinary FE program) were validated against the Abaqus program in this example. The Ordinary FE program is an independent validation program developed in-house for the finite element analysis of structures made of composite materials without functional gradation. In order to use the Ordinary FE program and the Abaqus program for analysing a FGC plate under tension, the macro-mechanical properties of each element of the FGC plate were manually computed at the midpoint of each element and fed into both programs.

Figure 7-11 shows the nodal displacement result along the y=0.5 line. The u-displacement results of the Mindlin programs were in good agreement (most data points overlap) with the result of the Abaqus program as shown in Figure 7-11. Also the results of the Mindlin programs and the Abaqus program were results of the FGC plate case with P=1 and V_1=0.5. In Figure 7-11, the classical lamination theory result for a traditional composite (i.e. composite case with P = 0) was plotted for comparison purpose. The maximum deflection results for all the Mindlin programs and the Abaqus package were in good agreement with each other. The u-displacement curves show that the FGC plate experience higher stiffness and hence lower nodal displacement around the x=0 edge (due to higher fibre volume fraction) relative to the traditional composite. The u-displacement curves also show that the FGC plate experience lower stiffness and hence higher nodal displacement around the x=2 edge (due to lower fibre volume fraction) relative to the traditional composite.
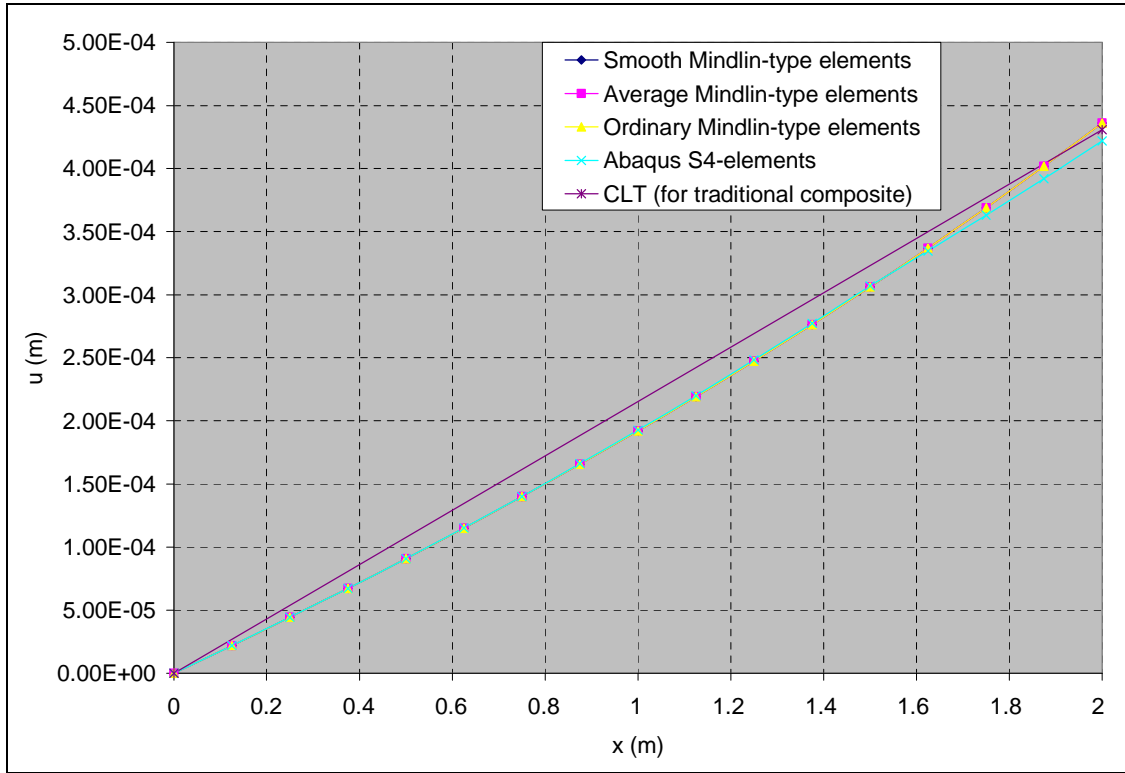
Figure 7-11: u-validation against Abaqus result for the tension case

Figure 7-12 shows the stress result in the fibre direction (σ_{11}) at x=0 and y=0.5. The σ_{11} results of the Mindlin programs were in good agreement (most data points overlap) with the result of the Abaqus package. The results shown below are for a FGC plate with a stacking sequence of "[[-45/0/45]$_2$]$_s$". It can be seen from Figure 7-12 that the 0° plies have the highest σ_{11} relative to the 45° plies and -45° plies. This is due to the fact that the fibres in the 0° plies are aligned in the tensile force direction. Hence they carry a higher share of the load relative to the share of load of fibres in the 45° plies and -45° plies.
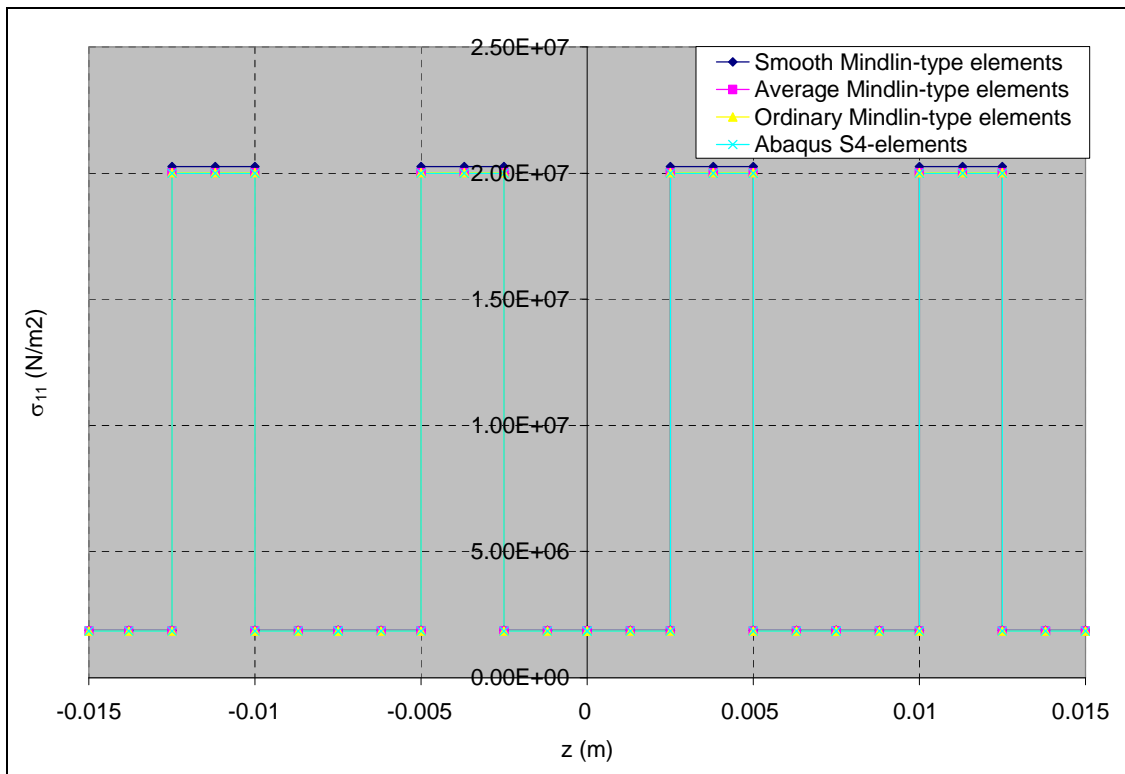
Figure 7-12: σ_{11} validation against Abaqus result for the tension case

Figure 7-13 shows the stress result in direction normal to the fibre direction (σ_{22}) at x=0 and y=0.5. The σ_{22} results of the Mindlin programs were in good agreement (most data points overlap) with the result of the Abaqus package. It can be seen from Figure 7-13 that the 0° plies have compressive σ_{22} values which are expected because the fibres are aligned in the direction of the tensile load. Also the fibres of the 0° plies would only be expected to experience compressive stress in the direction normal to the fibre direction.
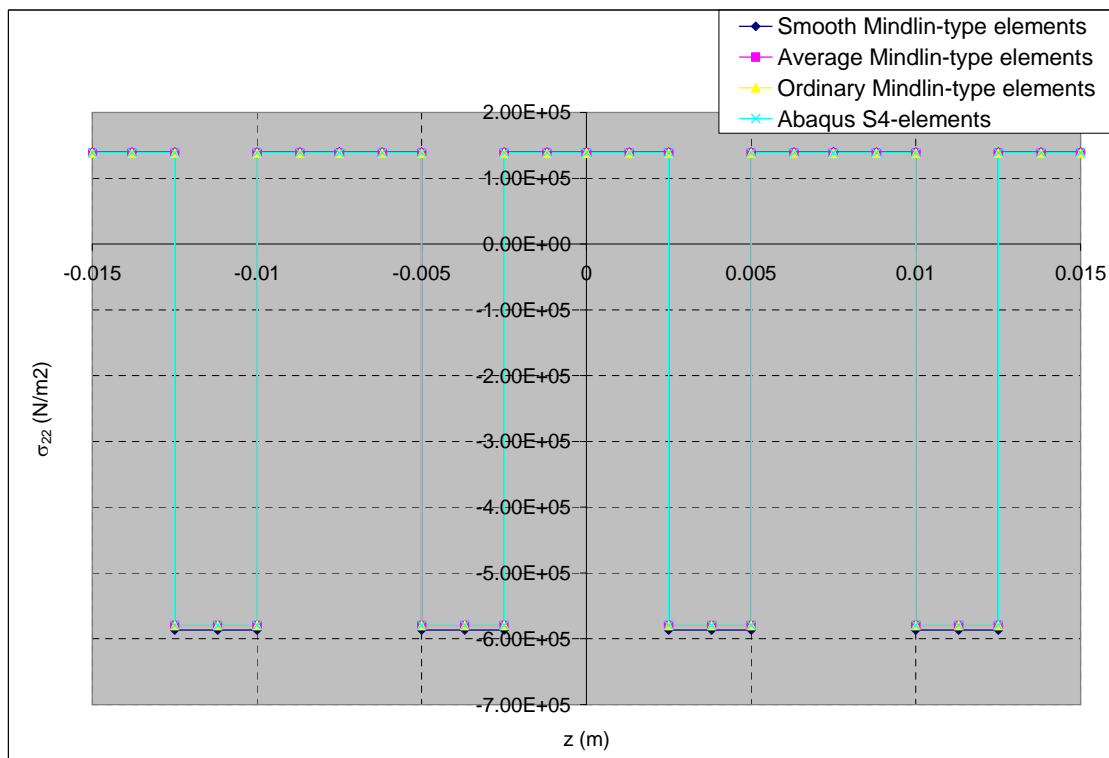
Figure 7-13: σ_{22} validation against Abaqus result for the tension case

Figure 7-14 shows the shear stress result (τ_{12}) at x=0 and y=0.5. The τ_{12} results of the Mindlin programs were in good agreement (most data points overlap) with the result of the Abaqus package. It can be seen from Figure 7-14 that the 0° plies have no shear stress which is expected because the fibres are aligned in the direction of the tensile load. It can also be seen that the 45° plies exhibit an equal but opposite shear stress in comparison with the -45° plies which is due to the stacking sequence of the composite.
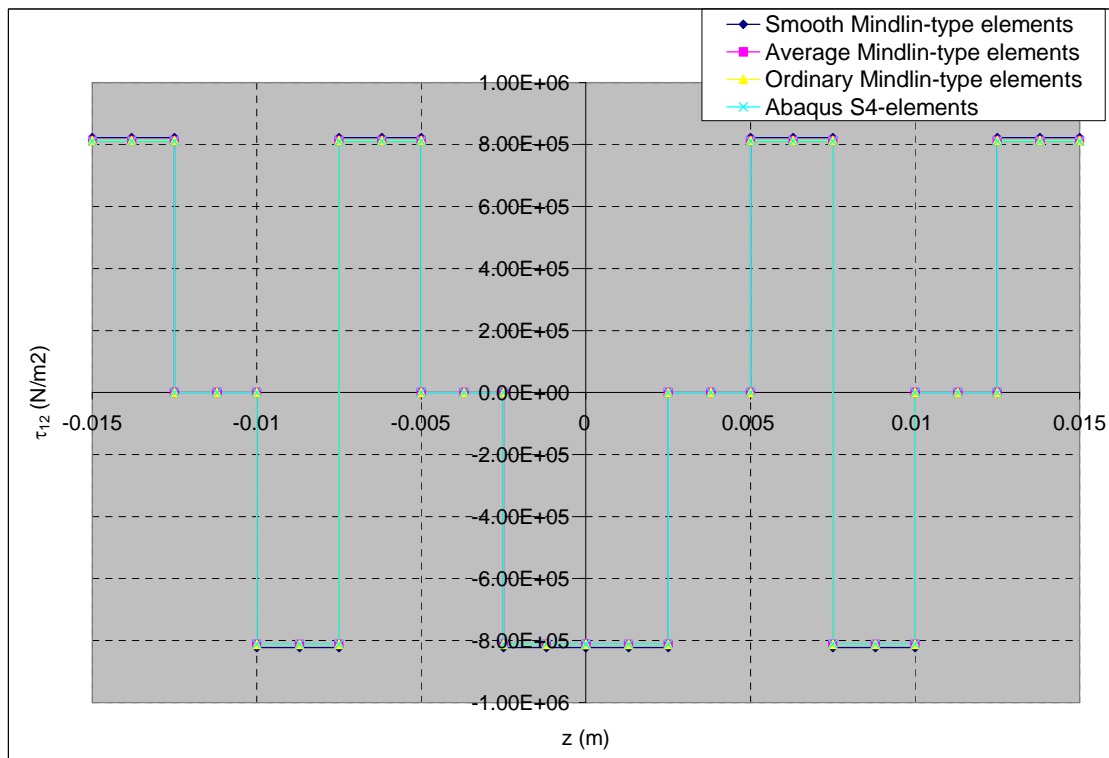
Figure 7-14: τ_{12} validation against Abaqus result for the tension case

7.2.2: FGC plate under out-of-plane bending

Example 7.2.2: A rectangular FGC plate with a "[[-45/0/45]$_2$]$_s$" stacking sequence was subjected to an out-of-plane bending load of 1.2kN. The task is to validate the displacement and stress result of the Average Mindlin FE program against the result of the Abaqus package. The FE modelling procedure is presented for this example. The geometrical properties and micro-mechanical properties are the same as the one given in Example 7.1.1.

FE Modelling

Different meshes were employed in this example to check for convergence. A mesh with 72 four-noded Mindlin-type elements was selected. An out-of-plane bending load of 1.2kN was applied as an equivalent nodal loads at the nodes on the x=2 edge with reduced load at the corner nodes. For example, in the 72 element case, the load was applied equally at nodes on the x=2 edge but with half the loads at the corner nodes on the x=2 edge as shown in Table 7-15.

Table 7-15: Applied load for the out-of-plane bending case

Nodes	Applied load
Nodes on the x=2 edge excluding corner nodes (i.e. node 13 and 14)	$F_z = 0.2$kN
Corner nodes (i.e. node 13 and 14)	$F_z = 0.1$kN

The boundary condition shown in Table 7-16 was applied to the FE models.

Table 7-16: Boundary condition for the out-of-plane bending case

Nodes	Boundary condition
Nodes on the x=0 edge	$u = v = w = \theta_x = \theta_y = 0$

In order to model the functional gradation of the FGC plate in the Abaqus package, the fibre and matrix volume fractions were computed for each element at their midpoints by

using the fibre distribution equations developed in chapter 3. The macro-mechanical properties were then computed for each element as described in Example 7.1.1.

FE convergence results

The w-displacement results of the Average Mindlin program and the Abaqus package were analysed for different mesh cases and the results showed good convergence as shown in Figures 7-15 and 7-16.
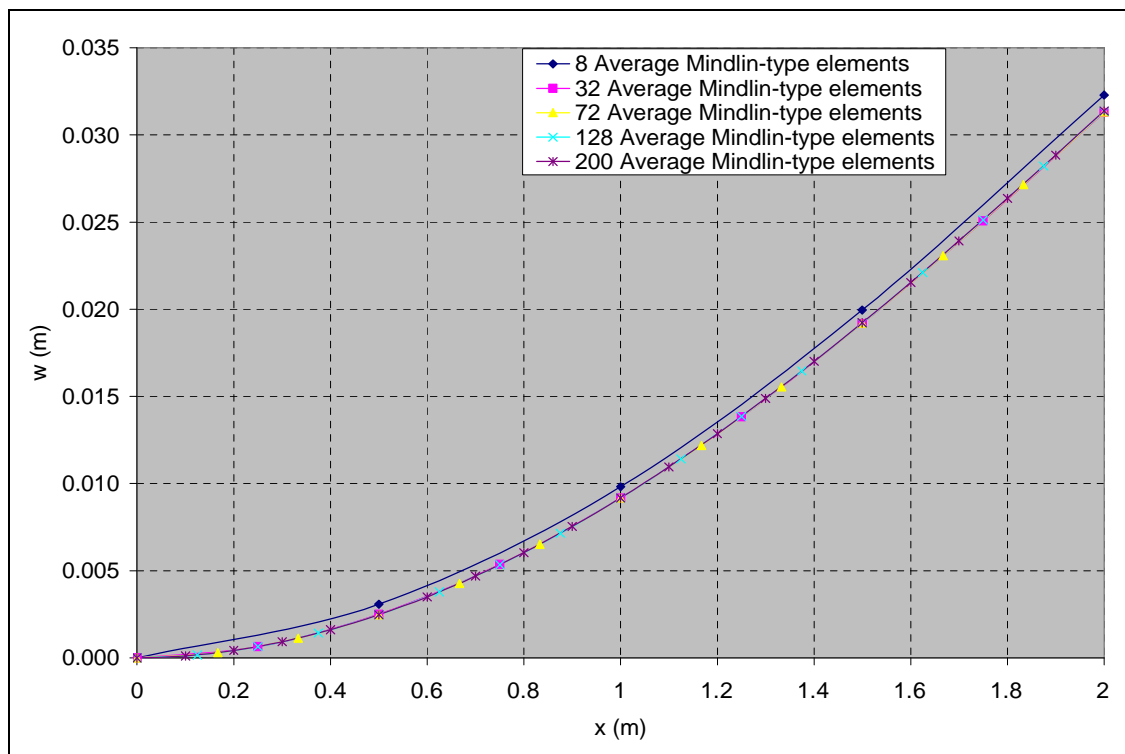
Figure 7-15: Mindlin program convergence check for the out-of-plane bending case
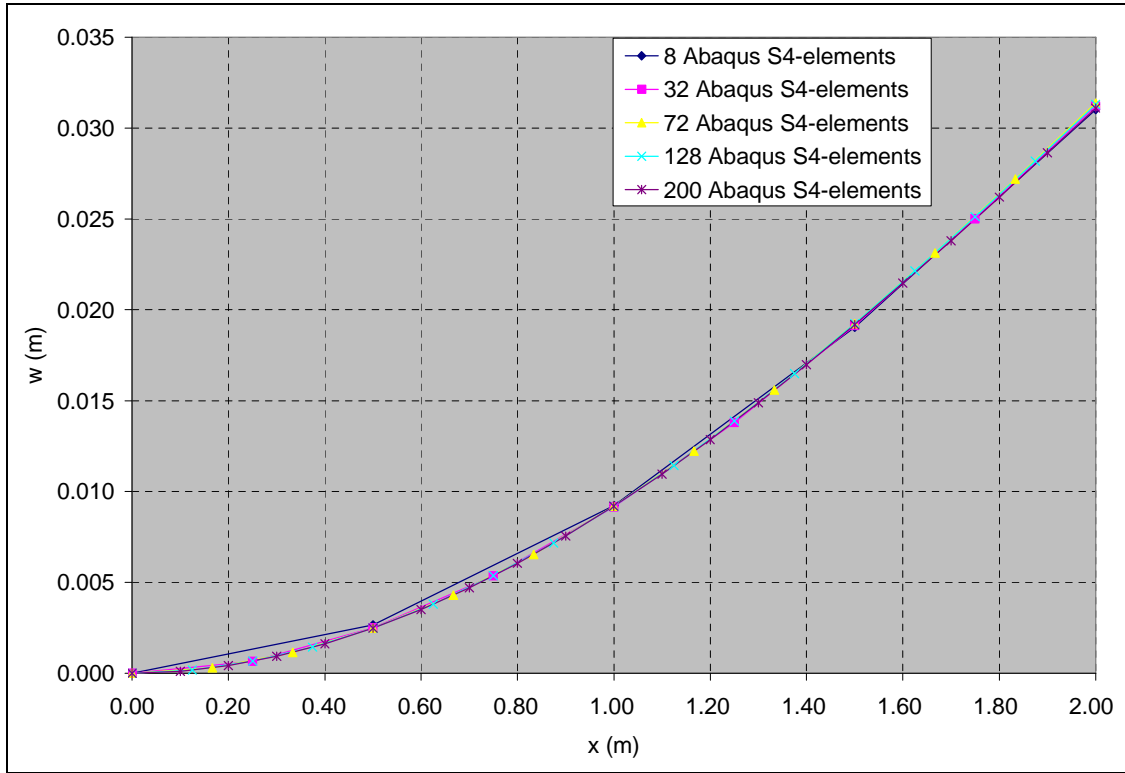
Figure 7-16: Abaqus program convergence check for the out-of-plane bending case

Mindlin program validation result

All the Mindlin programs including the independent validation program (i.e. the Ordinary FE program) were validated in this example. The results of the Mindlin programs and the Abaqus package shown in Figure 7-17 were results of the FGC plate case with P=1 and V_1=0.5. It can be seen from Figure 7-17 that the w-displacement results of the Mindlin programs were in good agreement (most data points overlap) with the result of the Abaqus package.
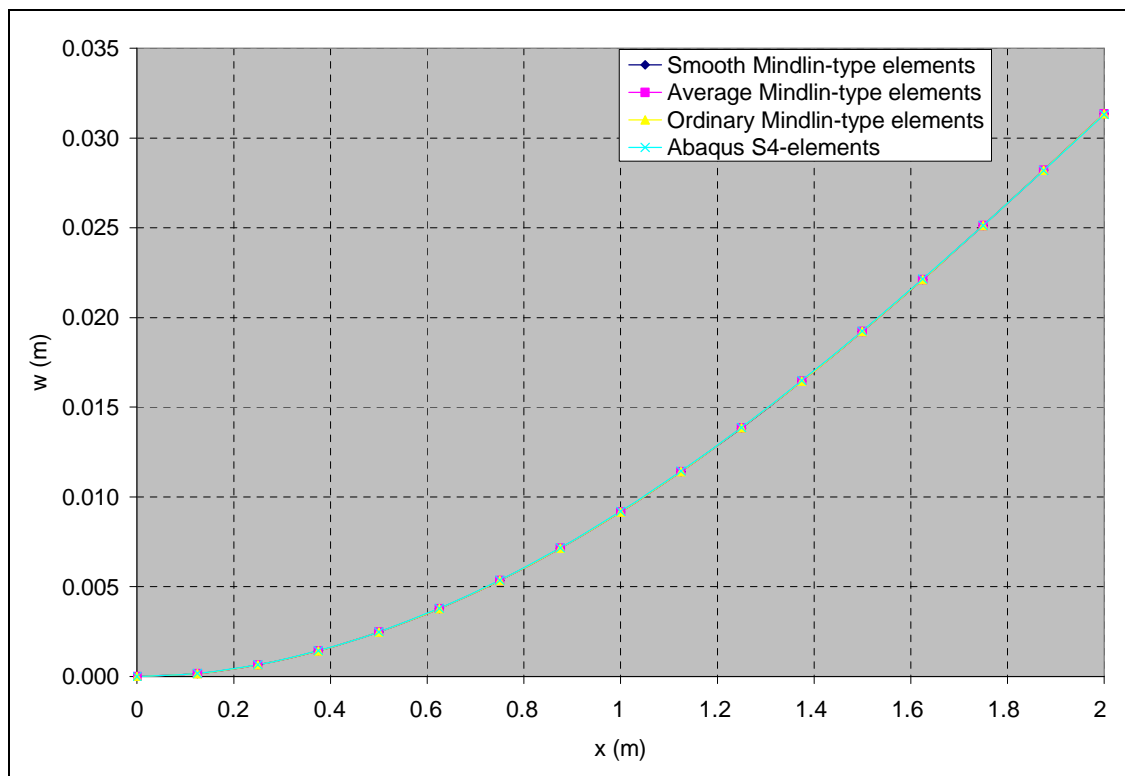
Figure 7-17: w-displacement validation against Abaqus result for the out-of-plane bending case

Figure 7-18 shows the stress result in the fibre direction (σ_{11}) at x=0 and y=0.5. The σ_{11} results of the Mindlin programs were in good agreement (most data points overlap) with the result of the Abaqus package. The results shown below are for a FGC plate with a stacking sequence of "$[[-45/0/45]_2]_s$". It can be seen from Figure 7-18 that the 2nd and 11th plies have the highest absolute σ_{11} values. This is due to the combined effect of 0° fibre orientation and the fact that the tensile and compressive stress (due to the applied out-of-plane bending load) increases away from the midplane of the composite plate. The 0° fibre orientations are aligned in the direction of the tensile and compressive stress caused by the out-of-plane bending load. Hence the 0° plies experience a higher share of σ_{11} relative to the 45° plies and -45° plies. Since the 2nd and 11th plies have 0° fibre orientation and they are the furthest 0° plies from the midplane, it is expected that they have the highest σ_{11} values which are equal in magnitude and opposite in direction.
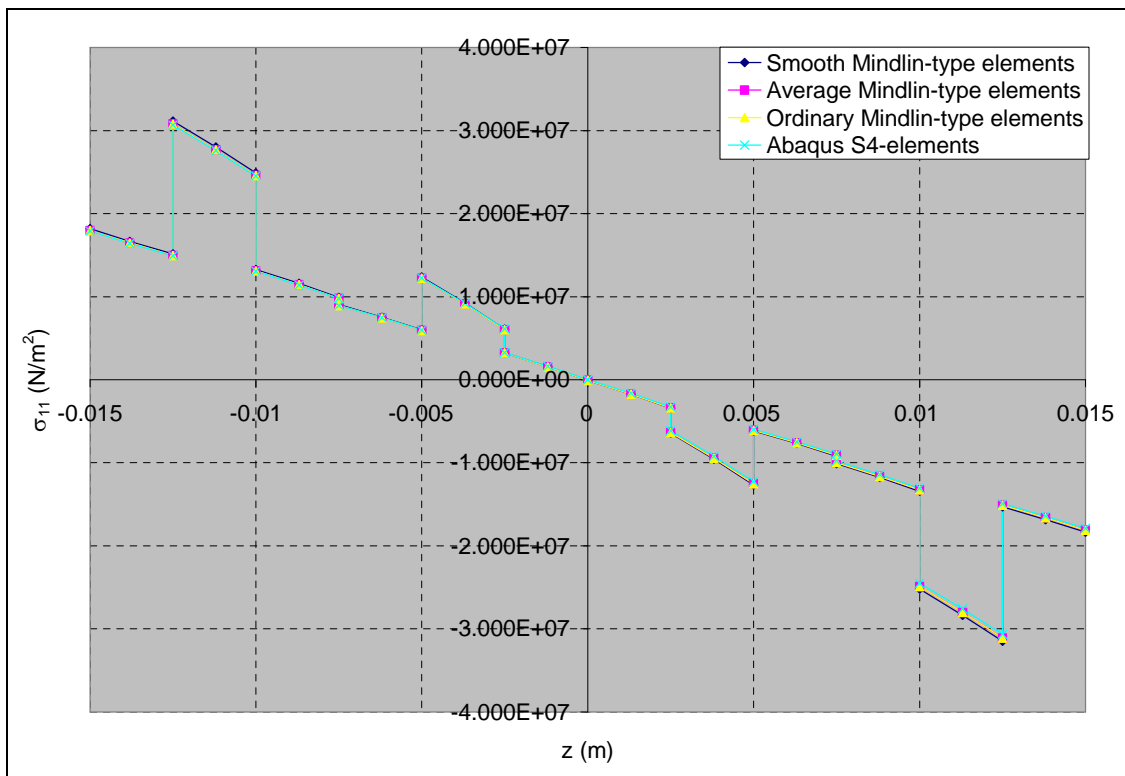
Figure 7-18: σ_{11} validation against Abaqus result for the out-of-plane bending case

Figure 7-19 shows the stress result in direction normal to the fibre direction (σ_{22}) at x=0 and y=0.5. The σ_{22} results of the Mindlin programs were in good agreement (most data points overlap) with the result of the Abaqus package. It can be seen from Figure 7-19 that the 1st and 12th plies have the highest absolute σ_{22} values. This is due to the combined effect of fibre orientation and the fact that the tensile and compressive stress (due to the applied out-of-plane bending load) increases away from the midplane of the composite plate. The -45° fibre orientations are not aligned in the direction of the tensile and compressive stress caused by the applied out-of-plane bending load. Hence the -45° plies experience a higher share of σ_{22} relative to 0° plies and 45° plies. Since the 1st and 12th plies have -45° fibre orientation and they are the furthest -45° ply from the midplane, it is expected that they have the highest σ_{22} values which are equal in magnitude and opposite in direction.

Figure 7-19: σ_{22} validation against Abaqus result for the out-of-plane bending case

141
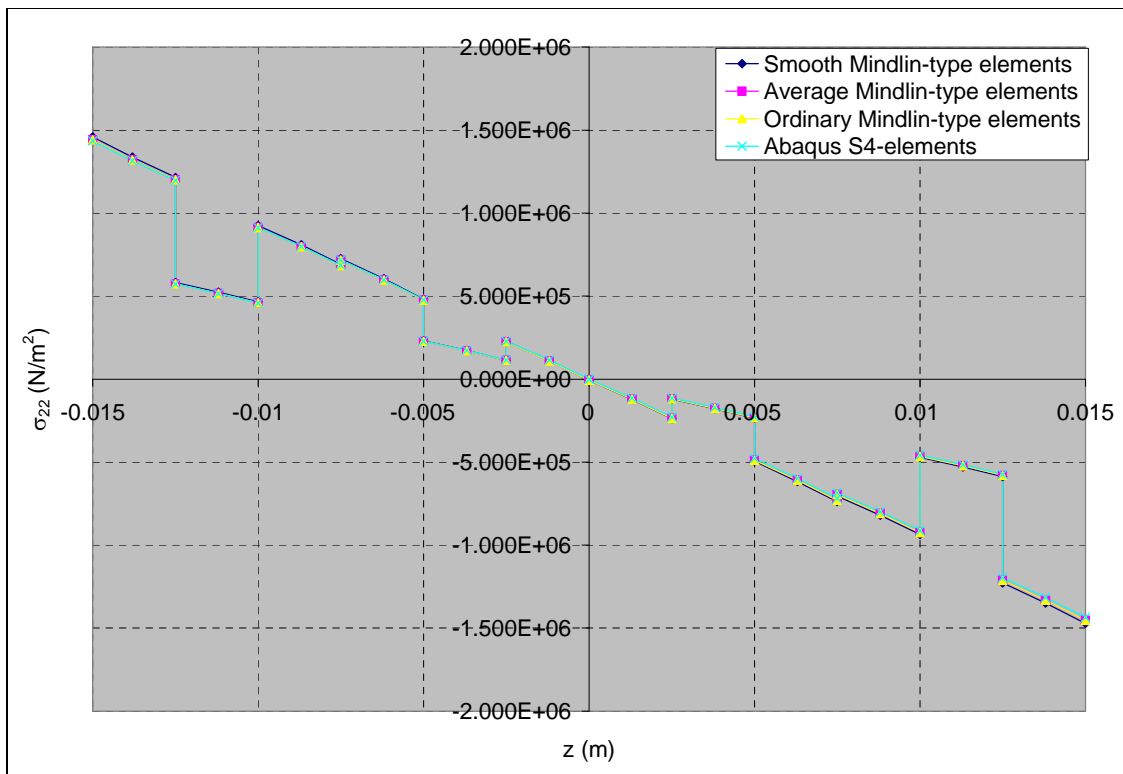
Figure 7-20 shows the shear stress result (τ_{12}) at x=0 and y=0.5. The τ_{12} results of the Mindlin programs were in good agreement (most data points overlap) with the result of the Abaqus package. It can also be seen from the graph that τ_{12} increases away from the midplane of the composite plate for each ply with specific fibre orientation.
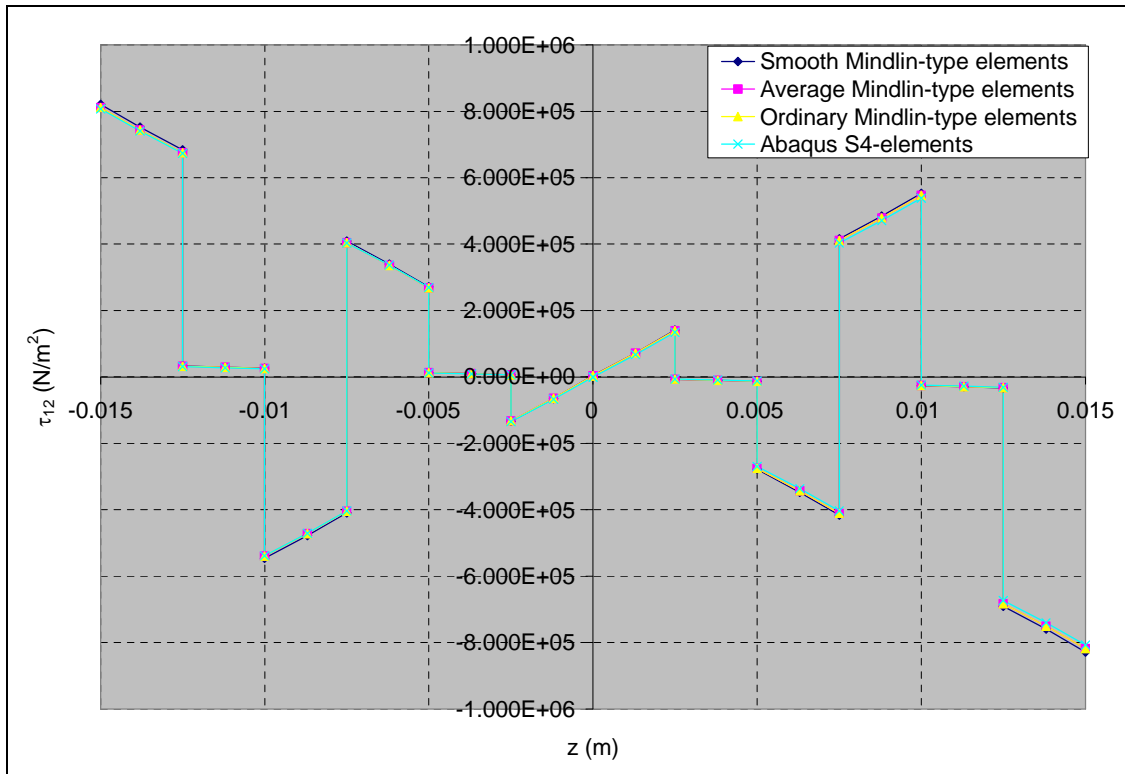
Figure 7-20: τ_{12} validation against Abaqus result for the out-of-plane bending case

7.2.3 FGC plate under compressive loading

Example 7.2.3: A rectangular FGC plate with a "$[[-45/0/45]_2]_s$" stacking sequence was subjected to a compressive load of 24kN. The values of the functional gradation properties include gradation exponent, P=1 and gradation offset, V_1=0.5. The task is to validate the buckling eigenvalue results of the Mindlin programs against the result of the Abaqus package. The FE modelling procedure is presented for this example. The geometrical properties and micro-mechanical properties are the same as the one given in Example 7.1.1.

FE Modelling

Different meshes were employed in this example to check for convergence. A mesh with 72 four-noded Mindlin-type elements was selected. A buckling load of 24kN was applied as an equivalent nodal loads at the nodes on the x=2 edge with reduced load at the corner nodes. For example, in the 72 element case, the load was applied equally at nodes on the x=2 edge but with half the loads at the corner nodes on the x=2 edge as shown in Table 7-17.

Table 7-17: Applied load for the buckling case

Nodes	Applied load
Nodes on the x=2 edge excluding corner nodes (i.e. node 13 and 14)	F_x = 4kN
Corner nodes (i.e. node 13 and 14)	F_x = 2kN

The boundary condition shown in Table 7-17 was applied to the FE model.

Table 7-18: Boundary condition for the buckling case

Nodes	Boundary condition
Nodes on the x=0 edge	$u = v = w = \theta_x = \theta_y = 0$
Nodes on the x=2 edge	$w = 0$

In order to model the functional gradation of the FGC plate in the Abaqus package, the fibre and matrix volume fractions were computed for each element at their midpoints by

using the fibre distribution equations developed in chapter 3. The macro-mechanical properties were then computed for each element as described in Example 7.1.1.

FE convergence and validation results

In this example, the first three buckling modes were analysed. The buckling eigenvalue is the ratio of critical buckling load to the applied load. The buckling eigenvalue results of the Mindlin programs and the Abaqus package were analysed for different mesh cases and the results showed good convergence as shown in Table 7-19. This table also shows that the buckling eigenvalue results of the Mindlin programs were in good agreement with the results of the Abaqus package. It can also be seen that for accurate eigenvalue prediction of higher buckling modes, finer meshes are required.

Table 7-19: Validation for the buckling case using Abaqus program

	Buckling Eigenvalues		
Abaqus S4-elements	1st Mode	2nd Mode	3rd Mode
8 Elements	25.62	88.49	141.65
32 Elements	20.79	67.06	87.69
72 Elements	20.00	61.20	83.61
128 Elements	20.26	61.81	87.54
Average Mindlin-type elements	1st Mode	2nd Mode	3rd Mode
8 Elements	23.97	82.74	99.44
32 Elements	20.65	67.19	86.18
72 Elements	20.01	61.57	83.22
128 Elements	19.77	59.68	82.08
Smooth Mindlin-type elements	1st Mode	2nd Mode	3rd Mode
8 Elements	23.98	82.39	99.47
32 Elements	20.65	67.18	86.09
72 Elements	20.01	61.57	83.17
128 Elements	19.77	59.68	82.05

7.2.4 FGC plate under free vibration

Example 7.2.4: Consider a rectangular FGC plate with a "[[-45/0/45]$_2$]$_s$" stacking sequence under free vibration. The values of the functional gradation properties include gradation exponent, P=1 and gradation offset, V$_1$=0.5. The task is to validate the natural frequency results of the Mindlin programs against the result of the Abaqus package. The FE modelling procedure is presented for this example. The geometrical properties and micro-mechanical properties are the same as the one given in Example 7.1.1.

FE Modelling

Different meshes were employed in this example to check for convergence. The boundary condition shown in Table 7-20 was applied to the FE model.

Table 7-20: Boundary condition for the free vibration case

Nodes	Boundary condition
Nodes on the x=0 edge	$u = v = w = \theta_x = \theta_y = 0$

In order to model the functional gradation of the FGC plate in the Abaqus package, the fibre and matrix volume fractions were computed for each element at their midpoints by using the fibre distribution equations developed in chapter 3. The macro-mechanical properties were then computed for each element as described in Example 7.1.1.

FE convergence and validation results

In this example, the first three free vibration modes were analysed. The first three fundamental frequency results of the Mindlin programs and the Abaqus package were analysed for different mesh cases and the results showed good convergence as shown in Table 7-21. This table also shows that the first three fundamental frequency results of the Mindlin programs were in good agreement with the results of the Abaqus package. The results also show that finer meshes are needed to accurately predict higher natural frequency modes.

Table 7-21: Validation for the free vibration case using Abaqus program

	Natural frequencies (Hz)		
Abaqus S4-elements	1st Mode	2nd Mode	3rd Mode
8 Elements	7.13	29.04	47.42
32 Elements	7.12	28.64	42.63
72 Elements	7.10	28.41	41.73
128 Elements	7.04	28.29	41.44
200 Elements	7.01	28.32	41.62
Average Mindlin-type elements	1st Mode	2nd Mode	3rd Mode
8 Elements	6.95	28.68	46.71
32 Elements	7.11	28.68	42.59
72 Elements	7.10	28.46	41.80
128 Elements	7.10	28.38	41.50
200 Elements	7.10	28.36	41.35
Smooth Mindlin-type elements	1st Mode	2nd Mode	3rd Mode
8 Elements	6.96	28.70	46.78
32 Elements	7.11	28.68	42.60
72 Elements	7.10	28.46	41.81
128 Elements	7.10	28.38	41.50
200 Elements	7.10	28.36	41.36

7.2.5 Traditional composite plate with a central hole under tension

Example 7.2.5: A rectangular traditional composite plate with a central hole a "[[-45/0/45]$_2$]$_s$" stacking sequence was subjected to a tensile loading of 24kN. The task is to validate the displacement results of the Average Mindlin FE program against the result of the Abaqus package. The FE modelling procedure is presented for this example. The geometrical properties, micro-mechanical properties and loading condition are as given in Example 7.1.4.

FE Modelling

In order to model the composite plate with a central hole under uniaxial tensile loading, the model was divided into four equal quarters. One of the quarter models was then used in the FE modelling by applying boundary conditions which takes advantage of symmetrical nature of the full model. These include specifying the u-displacement of the nodes on the x=0 edge as zero and also specifying the v-displacement of the nodes on the y=0 edge as zero. Different meshes were employed in this example to check for

convergence. A mesh with 180 four-noded Mindlin-type elements was selected. A tensile load of 24kN was applied as an equivalent nodal loads at the nodes on the x=2 edge with reduced load at the corner nodes. For example, in the 180 element case, the load was applied equally at nodes on the x=2 edge but with half the loads at the corner nodes on the x=2 edge. Hence the equivalent nodal loading for the 180 element case was 4.8kN at each nodes on the x=2 edge with 2.4kN at corner nodes on the x=2 edge.

FE convergence results

The displacement results of the Average Mindlin program and the Abaqus package were analysed for different mesh cases and the results showed good convergence as shown in Figures 7-21 and 7-22.
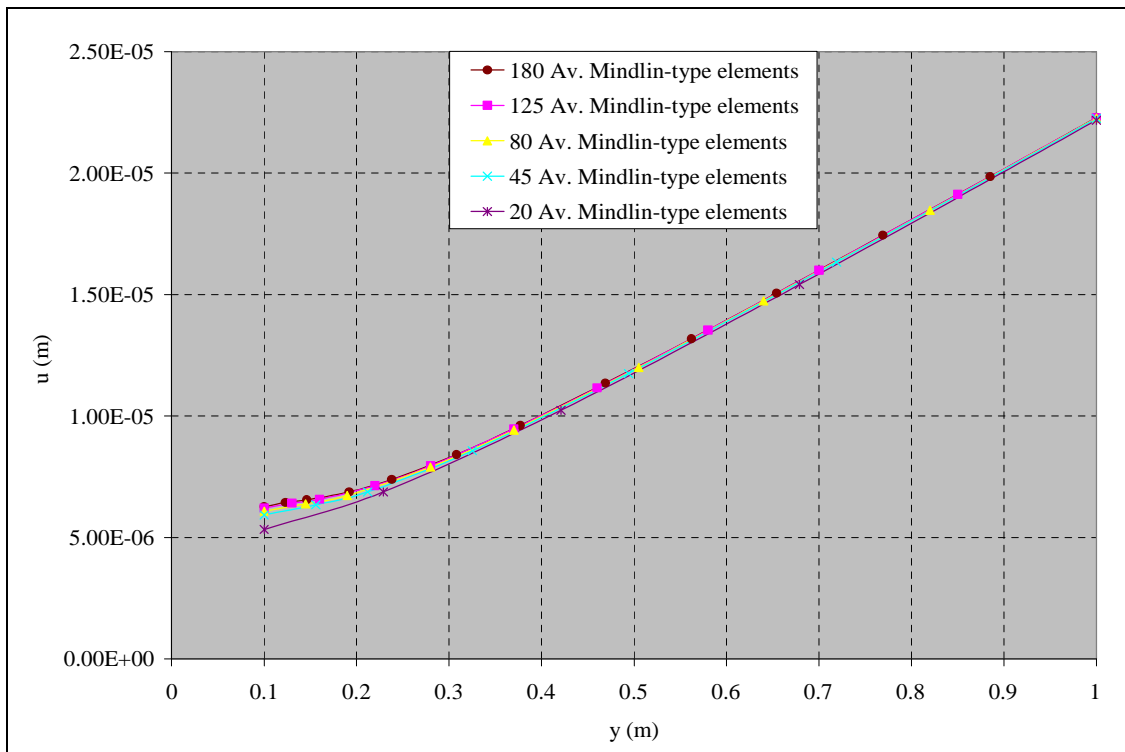
Figure 7-21: Mindlin program convergence check for the rectangular plate case with a hole
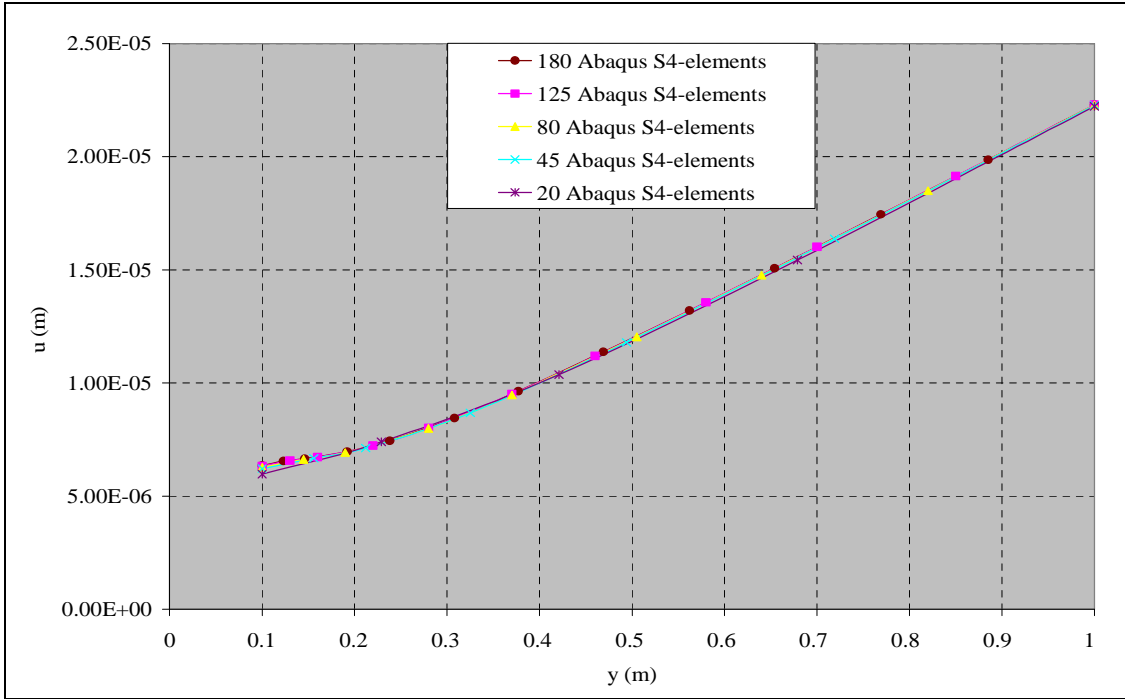
Figure 7-22: Abaqus program convergence check for the rectangular plate case with a hole

Mindlin program validation results

All the Mindlin programs including the independent validation program (i.e. the Ordinary FE program) were validated in this example. The Ordinary FE program is an independent validation program developed in-house for the finite element analysis of structures made of composite materials without functional gradation. The u-displacement results of the Mindlin programs were in good agreement (most data points overlap) with the result of the Abaqus package as shown in Figure 7-23.
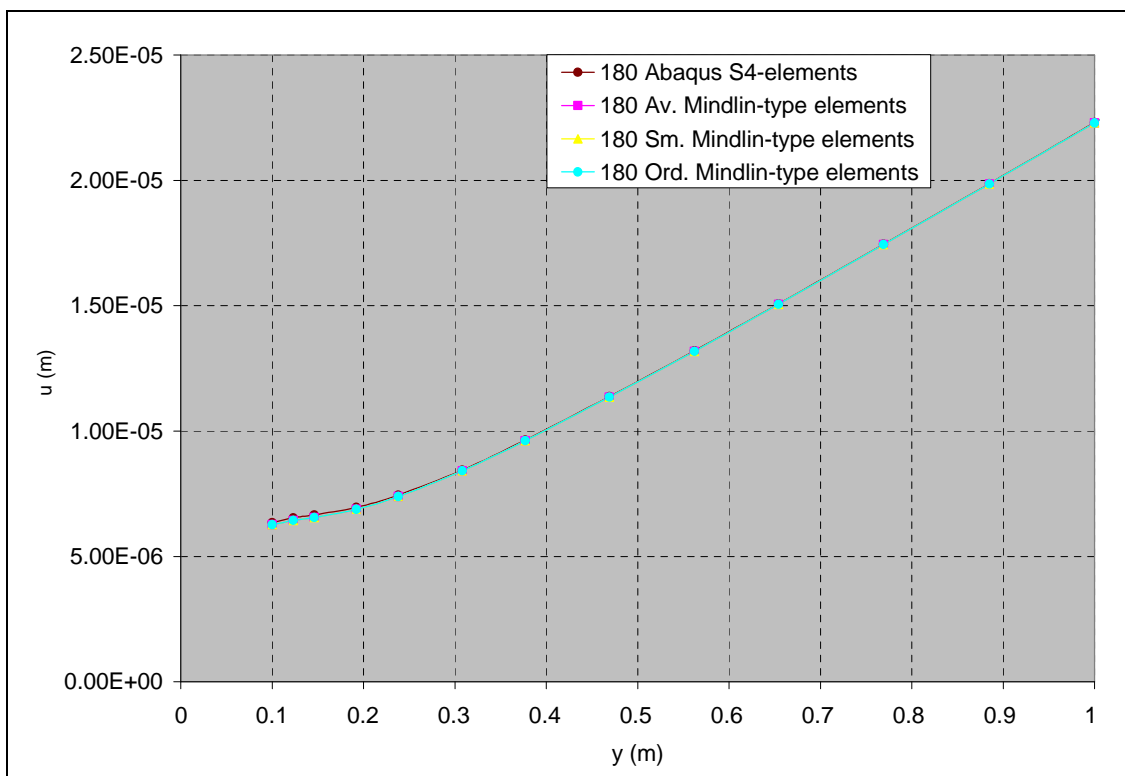
Figure 7-23: u-displacement validation against Abaqus result for the rectangular plate case with a hole

7.2.6 Simply supported FGC ring case

Example 7.2.6: A simply supported FGC ring with a "[[-45/0/45]$_2$]$_s$" stacking sequence was subjected to a pressure loading of 50kPa. The task is to validate the displacement and stress result of the Average Mindlin program against the result of the Abaqus package. The FE modelling procedure is presented for this example.

The geometrical properties and micro-mechanical properties are as given below. The micromechanical data were obtained from a textbook by Kaw (1997).

Table 7-22: Data for the simply supported ring case

Geometry					
R_i (m)	0.500	R_o (m)	1.000		
t (m)	0.030	No. of ply	12		
Fibre and matrix properties					
E_f (Pa)	2.300E+11	ν_f	3.500E-01	μ_f (Pa)	8.519E+10
E_m (Pa)	3.400E+09	ν_m	3.000E-01	μ_m (Pa)	1.308E+09

The notations used in Table 7-22 are as described below.

R_i, R_o and t, represent the inner radius, outer radius, thickness of ply respectively.

E_f and E_m represent the Young's modulus of the fibre and matrix respectively.

ν_f and ν_m represent the Poisson's ratio of the fibre and matrix respectively.

μ_f and μ_m represent the shear modulus of the fibre and matrix respectively.

FE Modelling

A quarter of the model has been modelled instead of the full ring model by taking advantage of the axisymmetry nature of the FE problem. Different meshes were employed in this example to check for convergence. A triangular element has been employed in order to demonstrate and validate the capability of the Mindlin programs in modelling with triangular elements. A mesh with 128 triangular elements is as shown in Figure 7-24. The element employed for the Mindlin programs is a triangular Average Mindlin-type element. The element employed for the Abaqus package is a triangular shell element called S3-element.
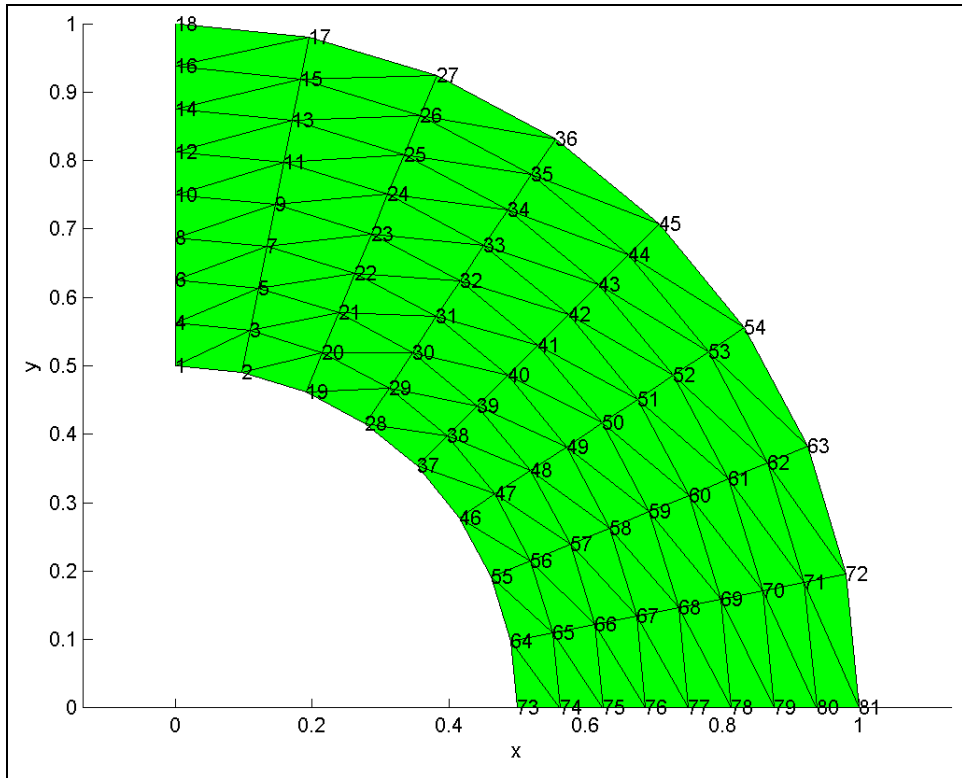
Figure 7-24: 3-noded triangular element mesh for a simply supported ring

The loading and boundary condition shown in Figure 7-25 was applied to the FE models in this example.
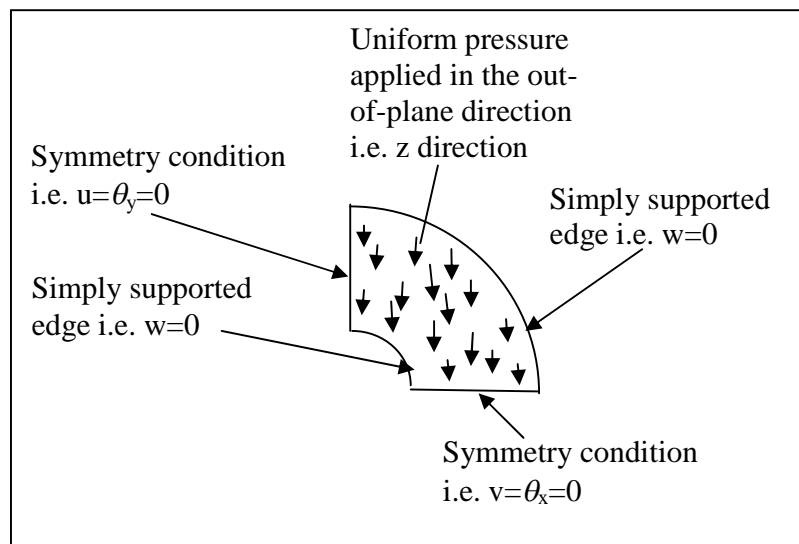
Figure 7-25: Loading and boundary condition for the simply supported ring case

In order to model the functional gradation of the FGC ring in the Abaqus package, the fibre and matrix volume fractions were computed for each element at their midpoints by using the fibre distribution equations developed in chapter 3. The macro-mechanical properties were then computed for each element as described in the spreadsheet below.

Table 7-23: Computation of macro-mechanical properties

Functional gradation properties							
P	1	$V_{f\_}$	0.4				
V_1	0.5						
r_i (m)	0.5	r_o (m)	1				
ξ_{min}	0	ξ_{max}	1				
Q	0.5						
V_2	0.3						
Macro-mechanical properties							
r (m)	ξ	V_f	V_m	E_{11} (Pa)	E_{22} (Pa)	ν_{12}	μ_{12} (Pa)
0.5313	0.0625	0.4875	0.5125	1.139E+11	6.542E+09	0.3244	2.515E+09
0.5938	0.1875	0.4625	0.5375	1.082E+11	6.246E+09	0.3231	2.402E+09
0.6563	0.3125	0.4375	0.5625	1.025E+11	5.976E+09	0.3219	2.298E+09
0.7188	0.4375	0.4125	0.5875	9.687E+10	5.728E+09	0.3206	2.203E+09
0.7813	0.5625	0.3875	0.6125	9.121E+10	5.500E+09	0.3194	2.115E+09
0.8438	0.6875	0.3625	0.6375	8.554E+10	5.289E+09	0.3181	2.034E+09
0.9063	0.8125	0.3375	0.6625	7.988E+10	5.094E+09	0.3169	1.959E+09
0.9688	0.9375	0.3125	0.6875	7.421E+10	4.912E+09	0.3156	1.889E+09

FE convergence results

The w-displacement results of the triangular Average Mindlin-type elements and the Abaqus S3-elements were analysed for different mesh cases and the results showed good convergence as shown in Figures 7-26 and 7-27.
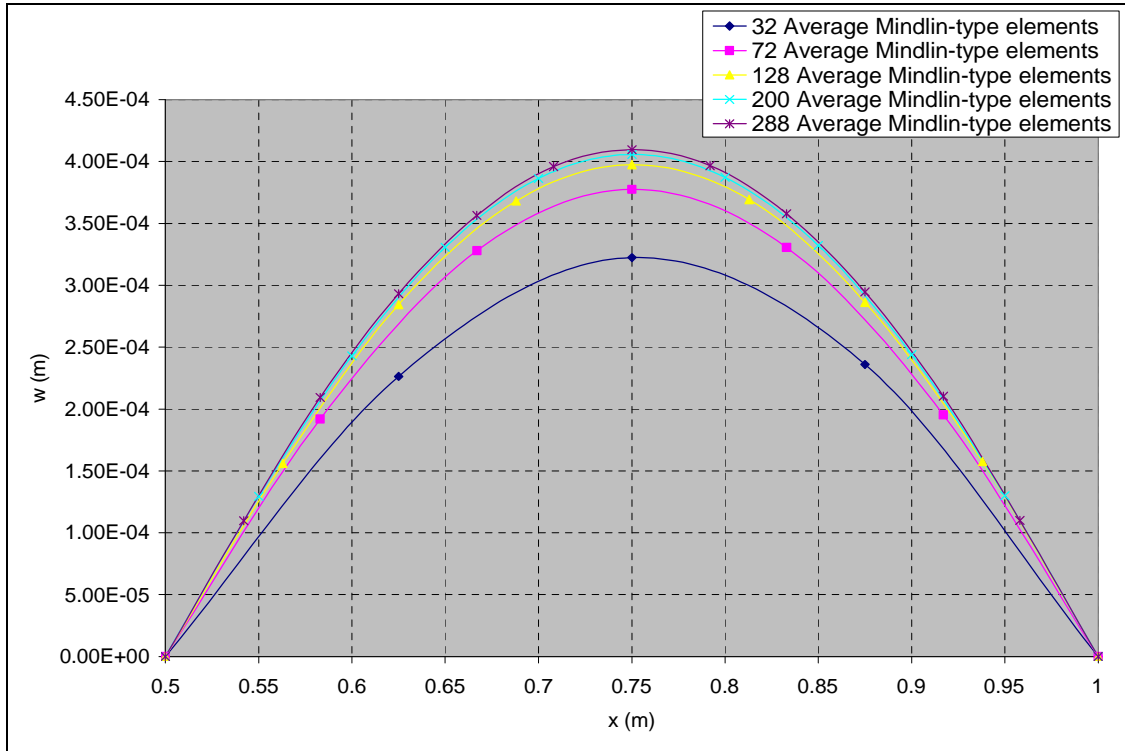
Figure 7-26: Mindlin program convergence check for the simply supported ring case
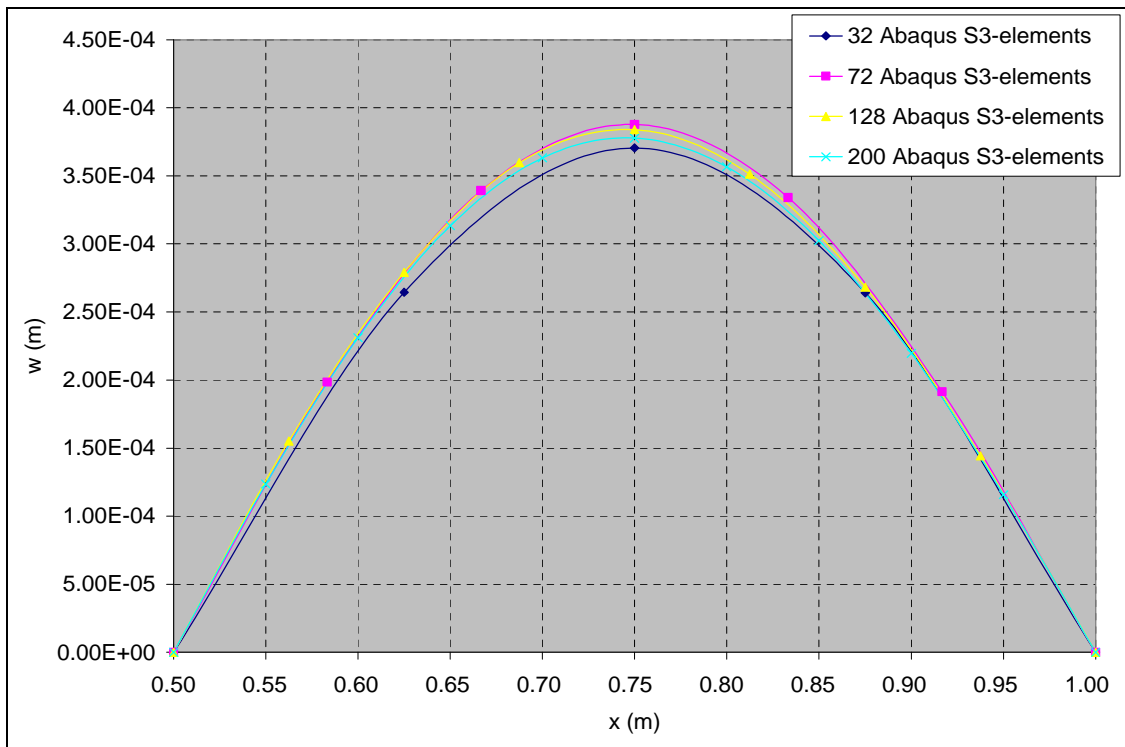
Figure 7-27: Abaqus program convergence check for the simply supported ring case

153

Mindlin program validation results

All the Mindlin programs including the independent validation program (i.e. the Ordinary FE program) were validated in this example using the mesh with 200 elements. The results of the Mindlin programs and the Abaqus package shown in Figure 7-28 were results of the FGC ring case with P=1 and V_1=0.5. It can be seen from Figure 7-28 that the w-displacement results of the Mindlin programs slightly differ from the result of the Abaqus package. In Figures 7-26 and 7-27, it can be seen that the result of the 200 Abaqus S3-elements agrees well (most data points overlap) with the results of the 72 triangular Mindlin-type elements.
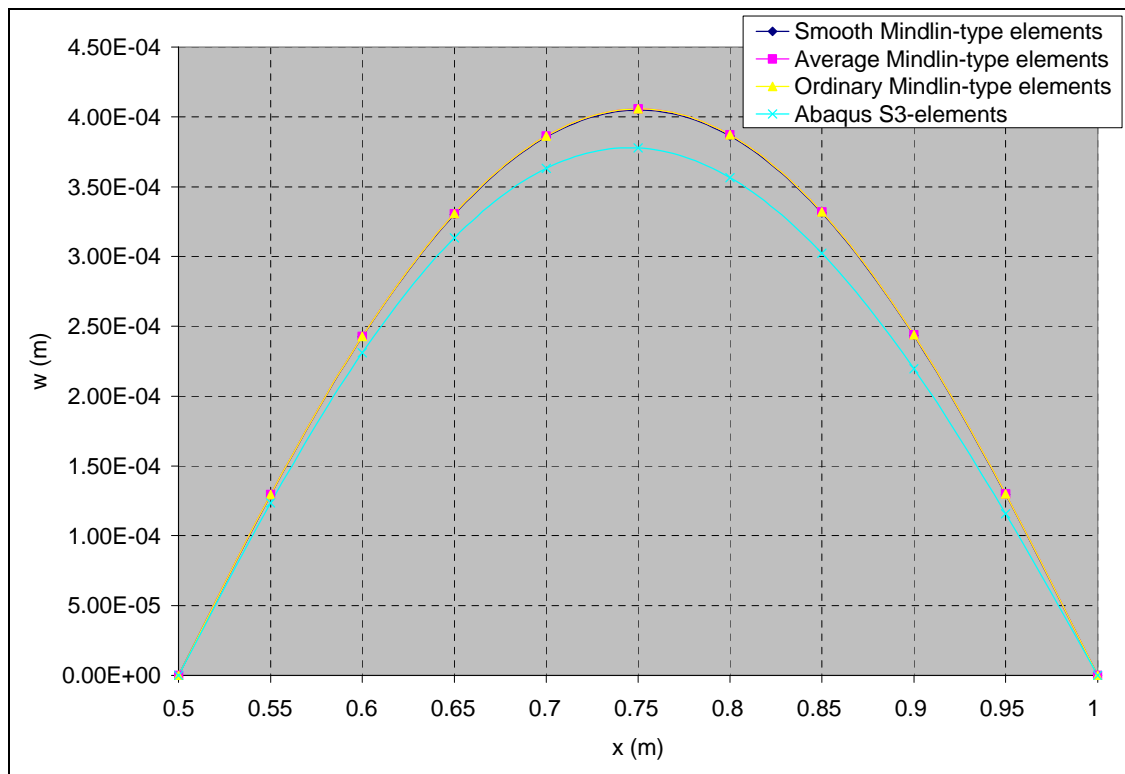
Figure 7-28: w-displacement validation against Abaqus result for the simply supported ring case

Figure 7-29 shows the stress result in the fibre direction (σ_{11}) at x=0 and y=0.75. The σ_{11} results of the Mindlin programs were in good agreement (most data points overlap) with the result of the Abaqus package. The results shown below are for a FGC ring with a stacking sequence of "[[-45/0/45]$_2$]$_s$". It is expected that the plies above the midplane experience tensile stresses and the ones below the midplane experience compressive stresses which is a shown in Figure 7-29. Also the plies equidistant from the midplane experience stresses which are equal in magnitude but opposite in direction.

Figure 7-29: σ_{11} validation against Abaqus result for the simply supported ring case

155
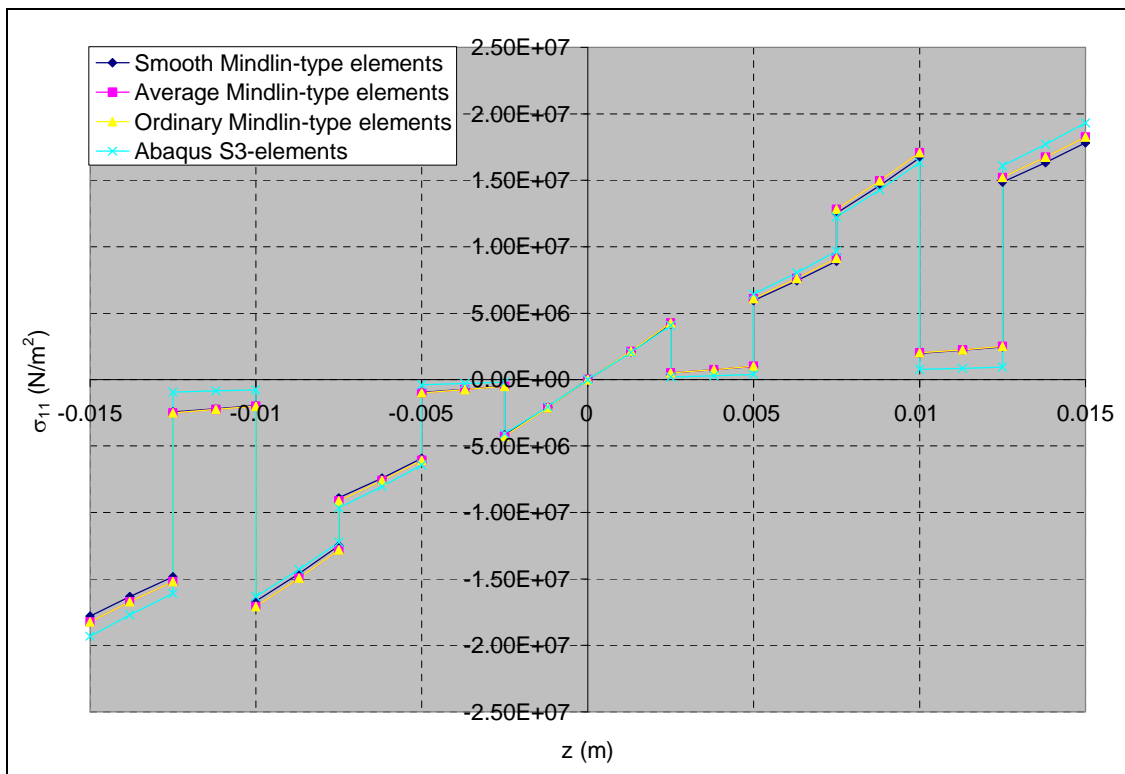
Figure 7-30 shows the stress result in the fibre direction (σ_{22}) at x=0 and y=0.75. The σ_{22} results of the Mindlin programs were in good agreement (most data points overlap) with the result of the Abaqus package. The results shown below are for a FGC ring with a stacking sequence of "[[-45/0/45]$_2$]$_s$". It is expected that the plies above the midplane experience tensile stresses and the ones below the midplane experience compressive stresses which is a shown in Figure 7-30. Also the plies equidistant from the midplane experience stresses which are equal in magnitude but opposite in direction.
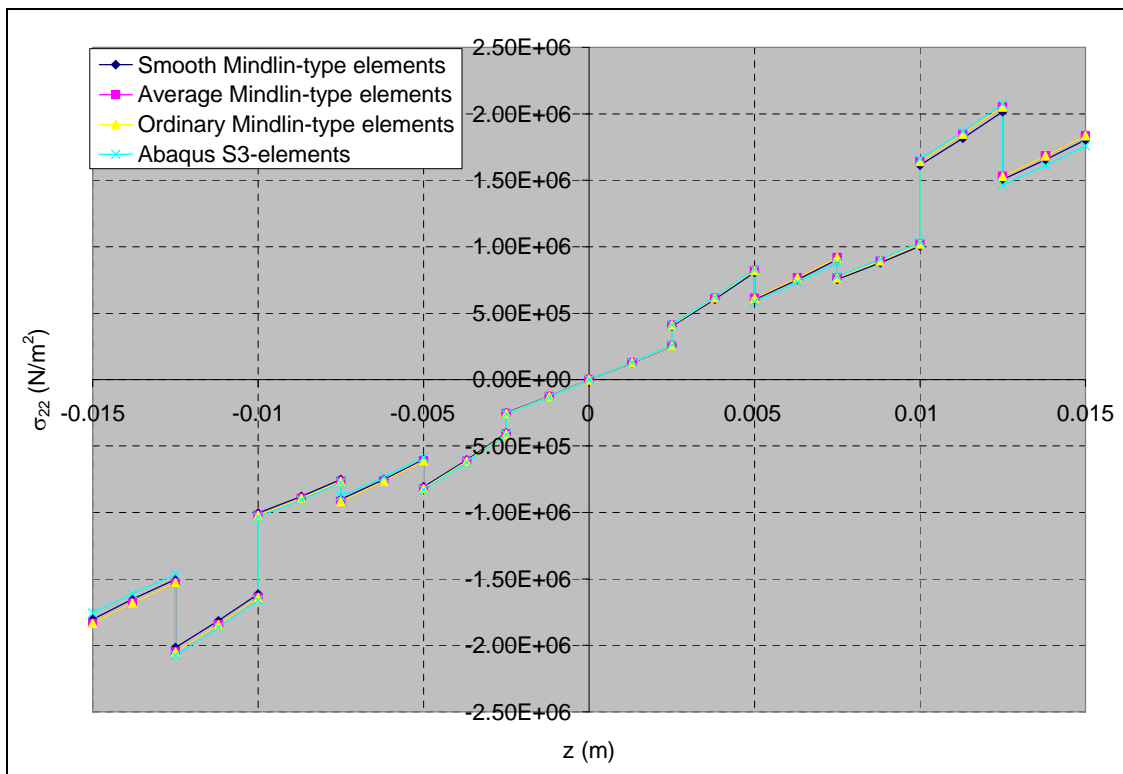
Figure 7-30: σ_{22} validation against Abaqus result for the simply supported ring case

Figure 7-31 shows the stress result in the fibre direction (τ_{12}) at x=0 and y=0.75. The τ_{12} results of the Mindlin programs were in good agreement (most data points overlap) with the result of the Abaqus package. The results shown below are for a FGC ring with a stacking sequence of "$[[-45/0/45]_2]_s$". It is expected that the plies equidistant from the midplane experience stresses which are equal in magnitude but opposite in direction. This phenomenon can be seen in Figure 7-31.
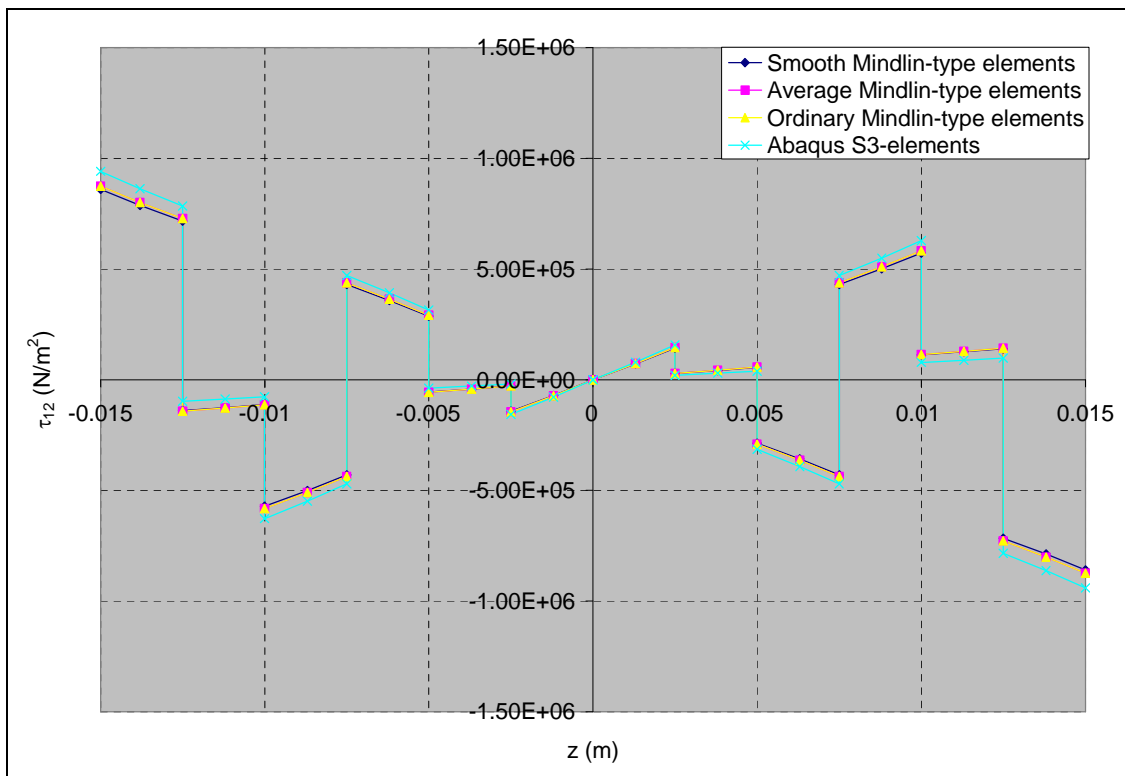
Figure 7-31: τ_{12} validation against Abaqus result for the simply supported ring case

7.2.7   Clamped FGC ring case

Example 7.2.7: A clamped FGC ring with a "[[-45/0/45]$_2$]$_s$" stacking sequence was subjected to a pressure loading of 50kPa. The task is to validate the displacement and stress result of the Average Mindlin program against the result of the Abaqus package. The FE modelling procedure is presented for this example. The geometrical properties and micro-mechanical properties are as in Example 7.2.5.

FE Modelling

A quarter of the model has been modelled instead of the full ring model by taking advantage of the axisymmetry nature of the FE problem. Different meshes were employed in this example to check for convergence. A triangular element has been employed in order to demonstrate and validate the capability of the Mindlin programs in modelling with triangular elements. The element employed for the Mindlin programs is a triangular Average Mindlin-type element. The element employed for the Abaqus package is a triangular shell element called S3-element.

The loading and boundary condition shown in Figure 7-32 was applied to the FE models in this example.
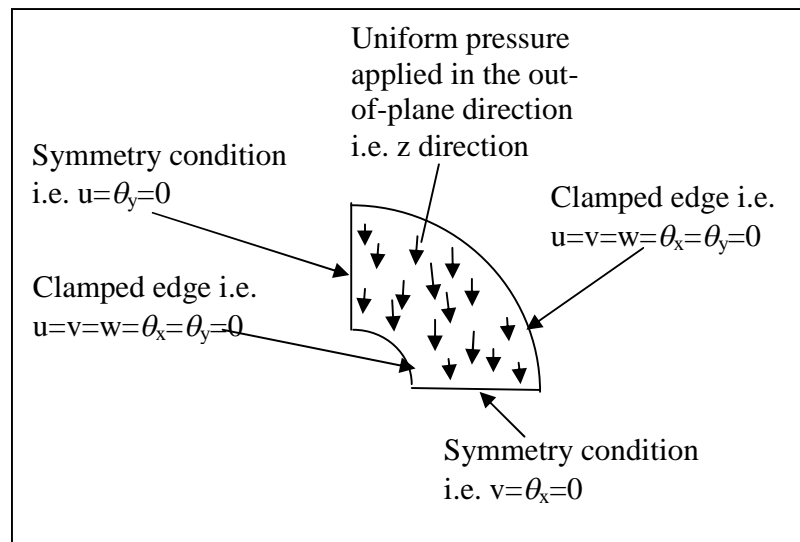
Figure 7-32: Loading and boundary condition for the simply supported ring case

In order to model the functional gradation of the FGC ring in the Abaqus package, the fibre and matrix volume fractions were computed for each element at their midpoints by

using the fibre distribution equations developed in chapter 3. The macro-mechanical properties were then computed for each element as described in Example 7.2.5.

FE convergence results

The w-displacement results of the triangular Average Mindlin-type elements and the Abaqus S3-elements were analysed for different mesh cases and the results showed good convergence as shown in Figures 7-33 and 7-34.
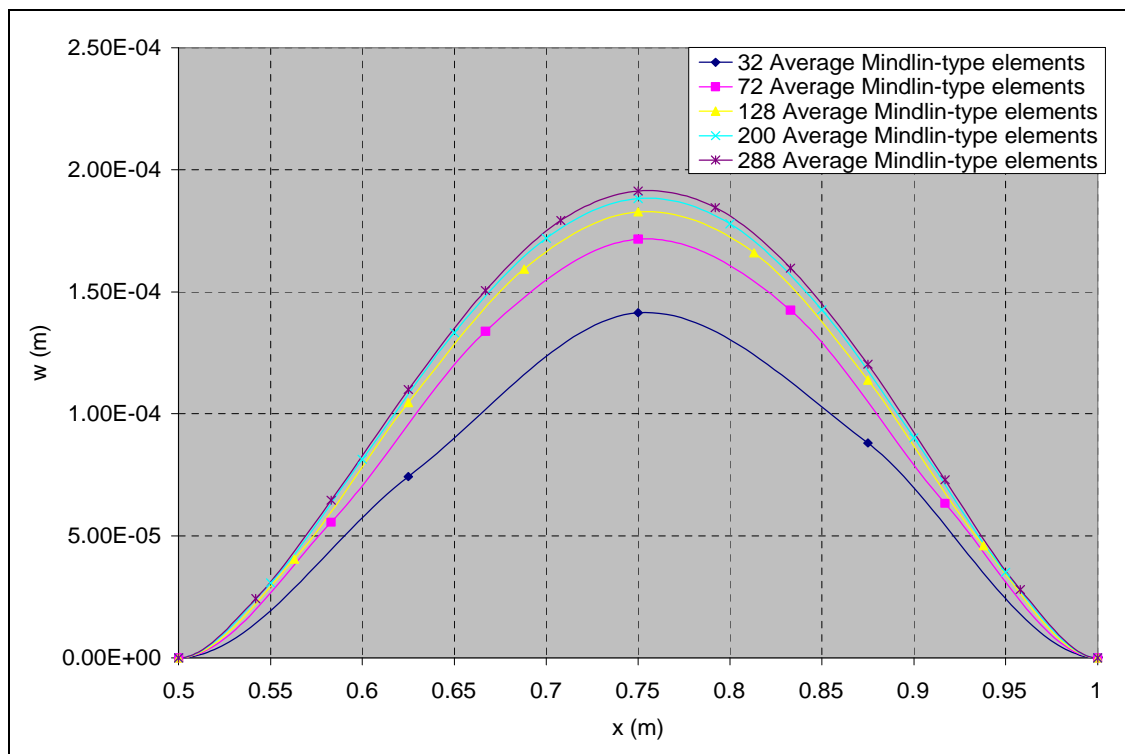
Figure 7-33: Mindlin program convergence check for the simply supported ring case
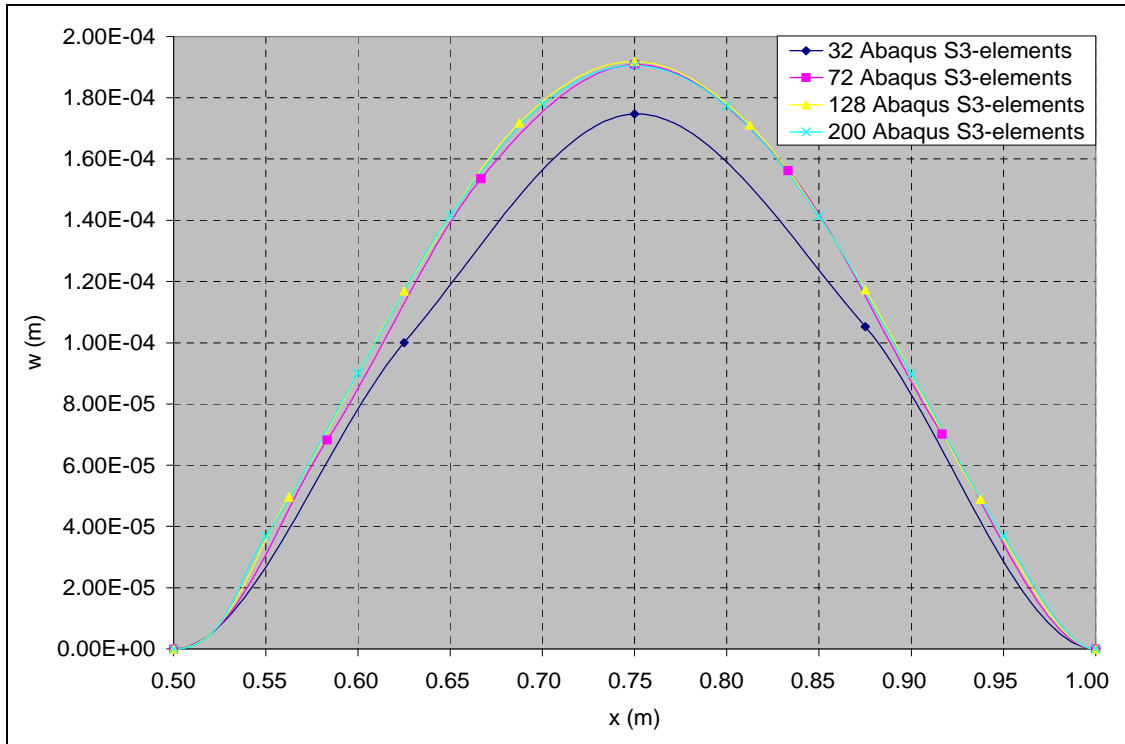
Figure 7-34: Abaqus program convergence check for the simply supported ring case

<u>Mindlin program validation results</u>

All the Mindlin programs including the independent validation program (i.e. the Ordinary FE program) were validated in this example using the mesh with 200 elements. The results of the Mindlin programs and the Abaqus package shown in Figure 7-35 were results of the FGC ring case with P=1 and V_1=0.5. It can be seen from Figure 7-35 that the w-displacement results of the Mindlin programs show a close agreement (most data points overlap) with the result of the Abaqus package.
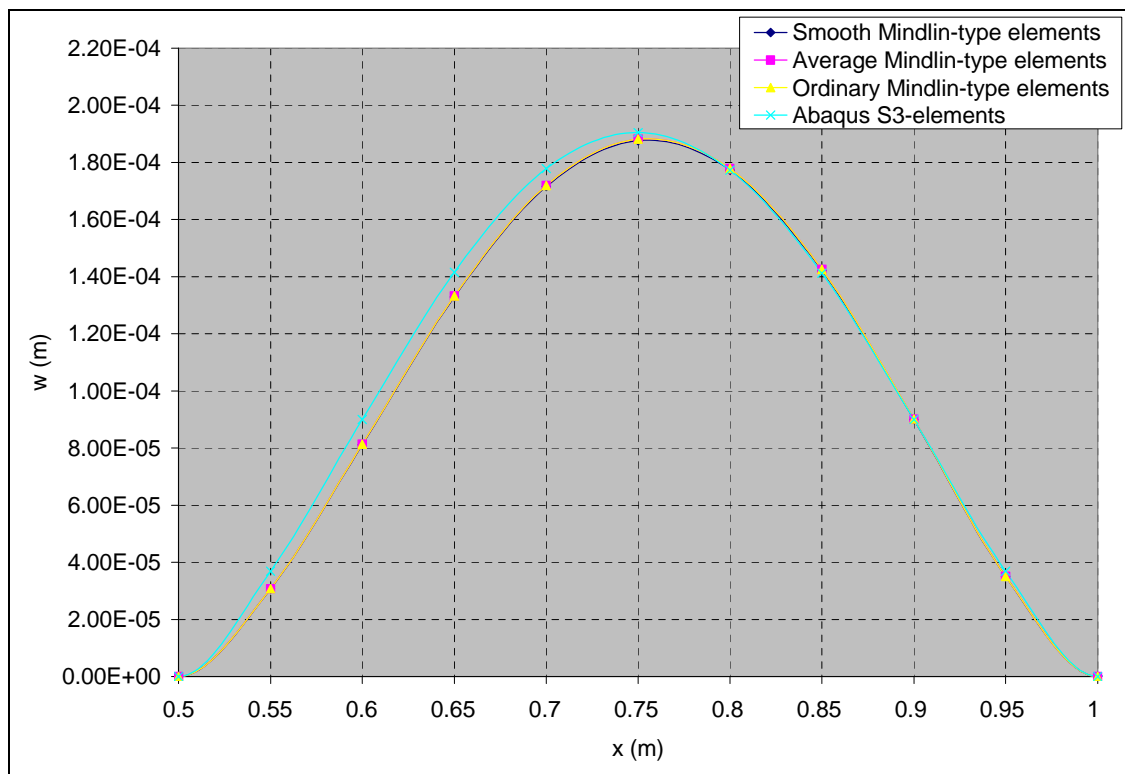
Figure 7-35: w-displacement validation against Abaqus result for the clamped ring case

Figure 7-36 shows the stress result in the fibre direction (σ_{11}) at x=0 and y=0.75. The σ_{11} results of the Mindlin programs were in good agreement (most data points overlap) with the result of the Abaqus package. The results shown below are for a FGC ring with a stacking sequence of "[[-45/0/45]$_2$]$_s$". It is expected that the plies above the midplane experience tensile stresses and the ones below the midplane experience compressive stresses which is a shown in Figure 7-36. Also the plies equidistant from the midplane experience stresses which are equal in magnitude but opposite in direction.
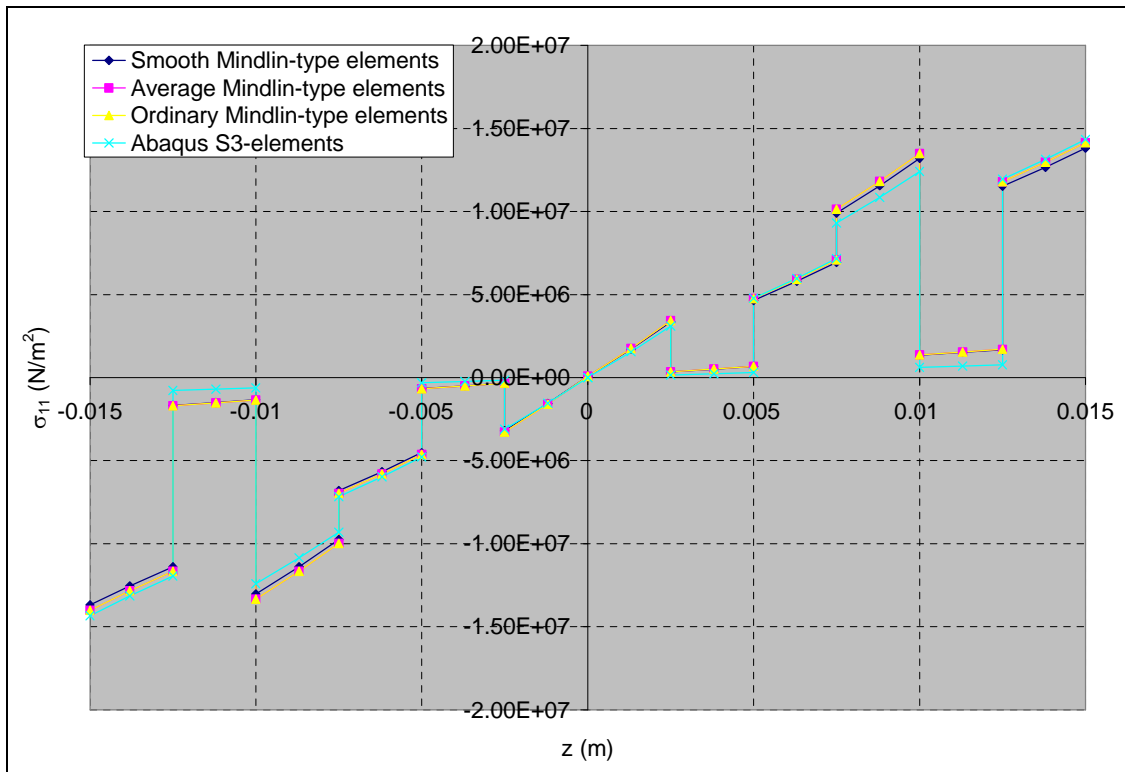
Figure 7-36: σ_{11} validation against Abaqus result for the clamped ring case

Figure 7-37 shows the stress result in the fibre direction (σ_{22}) at x=0 and y=0.75. The σ_{22} results of the Mindlin programs were in good agreement (most data points overlap) with the result of the Abaqus package. The results shown below are for a FGC ring with a stacking sequence of "[[-45/0/45]$_2$]$_s$". It is expected that the plies above the midplane experience tensile stresses and the ones below the midplane experience compressive stresses which is a shown in Figure 7-37. Also the plies equidistant from the midplane experience stresses which are equal in magnitude but opposite in direction.
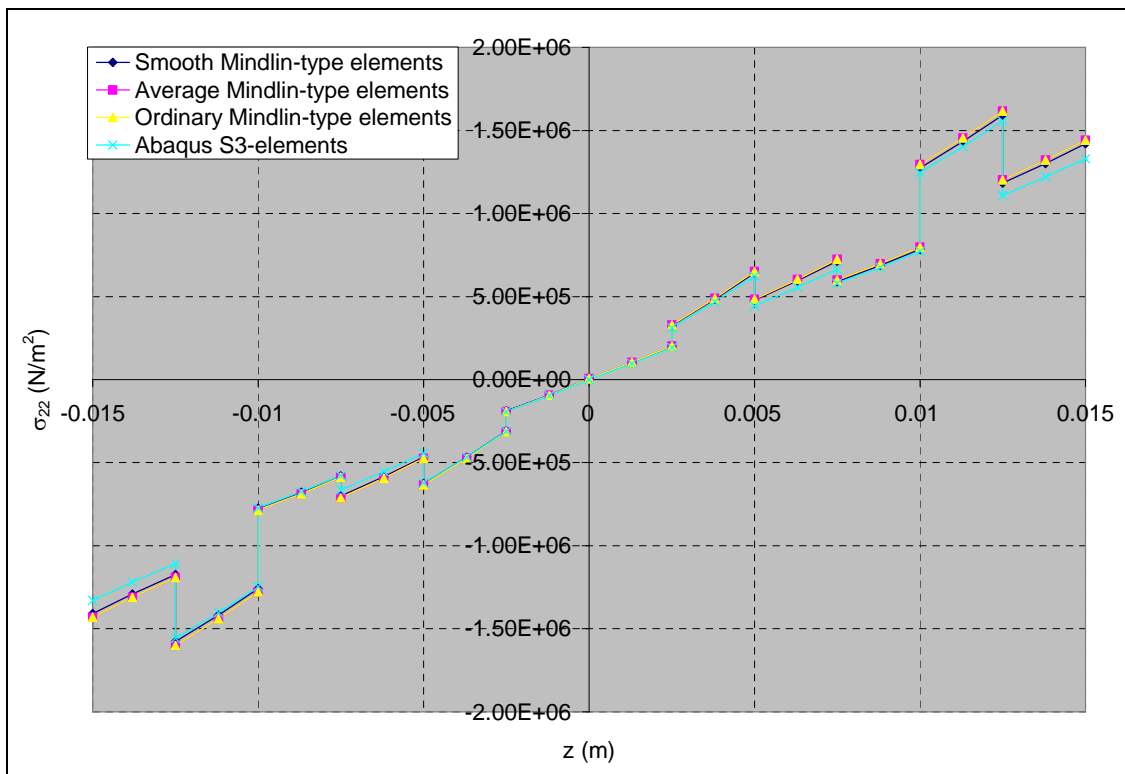
Figure 7-37: σ_{22} validation against Abaqus result for the clamped ring case

Figure 7-38 shows the stress result in the fibre direction (τ_{12}) at x=0 and y=0.75. The τ_{12} results of the Mindlin programs were in good agreement (most data points overlap) with the result of the Abaqus package. The results shown below are for a FGC ring with a stacking sequence of "[[-45/0/45]$_2$]$_s$". It is expected that the plies equidistant from the midplane experience stresses which are equal in magnitude but opposite in direction. This phenomenon can be seen in Figure 7-38.
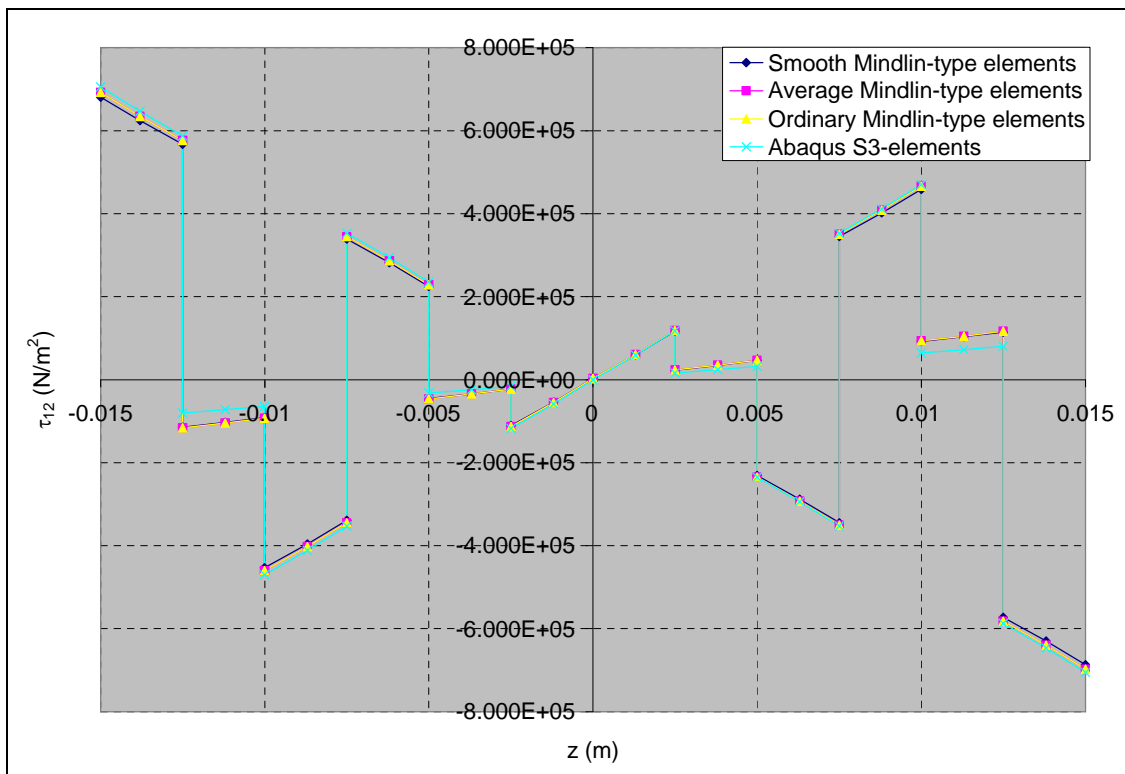
Figure 7-38: τ_{12} validation against Abaqus result for the clamped ring case

7.3 Program Validation against Ordinary Program

In this section, the Mindlin programs (i.e. Average and Smooth Mindlin program) were validated against the Ordinary Mindlin program. Also the Reissner programs (i.e. Average and Smooth Reissner program) were validated against the Ordinary Reissner programs. The Ordinary FE programs are programs developed in-house for the finite element analysis of structures made of composite materials without functional gradation. The Ordinary FE programs include the Ordinary Mindlin Program, Ordinary non-conforming and conforming Reissner program. The Ordinary FE programs were used to validate the infinitesimal and finite strain part of the Mindlin and Reissner programs for the analysis of functionally graded composite (FGC). Also, the progressive damage capabilities of the Mindlin and Reissner programs were validated. In this section, some numerical examples were presented for this validation exercise. These numerical examples include FGC plate subjected to tensile load, out-of-plane load; buckling load and free vibration; a simply supported ring subjected to uniform out-of-plane load; and a clamped ring subjected to uniform out-of-plane load.

7.3.1 FGC plate under tensile loading

<u>Example 7.3.1</u>: A rectangular FGC plate with a "$[[-45/0/45]_2]_s$" stacking sequence was subjected to a tensile loading of 8MN. The task is to validate the displacement, stress and the progressive damage result of the Mindlin and Reissner programs against the result of the Ordinary FE programs. The FE modelling procedure is presented for this example.

The geometrical properties and micro-mechanical properties are as given below. The micromechanical data were obtained from a textbook by Kaw (1997).

Table 7-24: Tensile case data

Geometry					
L (m)	2.000	w (m)	1.000		
t (m)	0.0300	No. of ply	12		
Fibre and matrix properties					
E_f (Pa)	2.300E+11	ν_f	3.500E-01	μ_f (Pa)	8.519E+10
E_m (Pa)	3.400E+09	ν_m	3.000E-01	μ_m (Pa)	1.308E+09
Strength properties					
X_{mt} (Pa)	7.200E7	X_{mc} (Pa)	1.020E8	X_{ms} (Pa)	3.400E7
X_{ft} (Pa)	2.067E9	X_{fc} (Pa)	1.999E9	σ_{rm} (Pa)	0.0
k_σ	1	k_τ	1		

The notations used in Table 7-24 are as described below.

L, w, and t, represent the length, width, thickness of ply respectively.

E_f and E_m represent the Young's modulus of the fibre and matrix respectively.

ν_f and ν_m represent the Poisson's ratio of the fibre and matrix respectively.

μ_f and μ_m represent the shear modulus of the fibre and matrix respectively.

X_{mt}, X_{mc} and X_{ms} represent the tensile, compressive and the shear strength of the matrix respectively.

X_{ft} and X_{fc} represent the tensile and compressive strength of the matrix respectively.

σ_{rm} represent the maximum residual radial stress at the interface.

k_σ and k_τ represent the stress concentration factor and the shear stress concentration factor respectively.

FE Modelling

A mesh containing 128 4-noded Mindlin-type elements was employed for the Mindlin programs. A mesh containing 128 4-noded conforming elements was employed for the conforming Reissner program. A mesh containing 128 4-noded non-conforming elements was employed for the non-conforming Reissner program. A tensile load of 8MN was applied as an equivalent nodal loads at the nodes on the x=2 edge with reduced load at the corner nodes. For example, in the 128 element case, the load was applied equally at nodes on the x=2 edge but with half the loads at the corner nodes on the x=2

166

edge. Hence the equivalent nodal loading for the 128 element case was 1MN at each nodes on the x=2 edge with 500kN at the corner nodes on the x=2 edge. In order to model the finite strain, a tenth of the equivalent nodal loading was applied at every load increment.

The boundary condition shown in Table 7-25 was applied to the FE model.

Table 7-25: Boundary condition for the tensile case

Nodes	Boundary condition
Node 20 (i.e. node at (0, 0.5) coordinate)	$u = v = w = \theta_x = \theta_y = 0$ (i.e. all degrees of freedom are fixed at Node 20)
Nodes on the x=0 edge excluding node 20	$u = 0$

In order to model the functional gradation of the FGC plate in the Ordinary FE programs, the fibre and matrix volume fractions were computed for each element at their midpoints by using the fibre distribution equations (i.e. Equation 3.34 and 3.38) developed in chapter 3. The macro-mechanical properties were then computed for each element by substituting the fibre and matrix volume fractions into the macro-mechanical equations developed in chapter 3. The computed macro-mechanical properties of each element of the FGC plate were then fed into the Ordinary FE programs.

Mindlin and Reissner program validation results

Figures 7-39 and 7-40 show the nodal displacement results along the y=0.5 line for a FGC plate case with P=1 and V_1=0.5 at the 9th load increment. The displacement results for the Mindlin and Reissner programs were in good agreement with the Ordinary FE program. The slope of the u-displacement curve, $\delta u/\delta x$ increases as the nodal position, x increases. This implies that the FGC plate experience increase in change in u-displacement, Δu; and hence reduction in longitudinal stiffness as the nodal position, x increases. This result can be attributed to reduction in fibre volume fraction as the nodal position, x increases. The v-displacement results along the y=0.5 line are zeroes as expected because the FGC plate is fixed in the x and y directions at the (0, 0.5) coordinate and it is subjected to a tensile load.

167
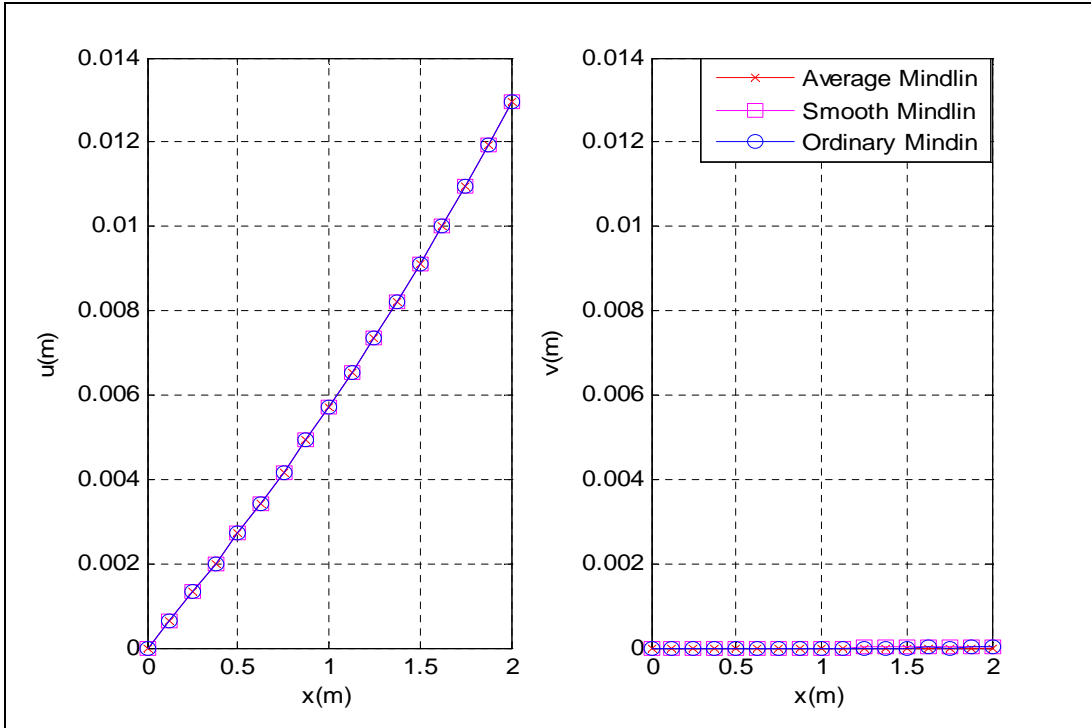
Figure 7-39: Displacement validation against Ordinary Mindlin program for the tension case
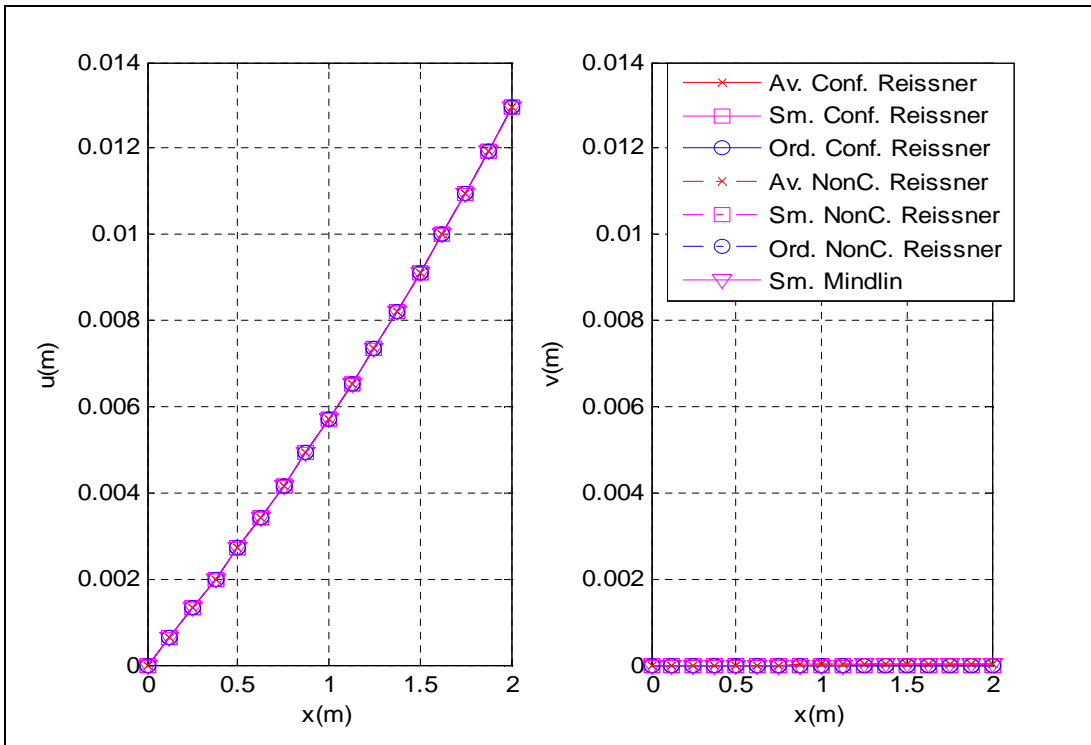
Figure 7-40: Displacement validation against Ordinary Reissner program for the tension case

Figure 7-41 shows the through-thickness stress result in the fibre direction at node 1 (i.e. the (0, 0) coordinate) for a FGC plate case with P=1 and V_1=0.5 at the 9th load increment. The stress results of the Average and Smooth Mindlin programs were in good agreement with the result of the Ordinary Mindlin program. It can be seen from Figure 7-41 that the 0° plies have the highest σ_{11} relative to the 45° plies and -45° plies. This is due to the fact that the fibres in the 0° plies are aligned in the tensile force direction. Hence they carry a higher share of the load relative to the share of load of fibres in the 45° plies and -45° plies.
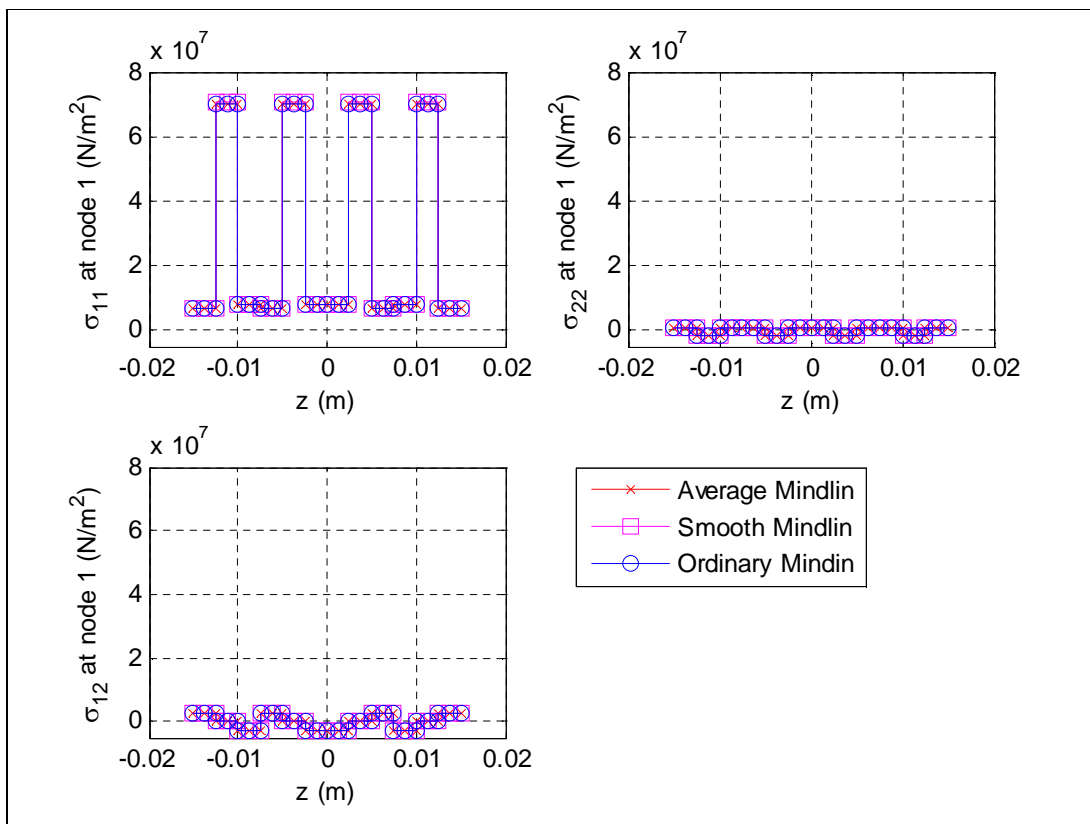
Figure 7-41: Stress validation against Ordinary Mindlin program for the tension case

In order to model the progressive damage, a check for failure was undertaken at the node of each element for every load increment and if failure is detected, material properties of the element are degraded and equilibrium is re-established. The failure criterion that was used in checking for failure is the Tsai-Hill failure criterion. Figure 7-42 shows the damage contour plot for the first three layers of a FGC plate case with P=1 and V_1=0.5 at the 9th load increment. This figure also shows the typical damage contour plot of all the programs for the FGC plate under tension. The damage contour plot is the plot of the Tsai-Hill failure index at all nodes on the FGC plate. If the Tsai-Hill failure index is greater than one, then the composite plate is damaged, else the composite plate is undamaged. The Tsai-Hill failure index was obtained using the equation provided in Chapter 3.

In order to understand the damage results in Figure 7-42, it must be noted that the damage are based on Tsai-Hill failure index which is a function of the micromechanical strength properties, fibre orientation of ply, functional gradation and stress transfer. It can be seen from the damage contour plot that the 0° plies were more susceptible to damage because they carry higher share of the load in comparison to the 45° and -45° plies. This is due to the fact that the fibre orientations in the 0° plies were aligned in the direction of the tensile load. The damage results were expected results because damage contour plot were based on Tsai-Hill failure index which is a function of fibre orientation. The effect of functional gradation can be seen in all the three plies but it is more pronounced in the 0° plies as shown for the 2nd ply in Figure 7-42. The figure shows that the ply is stronger around the x=0 edge than it is around the x=2 edge hence the undamaged regions are regions close the x=0 edge as shown in Figure 7-42. Also the results include the effect of stress transfer. This effect is due to the undamaged regions being stiffer than the damaged regions and they carry a large portion of the extra loads that were meant for the damaged regions and therefore the undamaged regions are stressed more. Hence this results in stress transfer occurring both in the in-plane and out-of-plane directions.
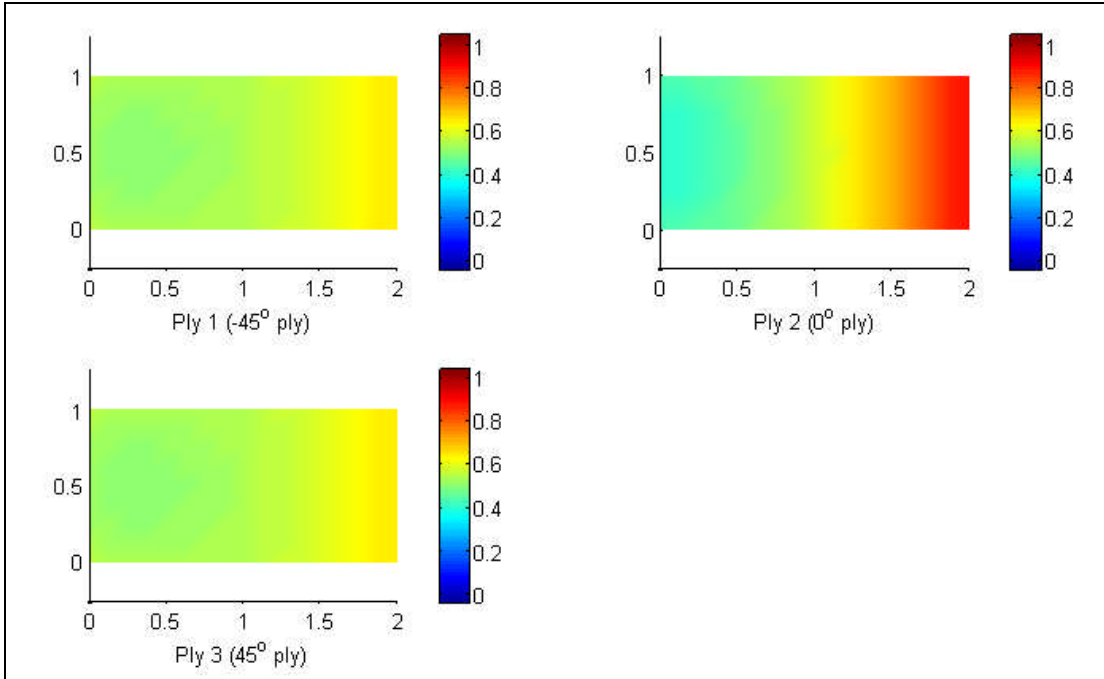
Figure 7-42: Damage contour plot of the first three plies for the tension case

Since failure was more pronounced in the 2nd ply, a closer study of the progressive damage of the 2nd ply was undertaken. Figure 7-43 shows the progressive damage contour plot for the 2nd ply (i.e. 0° ply) of a FGC plate case with P=1 and V$_1$=0.5 for nine load increments. This figure also shows the typical progressive damage contour plot of all the programs for the FGC plate under tension. The damage contour plot is the plot of the failure index at all nodes on the FGC plate. If failure index is greater than one, then the composite plate is damaged, else the composite plate is undamaged. It can be seen from the damage contour plot that failure index increases as the nodal position, x increases. This indicates that the weaker region is the region around the x=2 edge. Also no damage occurred at the first nine load increments but on the tenth load increment, the program could not establish equilibrium and hence it could not provide a solution. This implies that complete damage has occurred in the FGC plate at the tenth load increment.
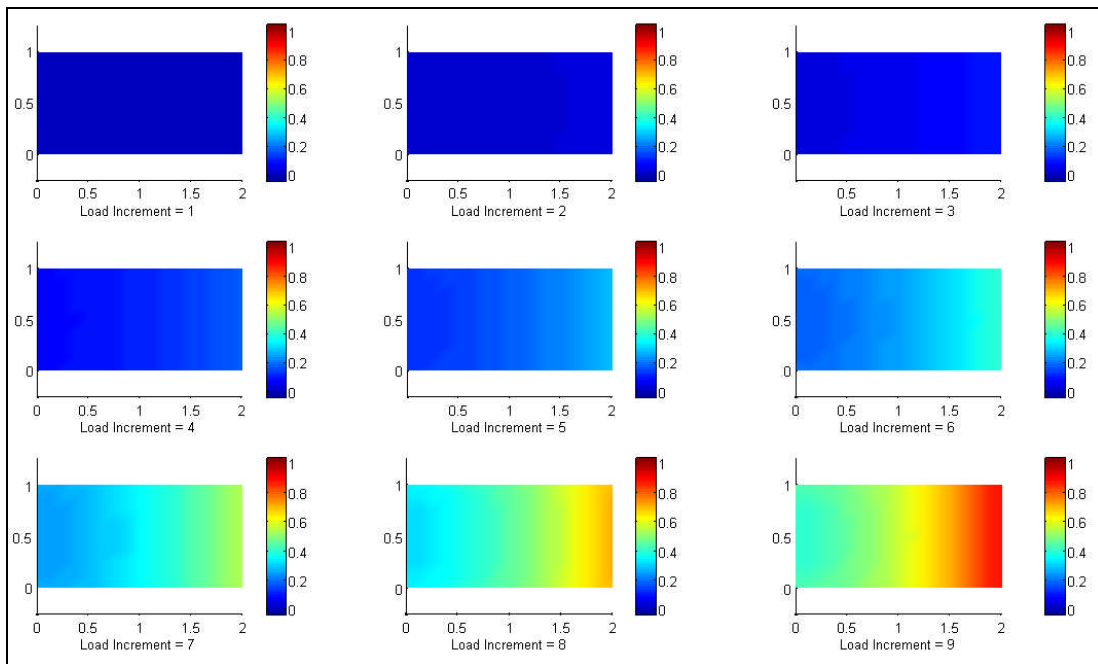
Figure 7-43: Progressive damage contour plot of the second ply for the tension case

Figure 7-44 shows the progressive damage plot for the 2nd ply (i.e. 0° ply) of a FGC plate case with P=1 and V$_1$=0.5 for the 6th to 9th load increment. This figure also shows the progressive damage plot of the Average and Smooth Mindlin programs for the FGC plate under tension. The results were in good agreement with each other. The damage plot is the plot of the failure index at all nodes on the y=0.5 line of the FGC plate. It can be seen from the damage plot that failure index increases as the nodal position, x increases. This indicates that the weaker region is the region around the x=2 edge.
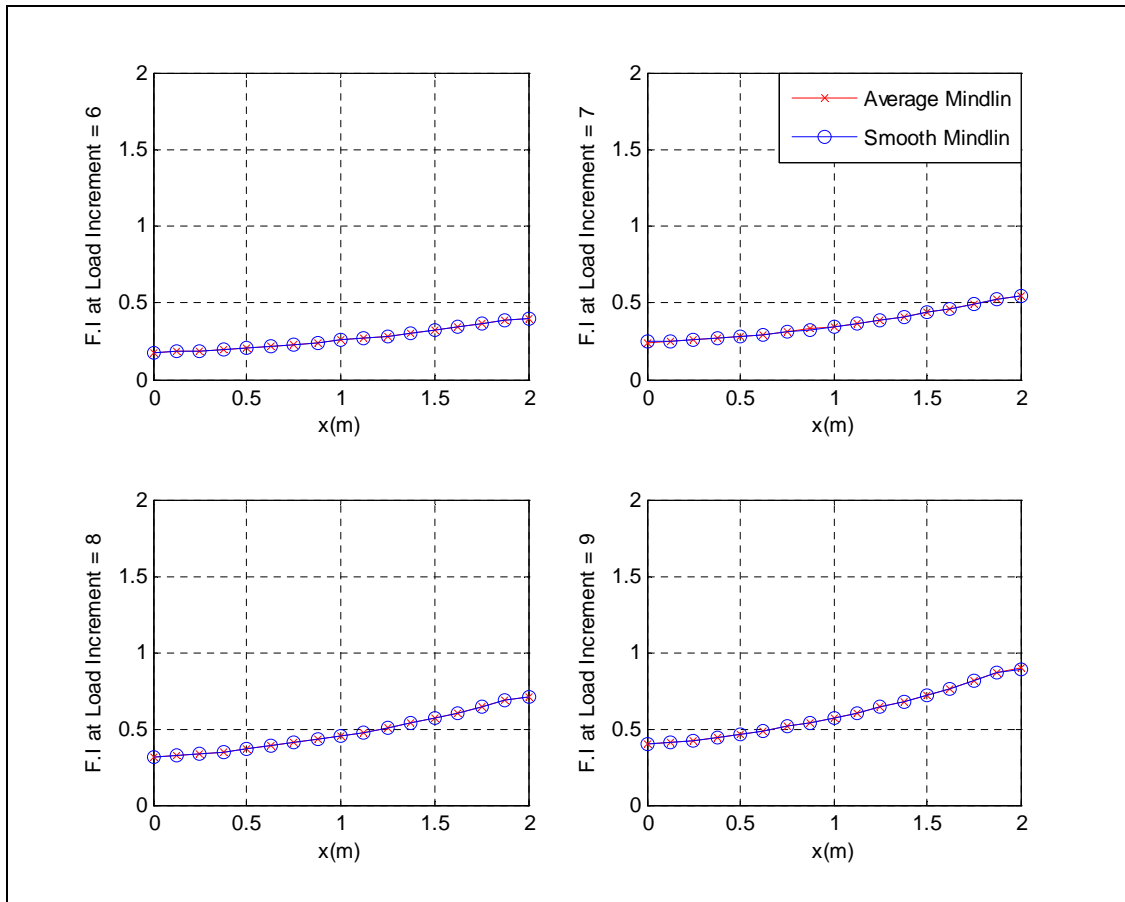
Figure 7-44: Progressive damage plot of the second ply for the tension case

7.3.2 FGC plate under in-plane bending

Example 7.3.2: A rectangular FGC plate with a "$[[-45/0/45]_2]_s$" stacking sequence was subjected to an in-plane bending load of 1.6MN. The task is to validate the displacement, stress and the progressive damage result of the Mindlin and Reissner programs against the result of the Ordinary FE programs. The FE modelling procedure is presented for this example. The geometrical properties and micro-mechanical properties are as given in Example 7.3.1.

FE Modelling

The FGC plate has a mid-plane as shown in Figure 7-45. A mesh containing 128 4-noded Mindlin-type elements was employed for the Mindlin programs. A mesh containing 128 4-noded conforming elements was employed for the conforming Reissner program. A mesh containing 128 4-noded non-conforming elements was employed for the non-conforming Reissner program. An in-plane load of 1.6MN was applied as an equivalent nodal loads at the nodes on the x=2 edge with reduced load at the corner nodes. For example, in the 128 element case, the load was applied equally at nodes on the x=2 edge but with half of the loads at the corner nodes on the x=2 edge as shown in Figure 7-45. Hence the equivalent nodal loading for the 128 element case was 200kN at each nodes on the x=2 edge with 100kN at corner nodes on the x=2 edge. In order to model the finite strain, a tenth of the equivalent nodal loading was applied at every load increment.

The boundary condition shown in Table 7-26 was applied to the FE model.

Table 7-26: Boundary condition for the in-plane bending case

Nodes	Boundary condition
Nodes on the x=0 edge	$u = v = w = \theta_x = \theta_y = 0$ (i.e. all degrees of freedom are fixed at the x=0 edge)
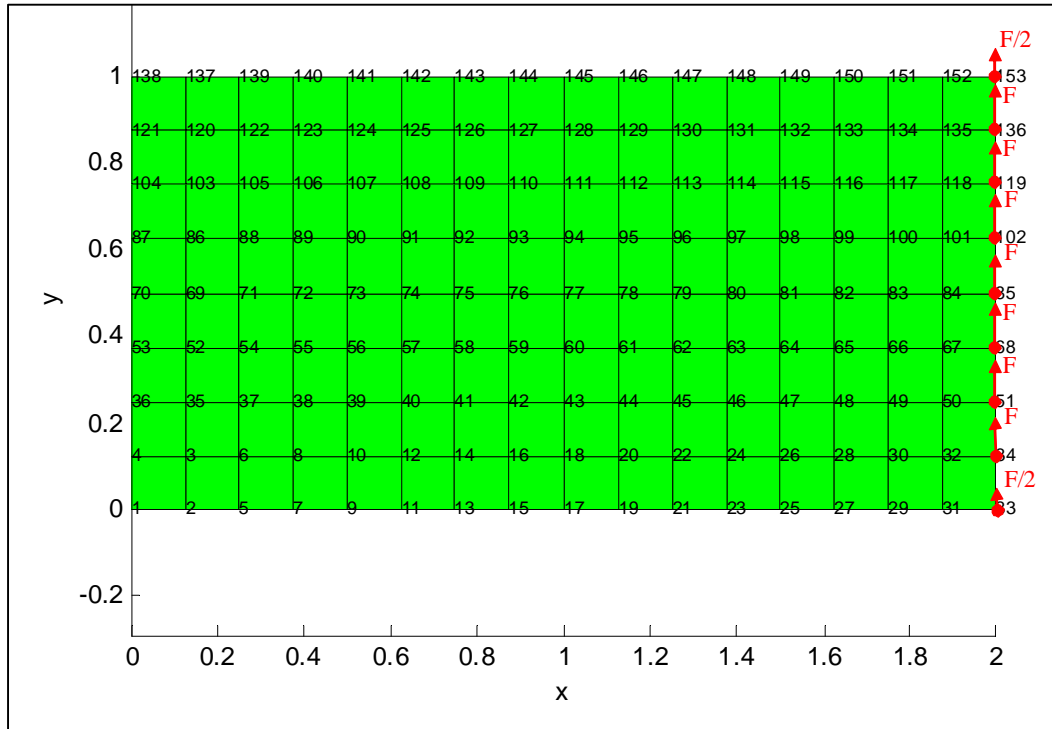
Figure 7-45: 4-noded element mesh for the in-plane bending case

In order to model the functional gradation of the FGC plate in the Ordinary FE programs, the fibre and matrix volume fractions were computed for each element at their midpoints by using the fibre distribution equations (i.e. Equation 3.34 and 3.38) developed in chapter 3. The macro-mechanical properties were then computed for each element by substituting the fibre and matrix volume fractions into the macro-mechanical equations developed in chapter 3. The computed macro-mechanical properties of each element of the FGC plate were then fed into the Ordinary FE programs.

Mindlin and Reissner program validation results

Figure 7-46 and 7-47 show the nodal displacement results along the y=0.5 line for a FGC plate case with P=1 and V_1=0.5 at the 9th load increment. The displacement results for the Mindlin and Reissner programs were in good agreement with the Ordinary FE program. It can be seen that the v-displacement curve has a zero slope at the x=0 edge which is due to the fact that the FGC plate is clamped at the x=0 edge. The slope of the v-displacement curve, δv/δx then gradually increases with increase in the nodal position, x; due to the coupled effect of the bending curvature and functional gradation properties.
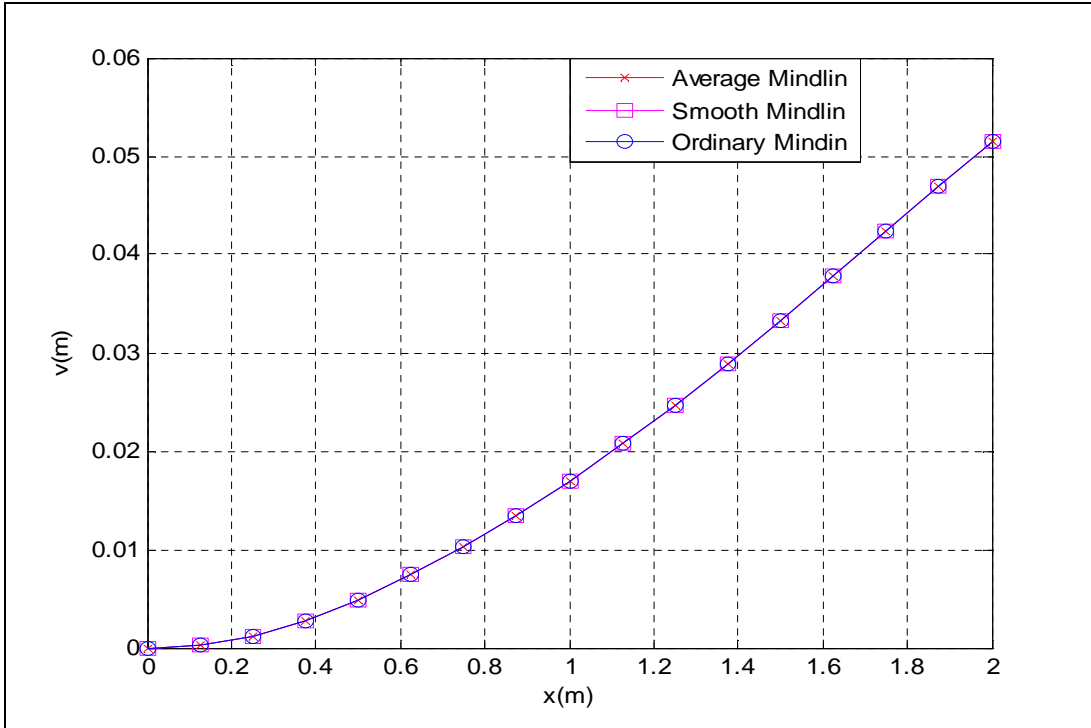
Figure 7-46: v-displacement validation against Ordinary Mindlin program for the in-plane bending case
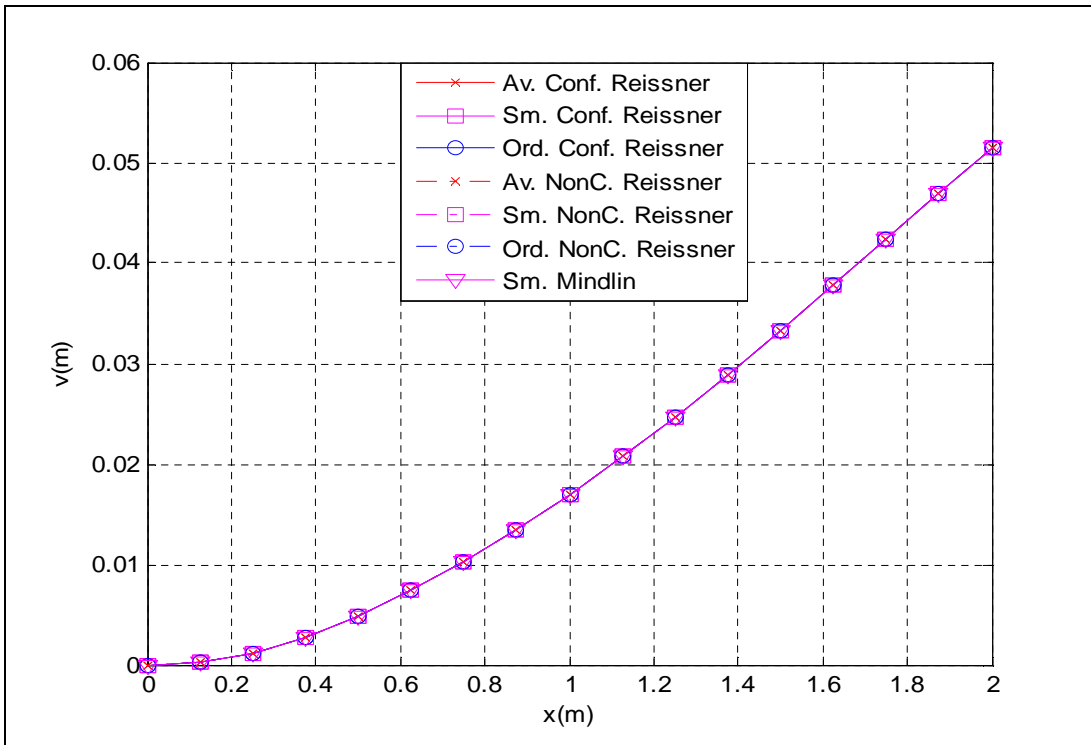
Figure 7-47: v-displacement validation against Ordinary Reissner program for the in-plane bending case

Figure 7-48 shows the through-thickness stress result in the fibre direction at node 1 (i.e. the (0, 0) coordinate) for a FGC plate case with P=1 and V_1=0.5 at the 9th load increment. The stress results of the Average and Smooth Mindlin programs were in good agreement with the result of the Ordinary Mindlin program. The in-plane bending load results in a tensile force on the y=0 edge and a compressive force on the y=1 edge. The tensile force on the y=0 edge results in the highest σ_{11} at node 1 on the 0° plies due to the alignment of the fibres with the tensile force. This effect results in the 0° plies carrying the highest share of the load. Also the combined effect of the tensile force on the y=0 edge and compressive force on the y=1 edge results in a high value of σ_{11} at node 1 on the 45° plies due to the fibre alignment of the plies.
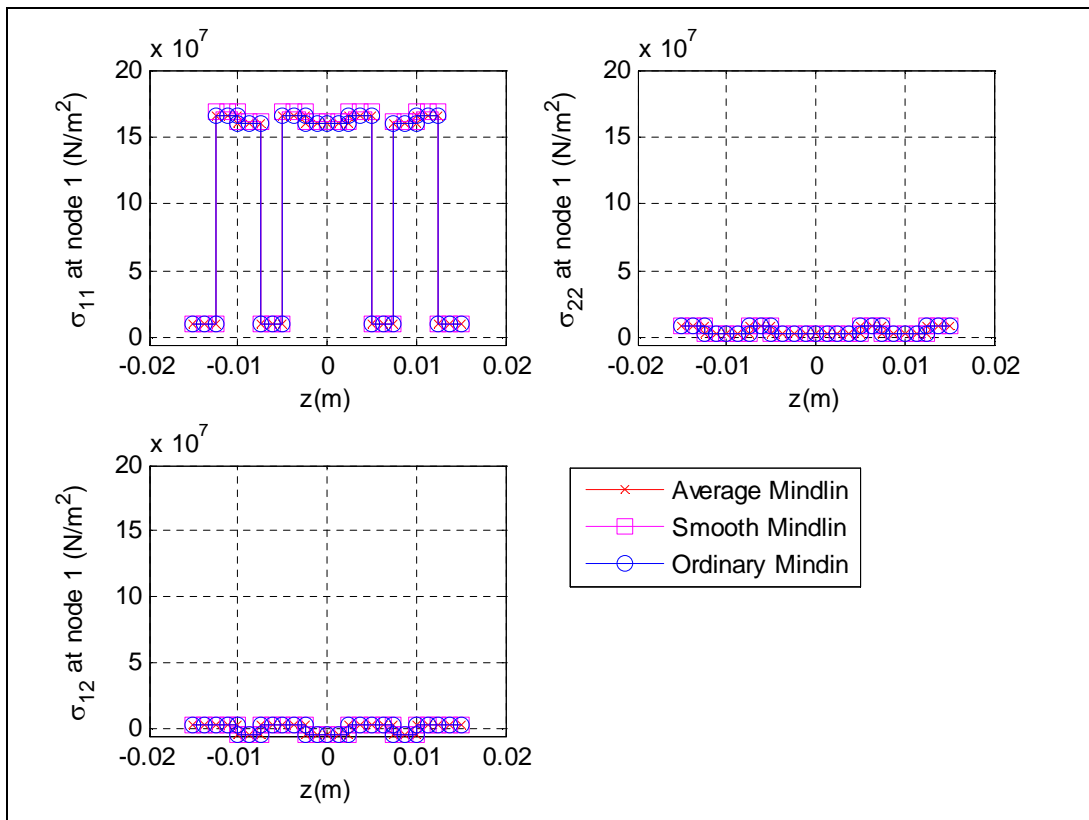
Figure 7-48: Stress validation against Ordinary Mindlin program for the in-plane bending case

The progressive damage modelling employed in this example is as described in Example 7.3.1. Figure 7-49 shows the damage contour plot for the first three layers of a FGC plate case with P=1 and V_1=0.5 at the 9th load increment. This figure also shows the typical damage contour plot of all the programs for the FGC plate under in-plane bending.

In order to understand the damage results in Figure 7-49, it must be noted that the damage are based on Tsai-Hill failure index which is a function of the micromechanical strength properties, fibre orientation of ply, functional gradation and stress transfer. It can be seen from the damage contour plots that most region around the y=0 and y=1 edges for most of the plies were damaged. But the y=1 edge of the 0° plies were less damaged in comparison to the other plies. This is expected because the fibre orientation of the 0° plies were aligned to the compressive force (due to in-plane bending load) on the y=1 edge. Hence the damage at the y=1 edge for the 0° plies were dependent on the strength of the fibre. Also the damage results include the effect of stress transfer. This effect is due to the undamaged regions being stiffer than the damaged regions and they carry a large portion of the extra loads that were meant for the damaged regions and therefore the undamaged regions are stressed more. Hence this results in stress transfer occurring both in the in-plane and out-of-plane directions.
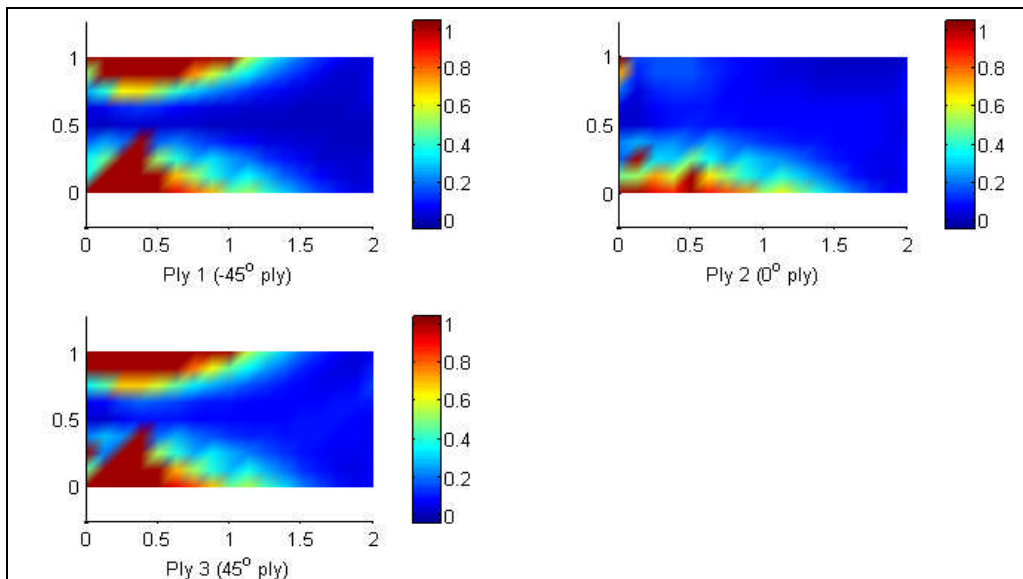

Figure 7-49: Damage contour plot of the first three plies for the in-plane bending case

Since failure was more pronounced in the 1st and 3rd ply, a closer study of the progressive damage of the 1st ply was undertaken. Figure 7-50 shows the progressive damage contour plot for the 1st ply (i.e. -45° ply) of a FGC plate case with P=1 and V$_1$=0.5 for nine load increments. This figure also shows the typical progressive damage contour plot of all the programs for the FGC plate under in-plane bending. The damage contour plot is the plot of the failure index at all nodes on the FGC plate. If failure index is greater than one, then the composite plate is damaged, else the composite plate is undamaged. It can be seen from the damage contour plot that damage was initiated during the 6th load increment at the corner nodes on the y=0 edge. The damage then spreads towards the y=0.5 line and towards the x=2 edge in subsequent load increments.
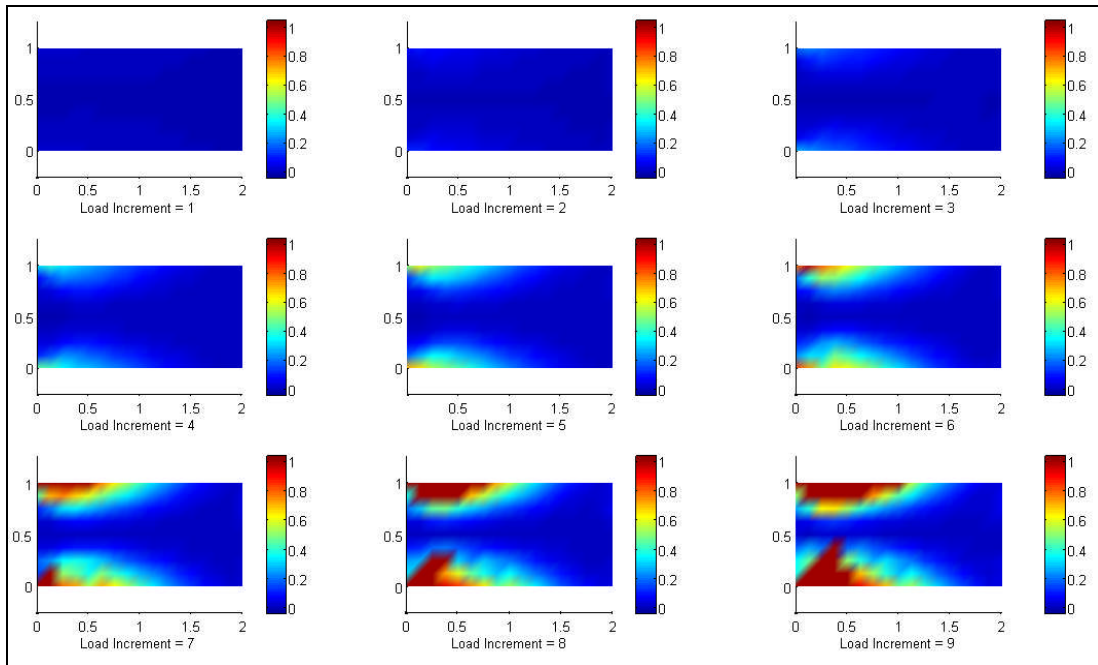
Figure 7-50: Progressive damage contour plot of the first ply for the in-plane bending case

Figure 7-51 shows the progressive damage plot for the 2nd ply (i.e. 0° ply) of a FGC plate case with P=1 and V$_1$=0.5 for the 5th to 8th load increment. This figure also shows the progressive damage plot of the Average and Smooth Mindlin programs for the FGC plate under in-plane bending. The results were in good agreement with each other. The damage plot is the plot of the failure index at all nodes on the y=0 edge of the FGC plate. It can be seen from the damage contour plot that failure index reduces as the nodal

position, x increases. This indicates that the maximum bending moment is experienced at the (0, 0) and (0, 1) coordinates, which results in maximum bending stress at this edge and hence maximum failure index.

The damage curves were smooth from the 1st load increment to the 5th load increment, which is the load increment before the onset of damage. After the damage at the 6th load increment, the curves is no longer smooth, this effect is due to stress transfer which occurs when undamaged region carry the extra load of the damaged region. Also the 7th and 8th load increments have some missing failure indices around the x=0 region. This effect is due to the fact that when an element has completely failed, the stiffness value at each node of the element is degraded to zero, hence nodal stress of the element is zero resulting in a nodal failure index value of zero. The nodal failure index values of zero are eliminated from the plot to best demonstrate the progressive damage, since damage occurs when failure index exceeds the value of one.
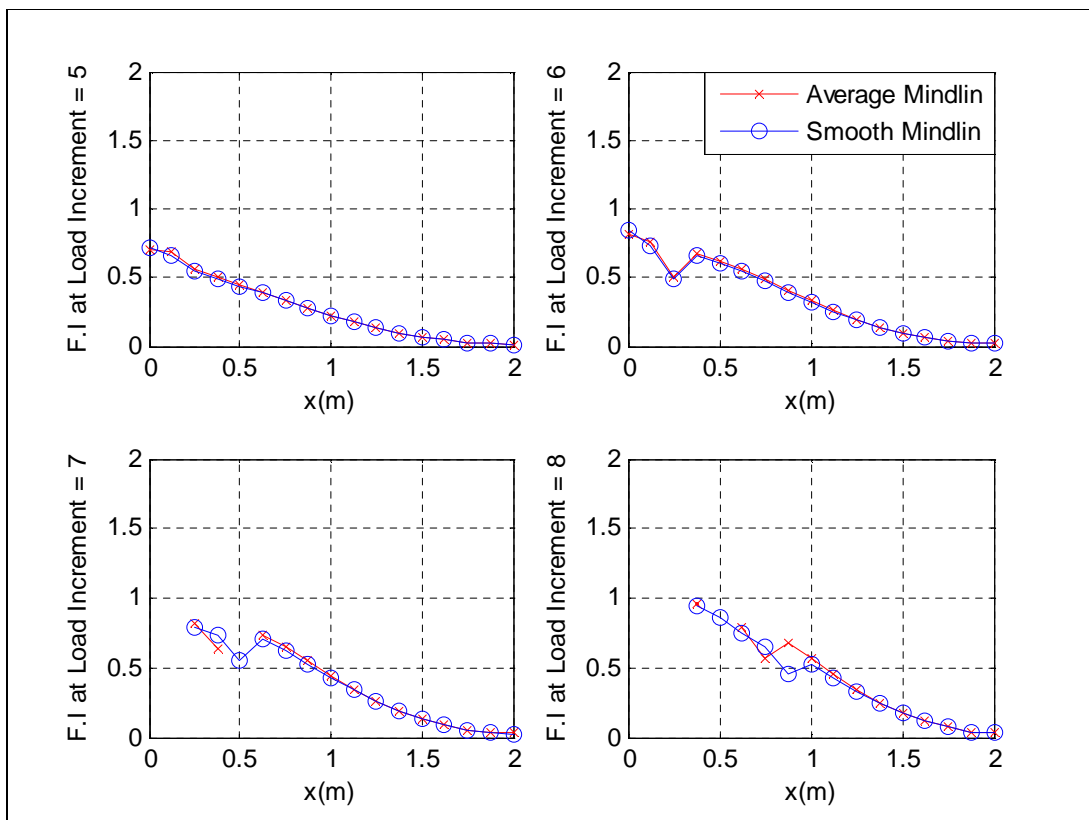
Figure 7-51: Progressive damage plot of the first ply for the in-plane bending case

7.3.3 FGC plate under out-of-plane bending

Example 7.3.3: A rectangular FGC plate with a "[[-45/0/45]$_2$]$_s$" stacking sequence was subjected to an out-of-plane bending load of 36kN. The task is to validate the displacement and stress result of the Mindlin and Reissner programs against the result of the Ordinary FE programs. The FE modelling procedure is presented for this example. The geometrical properties and micro-mechanical properties are the same as the one given in Example 7.3.1.

FE Modelling

A mesh containing 128 4-noded Mindlin-type elements was employed for the Mindlin programs. A mesh containing 128 4-noded conforming elements was employed for the conforming Reissner program. A mesh containing 128 4-noded non-conforming elements was employed for the non-conforming Reissner program. An out-of-plane bending load of 36kN was applied as an equivalent nodal loads at the nodes on the x=2 edge with reduced load at the corner nodes. For example, in the 128 element case, the load was applied equally at nodes on the x=2 edge but with half of the load at the corner nodes on the x=2 edge. Hence the equivalent nodal loading for the 128 element case was 4.5kN at each nodes on the x=2 edge with 2.25kN at corner nodes on the x=2 edge.

The boundary condition shown in Table 7-27 was applied to the FE models in this example.

Table 7-27: Boundary condition for the out-of-plane bending case

Nodes	Boundary condition
Nodes on the x=0 edge	$u = v = w = \theta_x = \theta_y = 0$ (i.e. all degrees of freedom are fixed at the x=0 edge)

In order to model the functional gradation of the FGC plate in the Ordinary FE programs, the fibre and matrix volume fractions were computed for each element at their midpoints by using the fibre distribution equations developed in chapter 3. The macro-mechanical properties were then computed for each element by substituting the fibre and matrix volume fractions into the macro-mechanical equations developed in chapter 3. The computed macro-mechanical properties of each element of the FGC plate were then fed into the Ordinary FE programs.

Mindlin and Reissner program validation results

Figures 7-52 and 7-53 show the nodal displacement results along the y=0.5 line for a FGC plate case with P=1 and V_1=0.5 at the 7th load increment. The displacement results for the Mindlin and Reissner programs were in good agreement with the Ordinary FE program. The displacement results of the Mindlin programs were not in good agreement with the Reissner programs. This discrepancy can be explained by the difference in transverse shear modelling employed in each program. Another reason for the discrepancy is that damage had occurred in the region of the x=0 edge at the 7th load increment for the Reissner programs but no damage had occurred in the FGC plate for the Mindlin programs. It can be seen that the w-displacement curve has a zero slope at the x=0 edge which is due to the fact that the FGC plate is clamped at the x=0 edge. The slope of the w-displacement curve, δw/δx then gradually increases with increase in the nodal position, x; due to the coupled effect of the bending curvature and functional gradation properties.
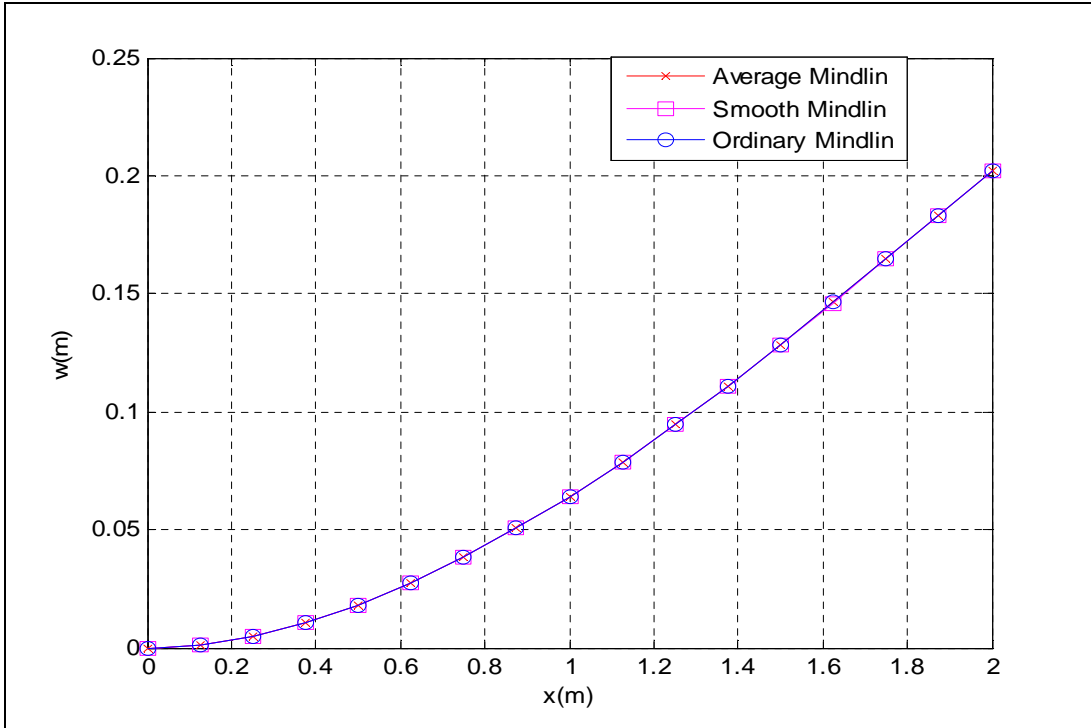
Figure 7-52: w-displacement validation against Ordinary Mindlin program for the out-of-plane bending case
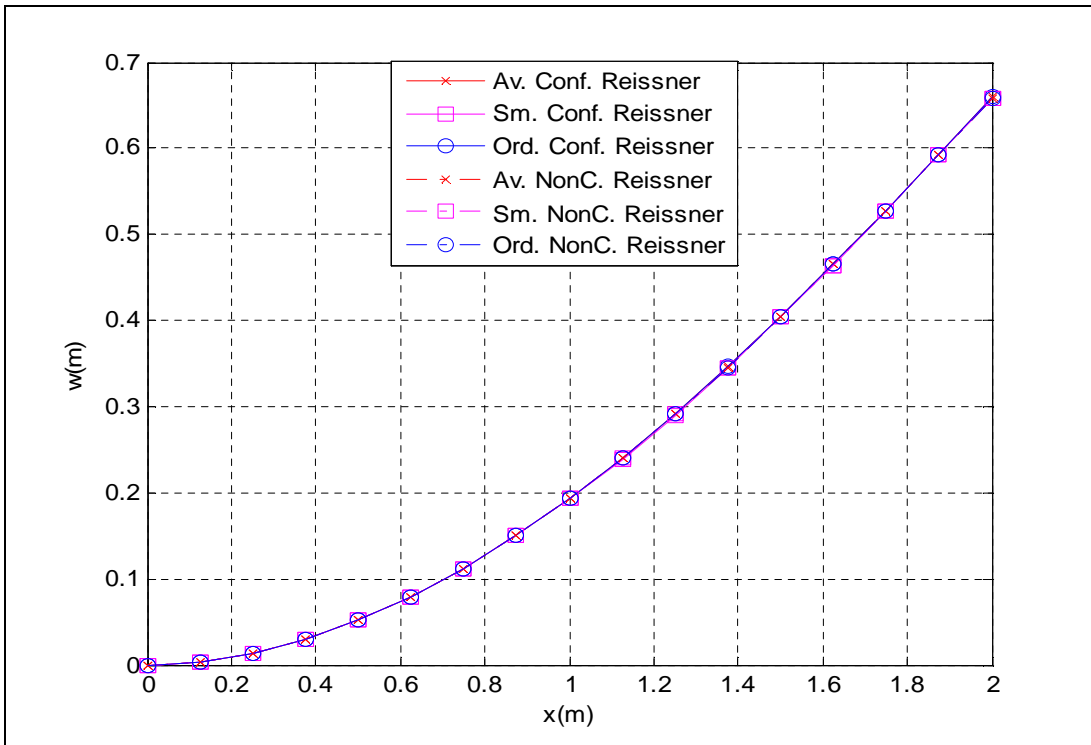

Figure 7-53: w-displacement validation against Ordinary Reissner program for the out-of-plane bending case

Figure 7-54 shows the through-thickness stress result in the fibre direction at node 1 (i.e. the (0, 0) coordinate) for a FGC plate case with P=1 and V_1=0.5 at the 7th load increment. The stress results of the Average and Smooth conforming Reissner programs were in good agreement with the result of the Ordinary conforming Reissner program. The out-of-plane bending load results in a tensile force on the top plies (i.e. plies at positive z positions) and compressive force on the bottom plies (i.e. plies at negative z positions). This effect results in a distribution of σ_{11} across the plies with the maximum tensile stress σ_{11} at the 1st ply (i.e. ply at z=0.015m) and maximum compressive stress σ_{11} at the 12th ply (i.e. ply at z=-0.015m).
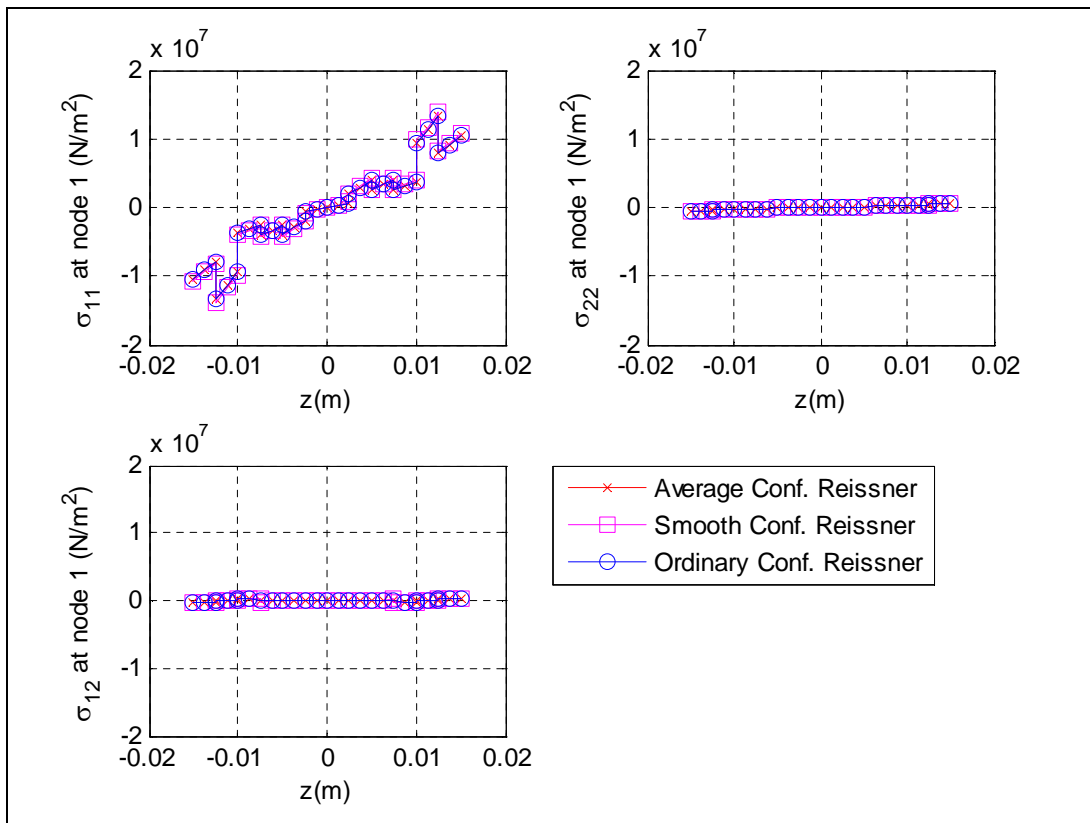
Figure 7-54: Stress validation against Ordinary Mindlin program for the out-of-plane bending case

The progressive damage modelling employed in this example is as described in Example 7.3.1. Figure 7-55 shows the damage contour plot for the first three layers of a FGC plate case with P=1 and V_1=0.5 at the 7th load increment. This figure also shows the typical damage contour plot of most programs for the FGC plate under out-of-plane bending.

In order to understand the damage results in Figure 7-55, it must be noted that the damage are based on Tsai-Hill failure index which is a function of the micromechanical strength properties, fibre orientation of ply, functional gradation and stress transfer. It can be seen from the damage contour plots that the region around the node at the (0, 1) coordinate of the 1st ply (i.e. ply at z=0.015m) experienced the worst damage. The 12th ply (i.e. ply at z=-0.015m) also experienced the same worst damage around the node at the (0, 1) coordinate. The damage reduces for each ply in the direction towards the midplane of the FGC plate. Also the damage results include the effect of stress transfer. This effect is due to the undamaged regions being stiffer than the damaged regions and they carry a large portion of the extra loads that were meant for the damaged regions and therefore the undamaged regions are stressed more. Hence this results in stress transfer occurring both in the in-plane and out-of-plane directions.
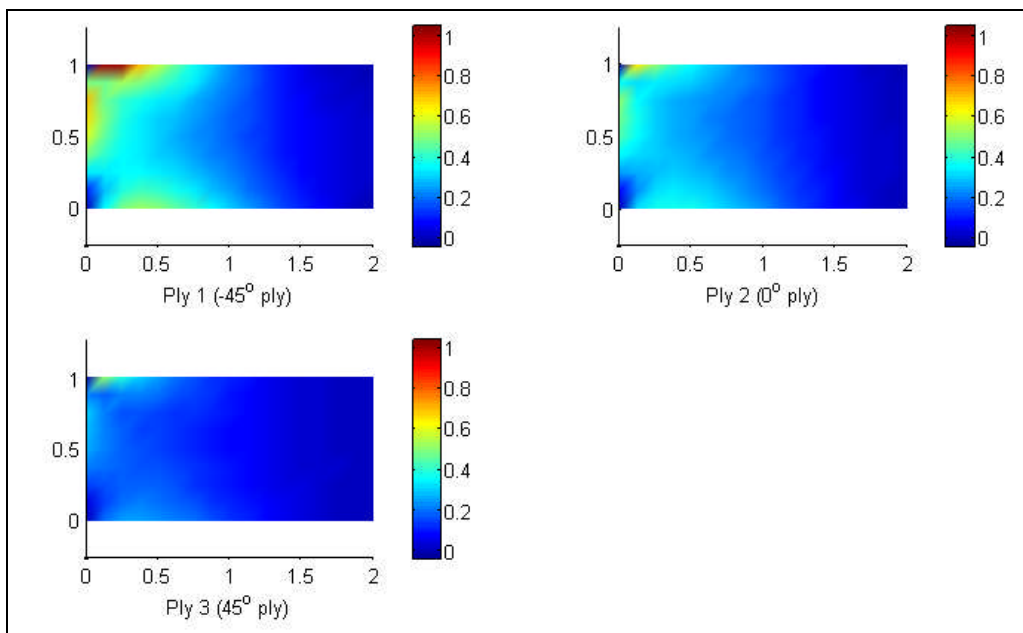

Figure 7-55: Damage contour plot of the first three plies for the out-of-plane bending case

Since failure was more pronounced in the 1st ply, a closer study of the progressive damage of the 1st ply was undertaken. Figure 7-56 shows the progressive damage contour plot for the 1st ply (i.e. -45° ply) of a FGC plate case with P=1 and V_1=0.5 for seven load increments. This figure also shows the typical progressive damage contour plot of most programs for the FGC plate under out-of-plane bending. The damage contour plot is the plot of the failure index at all nodes on the FGC plate. If failure index is greater than one, then the composite plate is damaged, else the composite plate is undamaged. It can be seen from the damage contour plot that damage was initiated during the 6th load increment at the corner nodes on the (0, 1) coordinate. The damage then spreads towards the x=2 edge in subsequent load increments.
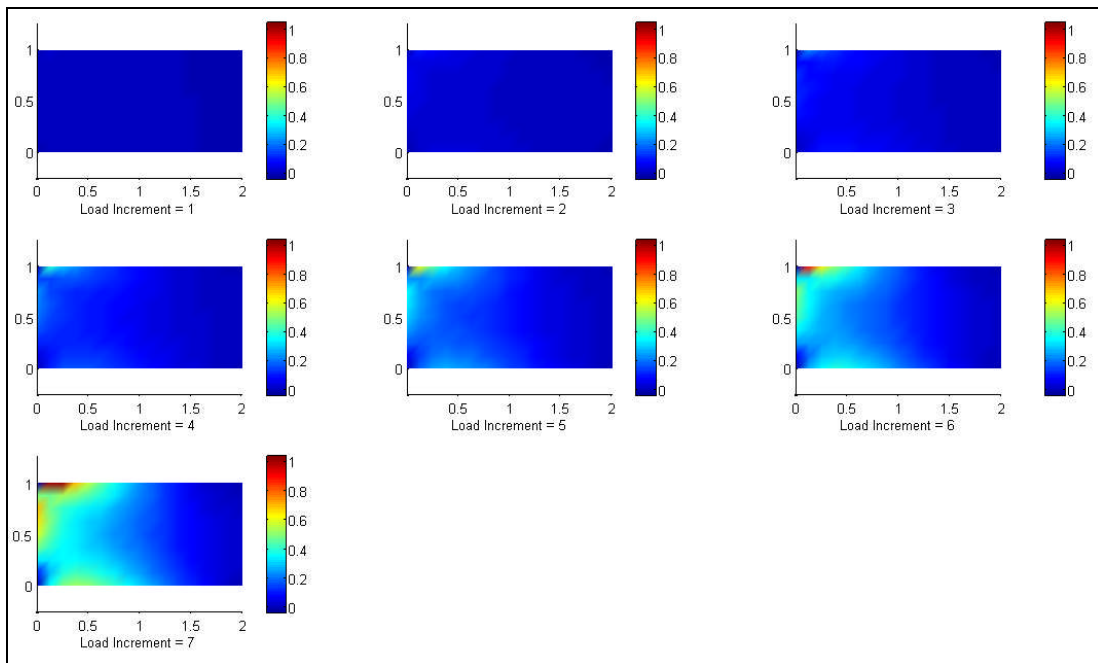

Figure 7-56: Progressive damage contour plot of the first ply for the out-of-plane bending case

Figure 7-57 shows the progressive damage plot for the 1st ply (i.e. -45° ply) of a FGC plate case with P=1 and V_1=0.5 for the 4th to 7th load increment. This figure also shows the progressive damage plot of the Average and Smooth conforming Reissner programs for the FGC plate under out-of-plane bending. The results were in good agreement with each other. The damage plot is the plot of the failure index at all nodes on the y=0.5 line of the FGC plate. It can be seen from the damage contour plot that the failure index decreases as the nodal position, x increases. This indicates that the maximum bending moment is experienced at the x=0 edge which results in maximum bending stress at this edge and hence maximum failure index. No damage was encountered on the nodes on the y=0.5 line of the FGC plate.
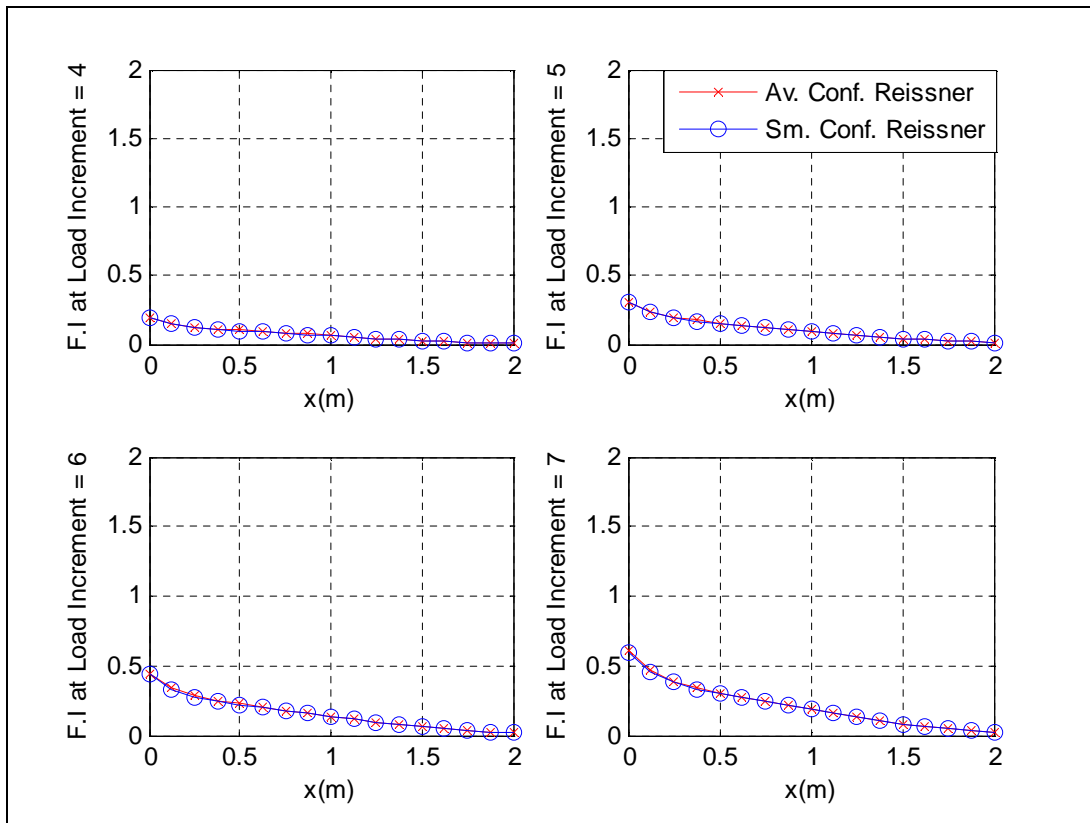

Figure 7-57: Progressive damage plot of the first ply for the out-of-plane bending case

7.3.4 FGC plate under compressive loading

<u>Example 7.3.4</u>: A rectangular FGC plate with a "$[[-45/0/45]_2]_s$" stacking sequence subjected to a compressive load of 24kN. The values of the functional gradation properties include gradation exponent, $P=1$ and gradation offset, $V_1=0.5$. The task is to validate the buckling eigenvalue results of the Reissner programs against the results of the Mindlin programs. The FE modelling procedure is presented for this example. The geometrical properties and micro-mechanical properties are the same as the one given in Example 7.1.1.

<u>FE Modelling</u>

A mesh containing 128 4-noded Mindlin-type elements was employed for the Mindlin programs. A mesh containing 128 4-noded conforming elements was employed for the conforming Reissner program. A mesh containing 128 4-noded non-conforming elements was employed for the non-conforming Reissner program. A buckling load of 24kN was applied as an equivalent nodal loads at the nodes on the x=2 edge with reduced load at the corner nodes. For example, in the 128 element case, the load was applied equally at nodes on the x=2 edge but with half of the load at the corner nodes on the x=2 edge. Hence the equivalent nodal loading for the 128 element case was 3.0kN at each nodes on the x=2 edge with 1.5kN at corner nodes on the x=2 edge.

The boundary condition shown in Table 7-28 was applied to the FE models in this example.

Table 7-28: Boundary condition for the buckling case

Nodes	Boundary condition
Nodes on the x=0 edge	$u = v = w = \theta_x = \theta_y = 0$ (i.e. all degrees of freedom are fixed at the x=0 edge)
Nodes on the x=2 edge	$w = 0$

Mindlin and Reissner program validation results

In this example, the first three buckling modes were analysed. The buckling eigenvalue is the ratio of critical buckling load to the applied load. The buckling eigenvalue results of the Mindlin programs, Reissner programs and the Abaqus package were analysed for the 128 element mesh case. Table 7-29 shows that the buckling eigenvalue results of the Mindlin and Reissner programs were in good agreement with the results of the Abaqus package.

Table 7-29: Validation for the buckling case using Abaqus program

FE Models	Buckling Eigenvalues		
	1st Mode	2nd Mode	3rd Mode
Abaqus S4-elements	20.26	61.81	87.54
Average Mindlin elements	19.77	59.68	82.08
Smooth Mindlin elements	19.77	59.68	82.05
Smooth non-conforming Reissner elements	19.62	57.73	82.94
Average non-conforming Reissner elements	19.60	57.70	82.92
Smooth conforming Reissner elements	19.52	57.31	82.61
Average conforming Reissner elements	19.50	57.28	82.59

7.3.5   FGC plate under free vibration

Example 7.3.5: Consider a rectangular FGC plate with a "[[-45/0/45]$_2$]$_s$" stacking sequence under free vibration. The values of the functional gradation properties include gradation exponent, P=1 and gradation offset, V_1=0.5. The task is to validate the natural frequency results of the Reissner programs against the result of the Mindlin programs. The FE modelling procedure is presented for this example. The geometrical properties and micro-mechanical properties are the same as the one given in Example 7.1.1.

FE Modelling

A mesh containing 128 4-noded Mindlin-type elements was employed for the Mindlin programs. A mesh containing 128 4-noded conforming elements was employed for the conforming Reissner program. A mesh containing 128 4-noded non-conforming elements was employed for the non-conforming Reissner program.

The boundary condition shown in Table 7-30 was applied to the FE model.

Table 7-30: Boundary condition for the free vibration case

Nodes	Boundary condition
Nodes on the x=0 edge	$u = v = w = \theta_x = \theta_y = 0$ (i.e. all degrees of freedom are fixed at the x=0 edge)

Mindlin and Reissner program validation results

In this example, the first three free vibration modes were analysed. The first three fundamental frequency results of the Mindlin programs, Reissner programs and the Abaqus package were analysed for 128 element mesh case. Table 7-31 shows that the first three fundamental frequency results of the Mindlin and Reissner programs were in good agreement with the results of the Abaqus package.

Table 7-31: Validation for the free vibration case using Abaqus program

FE Models	Natural Frequencies (Hz)		
	1st Mode	2nd Mode	3rd Mode
Abaqus S4-elements	7.04	28.29	41.44
Average Mindlin elements	7.10	28.38	41.50
Smooth Mindlin elements	7.10	28.38	41.50
Smooth non-conforming Reissner elements	7.10	28.50	41.21
Average non-conforming Reissner elements	7.10	28.50	41.20
Smooth conforming Reissner elements	7.11	28.50	41.12
Average conforming Reissner elements	7.11	28.50	41.11

7.3.6 FGC plate with a central hole under tensile loading

<u>Example 7.3.6</u>: A rectangular FGC plate with a central hole and a "[[-45/0/45]$_2$]$_s$" stacking sequence was subjected to a tensile loading of 7.5MN. The values of the functional gradation properties include gradation exponent, P=1 and gradation offset, V_1=0.5. The task is to validate the displacement results of Mindlin and Reissner programs against the result of the Ordinary FE programs. The FE modelling procedure is presented for this example.

The geometrical properties and micro-mechanical properties are as given below. The micromechanical data were obtained from a textbook by Kaw (1997).

Table 7-32: Data for the FGC plate with a central hole

Geometry					
L (m)	2.000	w (m)	1.000	R (m)	0.1
t (m)	0.0300	No. of ply	12		
Fibre and matrix properties					
E_f (Pa)	2.300E+11	ν_f	3.500E-01	μ_f (Pa)	8.519E+10
E_m (Pa)	3.400E+09	ν_m	3.000E-01	μ_m (Pa)	1.308E+09
Strength properties					
X_{mt} (Pa)	7.200E7	X_{mc} (Pa)	1.020E8	X_{ms} (Pa)	3.400E7
X_{ft} (Pa)	2.067E9	X_{fc} (Pa)	1.999E9	σ_{rm} (Pa)	0.0
k_σ	1	k_τ	1		

The notations used in Table 7-32 are as described below.

L, w, and t, represent the length, width, thickness of ply respectively.

R represents the radius of the hole.

E_f and E_m represent the Young's modulus of the fibre and matrix respectively.

ν_f and ν_m represent the Poisson's ratio of the fibre and matrix respectively.

μ_f and μ_m represent the shear modulus of the fibre and matrix respectively.

X_{mt}, X_{mc} and X_{ms} represent the tensile, compressive and the shear strength of the matrix respectively.

X_{ft} and X_{fc} represent the tensile and compressive strength of the matrix respectively.

σ_{rm} represent the maximum residual radial stress at the interface.

k_σ and k_τ represent the stress concentration factor and the shear stress concentration factor respectively.

<u>FE Modelling</u>

In order to model the FGC plate with a central hole under uniaxial tensile loading, the model was divided into four equal quarters. One of the quarter models was then used in the FE modelling by applying boundary conditions which takes advantage of symmetrical nature of the full model. A mesh containing 125 4-noded Mindlin-type elements was employed for the Mindlin programs. A mesh containing 125 4-noded non-conforming elements was employed for the non-conforming Reissner program. A tensile load of 7.5MN was applied as an equivalent nodal loads at the nodes on the x=2 edge with reduced load at the corner nodes. For example, in the 125 element case, the load was applied equally at nodes on the x=2 edge but with half the loads at the corner nodes on the x=2 edge. Hence the equivalent nodal loading for the 125 element case was 1.5MN at each nodes on the x=2 edge with 750kN at the corner nodes on the x=2 edge. The boundary condition shown in Table 7-33 was applied to the FE model.

Table 7-33: Boundary condition for the FGC plate with a central hole

Nodes	Boundary condition
Nodes on the x=0 edge	u = 0
Nodes on the y=0 edge	v = 0

<u>Mindlin and Reissner program validation results</u>

Figures 7-58 and 7-59 show the nodal displacement results along the y=0 edge for a FGC plate case with P=1 and V_1=0.5 at the 9th load increment. The displacement results for the Mindlin and Reissner programs were in good agreement with the Ordinary FE program. The slope of the u-displacement curve, $\delta u/\delta x$ gradually increases with increase in the nodal position, x; due to the coupled effect of the central hole and functional gradation properties. The v-displacement results along the y=0 edge are zeroes as expected because a symmetry boundary condition was applied at the edge.
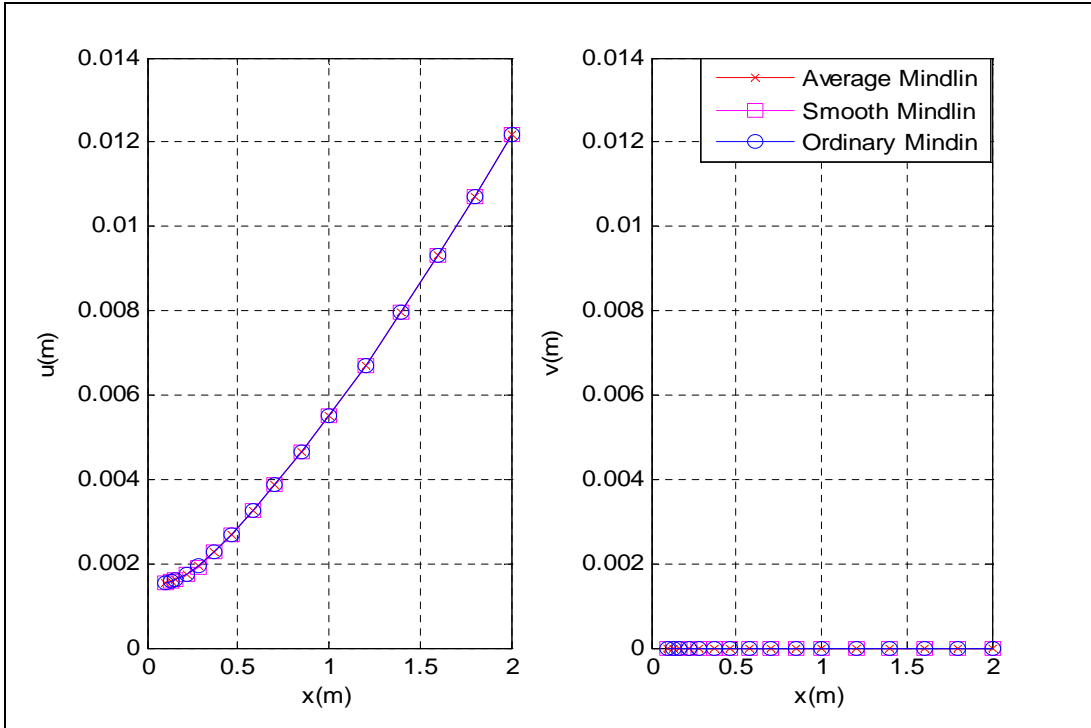
Figure 7-58: Displacement validation against Ordinary Mindlin program for the FGC plate with a hole
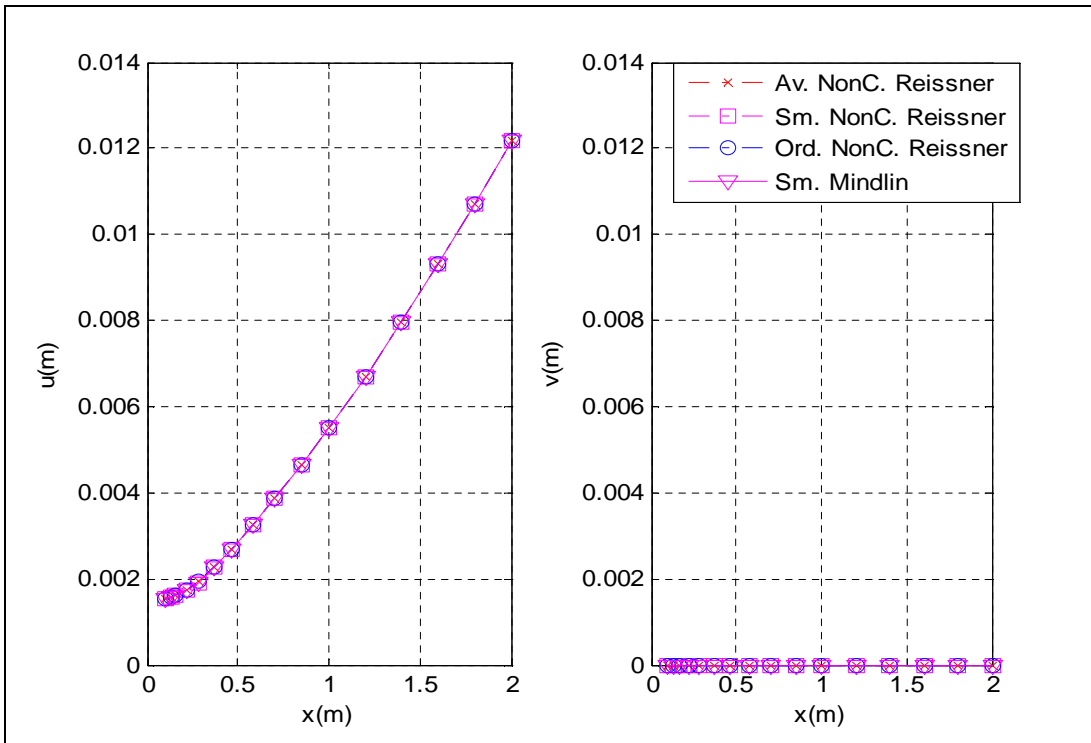

Figure 7-59: Displacement validation against Ordinary Mindlin program for the FGC plate with a hole

Figure 7-60 shows the through-thickness stress result in the fibre direction at node 1 (i.e. the (0, 0) coordinate) for a FGC plate case with P=1 and V_1=0.5 at the 9th load increment. The stress results of the Average and Smooth Mindlin programs were in good agreement with the result of the Ordinary Mindlin program. It can be seen from Figure 7-60 that the 0° plies have the highest σ_{11} relative to the 45° plies and -45° plies. This is due to the fact that the fibres in the 0° plies are aligned in the tensile force direction. Hence they carry a higher share of the load relative to the share of load of fibres in the 45° plies and -45° plies.
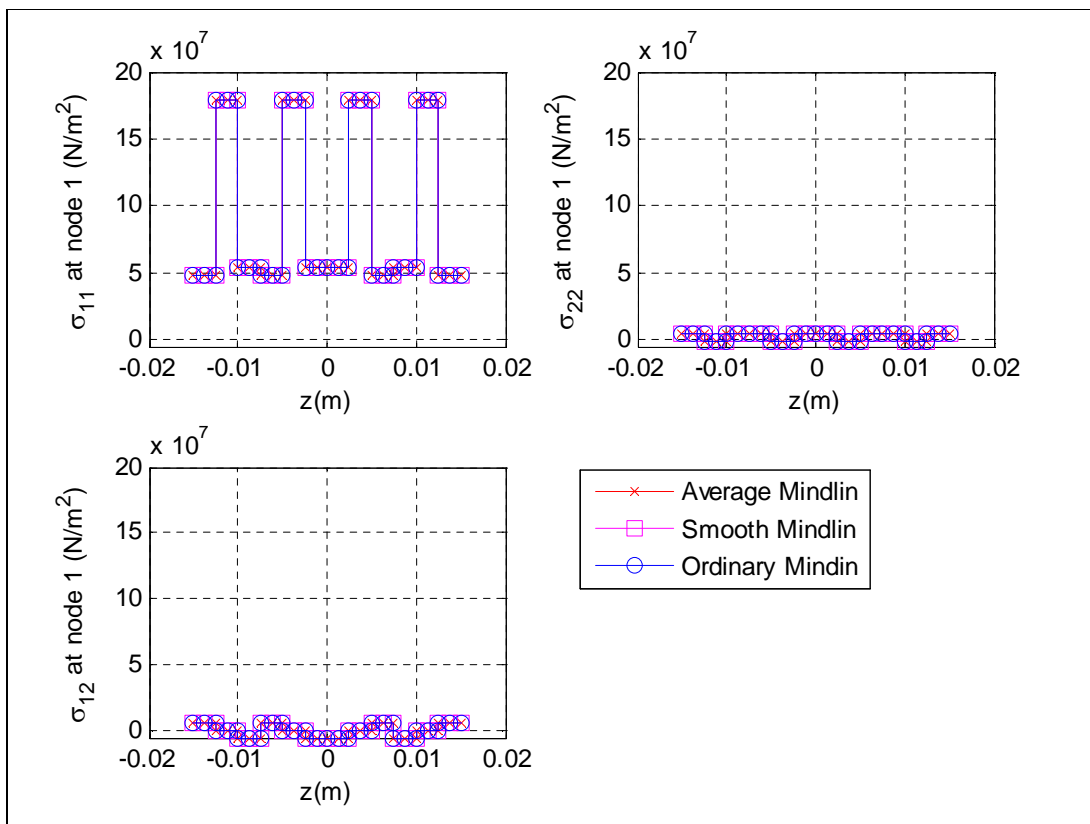
Figure 7-60: Stress validation against Ordinary Mindlin program for the FGC plate with a hole

The progressive damage modelling employed in this example is as described in Example 7.3.1. Figure 7-61 shows the damage contour plot for the first three layers of a FGC plate case with P=1 and V_1=0.5 at the 9th load increment. This figure also shows the typical damage contour plot of most programs for the FGC plate with central hole under tensile loading.

In order to understand the damage results in Figure 7-61, it must be noted that the damage are based on Tsai-Hill failure index which is a function of the micromechanical strength properties, fibre orientation of ply, functional gradation and stress transfer. It can be seen from the damage contour plot that the region around the edge of the central hole has high failure index due to high stress concentration because the central hole act as a stress raiser in the FGC plate. The effect of functional gradation can be seen in all the three plies but it is more pronounced in the 0° plies as shown for the 2nd ply in Figure 7-61. The figure shows that the ply is stronger around the x=0 edge than it is around the x=2 edge hence the undamaged regions are regions close the x=0 edge as shown in Figure 7-61. Also the results include the effect of stress transfer. This effect is due to the undamaged regions being stiffer than the damaged regions and they carry a large portion of the extra loads that were meant for the damaged regions and therefore the undamaged regions are stressed more. Hence this results in stress transfer occurring both in the in-plane and out-of-plane directions.
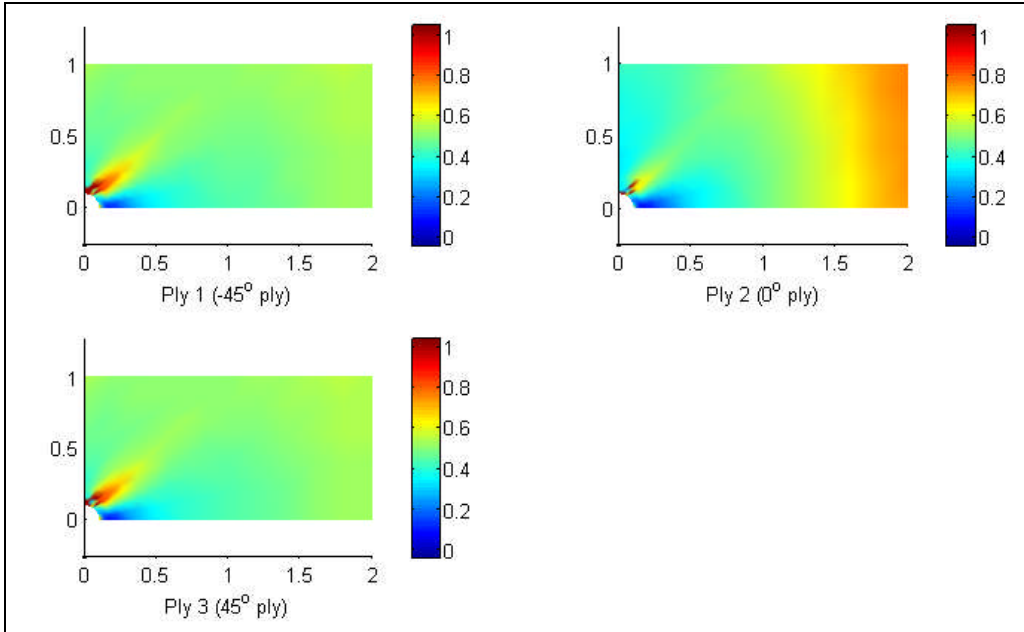
Figure 7-61: Damage contour plot of the first three plies for the FGC plate with a hole

The 1st ply has been selected for a closer study of its progressive damage. Figure 7-62 shows the progressive damage contour plot for the 1st ply (i.e. -45° ply) of a FGC plate case with P=1 and V$_1$=0.5 for nine load increments. This figure also shows the typical progressive damage contour plot of all the programs for the FGC plate with central hole under tension. The damage contour plot is the plot of the failure index at all nodes on the FGC plate. If failure index is greater than one, then the composite plate is damaged, else the composite plate is undamaged. It can be seen from the damage contour plot that damage was initiated during the 6th load increment at the region around the edge of the central hole. The damage then gradually spreads in the FGC plate in subsequent load increments.
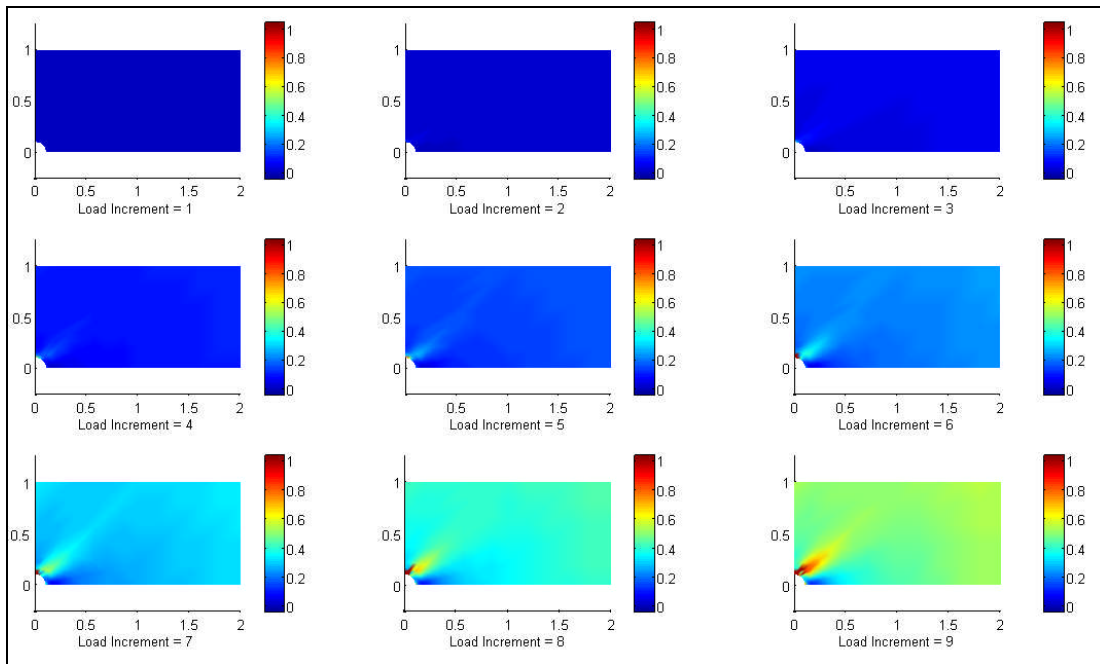
Figure 7-62: Progressive damage contour plot of the first ply for the FGC plate with a hole

Figure 7-63 shows the progressive damage plot for the 1st ply (i.e. -45° ply) of a FGC plate case with P=1 and V$_1$=0.5 for the 6th to 9th load increment. This figure also shows the progressive damage plot of the Average and Smooth Mindlin programs for the FGC plate under tension. The results were in good agreement with each other. The damage plot is the plot of the failure index at all nodes on the y=0 edge of the FGC plate. The failure index curve is dependent on the effect of the central hole and functional gradation properties.
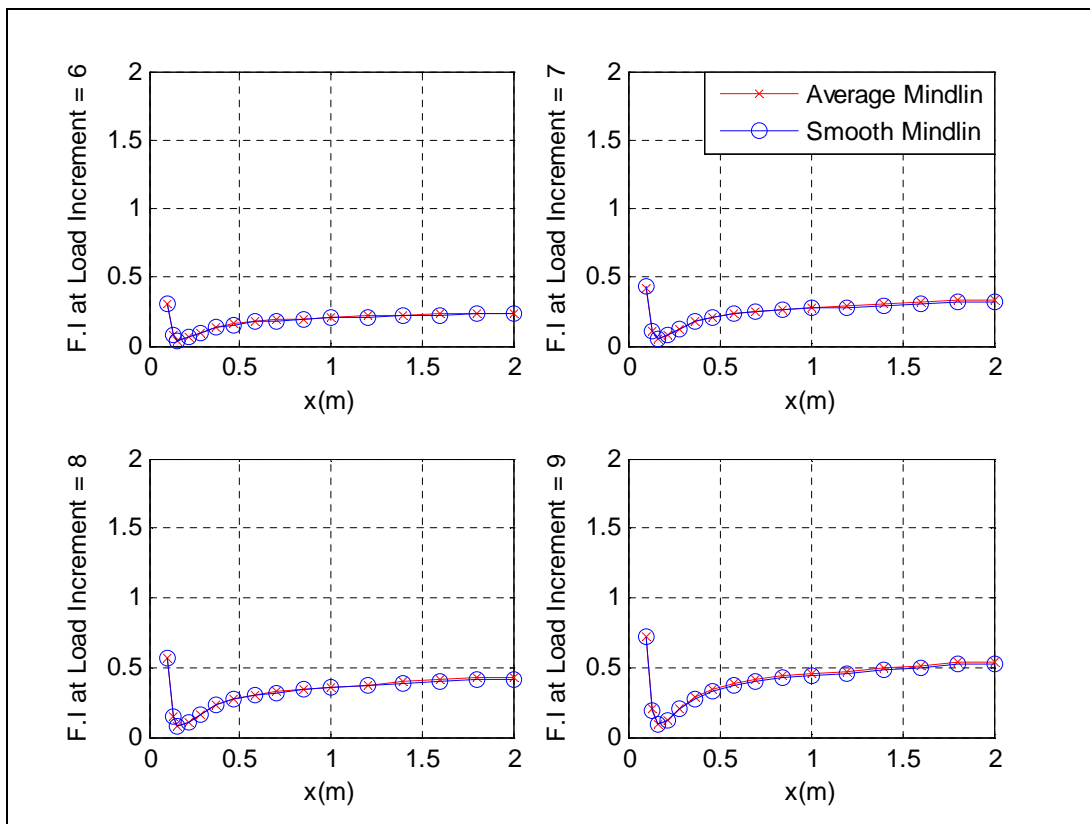
Figure 7-63: Progressive damage plot of the first ply for the FGC plate with a hole

7.3.7 Simply supported FGC ring case

Example 7.3.7: A FGC ring with a "[[-45/0/45]$_2$]$_s$" stacking sequence was subjected to a pressure loading of 2MPa. The values of the functional gradation properties include gradation exponent, P=1 and gradation offset, V$_1$=0.5. The task is to validate the displacement results of Mindlin and Reissner programs against the result of the Ordinary FE programs. The FE modelling procedure is presented for this example.

The geometrical properties and micro-mechanical properties are as given below. The micromechanical data was obtained from a textbook by Kaw (1997).

Table 7-34: Data for the simply supported ring case

Geometry					
R_i (m)	0.500	R_o (m)	1.000		
t (m)	0.030	No. of ply	12		
Fibre and matrix properties					
E_f (Pa)	2.300E+11	ν_f	3.500E-01	μ_f (Pa)	8.519E+10
E_m (Pa)	3.400E+09	ν_m	3.000E-01	μ_m (Pa)	1.308E+09
Strength properties					
X_{mt} (Pa)	2.067E9	X_{mc} (Pa)	1.999E9	X_{ms} (Pa)	3.600E7
X_{ft} (Pa)	7.200E7	X_{fc} (Pa)	1.020E8	σ_{rm} (Pa)	3.400E7
k_σ	1	k_τ	1		

The notations used in Table 7-34 are as described below.

R_i, R_o, and t, represent the inner radius, outer radius and thickness of ply respectively.

E_f and E_m represent the Young's modulus of the fibre and matrix respectively.

ν_f and ν_m represent the Poisson's ratio of the fibre and matrix respectively.

μ_f and μ_m represent the shear modulus of the fibre and matrix respectively.

X_{mt}, X_{mc} and X_{ms} represent the tensile, compressive and the shear strength of the matrix respectively.

X_{ft} and X_{fc} represent the tensile and compressive strength of the matrix respectively.

σ_{rm} represent the maximum residual radial stress at the interface.

k_σ and k_τ represent the stress concentration factor and the shear stress concentration factor respectively.

FE Modelling

A quarter of the model has been modelled instead of the full ring model by taking advantage of the axisymmetry nature of the FE problem. A triangular element has been employed in order to demonstrate and validate the capability of the FE programs in modelling with triangular elements. A mesh containing 200 3-noded triangular Mindlin-type elements was employed for the Mindlin programs. A mesh containing 200 3-noded triangular non-conforming elements was employed for the non-conforming Reissner program. The boundary condition shown in Table 7-35 was applied to the FE model.

Table 7-35: Boundary condition for the simply supported ring case

Nodes	Boundary condition
Nodes on the x=0 edge	$u = \theta_y = 0$ (i.e. symmetry boundary condition was applied to the x=0 edge)
Nodes on the y=0 edge	$v = \theta_x = 0$ (i.e. symmetry boundary condition was applied to the y=0 edge)
Nodes on the r=0.5 edge and the r=1 edge	w=0 (i.e. the r=0.5 edge and the r=1 edge are simply supported)

In order to model the functional gradation of the FGC ring in the Ordinary FE programs, the fibre and matrix volume fractions were computed for each element at their midpoints by using the fibre distribution equations developed in chapter 3. The macro-mechanical properties were then computed for each element by substituting the fibre and matrix volume fractions into the macro-mechanical equations developed in chapter 3. The computed macro-mechanical properties of each element of the FGC ring were then fed into the Ordinary FE programs.

<u>Mindlin and Reissner program validation results</u>

Figures 7-64 and 7-65 show the nodal displacement results along the y=0 edge for a FGC ring case with P=1 and V_1=0.5 at the 8th load increment. This FGC ring is graded in the radial direction. The displacement results for the Mindlin and Reissner programs were in good agreement with the Ordinary FE program. The displacement results of the Mindlin programs had small discrepancy in comparison to the displacement results of the Reissner programs. This discrepancy can be explained by the difference in transverse shear modelling employed in each program. The w-displacement value at r=0.5 and r=1 is zero as expected because the ring is simply supported at the r=0.5 and r=1 edges.
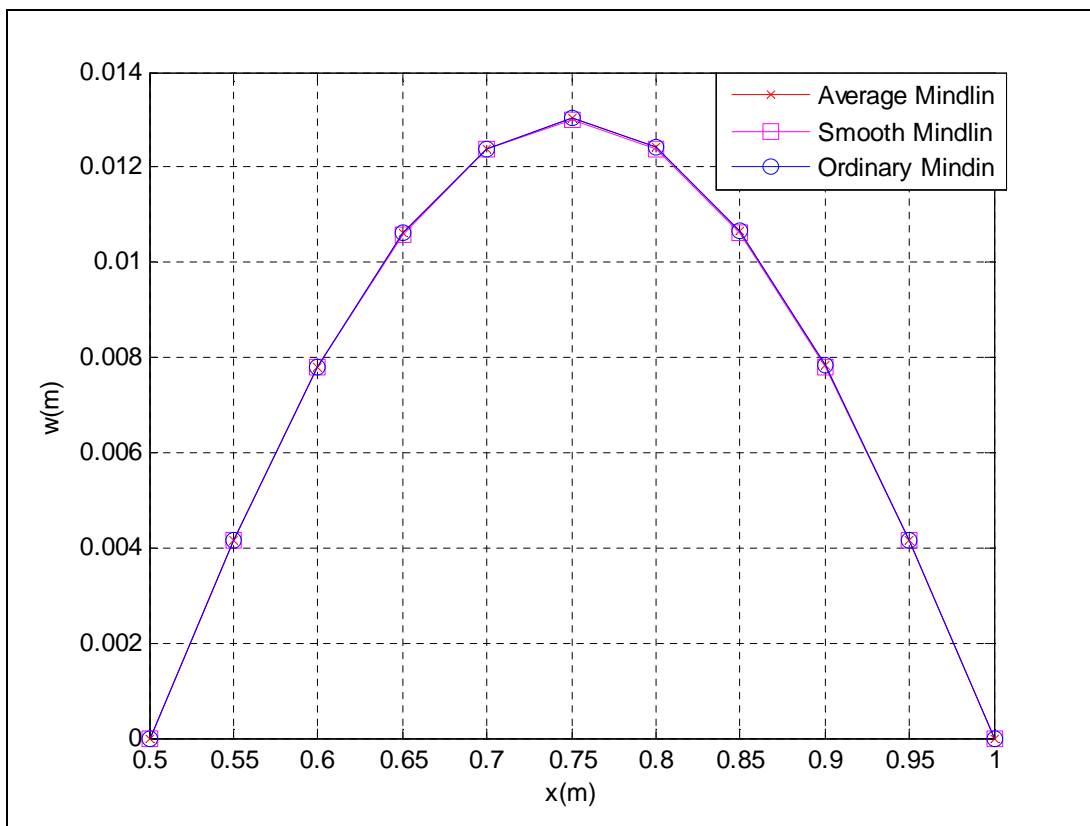
Figure 7-64: w-displacement validation against Ordinary Mindlin program for the simply supported ring case
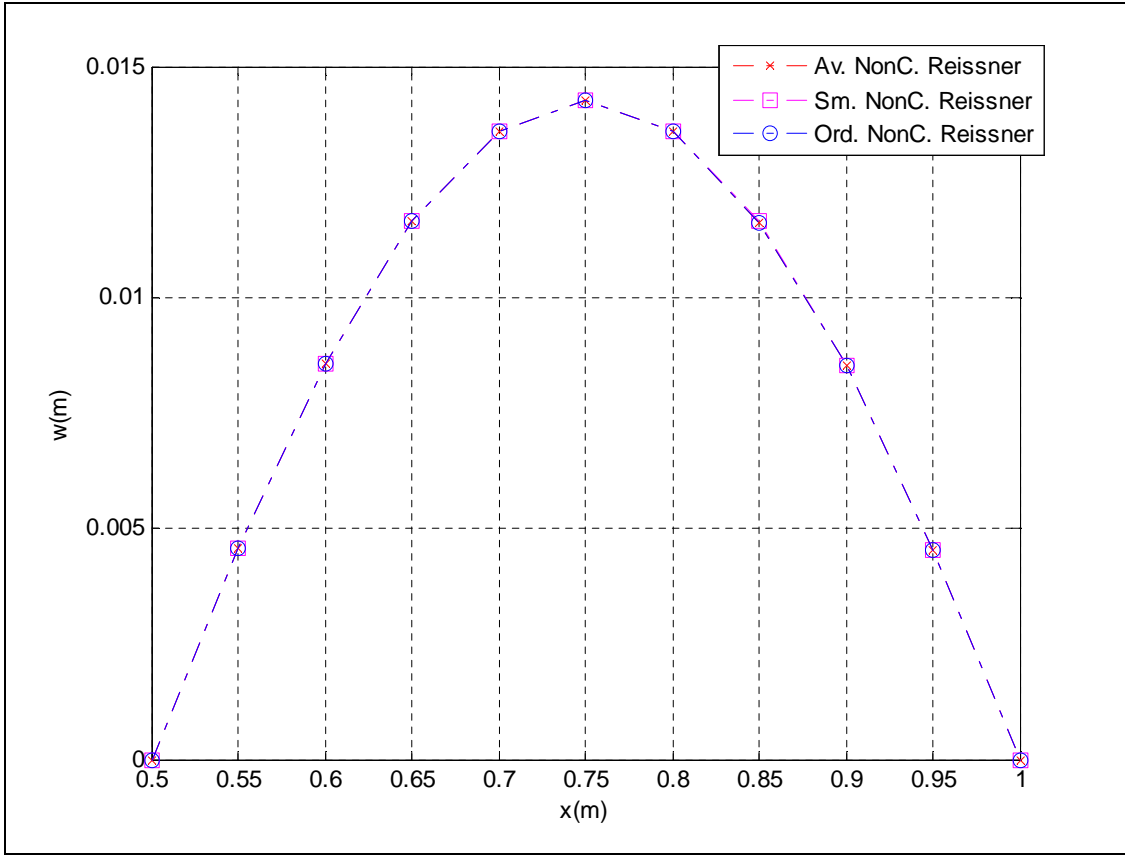
Figure 7-65: w-displacement validation against Ordinary Reissner program for the simply supported ring case

Figure 7-66 shows the through-thickness stress result in the fibre direction at node 20 (i.e. the (0, 0.95) coordinate) for a FGC ring case with P=1 and V_1=0.5 at the 8th load increment. The stress results of the Average and Smooth Mindlin programs were in good agreement with the result of the Ordinary Mindlin program. The out-of-plane bending load results in a tensile stress on the top plies (i.e. plies at positive z positions) and compressive stress on the bottom plies (i.e. plies at negative z positions). This effect results in a linear distribution of σ_{11} across the plies with the maximum tensile stress σ_{11} at the 1st ply (i.e. ply at z=0.015m) and maximum compressive stress σ_{11} at the 12th ply (i.e. ply at z=-0.015m).
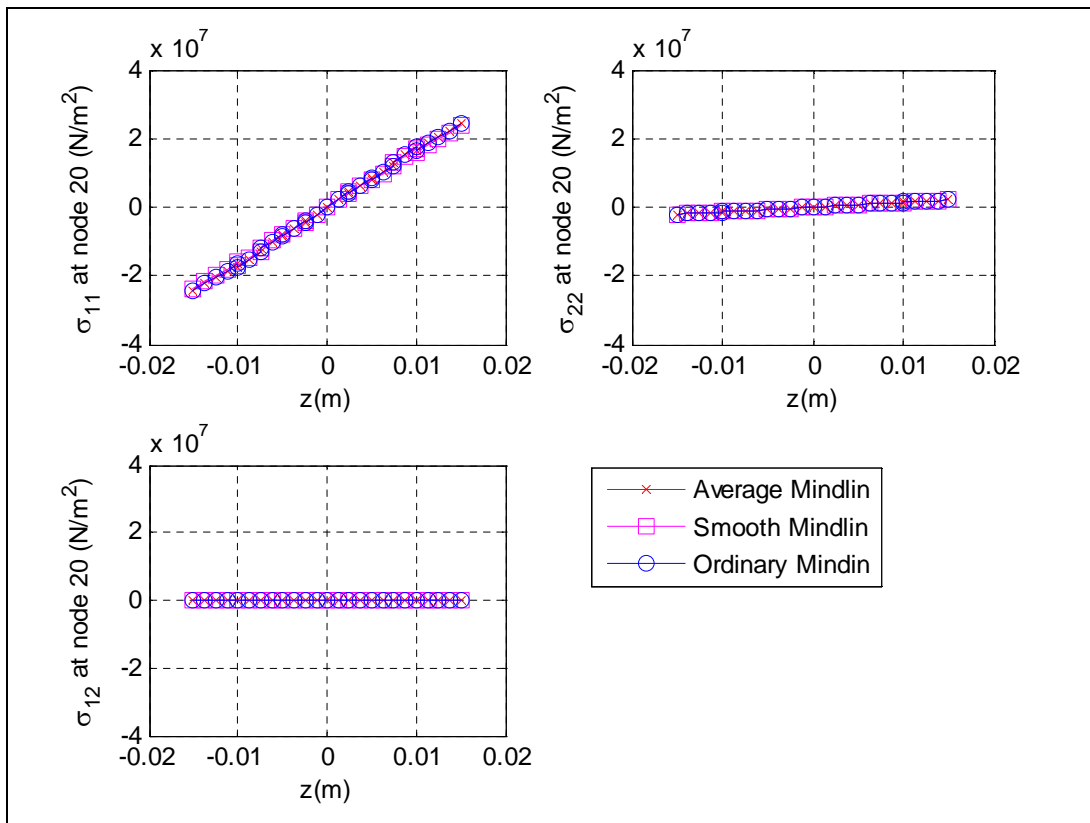

Figure 7-66: Stress validation against Ordinary Mindlin program for the simply supported ring case

The progressive damage modelling employed in this example is as described in Example 7.3.1. Figure 7-67 shows the damage contour plot for the first three layers of a FGC ring case with P=1 and V_1=0.5 at the 8th load increment. This figure also shows the typical damage contour plot of most programs for the FGC ring subjected to a pressure loading.

In order to understand the damage results in Figure 7-67, it must be noted that the damage are based on Tsai-Hill failure index which is a function of the micromechanical strength properties, fibre orientation of ply, functional gradation and stress transfer. It can be seen from the damage contour plots that the region around the x=0 edge of the 1st ply (i.e. ply at z=0.015m) experienced the worst damage. This effect can be explained by the fact that the applied pressure causes the ring to experience an out-of-plane bending which results in a tensile stress on the 1st ply in the radial direction. This tensile stress is not aligned with the resultant fibre direction (i.e. 0° for the stacking sequence of "[[-45/0/45]$_2$]$_s$") around the x=0 edge, hence the reason for damage at this region. Reduction in failure index occurs away from the x=0 edge because the difference in the orientation of the tensile stress in the radial direction and the resultant fibre direction of the FGC ring reduces. The damage reduces for each ply in the direction towards the midplane of the FGC ring. The damage results include the effect of stress transfer. This effect is due to the undamaged regions being stiffer than the damaged regions and they carry a large portion of the extra loads that were meant for the damaged regions and therefore the undamaged regions are stressed more. Hence this results in stress transfer occurring both in the in-plane and out-of-plane directions.
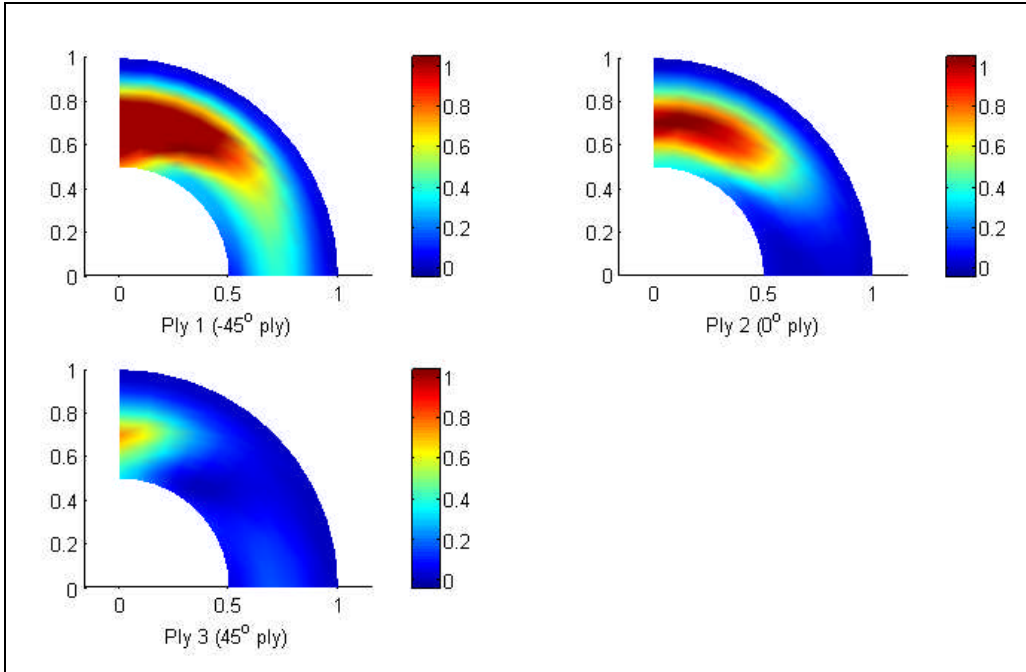
Figure 7-67: Damage contour plot of the first three plies for the simply supported ring case

Since failure was more pronounced in the 1st ply, a closer study of the progressive damage of the 1st ply was undertaken. Figure 7-68 shows the progressive damage contour plot for the 1st ply (i.e. -45° ply) of a FGC ring case with P=1 and V$_1$=0.5 for nine load increments. This figure also shows the typical progressive damage contour plot of most programs for the FGC ring subjected to a pressure loading. The damage contour plot is the plot of the failure index at all nodes on the FGC ring. If failure index is greater than one, then the composite ring is damaged, else the composite ring is undamaged. It can be seen from the damage contour plot that damage was initiated during the 7th load increment at the x=0 edge. The damage then spreads in the FGC ring in subsequent load increments.
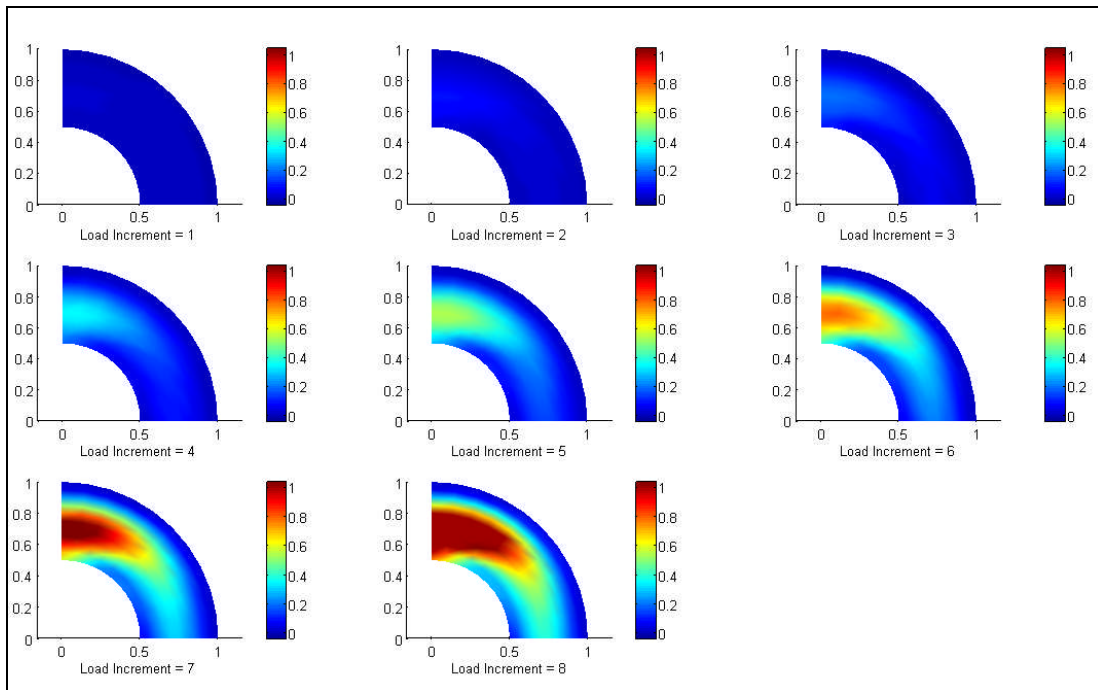

Figure 7-68: Progressive damage contour plot of the first ply for the simply supported ring case

Figure 7-69 shows the progressive damage plot for the 1st ply (i.e. -45° ply) of a FGC ring case with P=1 and V$_1$=0.5 for the 4th to 7th load increment. This figure also shows the progressive damage plot of the Average and Smooth Mindlin programs for the FGC ring subjected to pressure loading. The results were in good agreement with each other. The damage plot is the plot of the failure index at all nodes on the x=0 edge of the FGC ring. It can be seen from the damage contour plot that the maximum failure index occurs around the r=0.7m region and x=0 edge. This indicates that the maximum bending moment is experienced around the r=0.7 region which results in maximum bending stress at this region and hence maximum failure index.
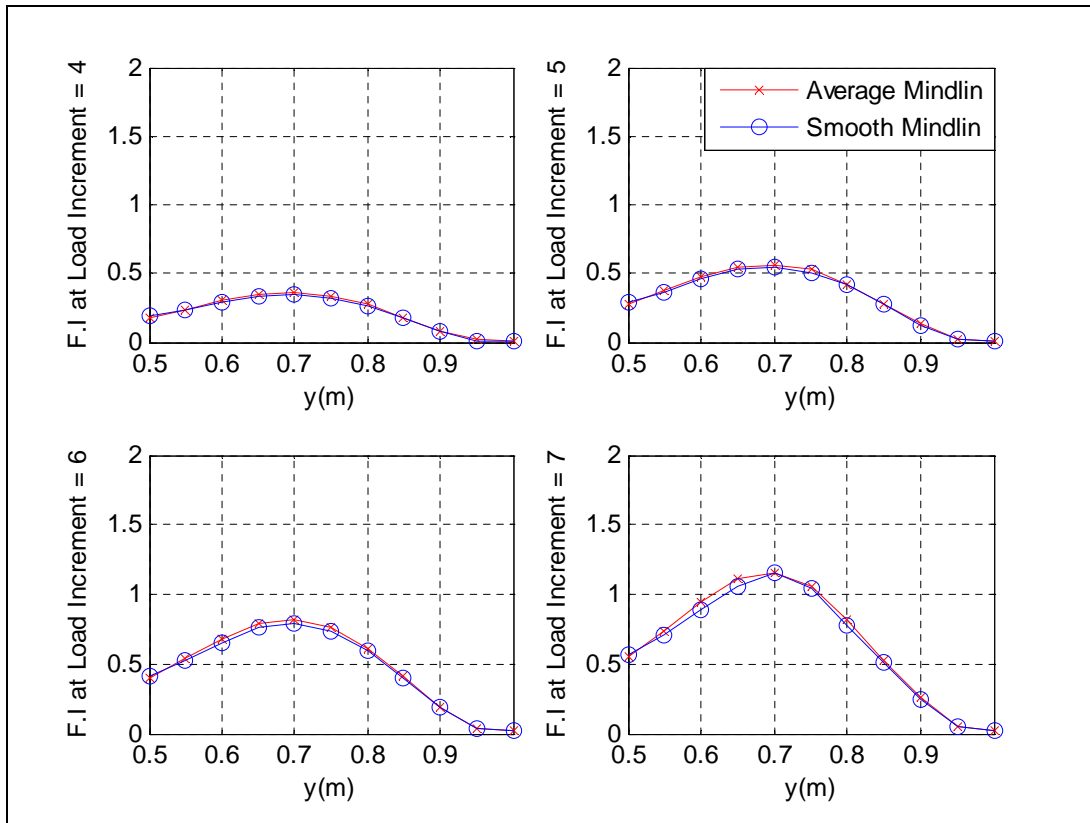

Figure 7-69: Progressive damage plot of the first ply for the simply supported ring case

7.3.8 Clamped FGC ring case

Example 7.3.8: A FGC ring with a "[[-45/0/45]$_2$]$_s$" stacking sequence was subjected to a pressure loading of 3.5MPa. The values of the functional gradation properties include gradation exponent, P=1 and gradation offset, V$_1$=0.5. The task is to validate the displacement results of Mindlin and Reissner programs against the result of the Ordinary FE programs. The FE modelling procedure is presented for this example. The geometrical properties and micro-mechanical properties are as given in Example 7.3.7.

FE Modelling

A quarter of the model has been modelled instead of the full ring model by taking advantage of the axisymmetry nature of the FE problem. A triangular element has been employed in order to demonstrate and validate the capability of the FE programs in modelling with triangular elements. A mesh containing 200 3-noded triangular Mindlin-type elements was employed for the Mindlin programs. A mesh containing 200 3-noded triangular non-conforming elements was employed for the non-conforming Reissner program. The boundary condition shown in Table 7-36 was applied to the FE model.

Table 7-36: Boundary condition for the clamped ring case

Nodes	Boundary condition
Nodes on the x=0 edge	u = θ_y = 0 (i.e. symmetry boundary condition was applied to the x=0 edge)
Nodes on the y=0 edge	v = θ_x = 0 (i.e. symmetry boundary condition was applied to the y=0 edge)
Nodes on the r=0.5 edge and the r=1 edge	u = v = w = θ_x = θ_y = 0 (i.e. the r=0.5 edge and the r=1 edge are clamped)

In order to model the functional gradation of the FGC plate in the Ordinary FE programs, the fibre and matrix volume fractions were computed for each element at their midpoints by using the fibre distribution equations developed in chapter 3. The macro-mechanical properties were then computed for each element by substituting the fibre and matrix volume fractions into the macro-mechanical equations developed in chapter 3. The

computed macro-mechanical properties of each element of the FGC plate were then fed into the Ordinary FE programs.

Mindlin and Reissner program validation results

Figures 7-70 and 7-71 show the nodal displacement results along the y=0 edge for a FGC ring case with P=1 and V_1=0.5 at the 9th load increment. This FGC ring is graded in the radial direction. The displacement results for the Mindlin and Reissner programs were in good agreement with the Ordinary FE program. The displacement results of the Mindlin programs had small discrepancy in comparison to the displacement results of the Reissner programs. This discrepancy can be explained by the difference in transverse shear modelling employed in each program. The w-displacement value at r=0.5 and r=1 is zero as expected because the ring is clamped at the r=0.5 and r=1 edges.
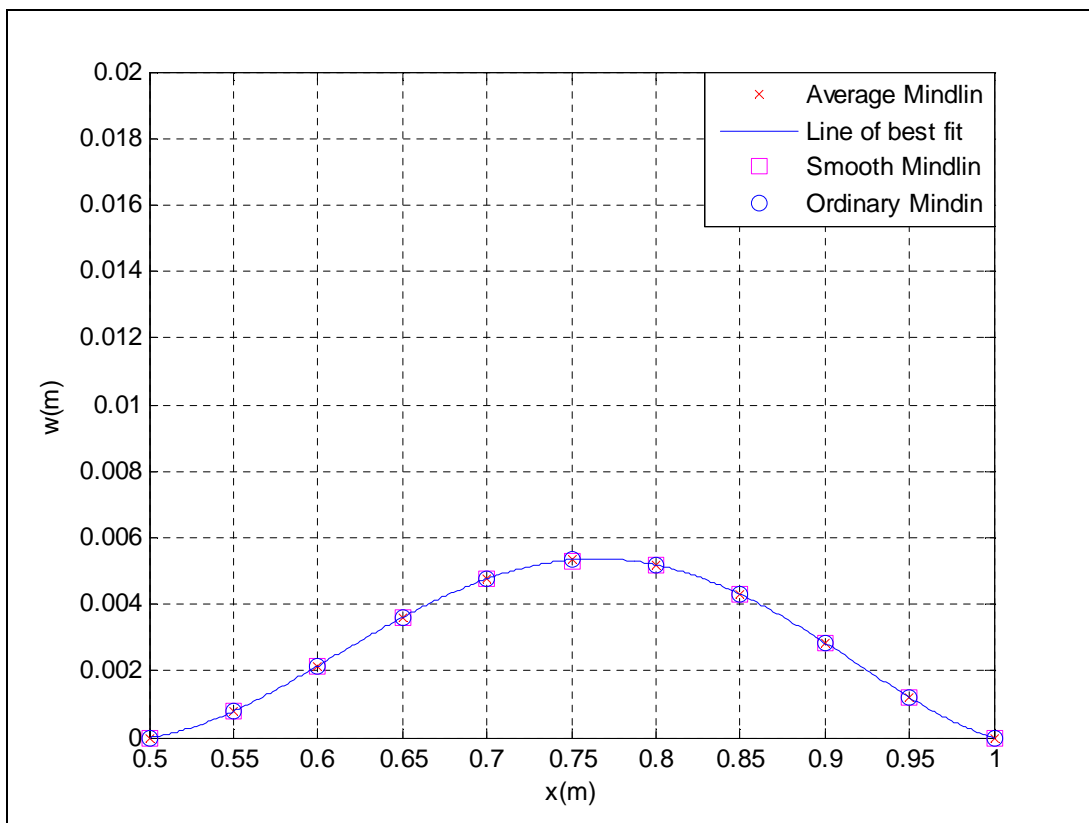

Figure 7-70: w-displacement validation against Ordinary Mindlin program for the clamped ring case
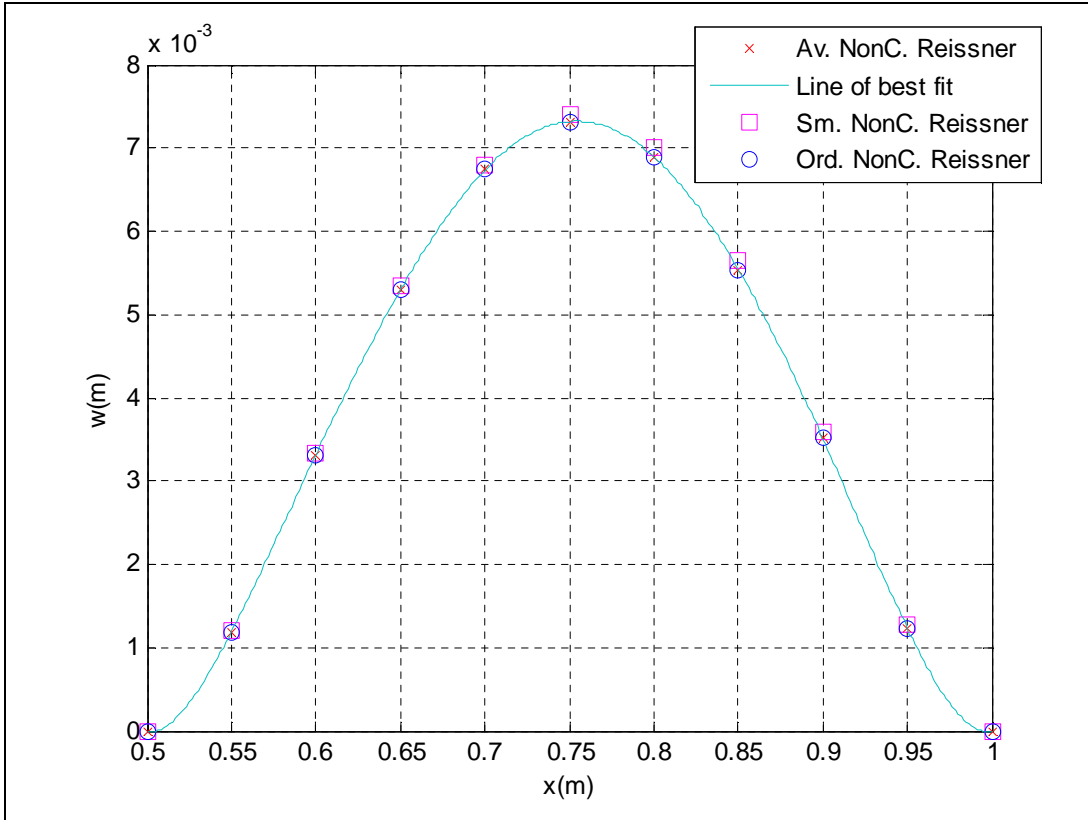
Figure 7-71: w-displacement validation against Ordinary Reissner program for the clamped ring case

Figure 7-72 shows the through-thickness stress result in the fibre direction at node 1 (i.e. the (0, 0.5) coordinate) for a FGC ring case with P=1 and V_1=0.5 at the 9th load increment. The stress results of the Average and Smooth Mindlin programs were in good agreement with the result of the Ordinary Mindlin program. The out-of-plane bending load results in a compressive stress on the top plies (i.e. plies at positive z positions) and tensile stress on the bottom plies (i.e. plies at negative z positions). This effect results in a distribution of σ_{11} across the plies with the maximum compressive stress σ_{11} at the 1st ply (i.e. ply at z=0.015m) and maximum tensile stress σ_{11} at the 12th ply (i.e. ply at z=-0.015m).
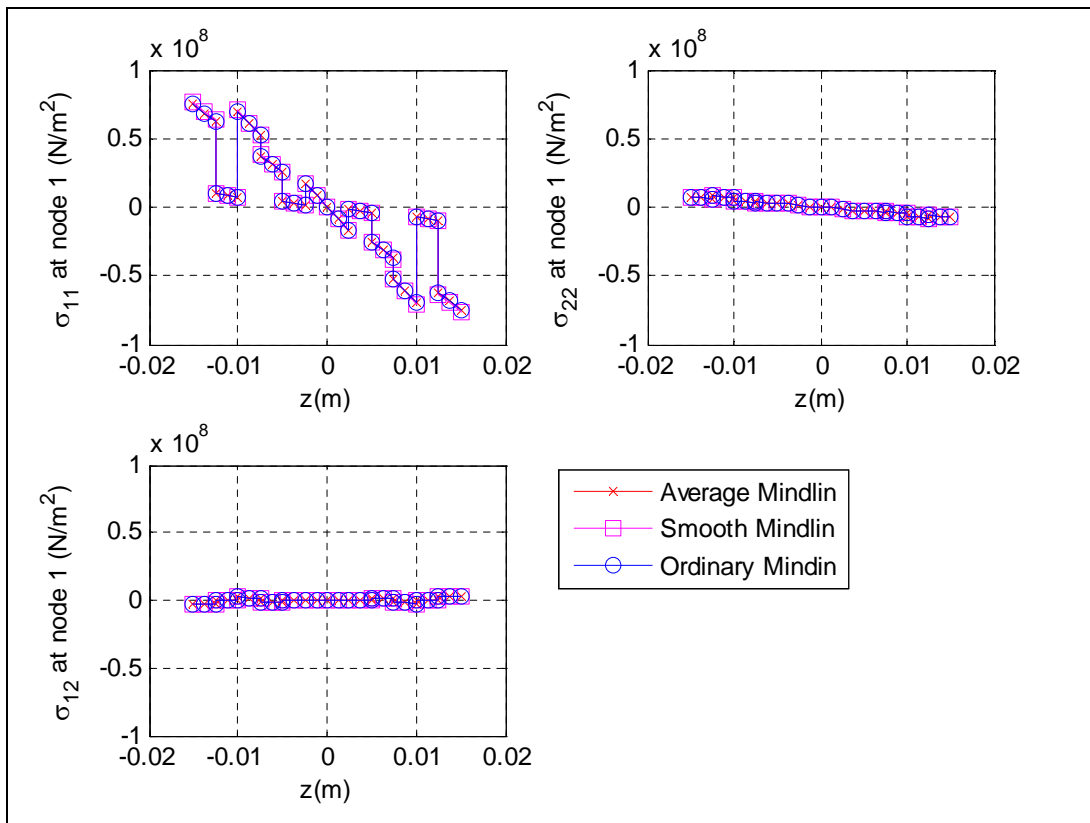

Figure 7-72: Stress validation against Ordinary Mindlin program for the clamped ring case

The progressive damage modelling employed in this example is as described in Example 7.3.1. Figure 7-73 shows the damage contour plot for the first three layers of a FGC ring case with P=1 and V_1=0.5 at the 9th load increment. This figure also shows the typical damage contour plot of most programs for the FGC ring subjected to a pressure loading.

In order to understand the damage results in Figure 7-73, it must be noted that the damage are based on Tsai-Hill failure index which is a function of the micromechanical strength properties, fibre orientation of ply, functional gradation and stress transfer. It can be seen from the damage contour plots that the region around the clamped edges of the 1st ply (i.e. ply at z=0.015m) experienced the worst damage. This effect can be explained by the fact that the applied pressure causes the ring to experience an out-of-plane bending which results in a compressive stress around the clamped edges on the 1st ply in the radial direction. This compressive stress is not aligned with the resultant fibre direction (i.e. 0° for the stacking sequence of "[[-45/0/45]$_2$]$_s$") around the x=0 edge, hence the reason for damage at this region. Reduction in failure index occurs away from the x=0 edge because the difference in orientation of the compressive stress in the radial direction and the resultant fibre direction of the FGC ring reduces. The damage reduces for each ply in the direction towards the midplane of the FGC ring. The damage results include the effect of stress transfer. This effect is due to the undamaged regions being stiffer than the damaged regions and they carry a large portion of the extra loads that were meant for the damaged regions and therefore the undamaged regions are stressed more. Hence this results in stress transfer occurring both in the in-plane and out-of-plane directions.
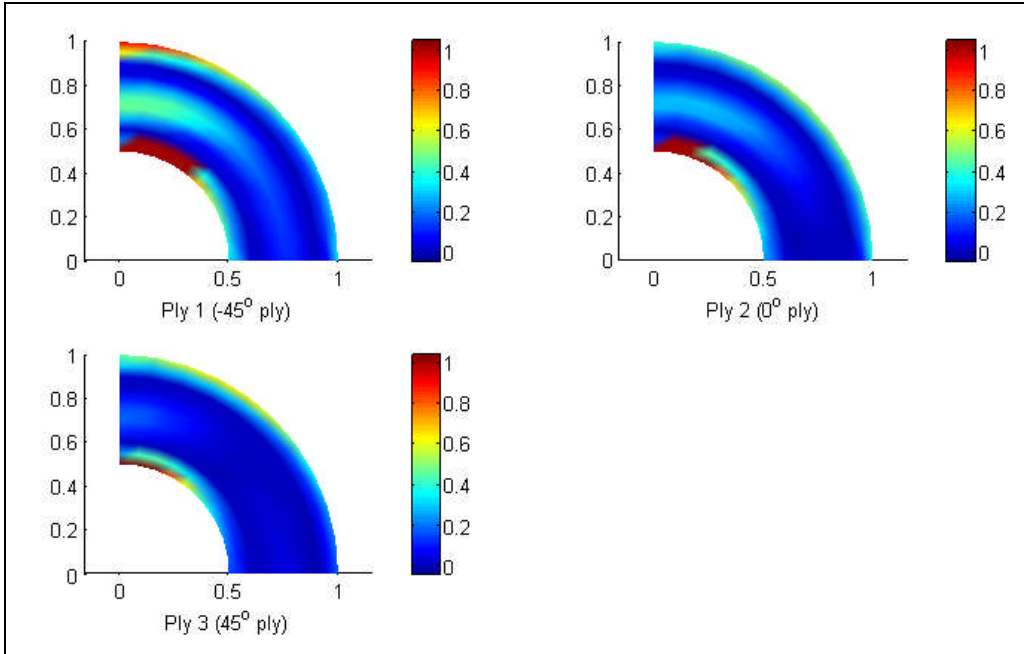
Figure 7-73: Damage contour plot of the first three plies for the clamped ring case

Since failure was more pronounced in the 1st ply, a closer study of the progressive damage of the 1st ply was undertaken. Figure 7-74 shows the progressive damage contour plot for the 1st ply (i.e. -45° ply) of a FGC ring case with P=1 and V$_1$=0.5 for nine load increments. This figure also shows the typical progressive damage contour plot of most programs for the FGC ring subjected to a pressure loading. The damage contour plot is the plot of the failure index at all nodes on the FGC ring. If failure index is greater than one, then the composite ring is damaged, else the composite ring is undamaged. It can be seen from the damage contour plot that damage was initiated during the 7th load increment at the (0, 0.5) coordinate. The damage then spreads along the clamped edges of the FGC ring in subsequent load increments.
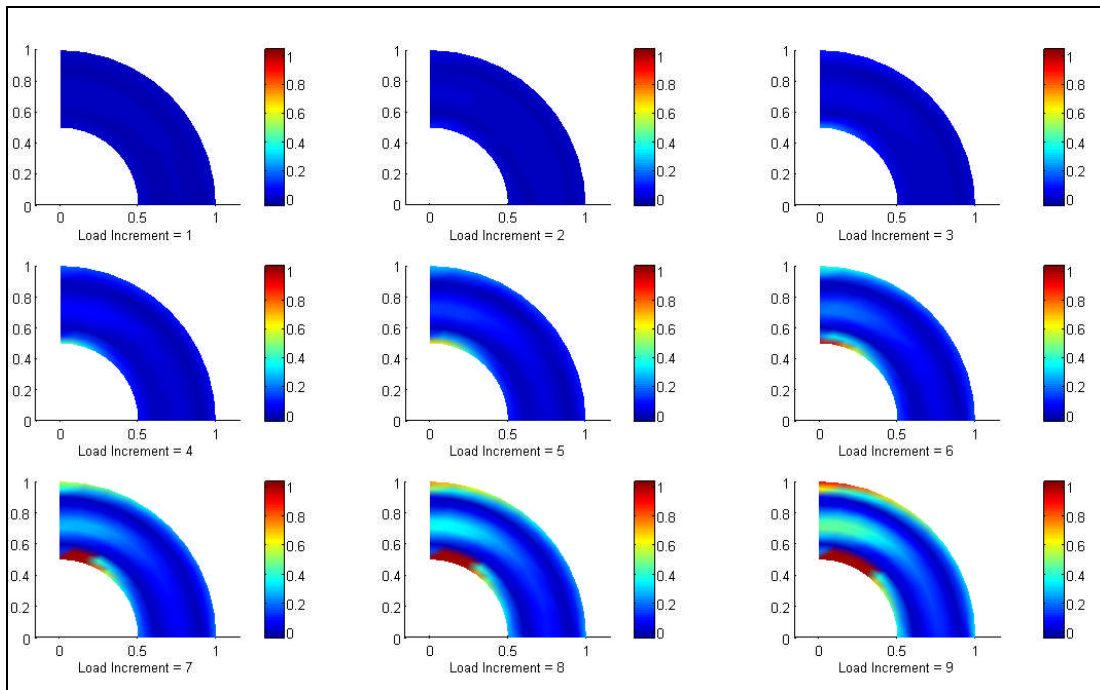

Figure 7-74: Progress damage contour plot of the first ply for the clamped ring case

Figure 7-75 shows the progressive damage plot for the 1st ply (i.e. -45° ply) of a FGC ring case with P=1 and V_1=0.5 for the 6th to 9th load increment. This figure also shows the progressive damage plot of the Average and Smooth Mindlin programs for the FGC ring subjected to pressure loading. The results were in good agreement with each other. The damage plot is the plot of the failure index at all nodes on the x=0 edge of the FGC ring. It can be seen from the damage contour plot that the maximum failure index occurs around the clamped edges. This indicates that the maximum bending moment is experienced around the clamped edges which results in maximum bending stress at these edges and hence maximum failure index. The 7th to 9th load increments have some missing failure indices around the r=0.5 edge. This effect is due to the fact that when an element has completely failed, the stiffness value at each node of the element is degraded to zero, hence nodal stress of the element is zero resulting in a nodal failure index value of zero. The nodal failure index values of zero are eliminated from the plot to best demonstrate the progressive damage, since damage occurs when failure index exceeds the value of one.
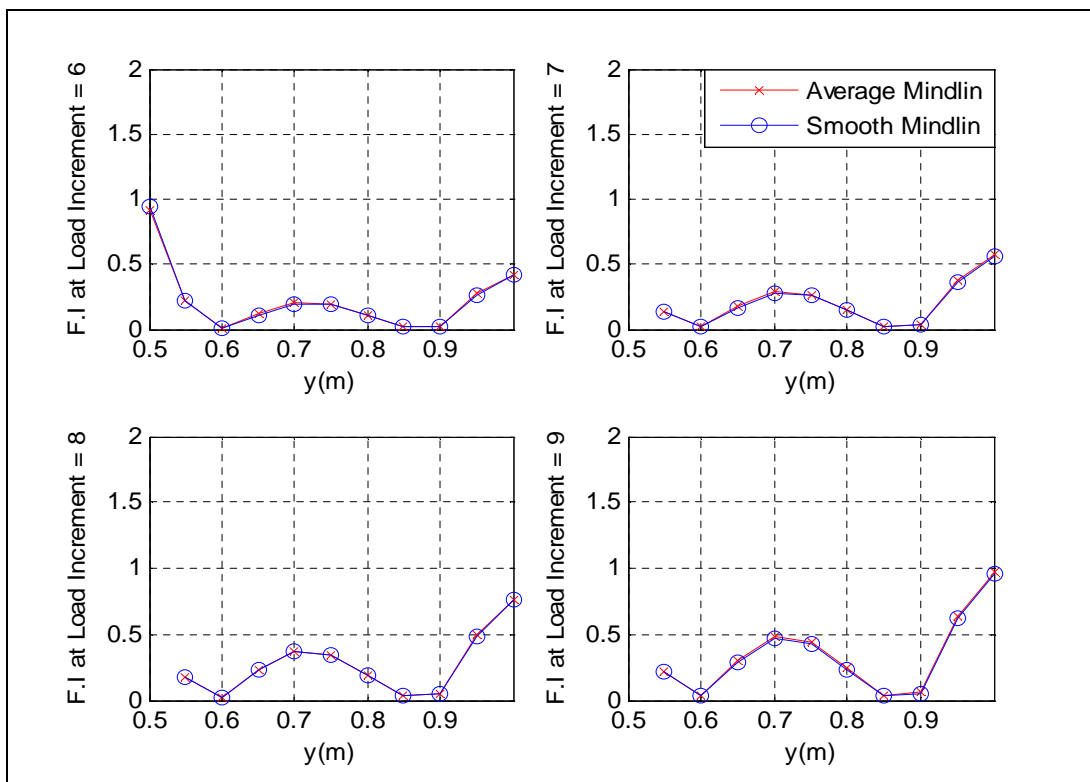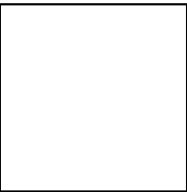

Figure 7-75: Progressive damage plot of the first ply for the clamped ring case

In this chapter, three stages of validation were undertaken. The first stage involves the validation of the infinitesimal strain part of the Average Mindlin programs against analytical solutions using traditional composite plate cases. The second stage involves the validation of the infinitesimal strain part of the Average, Smooth and Ordinary Mindlin programs against Abaqus results using the FGC cases. The third stage involves the validation of infinitesimal and finite strain part of the Average and Smooth programs against the Ordinary programs using the FGC cases. In the validation exercise, the results of the Average and Smooth programs were in good agreement with the analytical solutions, Abaqus program results and Ordinary program results.

8 Optimisation Result

The optimisation technique used in this thesis can be described as fail-safe design technique which involves the imposition of constraints to ensure that the physical limitations of materials or structural properties required for satisfactory performance are not exceeded. This optimisation technique involves changing the fibre distribution parameters and running the three FE codes for the given fibre distribution, checking to see if all constraints have been satisfied. The constraints that have been considered include displacement constraints, failure index constraints, buckling load constraints and natural frequency constraints. Figure 8-1 is a good description of this optimisation technique concept.

In this optimisation exercise, two geometry cases were considered. These cases include the rectangular functionally graded composite (FGC) plate case and the rectangular FGC plate case with a central hole. The two geometry cases are the same as the one used in the validation exercise and it is as described in the previous chapter.
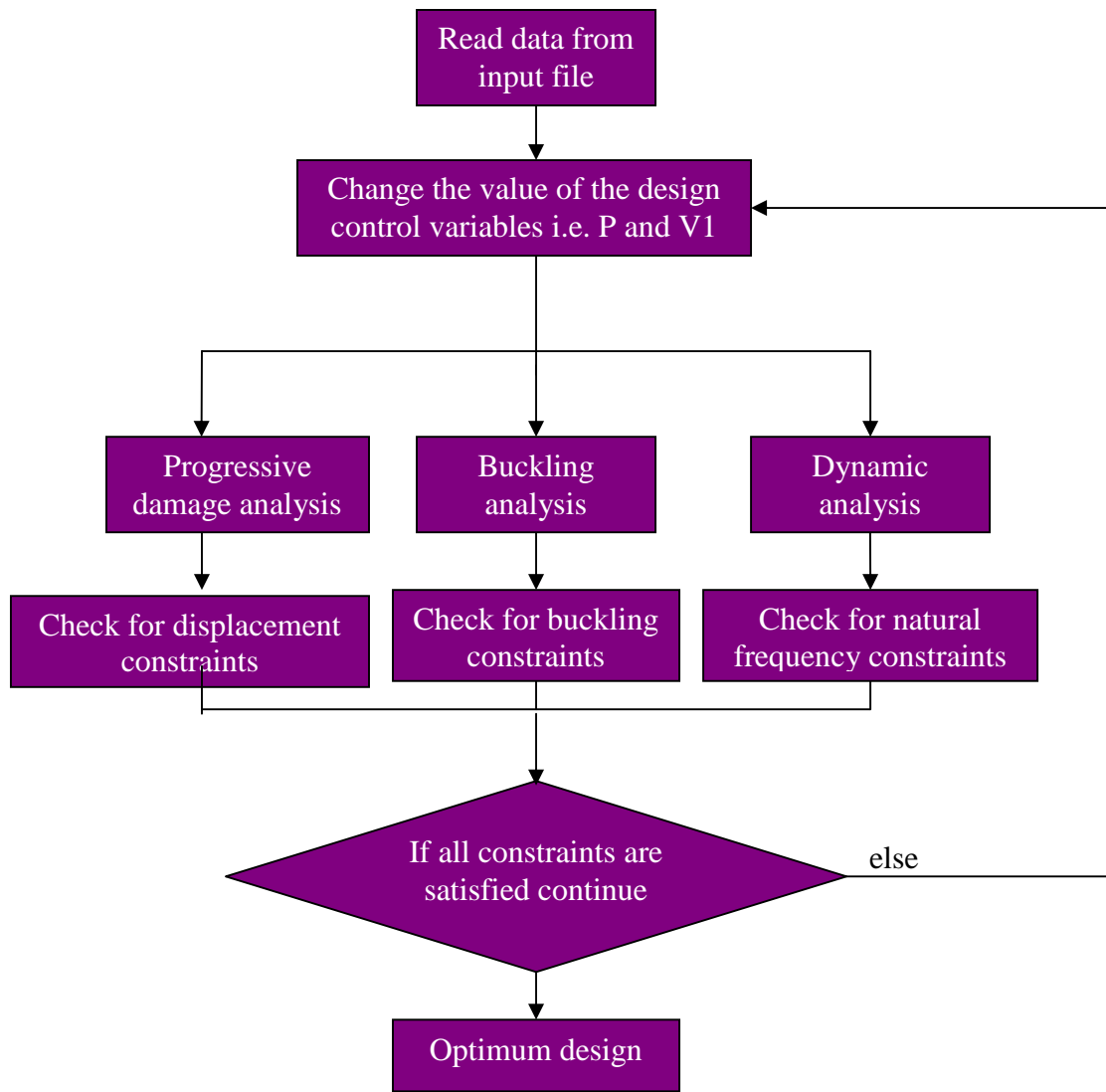
Figure 8-1: Optimisation Technique

8.1 Fibre Distribution Effect on Finite Strain and Progressive Damage Results

In this section, progressive damage analysis was carried on a rectangular FGC plate and rectangular FGC plate with hole. Ten different fibre ratio distribution cases were considered which was achieved by changing the different gradation exponent, P and different gradation offset, V_1 in the fibre distribution equation discussed in Chapter 3. The rectangular functionally graded composite (FGC) plate case was subjected to tensile loading, in-plane bending and out-of-plane bending. The rectangular FGC plate case with hole was subjected to tensile loading. The results obtained are presented in this section.

8.1.1 FGC plate case under tensile loading

Example 8.1.1: A rectangular FGC plate with a "[[-45/0/45]_2]_s" stacking sequence was subjected to a tensile load of 8MN. The task is to compute the displacement and failure index results using conforming Reissner programs for ten fibre distribution cases and to study the fibre distribution effect on the displacement and failure index results. The FE modelling procedure is presented for this example.

The geometrical properties, micro-mechanical properties and loading condition are as given below. The micromechanical data were obtained from a textbook by Kaw (1997).

Table 8-1: Tensile case data

Geometry					
L (m)	2.000	w (m)	1.000		
t (m)	0.0300	No. of ply	12		
Fibre and matrix properties					
E_f (Pa)	2.300E+11	ν_f	3.500E-01	μ_f (Pa)	8.519E+10
E_m (Pa)	3.400E+09	ν_m	3.000E-01	μ_m (Pa)	1.308E+09
Strength properties					
X_{mt} (Pa)	7.200E7	X_{mc} (Pa)	1.020E8	X_{ms} (Pa)	3.400E7
X_{ft} (Pa)	2.067E9	X_{fc} (Pa)	1.999E9	σ_{rm} (Pa)	0.0
k_σ	1	k_τ	1		

The notations used in Table 8-1 are as described below.

L, w, and t, represent the length, width, thickness of ply respectively.

E_f and E_m represent the Young's modulus of the fibre and matrix respectively.

ν_f and ν_m represent the Poisson's ratio of the fibre and matrix respectively.

μ_f and μ_m represent the shear modulus of the fibre and matrix respectively.

X_{mt}, X_{mc} and X_{ms} represent the tensile, compressive and the shear strength of the matrix respectively.

X_{ft} and X_{fc} represent the tensile and compressive strength of the matrix respectively.

σ_{rm} represent the maximum residual radial stress at the interface.

k_σ and k_τ represent the stress concentration factor and the shear stress concentration factor respectively.

FE Modelling

A mesh containing 128 4-noded conforming elements was employed for the conforming Reissner program. A tensile load of 8MN was applied as an equivalent nodal loads at the nodes on the x=2 edge with reduced load at the corner nodes. For example, in the 128 element case, the load was applied equally at nodes on the x=2 edge but with half the loads at the corner nodes on the x=2 edge. Hence the equivalent nodal loading for the 128 element case was 1MN at each nodes on the x=2 edge with 500kN at the corner nodes on the x=2 edge. In order to model the finite strain, a tenth of the equivalent nodal loading was applied at every load increment. Also in order to model the progressive damage, a check for failure was undertaken at the node of each element for every load increment and if failure is detected, material properties of the element are degraded and equilibrium is re-established.

The boundary condition shown in Table 8-2 was applied to the FE model.

Table 8-2: Boundary condition for the tensile case

Nodes	Boundary condition
Node 20 (i.e. node at x=0 and y=0.5)	$u = v = w = \theta_x = \theta_y = 0$ (i.e. all degrees of freedom are fixed at Node 20)
Nodes on the x=0 edge excluding node 20	$u = 0$

Displacement Results

Figure 8-2 to 8-4 show the nodal displacement results at the 2nd load increment along the y=0.5 line for a FGC plate with ten fibre distribution cases. The nodal displacement results for the 2nd load increment have been presented because it is the increment at which none of the ten fibre distribution cases have experienced complete damage. In the tension case, the parameter that is of major interest is the u-displacement. Minimisation of u-displacement is usually the desired effect for design purposes.

Figure 8-2 shows the comparison of the displacement results for the tension cases with P=0 and P=0.5. And it shows that the fibre distribution case with P=0.5 and V_1=0.5, and the traditional composite case (i.e. P=0 and V_1=0.4) satisfy the minimum u-displacement constraint at the x=2 edge.

Figure 8-3 shows the comparison of the displacement results for the tension cases with P=0 and P=1. And it shows that the traditional composite case (i.e. P=0 and V_1=0.4) satisfies the minimum u-displacement constraint at the x=2 edge.

Figure 8-4 shows the comparison of the displacement results for the tension cases with P=0 and P=2. And it shows that the traditional composite case (i.e. P=0 and V_1=0.4) satisfies the minimum u-displacement constraint at the x=2 edge.

The results of the tensile load case showed that the less stiff region of the FGC plates experienced higher u-deflection in comparison with the traditional composite plate. It can be seen from the displacement plots that increase in gradation offset, V_1 causes slight increase in u-displacement at the x=2 edge. The increase in gradation exponent, P causes significant increase in u-displacement at the x=2 edge. Since the desirable fibre distribution effect on the u-displacement result is to minimise the u-displacement at the x=2 edge, the optimum fibre distribution effect is achievable by decreasing the gradation exponent, P or gradation offset, V_1. Hence the optimum fibre distribution effect is achieved by the fibre distribution case with P=0.5 and V_1=0.5, and the traditional composite case (i.e. P=0). These fibre distribution cases are the best cases of all the ten fibre distribution cases that satisfy the minimum u-displacement constraint.
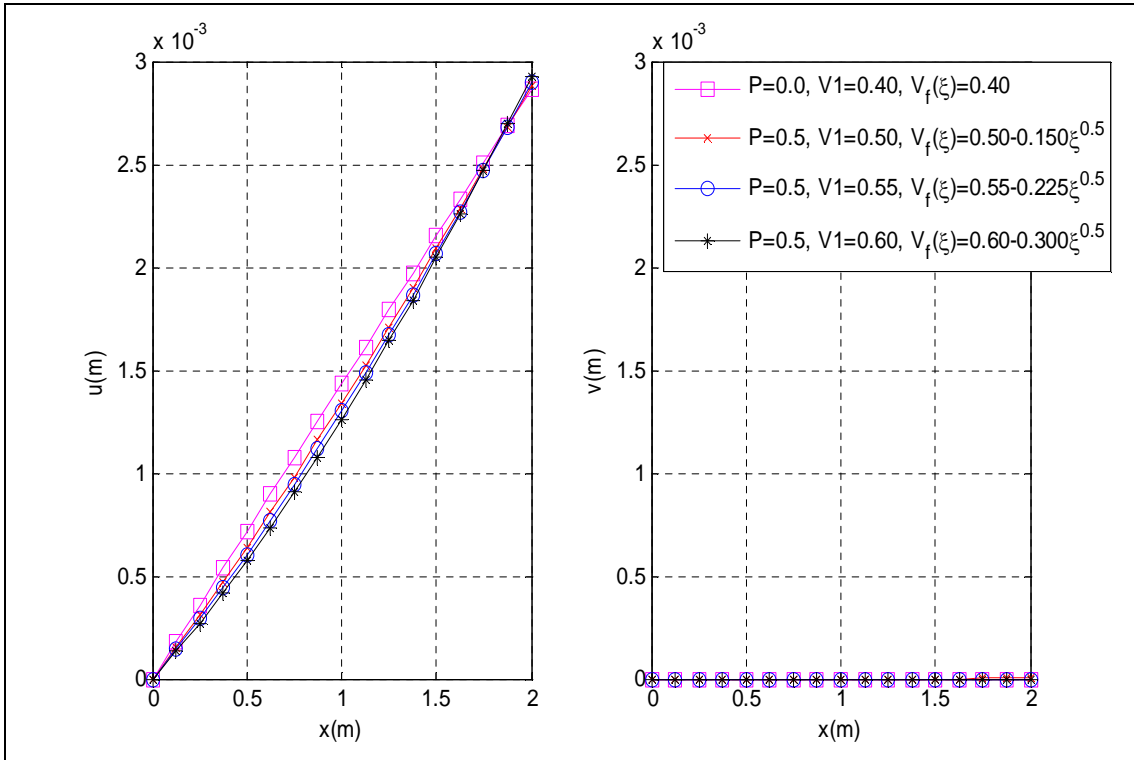
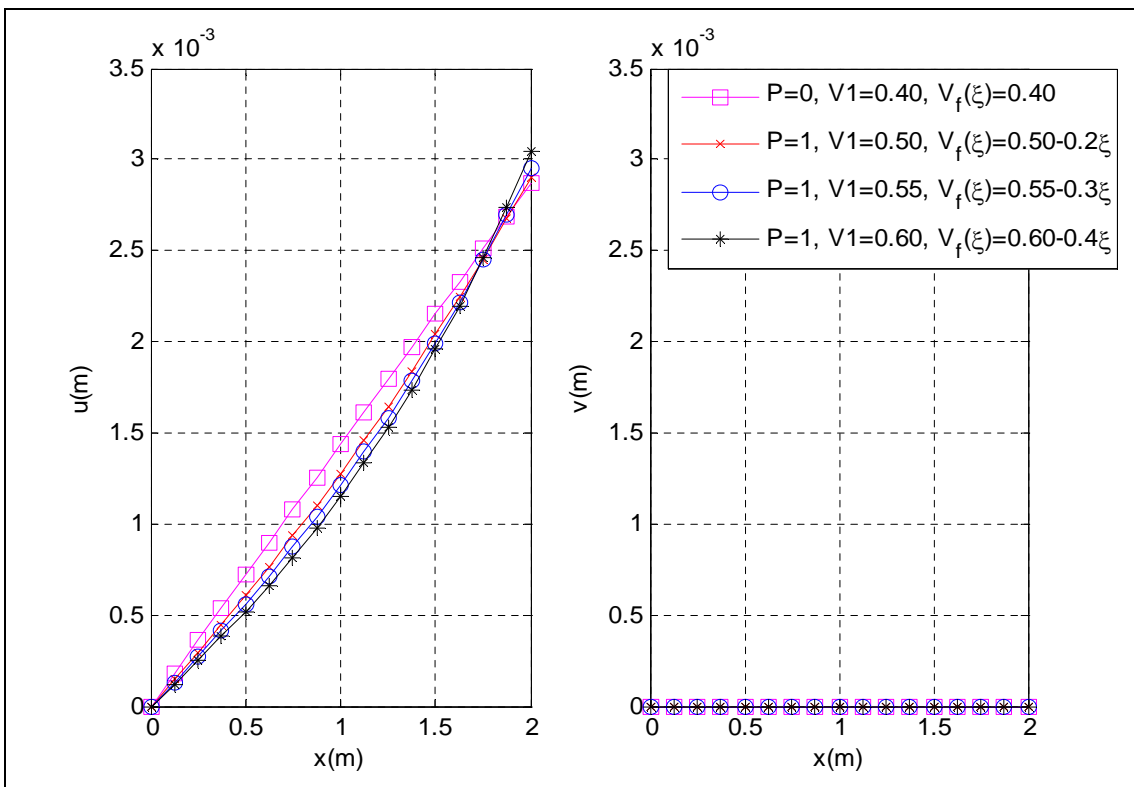**Figure 8-2: Displacement plot for tension cases with P=0 and P=0.5**

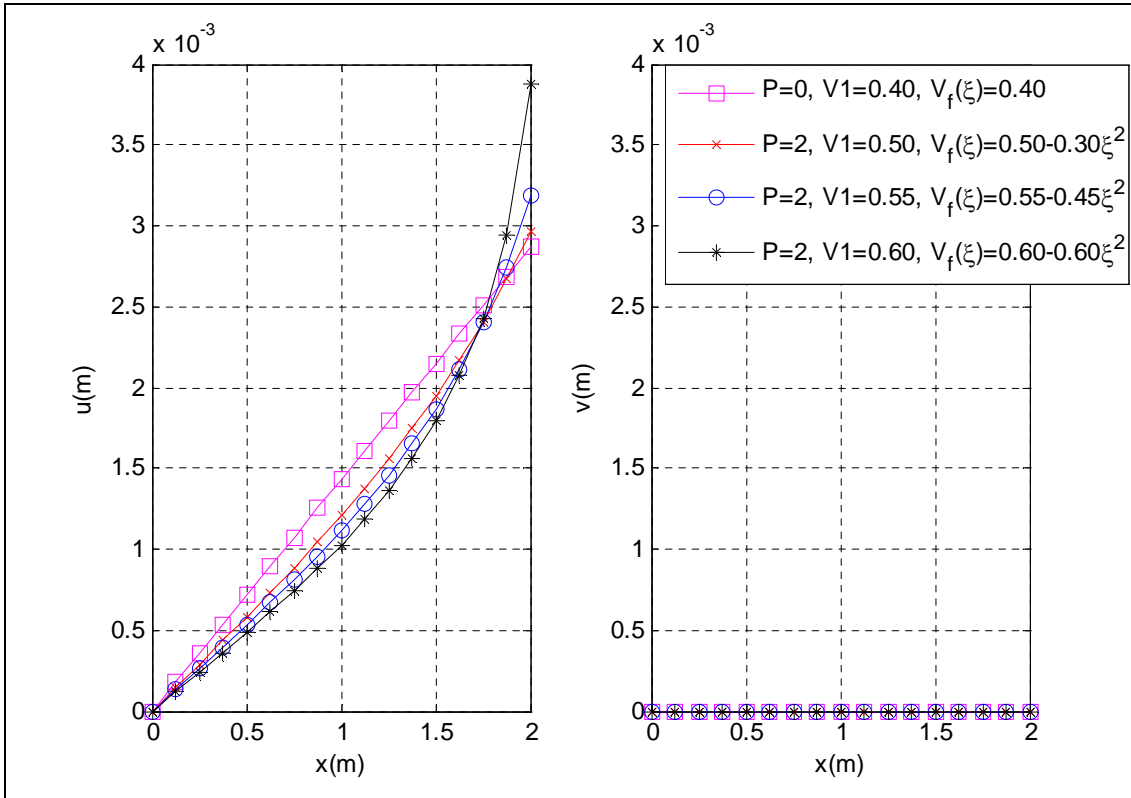**Figure 8-2: Displacement plot for tension cases with P=0 and P=1**

Figure 8-4: Displacement plot for tension cases with P=0 and P=2

Progressive Damage Results

Figures 8-5 to 8-7 show the progressive damage plots for the 2nd ply (i.e. 0° ply) of a FGC plate case with ten fibre distribution cases for different load increments. In some of the plots, failure index results were not plotted for some FGC plate cases because they were already completely damaged at the given load increment. The damage plot is the plot of the failure index (F.I.) at all nodes on the y=0.5 line of the FGC plate. It can be seen from the damage contour plot that the failure index increases as the nodal position, x increases for all the FGC plate cases. This indicates that the weaker region is the region around the x=2 edge for all FGC plate cases. The damage plots show that constant failure index occurs at all nodal positions on the traditional composite plate (i.e. P=0).

Figure 8-5 shows the comparison of the failure index along the y=0.5 line for the tension cases with P=0 and P=0.5. Minimisation of the failure index at the weaker

region (i.e. x=2 edge) is usually the desired effect for design purposes. The figure shows that the traditional composite case (i.e. P=0 and V_1=0.4) satisfies the minimum failure index constraint.

Figure 8-6 shows the comparison of the failure index along the y=0.5 line for the tension cases with P=0 and P=1. It also shows that the traditional composite case (i.e. P=0 and V_1=0.4) satisfies the minimum failure index constraint.

Figure 8-7 shows the comparison of the failure index along the y=0.5 line for the tension cases with P=0 and P=2. It also shows that the traditional composite case (i.e. P=0 and V_1=0.4) satisfies the minimum failure index constraint.

The results of the tensile load case showed that the less stiff region of the FGC plates experienced higher failure index in comparison with the traditional composite plate. It can be seen from the damage plots that increase in gradation offset, V_1 causes slight increase in the failure index at the x=2 edge. The increase in gradation exponent, P causes significant increase in the failure index at the x=2 edge. Since the desirable fibre distribution effect on the damage result is to minimise the failure index at the x=2 edge, the optimum fibre distribution effect is achievable by decreasing the gradation exponent, P or gradation offset, V_1. Hence the optimum fibre distribution effect is achieved by the traditional composite case (i.e. P=0 and V_1=0.4). These fibre distribution cases are the best cases of all the ten fibre distribution cases that satisfy the minimum failure index constraint.
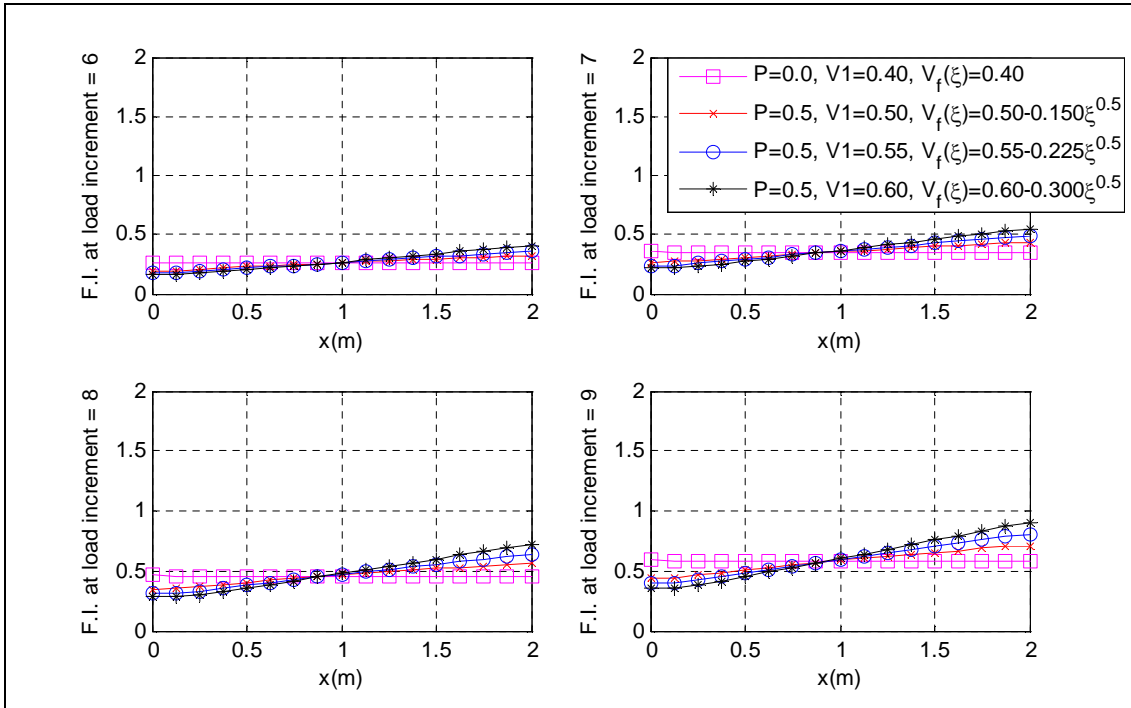
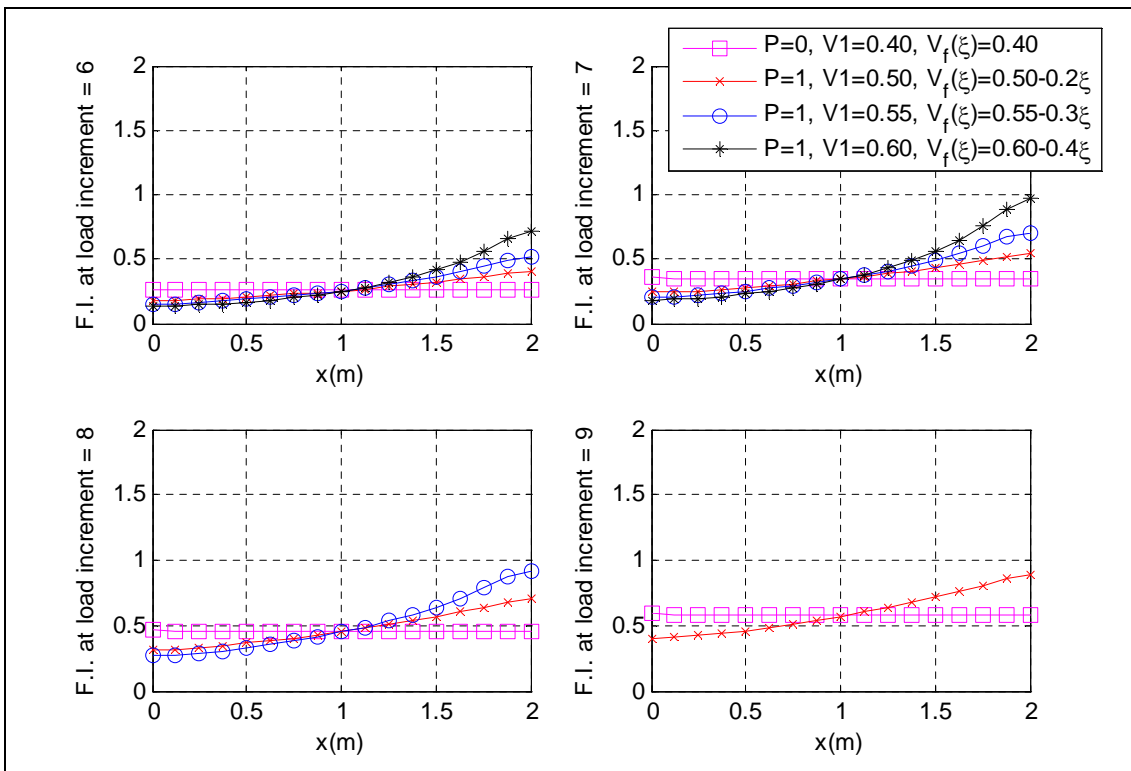**Figure 8-5: Progressive damage plot for tension cases with P=0 and P=0.5**

Figure 8-6: Progressive damage plot for tension cases with P=0 and P=1
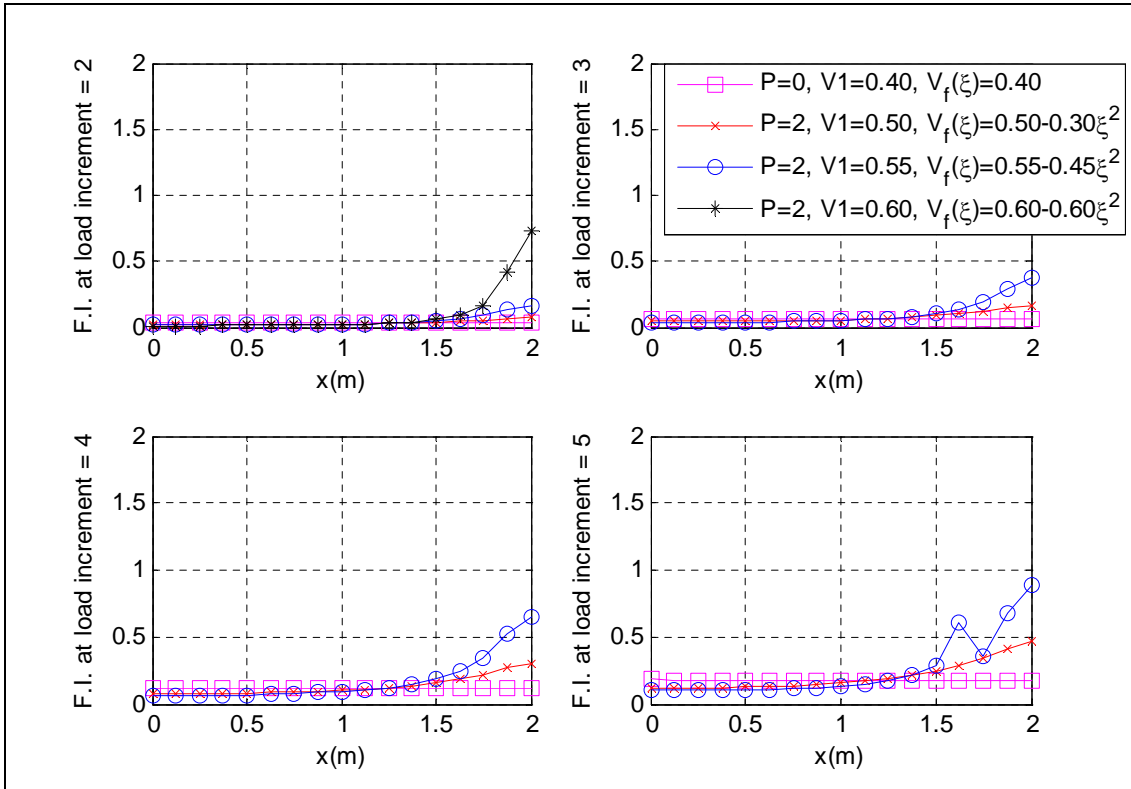
225

Figure 8-3: Progressive damage plot for tension cases with P=0 and P=2

8.1.2 FGC plate case under in-plane bending

Example 8.1.2: A rectangular FGC plate with a "[[-45/0/45]$_2$]$_s$" stacking sequence was subjected to an in-plane bending load of 1.6MN. The task is to compute the displacement and failure index results using conforming Reissner programs for ten fibre distribution cases and to study the fibre distribution effect on the displacement and failure index results. The FE modelling procedure is presented for this example. The geometrical properties and micro-mechanical properties are as given in Example 8.1.1.

FE Modelling

A mesh containing 128 4-noded conforming elements was employed for the conforming Reissner program. An in-plane bending load of 1.6MN was applied as an equivalent nodal loads at the nodes on the x=2 edge with reduced load at the corner nodes. For example, in the 128 element case, the load was applied equally at nodes on the x=2 edge but with half the loads at the corner nodes on the x=2 edge. Hence the equivalent nodal loading for the 128 element case was 200kN at each nodes on the x=2 edge with 100kN

at the corner nodes on the x=2 edge. In order to model the finite strain, a tenth of the equivalent nodal loading was applied at every load increment. Also in order to model the progressive damage, a check for failure was undertaken at the node of each element for every load increment and if failure is detected, material properties of the element are degraded and equilibrium is re-established.

The boundary condition shown in Table 8-3 was applied to the FE model.

Table 8-3: Boundary condition for in-plane bending case

Nodes	Boundary condition
Nodes on the x=0 edge	$u = v = w = \theta_x = \theta_y = 0$ (i.e. all degrees of freedom are fixed at the x=0 edge)

Displacement Results

In the in-plane bending case, the parameter that is of major interest is the v-displacement. Minimisation of v-displacement is usually the desired effect required for design purposes. Figure 8-8 to 8-10 show the nodal displacement results at the 9th load increment along the y=0.5 line for a FGC plate with ten fibre distribution cases.

Figure 8-8 shows the comparison of the v-displacement results for the in-plane bending case with P=0 and P=0.5. And it shows that the case with P=0.5 and V_1=0.6 satisfy the minimum v-displacement constraint at the x=2 edge.

Figure 8-9 shows the comparison of the v-displacement results for the in-plane bending case with P=0 and P=1. And it shows that the case with P=1 and V_1=0.6 satisfy the minimum v-displacement constraint at the x=2 edge.

Figure 8-10 shows the comparison of the v-displacement results for the in-plane bending case with P=0 and P=2. And it shows that the case with P=2 and V_1=0.55 satisfy the minimum v-displacement constraint at the x=2 edge.

It can be seen from the v-displacement plots that increase in gradation offset, V_1 causes slight decrease in v-displacement at the x=2 edge. The increase in gradation exponent, P causes significant decrease in v-displacement at the x=2 edge. Since the desirable fibre distribution effect on the v-displacement result is to minimise the v-displacement at the x=2 edge, the optimum fibre distribution effect is achievable by increasing the

gradation exponent, P or gradation offset, V_1. Hence the optimum fibre distribution effect is achieved by the fibre distribution case with P=2 and V_1=0.55. In comparison with the traditional composite case, a desirable effect of 28% reduction in v-displacement at the x=2 edge is achieved by using this FGC plate case. This fibre distribution case is the best case of all the ten fibre distribution cases that satisfy the minimum v-displacement constraint.
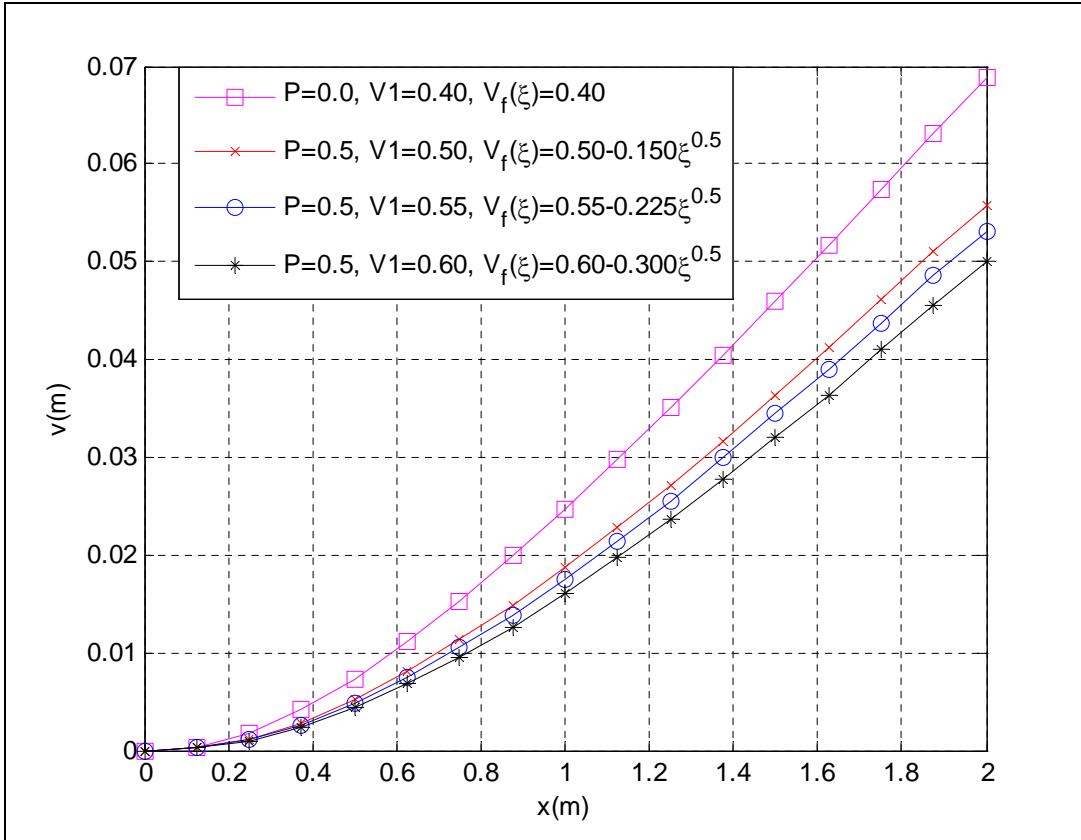

Figure 8-8: Displacement plot for in-plane bending cases with P=0 and P=0.5

9 Conclusion

In this thesis, a Reissner-type element and a Mindlin-type element have been formulated and used in performing a progressive damage analysis, buckling analysis and vibration analysis of a functionally graded composite (FGC) structure. This thesis presents four unique contributions to research which include:

- A Mindlin-type element was formulated for functionally graded composite structure based on averaging of transverse shear distribution over plate thickness using Lagrangian interpolation.

- A Reissner-type element was formulated for functionally graded composite structure based on parabolic transverse shear distribution over plate thickness using Lagrangian and Hermitian interpolation.

- A finite strain analysis was undertaken based on Green's strain-displacement equation.

- A smooth fibre distribution technique was employed in this thesis based on numerical computation of macro-mechanical properties at Gaussian quadrature points.

In this thesis, the validation of the progressive damage results and finite strain results of the Mindlin program and Reissner program were undertaken. The validation exercises for two geometry cases (i.e. rectangular plate and ring) were undertaken. The validation exercises were able to demonstrate the capability of the program to predict the progressive damage of functional graded structures under finite strain condition. In the validation exercise, the following results were obtained.

- The results of the Average and Smooth Mindlin program were in good agreement with the analytical solution.

- The results of the Average and Smooth Mindlin program were in good agreement with the Abaqus results.

- The results of the Average and Smooth FE programs were in good agreement with the Ordinary FE programs using both Mindlin-type elements and Reissner-type elements.

In this thesis, two geometry cases were considered for the optimisation exercise which includes the rectangular FGC plate case and the rectangular FGC plate case with a central hole. A methodical approach was used in demonstrating the design optimisation process and an optimum fibre distribution was obtained for the load cases considered. The fibre distribution effect on the progressive damage results, finite strain results, buckling results and vibration results were investigated. This optimisation exercise was able to demonstrate that constraints such as minimum failure index constraint, minimum displacement constraint, maximum stiffness constraint, maximum critical buckling load and maximum natural frequency can be use to determine the optimum fibre distribution case.

Finally, this thesis achieved its objective by presenting a detailed explanation of the functional graded technology from theoretical concept through to optimum design application.

9.1 Recommendation of Future Work

Future work recommendation would be to extend this work to cover thermo-elasticity and thermo-elastodynamics.

Thermo-elasticity

Thermo-elastic analysis can be introduced to this FE model by adding an additional term (i.e. thermal strain) to the stress-strain equation which accounts for the effect of temperature. The thermal strain is a function of the material thermal expansion coefficient.

Thermo-elastodynamics

This requires the consideration of mechanical and thermal loadings as functions of time. Hence the change of temperature and displacement at a point inside the composite material during an increment of time would result in corresponding energy increments.

REFERENCES

Agarwal, B. D., Broutman, L. J. and Chandrashekhara, K. (2006). Analysis and performance of fiber composites. 3rd edition, John Wiley & Sons, Inc., Hoboken, New Jersey.

Apetre, N. A. and Sankar, B. V. (2008). Analytical modelling of sandwich beams with functionally graded core. *Journal of Sandwich Structures and Materials,* 10(1), p. 53-74.

Argyris, J. H. (1960). Energy theorems and structural analysis. In: *Collection of papers published in Aircraft Engineering in 1954 and 1955.* Butterworths, London.

Attia, O. (1996). Finite element static, dynamic and flutter analysis of rotating composite layered plates and shells. PhD Thesis, SOE, Cranfield University.

Attia O. and El-Zafrany A. (1999). A high order shear element for non-linear vibration analysis of composite layered plates and shells. *International Journal of Mechanical Science,* 41, p. 461-486.

Bathe, K. J. and Wilson, E. L. (1976). *Numerical methods in finite element analysis*, Prentice Hall Englewood Cliffs, New Jersey.

Bey, K. S. (2002). Synergistic tailored design of metals and structures. In: *AVST morphing project research summaries in fiscal year 2001,* NASA Langley Research Center.

Bobaru, F. and Jian, H. (2004) Optimisation of functionally graded materials with temperature dependent properties. A meshfree solution. In: *21st International Congress of Theoretical and Applied Mechanics*, Warsaw, Poland.

Chang, F. K. and Chang, K. Y. (1987). A progressive damage model for laminated composites containing stress concentrations. *Journal of Composite Materials*, 21, p. 834-855.

Chang, F. K. and Lessard, L. B. (1991). Damage tolerance of laminated composites containing an open hole and subjected to comprehensive loadings: Part 1. Analysis. *Journal of Composite Materials,*, 25, p. 2-43.

Chen, X. L. and Liew, K. M. (2004). Buckling of rectangular functionally graded material plates subjected to nonlinearly distributed in-plane edge loads. *Smart Materials and Structures*, 13, p. 1430-1437.

Clint, M. and Jennings, A. (1970). The evaluation of eigenvalues by simultaneous iterations. *Computer Journal*, 13, p. 76-80.

Clough, R. W. (1960). The finite element method in plane stress analysis. *Proceedings of American Society of Civil Engineers, 2nd Conference on Electronic Computations*, 23, p. 345-378.

Corr, R. B. and Jennings, A. (1976). A simultaneous iteration algorithm for symmetric eigenvalue problem. *International Journal of Numerical Methods in Engineering*, 10, p. 647-663.

Courant, R. (1943). Variational methods for the solution of problems of equilibrium and vibrations. *Bulleting of the American Mathematical Society*, 49, p. 1-23.

Daniel, I. M. and Ishai, O. (2006). Engineering mechanics of composite materials, 2nd edition. Oxford University Press.

Datoo, M. H. (1991). Mechanics of fibrous composites. Elsevier Applied Science, London and New York.

Durodola, J. F. and Adlington, J. E. (1997). Functionally graded material properties for disks and rotors. *Key Engineering Materials,* 127-131, p. 1199-1206.

Echaabi, J., Trochu, F., Pham, X. T. and Ouellet, M. (1996). Theoretical and experimental investigation of failure and damage progression of graphite-epoxy composites in flexural bending test. *Journal of Reinforced Plastics and Composites.* 15, p. 740-750.

El-Zafrany, A. and Cookson, R. A. (1986a). Derivation of Lagrangian and Hermitian shape functions for triangular elements. *International Journal of Numerical Engineering*, 23, p. 275-285.

El-Zafrany, A. and Cookson, R. A. (1986b). Derivation of Lagrangian and Hermitian shape functions for quadrilateral elements. *International Journal of Numerical Engineering*, 23, p. 1939-1958.

Essenburg, F. (1975). On the significance of the inclusion of the effect of transverse normal strain in problems involving beams with surface constraints. *ASME Journal of applied Mechanics*, 97, p. 127-132.

Guan, Y. and Tang, L. M. (1992). A quasi-conforming nine-node degenerated shell finite element. *Finite Element Analysis and Design*, 11 p. 165-176.

Guan, Y. and Tang, L.. M. (1995). A geometrically non-linear quasi-conforming nine-node quadrilateral degenerated solid shell element, *International Journal for Numerical Methods in Engineering*, 38 p. 927-942.

Hill, R. (1950). The Mathematical theory of plasticity, Oxford University Press, London.

Hinton, E., Razzaque, A., Zienkiewicz, O. C. and Davies, J. D. (1975). A simple finite element solution for plates of homogenous, sandwich and cellular construction. *Proceedings of the Institution of Civil Engineers*, 59, p. 43-65.

Hrennikoff, A. (1941). Solution of problems in elasticity by the framework method. *Journal of Applied Mechanics,* A8, p. 169-175.

Hughes, T. and Cohen, M. (1978). The heterosis finite element for plate bending. *Computers and Structures*, 9, p. 445-450.

Hughes, T., Cohen, M. and Haroun, M. (1978). Reduced and selective integration techniques in the finite element analysis of plates. *Nuclear Engineering and Design*, 46, p. 203-222.

Javaheri, R. and Eslami, M. R. (2002). Buckling of functionally graded plates under in-plane compressive loading. *Z. Angew. Math. Mech*. 82 (4), p. 277-283.

Kam, T. Y. and Sher, H. F. (1995). Non-linear and first ply failure analyses of laminated composite cross ply plates. *Journal of Composite Materials,*. 29, p. 463-482.

Kaw, A. K. (1997). Mechanics of Composite Materials. CRC Press, Boca Raton, London, New York, Washington.

Kim, Y., Davalos, J. F. and Barbero, E. J. (1996). Progressive failure analysis of laminated composite beams. *Journal of Composite Materials*, 30, p. 536-558.

Kim, K. D. and Lomboy, G. R. (2006). A co-rotational quasi-conforming 4-node resultant shell element for large displacement of elasto-plastic analysis. *Computer Methods in Applied Mechanics and Engineering*, 195(44-47), p. 6502-6522.

Kim, K., Lomboy, G. R. and Han, S. (2008). Geometrically non-linear analysis of functionally graded material (FGM) plates and shells using a four-node quasi-conforming shell element. *Journal of Composite Materials,* 42, p. 485.

Koch and Gunter. (2003). A new generation of cutting tools based on functionally graded sialons for solving the machining problems of the 21st century.

Koizumi, M. (1997). FGM activities in Japan. *Composites Part B*, 28B, p. 1-4.

Levy, S. (1953). Structural analysis and influence coefficients for delta wings. *Journal of Aeronautical Sciences,* 20, p. 449-454.

Lo, D. C., Coats, T. W., Harris, C. E. and Allen, D. H. (1996). Progressive damage analysis of laminated composite (PDALC) – a computational model implemented in the NASA COMET finite element code. *NASA Technical Memo,* No. 4724, NASA.

Lo, K. H., Christensen, R. M. and Wu, E. M. (1977). A higher-order theory of plate deformation, Part 1: Homgeneous Plates, Part 2: Laminate Plates, *ASME Journal of Applied Mechanics*, 44, p. 663-676.

Martinez, N. F. (2001). Finite element analysis of engineering components made of functionally graded materials. *MSc thesis*, Cranfield University, UK.

Mathews, F. L. and Rawlings, R. D. (1999). Composite materials: engineering and science, Imperial College, UK.

McHenry, D. (1943). A lattice analogy for the solution of plane stress problems. *Journal of the Institution of Civil Engineers,* 21, p. 59-82.

Melosh, R. J. (1963). Basis for derivation of matrices for direct stiffness method. *A.I.A.A. Journal*, 1, p. 1631-1637.

Mindlin, R. D. (1951). Influence of Rotary inertia and shear on flexural motion of isotropic elastic plates. *ASME Journal of Applied Mechanics*, 73, p. 69-77.

Nogata, F. and Takahashi, H. (1995). Intelligent functionally graded material: bamboo; *Composites Engineering*, 5(7), p. 743-751.

Padhi, G. S., Shenoi, R. A., Moy, S. S. J. and Hawkins, G. L. (1998). Progressive failure and ultimate collapse of laminated composite plates in bending. *Composite structures,* 40(3-4), p. 277-291.

Park, T. H., Kim, K. D. and Han, S. C. (2006). Linear static and dynamic analysis of laminated composite plates and shells using a 4-node quasi-conforming shell element, *Composites Part B-Engineering*, 37(2-3), p. 237-248.

Paulino, G. H., Sutradhar, A. and Gray, L. J. (2002). Boundary element methods for functionally graded materials. *IABEM*, UT Austion, TX, USA.

Paulino, G. H. and Kim, J. (2003). A new approach to compute T-stress in functionally graded materials by means of the Interaction Integral Method. *Engineering Fracture Mechanics*, 71(13-14), p. 1907-1950.

Pervaiz, T. (1999). Structural integrity of functionally graded materials using finite element methods. *MSc Thesis,* Cranfield University, UK.

Pompe, W., Worch, H., Epple, M., Friess, W., Gelinsky, M., Greil, P., Hempel, U., Scharnweber, D. and Schulte, K. (2003). Functionally graded materials for biomedical applications. *Materials Science and Engineering*, A362, p. 40-60.

Prager, W. and Synge, J. L. (1947). Approximation in elasticity based on the concept of function space. *Quarterly Journal of Applied Mathematics,* 5, p. 241-269.

Prusty, B. G., Ray, C. and Satsangi, S. K. (2001). First ply failure analysis of stiffened panels – a finite element approach. *Composite structures,* 51, p. 73-81.

Pugh, E. D. (1978). A study of quadrilateral plate bending elements with reduced integration. *International Journal of Numerical Methods in Engineering,* 12, p. 1059-1079.

Reddy, J. N. (1984). A simple higher-order theory for laminated composite plates, *Jounal of Applied Mechanics*, 51, p. 745-752.

Reddy, J. N. (2000). Analysis of functionally graded plates. *International Journal of Numerical Methods in Engineering*, 47, p. 663-684.

Reddy, Y. S. N. and Reddy, J. N. (1993). An accurate prediction of failures in composite laminates using a layer-wise model. *Proceedings of the 9th International Conference on Composite Materials*, 3, p. 15-22.

Reissner, E. (1945). The effects of transverse shear deformation on the bending of elastic plates. *ASME Journal of Applied Mechanics*, 67, p. 69-77.

Reissner, E. (1950). On a Variational Theorem in Elasticity. *Journal of Mathematics and Physics*, 29, p. 90-97.

Reissner, E. (1975). On transverse bending of plates, including the effects of transverse shear deformation. *International Journal of Solids and Structures*, 11, p. 569-573.

Shahid, I. and Chang, F. K. (1995). An accumulative damage model for tensile and shear failures of laminated composite plates. *Journal of Composite Materials,* 29, p. 926-981.

Shi, G. and Voyiadjis, G. Z. (1991a). A simple C^0 quadrilateral thick/ thin shell element based on the refined shell theory and the assumed strain fields. *International Journal of Solids and Structures*, 27, p. 283-298.

Shi, G. and Voyiadjis, G. Z. (1991b). Efficient and accurate four-node quadrilateral C^0 plate bending lement based on assumed strain fields. *International Journal for Numerical Methods in Engineering* 32, p. 1041-1055.

Shi, G. and Voyiadjis, G. Z. (1991c). Geometrical nonlinear analysis of plates by assumed strain element with explicit tangent stiffness matrix. *Computers and Structures*, 41, p. 757-763.

Shi, G. and Voyiadjis, G. Z. (1992). A simple non-layered finite element for the elasto-plastic analysis of shear flexible plates. *International Journal for Numerical Methods in Engineering*, 33, p. 85-99.

Shi, G. and Voyiadjis, G. Z. (1993). A computational model for FE ductile plastic damage analysis of plate bending. *ASME Journal of Applied Mechanics*, 60, p. 749-758.

Shi, J. and Askew, C. (1997). Thermal stress in cylinders made of composite materials. *Key Engineering Materials*, 127-131, p. 1109-1116.

Siegmund, T. (2005). Indiana 21st century research and technology fund: Low cost carbon-carbon technology for pervasive economic growth, Purdue University, West Lafayette.

Silvia, E. C. N. and Paulino, G. H. (2004). Topology optimisation applied to the design of functionally graded material (FGM) structures. *XXI ICTAM*, Warsaw, Poland.

Sleight, D. W. (1999). Progressive failure analysis methodology for laminated composite structures. NASA/TP-1999-209107.

Spottswood, S. M. and Palazotto, A. N. (2001). Progressive failure analysis of a composite shell. *Composite Structures*, 53, 117-131.

STA. (1987). Research on the basic technology for the development of FGMs for relaxation of thermal-stress. In: Report from Science and Technology Agency (STA) of Japanese Government.

STA. (1993). Investigation report on the improvement of energy conversion efficiency by FGM technology. In: Report from Scientist and Technology Agency (STA) of Japan.

Sutradhar, A., Paulino, G. H. and Gray, L. J. (2002). Three-dimensional transient heat conduction in functionally graded materials. *IABEM 2002 Symposium*, UT Austion, TX, USA.

Swedish Defence Research Agency. (2002). Armour for future combat vehicles. *Citing Internet resources* (WWW document), http://www.foi.se/upload/omfoi/infomaterial/foi-annual-report-2002.pdf, p. 17

Tang, L. M., Chen, W. J. and Liu, Y. X. (1983). String net approximation and quasi-conforming technique, In: *Hybrid and Mixed Finite Element Methods*, edited by Alturi, S N, Gallagher R H and Zienkiewicz O C.

Tang, L. M., Chen, W. J. and Liu, Y. X. (1984). Formulation of quasi-conforming element and Hu-Washizu principle, *Computers and Structures*, 19(1-2), p. 247-250.

The Society of Non-Traditional Technology. (1991). Survey for application of FGM. (Eds by FGM Forum), Tokyo.

Tolson, S. and Zabaras, N. (1991). Finite element analysis of progressive failure in laminated composite plates. *Computers and Structures*. 38(3), p. 361-376.

Tsach, U. (1981). Locking of thin plate/shell elements. *International Journal of Numerical Methods in Engineering*, 17, p. 633-644.

Tsai, S. W. (1968). Strength theories of filamentary structures, In: *Fundamental aspects of fiber reinforced plastic composites*, edited by Schwartz, R. T. and Schwartz, H. S., Eds., Wiley Inter-science, New York.

Tsai, S. W., and Hahn, H. T. (1980). Introduction to composite materials. Technomic, Lancaster, PA.

Tsai, S. W., and Wu, E. M. (1971). A general theory of strength for anisotropic materials. *Journal of Composite Materials*, 5, p. 58-80.

Turner, M. J., Clough, R. W., Martin, H. C. and Topp, L. C. (1956). Stiffness and deflection analysis of complex structures. *Journal of Aeronautical Sciences,* 23(9), p. 805-824.

U.S. Department of Defence. (2002). Functionally graded thermal barrier coating for F402 turbine engine components. *Citing Internet resources* (WWW document), https://www.dodmantech.com/successes/index_archive.asp?main=success.

Whitney, J. M. and Pagano, N. J. (1970). Shear deformation in heterogeneous anisotropic plates. *Journal of Applied Mechanics*, 37, p. 1031-1036.

Whitney, J. M., Daniel, I. M. and Pipes, R. B. (1984). Experimental mechanics of fiber reinforced composite materials. Revised edition. The society for experimental mechanics, Brookfield Center, Connecticut.

Whitney, J. M. (1990). A modified shear deformation theory for laminated anisotropic plates. Proceedings of the American Society for Composites, Fifth Technical Conference, Technomic Publishing Co., Lancaster, PA, pp.469-478.

Whitney, J. M. and Rose, D. H. (1991). Effect of transverse normal stress on the bending of thick laminated plates. Proceedings of ICCM VIII, Edited by S. W. Tsai and

G. S. Springer, Society for the Advancement of Material and Process Engineering (SAMPE), Covina, CA, pp.30-B-1 – 30-B-10.

Whitney, J. M. (1992). Cylindrical bending of thick laminated plates, *Recent Advances in the Structural Dynamic Modelling of Composite Rotor Blades and Thick Composites*, AD-Vol.30, ASME, New York, NY, USA, p. 171-178.

Yang, P. C., Norris, C. H. and Stavsky, Y. (1966). Elastic wave propagation in heterogenous plates. *International Journal of Solids and Structures*, 2, p. 665-684.

Yang, Y. Y. (1998). Stress analysis in a joint with a functionally graded material under a thermal loading by using the Mellin transform method. *International Journal of Solids and Structures,* 35(12), p. 1261-1287.

Zahari, R. (2005). Progressive damage analysis of composite layered plates and shells using finite strip methods. PhD Thesis, SOE, Cranfield University.

Zienkiewicz, O. C. and Cheung, Y. K. K. (1967). The finite element method in structural and continuum mechanics, London, McGraw-Hill.

Zienkiewicz, O. C. (1977). The finite element method. 3rd Ed. McGraw-Hill, London.

APPENDICES

The following topics are dealt with in this section.

- Constitutive equations for laminates
- Integrated D matrices

A   Constitutive Equations for Laminates

A lamina is in, or parallel to, the *x-y* plane, with *x, y, z* being the geometrical axes, as shown in Figure A.1. If x', y', z' are the material axes, where x' is usually in the fibre direction, then the elastic properties of the lamina are:

Fig. A.1 Axes of a lamina
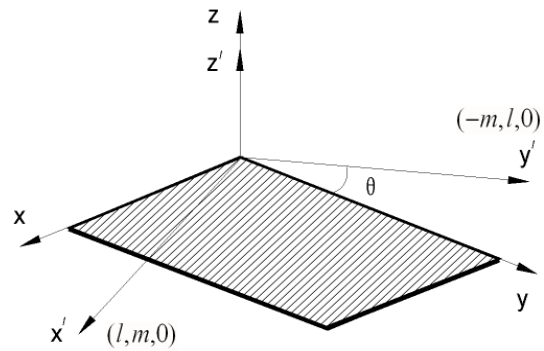
(i)   Young's modulus in the fibre direction (E_{11}).

(ii)   Young's modulus in y' direction (E_{22}).

(iii)   Major Poisson's ratio (v_{12}).

(iv)   Shear modulus in $x' - y'$ plane (μ_{12}).

(v)   Transverse shear moduli ($\mu_{23} = \mu_{31} \equiv \mu$).

Notice also that:

$$\frac{v_{21}}{E_{22}} = \frac{v_{12}}{E_{11}} \tag{A.1}$$

and σ_z is considered negligible.

The lamina is orthotropic with respect to $x'-y'-z'$ axes. Using generalized Hooke's equations, then it can be deduced that:

$$\varepsilon_{x'} = \frac{1}{E_{11}}\sigma_{x'} - \frac{v_{21}}{E_{22}}\sigma_{y'} \qquad (A.2)$$

$$\varepsilon_{y'} = -\frac{v_{12}}{E_{11}}\sigma_{x'} + \frac{1}{E_{22}}\sigma_{y'} \qquad (A.3)$$

$$\gamma_{x'y'} = \frac{1}{\mu_{12}}\tau_{x'y'} \qquad (A.4)$$

$$\gamma_{y'z'} = \frac{1}{\mu_{23}}\tau_{y'z'} \qquad (A.5)$$

$$\gamma_{z'x'} = \frac{1}{\mu_{31}}\tau_{z'x'} \qquad (A.6)$$

From which it can be deduced that:

$$\boldsymbol{\sigma}' = \mathbf{D}'\,\boldsymbol{\varepsilon}' \qquad (A.7)$$

and

$$\boldsymbol{\tau}' = \boldsymbol{\mu}'\,\boldsymbol{\gamma}' \qquad (A.8)$$

where

$$\boldsymbol{\varepsilon}' = \begin{bmatrix} \varepsilon_{x'} \\ \varepsilon_{y'} \\ \gamma_{x'y'} \end{bmatrix}, \quad \boldsymbol{\sigma}' = \begin{bmatrix} \sigma_{x'} \\ \sigma_{y'} \\ \tau_{x'y'} \end{bmatrix}, \quad \boldsymbol{\gamma}' = \begin{bmatrix} \gamma_{x'z'} \\ \gamma_{y'z'} \end{bmatrix}, \quad \boldsymbol{\tau}' = \begin{bmatrix} \tau_{x'z'} \\ \tau_{y'z'} \end{bmatrix}$$

and

$$\mathbf{D}' = \frac{1}{(1-v_{12}v_{21})}\begin{bmatrix} E_{11} & v_{21}E_{11} & 0 \\ v_{12}E_{22} & E_{22} & 0 \\ 0 & 0 & (1-v_{12}v_{21})\mu_{12} \end{bmatrix} \qquad (A.9)$$

$$\boldsymbol{\mu}' = \begin{bmatrix} \mu_{31} & 0 \\ 0 & \mu_{23} \end{bmatrix} \equiv \mu\begin{bmatrix} 1 & 0 \\ 0 & 1 \end{bmatrix} \qquad (A.10)$$

Notice also that the $\mathbf{D}'$ matrix is symmetric.

Using planar transformation for a lamina, as shown in Figure A.1, it can be deduced that:

$$\boldsymbol{\sigma}' = \begin{bmatrix} l^2 & m^2 & 2lm \\ m^2 & l^2 & -2lm \\ -lm & lm & l^2 - m^2 \end{bmatrix} \boldsymbol{\sigma}^{(l)} \tag{A.11}$$

$$\boldsymbol{\varepsilon}' = \begin{bmatrix} l^2 & m^2 & lm \\ m^2 & l^2 & -lm \\ -2lm & 2lm & l^2 - m^2 \end{bmatrix} \boldsymbol{\varepsilon}^{(l)} \tag{A.12}$$

where the lamina is considered to be the lth layer of a composite plate, and:

$$\boldsymbol{\sigma}^{(l)} = \begin{bmatrix} \sigma_x \\ \sigma_y \\ \tau_{xy} \end{bmatrix}, \qquad \boldsymbol{\varepsilon}^{(l)} = \begin{bmatrix} \varepsilon_x \\ \varepsilon_y \\ \gamma_{xy} \end{bmatrix} \tag{A.13}$$

$$l = \cos\theta, \quad m = \sin\theta \tag{A.14}$$

Hence, it can be deduced that:

$$\boldsymbol{\sigma}^{(l)} = \begin{bmatrix} l^2 & m^2 & -2lm \\ m^2 & l^2 & 2lm \\ lm & -lm & l^2 - m^2 \end{bmatrix} \mathbf{D}' \begin{bmatrix} l^2 & m^2 & lm \\ m^2 & l^2 & -lm \\ -2lm & 2lm & l^2 - m^2 \end{bmatrix} \boldsymbol{\varepsilon}^{(l)}$$

$$\equiv \mathbf{D}^{(l)} \boldsymbol{\varepsilon}^{(l)} \tag{A.15}$$

where

$$\mathbf{D}^{(l)} = \begin{bmatrix} l^2 & m^2 & -2lm \\ m^2 & l^2 & 2lm \\ lm & -lm & l^2 - m^2 \end{bmatrix} \mathbf{D}' \begin{bmatrix} l^2 & m^2 & lm \\ m^2 & l^2 & -lm \\ -2lm & 2lm & l^2 - m^2 \end{bmatrix} \tag{A.16}$$

Writing

$$\mathbf{D} \equiv \begin{bmatrix} d_{11} & d_{12} & d_{13} \\ d_{21} & d_{22} & d_{23} \\ d_{31} & d_{32} & d_{33} \end{bmatrix}, \quad \mathbf{D}' \equiv \begin{bmatrix} d'_{11} & d'_{12} & 0 \\ d'_{12} & d'_{22} & 0 \\ 0 & 0 & d'_{33} \end{bmatrix} \tag{A.17}$$

then it can be deduced from Equation (A.16) that:

$$d_{11} = l^4 d'_{11} + m^4 d'_{22} + 2 l^2 m^2 \left(d'_{12} + 2 d'_{33} \right)$$

$$d_{22} = l^4 d'_{22} + m^4 d'_{11} + 2 l^2 m^2 \left(d'_{12} + 2 d'_{33} \right)$$

$$d_{12} = d_{21} = \left(l^4 + m^4 \right) d'_{12} + l^2 m^2 \left(d'_{11} + d'_{22} - 4 d'_{33} \right)$$

$$d_{33} = \left(l^2 - m^2 \right)^2 d'_{33} + l^2 m^2 \left(d'_{11} + d'_{22} - 2 d'_{12} \right)$$

$$d_{13} = d_{31} = l m \left[l^2 d'_{11} - m^2 d'_{22} - \left(l^2 - m^2 \right) \left(d'_{12} + 2 d'_{33} \right) \right]$$

$$d_{23} = d_{32} = l m \left[m^2 d'_{11} - l^2 d'_{22} + \left(l^2 - m^2 \right) \left(d'_{12} + 2 d'_{33} \right) \right]$$

It can also be deduced from planar rotation that:

$$\boldsymbol{\tau}' = \begin{bmatrix} l & m \\ -m & l \end{bmatrix} \boldsymbol{\tau}^{(l)}, \quad \boldsymbol{\gamma}' = \begin{bmatrix} l & m \\ -m & l \end{bmatrix} \boldsymbol{\gamma}^{(l)} \tag{A.18}$$

where

$$\boldsymbol{\tau}^{(l)} \equiv \begin{bmatrix} \tau_{xz} \\ \tau_{yz} \end{bmatrix}, \quad \boldsymbol{\gamma}^{(l)} \equiv \begin{bmatrix} \gamma_{xz} \\ \gamma_{yz} \end{bmatrix} \tag{A.19}$$

Hence, it can be deduced from Equations (A.18) and (A.8) that:

$$\boldsymbol{\tau}^{(l)} = \begin{bmatrix} l & -m \\ m & l \end{bmatrix} \boldsymbol{\mu}' \begin{bmatrix} l & m \\ -m & l \end{bmatrix} \boldsymbol{\gamma} \equiv \boldsymbol{\mu}^{(l)} \boldsymbol{\gamma} \tag{A.20}$$

where

$$\boldsymbol{\mu}^{(l)} = \begin{bmatrix} l & -m \\ m & l \end{bmatrix} \boldsymbol{\mu}' \begin{bmatrix} l & m \\ -m & l \end{bmatrix} \equiv \begin{bmatrix} l^2 \mu_{31} + m^2 \mu_{23} & lm(\mu_{31} - \mu_{23}) \\ lm(\mu_{31} - \mu_{23}) & l^2 \mu_{23} + m^2 \mu_{31} \end{bmatrix} \tag{A.21}$$

$$\equiv \boldsymbol{\mu}'$$

B   Integrated D matrices

B.1 $\mathbf{D_n}$

The integrated $\mathbf{D_n}$ matrices are defined generally by Equation (1.82), from which it can be deduced that:

$$\mathbf{D}_n = \int_{-h/2}^{h/2} z^n \mathbf{D}^{(l)} dz \equiv \sum_{l=1}^{N_l} \int_{z=Z_L^{(l)}}^{z=Z_U^{(l)}} z^n \mathbf{D}^{(l)} dz \tag{B.1}$$

Hence, it can be proved that:

$$\mathbf{D}_n = \sum_{l=1}^{N_l} \left\{ \left[\frac{\left(Z_U^{(l)}\right)^{n+1} - \left(Z_L^{(l)}\right)^{n+1}}{n+1} \right] \mathbf{D}^{(l)} \right\} \tag{B.2}$$

from which it can be deduced that:

$$\mathbf{D}_o = \sum_{l=1}^{N_l} \left\{ h^{(l)} \mathbf{D}^{(l)} \right\} \tag{B.3}$$

$$\mathbf{D}_1 = \sum_{l=1}^{N_l} \left\{ \left[\frac{\left(Z_U^{(l)}\right)^2 - \left(Z_L^{(l)}\right)^2}{2} \right] \mathbf{D}^{(l)} \right\} \tag{B.4}$$

$$\mathbf{D}_2 = \sum_{l=1}^{N_l} \left\{ \left[\frac{\left(Z_U^{(l)}\right)^3 - \left(Z_L^{(l)}\right)^3}{3} \right] \mathbf{D}^{(l)} \right\} \tag{B.5}$$

$$\mathbf{D}_3 = \sum_{l=1}^{N_l} \left\{ \left[\frac{\left(Z_U^{(l)}\right)^4 - \left(Z_L^{(l)}\right)^4}{4} \right] \mathbf{D}^{(l)} \right\} \tag{B.6}$$

$$D_4 = \sum_{l=1}^{N_l} \left\{ \left[\frac{\left(Z_U^{(l)}\right)^5 - \left(Z_L^{(l)}\right)^5}{5} \right] D^{(l)} \right\} \tag{B.7}$$

Notice that for symmetric composites:

$$D_1 = O , \quad D_3 = O$$

B.2 Other Integrated D Matrices

These are defined by Equations (1.83)-(1.86), and if we use the following generalized expression:

$$D_p = \int_{-h/2}^{h/2} \left(\frac{dg_p(z)}{dz} \right) D^{(l)} \, dz \tag{B.8 a}$$

then it can be deduced that:

$$D_p = \sum_{l=1}^{N_l} \int_{z=Z_L^{(l)}}^{z=Z_U^{(l)}} \left(\frac{dg_p}{dz} \right) D^{(l)} \, dz = \sum_{l=1}^{N_l} \left\{ \left[g_p\left(Z_U^{(l)}\right) - g_p\left(Z_L^{(l)}\right) \right] D^{(l)} \right\} \tag{B.8b}$$

Different $g_p(z)$ functions for different D_p matrices, employed in the report are as follows:

(i) $D_{\psi 0}$

$$g_{\psi 0}(z) = \int_0^z f_\psi \, dz = z^2 \left[\frac{3}{4} - \frac{1}{2} \left(\frac{z}{h} \right)^2 \right] \tag{B.9}$$

(ii) $D_{\psi 1}$

$$g_{\psi 1}(z) = \int_0^z z\, f_\psi \, dz = z^3 \left[\frac{1}{2} - \frac{2}{5} \left(\frac{z}{h} \right)^2 \right] \qquad (\text{B.10})$$

(iii) $\mathbf{D}_{\psi 2}$

$$g_{\psi 2}(z) = \int_0^z z^2 f_\psi \, dz = z^4 \left[\frac{3}{8} - \frac{1}{3} \left(\frac{z}{h} \right)^2 \right] \qquad (\text{B.11})$$

(iv) $\mathbf{D}_{\psi 3}$

$$g_{\psi 3}(z) = \int_0^z z^3 f_\psi \, dz = z^5 \left[\frac{3}{10} - \frac{2}{7} \left(\frac{z}{h} \right)^2 \right] \qquad (\text{B.12})$$

(v) $\mathbf{D}_{\psi \psi}$

$$g_{\psi \psi}(z) = \int_0^z f_\psi^2 \, dz = z^3 \left[\frac{3}{4} - \frac{6}{5} \left(\frac{z}{h} \right)^2 + \frac{4}{7} \left(\frac{z}{h} \right)^4 \right] \qquad (\text{B.13})$$

(vi) $\mathbf{D}_{\psi \psi 1}$

$$g_{\psi \psi 1}(z) = \int_0^z z\, f_\psi^2 \, dz = z^4 \left[\frac{9}{16} - \left(\frac{z}{h} \right)^2 + \frac{1}{8} \left(\frac{z}{h} \right)^4 \right] \qquad (\text{B.14})$$

(vii) $\mathbf{D}_{\psi \psi 2}$

$$g_{\psi \psi 2}(z) = \int_0^z z^2 f_\psi^2 \, dz = z^5 \left[\frac{9}{20} - \frac{6}{7} \left(\frac{z}{h} \right)^2 + \frac{4}{9} \left(\frac{z}{h} \right)^4 \right] \qquad (\text{B.15})$$

(viii) $\mathbf{D}_{\psi \psi \psi}$

$$g_{\psi \psi \psi}(z) = \int_0^z f_\psi^3 \, dz = z^4 \left[\frac{27}{32} - \frac{9}{4} \left(\frac{z}{h} \right)^2 + \frac{9}{4} \left(\frac{z}{h} \right)^4 - \frac{4}{5} \left(\frac{z}{h} \right)^6 \right] \qquad (\text{B.16})$$

(ix) $\mathbf{D}_{\psi\psi\psi 1}$

$$g_{\psi\psi\psi 1}(z) = \int_0^z z\, f_\psi^3 \, dz = z^5 \left[\frac{27}{40} - \frac{27}{14} \left(\frac{z}{h} \right)^2 + 2 \left(\frac{z}{h} \right)^4 - \frac{8}{11} \left(\frac{z}{h} \right)^6 \right] \qquad \text{(B.17)}$$

(x) $\mathbf{D}_{\psi\psi\psi\psi}$

$$g_{\psi\psi\psi\psi}(z) = \int_0^z f_\psi^4 \, dz = z^5 \left[\frac{81}{80} - \frac{27}{7} \left(\frac{z}{h} \right)^2 + 6 \left(\frac{z}{h} \right)^4 - \frac{48}{11} \left(\frac{z}{h} \right)^6 + \frac{16}{13} \left(\frac{z}{h} \right)^8 \right] \text{(B.18)}$$

For symmetric composites:

$$\mathbf{D}_{\psi 0} = \mathbf{O}, \qquad \mathbf{D}_{\psi 2} = \mathbf{O}$$
$$\mathbf{D}_{\psi\psi 1} = \mathbf{O}, \qquad \mathbf{D}_{\psi\psi\psi} = \mathbf{O}$$